Development of 1D and 2D Joint Inversion Algorithms for Semi-Airborne and LOTEM Data: A Data Application from Eastern Thuringia, Germany

Inaugural-Dissertation

zur Erlangung des Doktorgrades
der Mathematisch-Naturwissenschaftlichen Fakultät
der Universität zu Köln

vorgelegt von

Cai Ji

aus Xiamen, China

1. Gutachter: Prof. Dr. B. Tezkan
2. Gutachter: Prof. Dr. M. Becken

Tag der mündlichen Prüfung: 29.05.2020

Abstract

By combining the resolution advantages of different electromagnetic (EM) methods, joint inversion can result in a better resolution of subsurface structures than the individual inversions of each single method. To reduce the ambiguities and parameter uncertainty in the results, joint inversion algorithms are developed to couple spatially dense sampled data from semi-airborne frequency-domain electromagnetic measurements and horizontal electric fields measured using the long-offset transient electromagnetic (LOTEM) method.

The novel semi-airborne frequency-domain electromagnetic system was developed and tested successfully within the DESMEX project funded by the BMBF (German Ministry for Science and Education). The method takes advantages of both ground and airborne techniques by combining ground-based high power sources with large scale and spatially dense covered data. However, the method usually has a reduced signal-to-noise ratio compared to the ground-based method. For example, compared to LOTEM, the semi-airborne technique has a smaller depth of investigation (DOI) due to the reduced data quality and offset limitations. On the other hand, compared to helicopter-borne EM (HEM), semi-airborne indicates reduced resolution for shallow subsurface structures. Aiming at combining and validating the advantages of all these methods using joint inversion, resolution studies are performed for the HEM, LOTEM and semi-airborne data.

Based on the insights of their different resolution properties, the joint inversion algorithm was developed to combine the advantages of each method effectively. For selected field data cases, the 1D joint inversion could improve the inversion results significantly. However, due to 2D effects in the field data, the 1D joint inversion faces convergence problems. Additional synthetic modeling studies are conducted to investigate and effects of 2D structures on the 1D interpretation using joint inversion.

Because of multidimensional effects in the field data, a 2D joint inversion algorithm was further developed for the frequency-domain semi-airborne EM data and the time-domain LOTEM electric field data. 2D synthetic modeling studies were performed to gain insights regarding the resolution differences between the two data-sets. The 2D synthetic modeling studies show that the different field components observed in each method are the key factor that leads to different resolution properties. However, the influence of the different measurement configurations is also significant. For the inversion of the field data, characteristic structures seen in both individual inversion results can also be found in the 2D joint inversion result. Due to possible 3D, anisotropic, or even induced polarization

(IP) effects in data, the applied 2D joint inversion cannot fully explain all the discrepancies observed between the single method inversions. The influence of 3D structures on 2D inversions of semi-airborne data is investigated.

Kurzzusammenfassung

Durch die Kombination der Auflösungsvorteile mehrerer verschiedener elektromagnetischer (EM) Methoden können gemeinsame Inversionen zu einer besseren Auflösung von Untergrund-Strukturen führen als die einzelnen Inversionen der jeweiligen Methode. Um die Mehrdeutigkeit und Parameterunsicherheit in den Inversionsergebnissen zu reduzieren, werden Joint-Inversions-Algorithmen entwickelt,um räumlich dicht aufgezeichnete Daten einer semi-airborne elektromagnetische Messungen im Frequenzbereich und die Horizontalkomponente des elektrischen Feldes einer long-offset transienten (LOTEM) Messung gemeinsam zu interpretieren.

Das neuartige semi-airborne Frequenzbereichs-EM System wurde im Rahmen des vom BMBF (Bundesministerium für Wissenschaft und Bildung) geförderten DESMEX-Projekts erfolgreich entwickelt und getestet. Es nutzt die jeweiligen Vorteile von Boden- und luftgestützten Systemen aus, indem es eine bodengebundene Hochleistungsquelle mit einer großflächigen und hohen räumlichen Datendichte kombiniert. Das Verfahren weist jedoch üblicherweise ein verringertes Signal-zu-Rausch-Verhältnis im Vergleich zu einem bodengebundenen Verfahren auf. Beispielsweise ist die Untersuchungstiefe (DOI) des semi-airborne Verfahrens durch eine Begrenzungen der Datenqualität und des Offsets im Vergleich zu LOTEM geringer. Auf der anderen Seite zeigt sich im Vergleich zu Hubschrauber-EM (HEM) eine verringerte Auflösung für oberflächennahe Untergrund-Strukturen. Um die Vorteile all dieser Methoden durch eine Joint-Inversion zu kombinieren und zu validieren, werden Auflösungsstudien für die HEM-, LOTEM- und semi-airborne-Daten durchgeführt.

Basierend auf den Erkenntnissen über die Auflösungsunterschiede der einzelnen Methoden wurde ein Joint-Inversions Algorithmus entwickelt, der die jeweiligen Vorteile kombiniert. In ausgewählten Fällen konnte die 1D-Joint Inversion die Inversionsergebnisse signifikant verbessern. Aufgrund der 2D-Effekte in den Felddaten treten bei der 1D-Joint Inversion jedoch Konvergenzprobleme auf. Weitere synthetische Modellierungen werden durchgeführt, um den Einfluss der 2D-Effekte auf die 1D-Joint-Inversion zu untersuchen.

Aufgrund von mehrdimensionalen Effekten in den Felddaten wurde ein 2D-Joint-Inversions-Algorithmus für die semi-airborne Frequenzbereichs-Daten und die elektrischen LOTEM Zeitbereichs-Daten weiter entwickelt. Um die Auflösungsunterschiede zwischen den zwei Datensätzen im 2D-Fall zu ermitteln, wurden synthetische 2D-Modellierungsstudien durchgeführt. Die synthetischen 2D-Modellierungen zeigen, das die verschiedenen aufgezeichneten Feld-Komponenten der Hauptfaktor für die unterschiedlichen Auflösungseigenschaften sind. Ebenfalls signifikant sind die Auswirkungen verschiedener Messkonfigurationen. Die 2D-Inversion der Felddaten weist Merkmale aus beiden Einzelinversionsergebnissen auf. Aufgrund möglicher 3D-, Anisotropie- oder induzierte Polarisations (IP) -Effekte in den Felddaten kann die 2D-Joint-Inversion jedoch noch nicht alle Unterschiede erklären, die zwischen den Inversionen der einzelnen Methoden beobachtet wurden. Der Einfluss von 3D-Strukturen auf die 2D-Inversion von semi-airborne Daten wird untersucht.

Contents

List of Figures

1 Introduction

The main focus of this thesis is the development of the joint inversion for semi-airborne electromagnetic (EM) and long offset transient electromagnetic (LOTEM) data. The developed 1D and 2D joint inversion algorithms are applied to the field data acquired in eastern Thuringia, Germany. For validating the algorithms, the characteristics of each involved EM method and their effect on the joint inversion algorithms are investigated.

Natural resources such as mineral resources, hydrocarbons, and groundwater can cause significant variations of the resistivity distributions in the earth subsurface (E.g. Edwards, 1997; Haroon, 2016; Spagnoli et al., 2016). EM methods have the capability to detect these resistivity variations and then distinguish these resources form the host rocks or sediments. Therefore, in practice, the EM measurements can optimally explore the earth subsurface at rather deep scales, on large spatial scales, and with a high resolution. A lot of efforts are made to achieve these goals. For instance, a novel EM method named Differential Electrical Dipole (DED) is developed to enhance the resolution of the lateral boundary of a resistor related to a submarine aquifer (Haroon, 2016). The newly developed semi-airborne system involved in this thesis is aiming at realising a fast and deep subsurface exploration (Smirnova et al., 2019). The general direction of this study is improving the accuracy of the deviated resistivity model by jointly considering the data from multiple EM methods.

Many factors challenge the reconstruction of accurate and meaningful resistivity models. The non-uniqueness problem of the inversion of EM data is one of the most important. The data measured by EM methods can usually be interpreted by a suite of different resistivity models (Moghadas et al., 2015; Gehrmann et al., 2016; Cai et al., 2018). In order to ensure reliable results, a large amount of data usually need to be measured in EM surveys. Often the amount of measured data is even larger than the unknowns or model parameters. However, these data are not necessarily independent, are usually affected by noise and the resolution properties limited. The EM inverse problem remains ill-posed. As a result, parts of the parameters in the derived resistivity models cannot be uniquely determined. In this case, the joint inversion of several geophysical datasets could contribute to increasing the reliability of the inversion result and decreasing the ambiguity of the resulting models (Meqbel and Ritter, 2015). By taking the data of different geophysical methods into account, more independent information is considered the inversion problem, resulting in the stronger constrain of the model parameters. The advantages of applying an joint inversion on the EM data are discussed by Vozoff and

Jupp (1975) as early as 1970s. They combined DC resistivity and magnetotelluric measurements for resolving a simple 3-layer model. As concluded by them, the resistivity of a thin resistive layer was resolved by the combination, even though neither of the two methods can do so alone. In the following decades, plenty of other EM methods take part in the joint inversions. By jointly inverting the MT and transient electromagnetic(TEM) data, Meju (1996) tried to remove the static shift in MT sounding curves. Sudha et al. (2014) proposed a 1D joint inversion of TEM, helicopter-borne EM (HEM) and radio-magnetotellurics (RMT) to combine the independent information from different depths. Commer and Newman (2009) and Meqbel and Ritter (2015) realized the 3D joint inversion of MT and controlled-source electromagnetic (CSEM) data by non-linear conjugate gradient (NLCG) inversion. For improving joint inversion results, weighting schemes between datasets were also investigated by them (Commer and Newman, 2009; Meqbel and Ritter, 2015; Sudha et al., 2014). The joint inversions include not only the EM and electrical methods that are sensitive to electrical resistvity but also other geophysical methods that are sensitive to other physical parameters. Moorkamp et al. (2011) applied the 3D joint inversion for seismic, MT, and gravity data. Wagner et al. (2019) imaged the water, ice and air in permafrost systems by applying the joint inversion on seismic refraction and electrical resistivity data. As stated, in this thesis, the major jointly inverted data come from semi-airborne and LOTEM measurements. Additionally, the HEM data are also taken into account in the 1D joint inversions. All these methods are particularly sensitive to electrical conductivity.

One major part of this thesis is the semi-airborne data acquired in the frame of the DESMEX project (Deep electromagnetic sounding for mineral exploration). The BMBF funded project is aiming at developing a semi-airborne EM exploration method, which combines a large penetration depth with a fast and dense area coverage (Smirnova et al., 2019). Compared to land-based measurements, the receivers installed on the aircraft enable the quick covering of a large survey area Seigel (1971), which is a significant advantages in a large-scale survey. Compared to typical air-borne (AEM) surveys, the deployed ground-based transmitters have the potential to reach a detection depth of several kilometers. However, the semi-airborne system in frequency-domain also has some weak points. The receivers moving in the air can usually not ensure data quality as good as land-based measurement. The dominating primary field in the vicinity of the source leads to a reduced resolution for the shallow layers. Therefore, the DESMEX project and applied exploration concept involve various EM methods, including ground-based techniques to improve the resolution or also near-surface high-resolution HEM for first reconnaissance on the regional scale. In 2016 and 2017, the first semi-airborne EM experiments were conducted in eastern Thuringia, Germany. Because the semi-airborne EM technique is a new approach, various additional ground-based validation experiments were done, for example, a large scale 2D LOTEM survey along a selected flight line.

The LOTEM method routinely operates in time-domain, and it is classified as a controlled source electromagnetic method (CSEM). It has been developed for several decades. The theoretical details of LOTEM are provided, for example, by Strack (1992). By utilizing a horizontal electrical dipole (HED) with large cable length (1-2 km) as the transmitter, as well as transmitter-receiver separations ranging from 1 km up to several km, the LOTEM method can typically investigate the subsurface down to several kilometers Haroon (2012); Mörbe (2019). LOTEM has also been widely applied in various field experiments and has been abundantly studied (e.g., Newman, 1989; Hördt, 1992; Hördt et al., 2000; Hördt and Scholl, 2004). In recent years, it was employed to explore mud-volcanoes in Azerbaijan (Haroon, 2012; Haroon et al., 2015), and also extended its application to the marine environment Lippert and Tezkan (2019). The LOTEM measurements involved in this thesis are described in detail by Mörbe (2019). Mörbe (2019) also evaluates the acquired time-domain LOTEM field data in the frequency-domain.

The HEM data considered in this thesis is measured by the system of the German Federal Institute of Geosciences and Natural Resources (Siemon, 2012), which operates in frequency-domain. This system acquires accurate data at rather high frequencies and has significant advantages in resolving shallow structures. The HEM system has been used for numerous applications, such as geological mapping, mineral prospecting Steuer et al. (2015), groundwater exploration (Steuer et al., 2009) as well as environmental and geotechnical surveys (Siemon et al., 2009). Because of the small source footprint, the HEM data are routinely inverted in the 1D case (Steuer et al., 2015). Aiming at improving the constrains in the joint inversion for shallow structures, the HEM data are utilized in the 1D joint inversions.

For the application of the joint inversion, the 1D inversion algorithm EMUPLUS developed at the University of Cologne (e.g., Scholl, 2005) is utilized for the 1D cases, and the open-source 2D algorithm MARE2DEM is employed for the 2D modeling (Key, 2016). The 1D forward modeling algorithm of semi-airborne was recently provided by Janser (2017). With the original functions for LOTEM and HEM forward modeling (Scholl, 2005; Siemon, 2012; Sudha et al., 2014), the joint inversion of all three EM methods is realized in EMUPLUS within this thesis. On the other hand, the 2D joint inversion of time-domain LOTEM data and frequency-domain semi-airborne data is also realized in

MARE2DEM, based on the time-domain solution implemented by Haroon et al. (2018).

Thesis overview

The structure of this thesis is as follows. In the second chapter, the research background is introduced. Since multiple EM methods are involved in this thesis, the corresponding theories for each EM methods are concisely stated in the same chapter. In chapter 3, the inversion theory is described, which includes the key techniques utilized for the following chapters. In Chapter 4, the 1D modeling studies and inversions are provided. Firstly, the resolution studies are applied to the three EM methods used. According to the gained insights regarding their resolution characteristics, the advantages shown by 1D joint inversions are discussed. Furthermore, the different weighting schemes for 1D joint inversion are discussed. Subsequently, the 1D inversion is applied to the field data acquired in eastern Thuringia, Germany. Finally, the 2D effects and their influence in the 1D joint inversion is investigated. The 2D modeling and inversion are presented in chapter 5. In order to fulfil the joint inversion of frequency- and time-domain data, MARE2DEM was modified and further developed. The details of the modification, adjustment and necessary validations are given in the first part of this chapter. Because the LOTEM data are available in both frequency- and time-domain, the subsequently shown 2D synthetic modeling and inversions are divided into two sections — one section considers the frequency-domain LOTEM data, and the other one is for time-domain LOTEM data evaluation. In each section, the 2D inversions are firstly applied to synthetic data and afterward to field data. Most of the synthetic 2D resistivity models are based on the inversion results of field data. Therefore, the synthetic modeling plays an important role in the following analyses of all field inversion results. According to the inversion results of field data, some extra modeling studies are performed to further understand, for example, the influence of 3D effects in the developed 2D inversion. This thesis closes with a general conclusion and an outlook, which are given in 6.

Preliminary Notes

In the particular case of this thesis, the LOTEM data include only source current normalized horizontal electric fields (Ex) measured by a broadside configuration. The semi-airborne data indicate the transfer function of vertical magnetic fields, which are also denoted by Bz for simplification. The studies presented in this thesis are highly related to the research of Mörbe (2019).

2 Research background and theory

Because multiple electromagnetic methods are involved in this thesis, the related basic theory is presented together with the introduction to the overall research background in order to keep a clear and logical structure. Firstly, the basic theories of each EM method is presented. What are the targets of the EM measurements and how these methods work in general are briefly described. Subsequently, the specific research background of this thesis is introduced. This part will discuss the concepts of the EM measurements done in the field surveys, including the different measuring configurations and the part of the technical details for each EM measurement. Naturally, the specific theory and fundamental equations for each EM method are concisely listed. At last, the overall characteristics of the three EM methods are compared, and the main motivation of this thesis is introduced in more detail.

2.1 Applied EM Methods

Based on the different physical properties, various applied geophysical measurements can be employed in exploring earth subsurface. Depending on the characteristics of different geological structures, like porosity, water content, or mineral content, the electromagnetic properties between these structures are distinct. The EM surveys are utilized to detect the variations of the electromagnetic quantities in the space, aiming at providing the electromagnetic information of subsurface. Usually, the electrical conductivity σ or its inverse $\rho = 1/\sigma$ are measured. Naturally, it is also possible that different materials share similar resistivity ranges, which contributes to the uncertainties and ambiguity of EM measurements. Thus, to interpret subsurface models adequately, the prior information from geology or other geophysical measurements are always expected. Nevertheless, based on evaluating the resistivity distribution of the surface, EM methods are helpful in many situations, such as mineral, oil and groundwater explorations (e.g., Key, 2012; Haroon, 2012, 2016; Cai et al., 2018). For acquiring the desired resistivity distribution of the subsurface, the conductivity-dependent quantities like magnetic and electric fields are observed. The positions of observations vary among different EM methods. Conventional methods like magnetotelluric sounding (MT) or transient electromagnetic sounding (TEM) usually observe the electromagnetic fields on the land. The airborne or semi-airborne EM surveys measure the magnetic field in the air. The deduction of conductivity or resistivity from the observed magnetic fields is realized by the inversion, which will be introduced in the next chapter. On the other hand, as fundamental of inversion, the forward modeling for each EM methods are presented in this chapter. Before detailed formulas or equations, the variables and constants used in this thesis are listed in the following table.

Table 1: Variables and constants. Vectors are presented as bold characters.

Variable	Symbol	Units
Electric Field Strength	$\mathbf{E}$	V/m
Electric Displacement	$\mathbf{D}$	As/m^2
Magnetic Flux Density	$\mathbf{B}$	T = Vs/m^2
Magnetic Field Strength	$\mathbf{H}$	A/m
Current Denisty	$\mathbf{j}$	A/m^2
Current	I	A
Electric Charge Density	ϱ	As/m^3
Electrical Permittivity	$\varepsilon = \varepsilon_0\varepsilon_r$	As/(Vm)
Relative Dielectric Permittivity	ε_r	1
Electrical Free Space Permittivity	ε_0	As/(Vm)
Magnetic Permeability	$\mu = \mu_0\mu_r$	Vs/(Am)
Relative Magnetic Permeability	μ_r	1
Permeability of Free Space	μ_0	Vs/(Am)
Electrical Conductivity	σ	S/m = $(\Omega \cdot m)^{-1}$
Electrical Resistivity	ρ	$\Omega \cdot m$
Angular Frequency	ω	s^{-1}
Frequency	f	Hz
Time	t	s
Wavenumber	k	m^{-1}

2.1.1 Electrical Conductivity

The conductivity of different materials is controlled by the mechanisms of charge exchange Telford et al. (1990). The following aspects contribute to the total conductivity.

- Electronic conduction: The free electrons transport the charges in materials (e.g., metal), and the current flow is established. For material like common rocks, this mechanism can be neglected due to the sparse free electrons.

- Dielectric conductivity: This mechanism contributes to the total conductivity only when the electric field with a large frequency. For the EM measurements carried out by using a horizontal electric dipole (HED) in this thesis, the effect of this mechanism can be neglected (Haroon, 2012; Janser, 2017).

- Interface conductivity: At the interface of rock and surrounding pore fluid, an electrical double layer can be formed. This mechanism could be dominating for clay materials.

- Electrolytic conductivity: Caused by the ions as charge carriers in the pore fluid. For a clay-free medium, the empirical formula named Archie law (Archie, 1942) provides the descriptions for the electrolytic conduction.

2.2 Quasi static maxwell's equations

The Maxwell equations describing the electromagnetic fields are the basic principal of electromagnetic induction.

$$\nabla \cdot \mathbf{D} = \varrho \tag{2.1}$$

$$\nabla \cdot \mathbf{B} = 0 \tag{2.2}$$

$$\nabla \times \mathbf{E} = -\frac{\partial \mathbf{B}}{\partial t} \tag{2.3}$$

$$\nabla \times \mathbf{H} = \frac{\partial \mathbf{D}}{\partial t} + \mathbf{j} \tag{2.4}$$

The basic quantities and units are summarised in table 1, while these quantities have the following relationship.

$$\mathbf{j} = \sigma \mathbf{E} \tag{2.5}$$

$$\mathbf{D} = \varepsilon \mathbf{E} \tag{2.6}$$

$$\mathbf{B} = \mu \mathbf{H} \tag{2.7}$$

For an isotropic conductor, the relationship between the total electric current density $\mathbf{j}$ and the electrical conductivity σ is described by Ohms law (equation (2.5)).

For the cases of EM measurements, the relative permeability μ_r and permittivity ε_r are commonly considered as scalar, therefore $\mu = \mu_0$ and $\varepsilon = \varepsilon_0 = 4\pi \times 10^{-7} Vs/Am$. Use $\mathbf{F}$ to denote $\mathbf{E}$ and $\mathbf{H}$. Based on the vector identity $\nabla \times (\nabla \times \mathbf{F}) = \nabla(\nabla \cdot \mathbf{F}) - \nabla^2 \mathbf{F}$, one can deduce $\nabla \times (\nabla \times \mathbf{F}) = -\nabla^2 \mathbf{F}$. Therefore, the Telegrapher's equations can be deviated from the equations (2.5), (2.7) and (2.6) (Ward and Hohmann, 1988).

$$\nabla^2 \mathbf{F} = \mu_0 \sigma \frac{\partial \mathbf{F}}{\partial t} + \mu_0 \epsilon \frac{\partial^2 \mathbf{F}}{\partial t^2} \tag{2.8}$$

By applying the Fourier transformation, equation (2.8) is rewritten as Helmholtz equation for frequency domain.

$$\nabla^2 \mathbf{F} = i\omega\mu_0\sigma\mathbf{F} - \mu_0\epsilon\omega^2\mathbf{F} \tag{2.9}$$

where the time derivative in equation (2.8) is described as $\partial\mathbf{F}/\partial t = i\omega\mathbf{F}$.

Quasi static approximation

For the common earth material resistivity and operating frequencies of the typical geophysical induction methods, the displacement currents are insignificant compared to the conduction currents $\omega\varepsilon \ll \sigma$. Thus, the second terms in right side of equation 2.8 and 2.9 are neglected. The resulted equations are referred to as the diffusion equation (in time- and frequency-domain).

$$\nabla^2 \mathbf{F} = \mu_0\sigma\frac{\partial\mathbf{F}}{\partial t} \tag{2.10}$$

$$\nabla^2 \mathbf{F} = i\omega\mu_0\sigma\mathbf{F} \tag{2.11}$$

2.3 Skin depth and diffusion depth

The first solution describes the propagation of monochromatic waves. The downward decaying solution are preseted as

$$\mathbf{F}(z,t) = \mathbf{F}_0^+ e^{i(\omega t - kz)} \tag{2.12}$$

where z denotes the depth, $k = \sqrt{-i\omega\mu\sigma}$. the field amplitude decays exponentially with the increasing of depth. The skin depth indicates the depth where the field amplitude decreased by a factor of $1/e$

$$\delta_{FD} = \sqrt{\frac{2}{\omega\mu\sigma}}. \tag{2.13}$$

The term is routinely used as an estimation for the depth of investigation (DOI) for an operated frequency in the frequency-domain EM measurement. The other type of solutions describes transient waves.

$$\mathbf{F}(z,t) = \mathbf{F}_0^+ \sqrt{\frac{\sigma\mu z^2}{4\pi t^3}} e^{-\frac{\sigma\mu z^2}{4t}}. \tag{2.14}$$

Its solution can be written as, where δ_{TD} is known as diffusion depth (Ward and Hohmann, 1988).

$$\delta_{TD} = \sqrt{\frac{2t}{\mu\sigma}}. \tag{2.15}$$

2.4 Brief introduction of DESMEX project

Electromagnetic methods are the important approaches for mineral exploration because of the usually low electrical resistivity of mineral resources. In the practice of mineral exploration, detecting deeply, widely and accurately is always appreciated. The BMBF funded DESMEX (Deep Electromagnetic Sounding for Mineral Exploration) project is aiming at develop the semi-airborne EM method which combines a large penetration depth with a fast and dense area coverage (Smirnova et al., 2019; Mörbe, 2019). Figure 2.1 shows the measurement concept. The semi-airborne method employs a ground-based

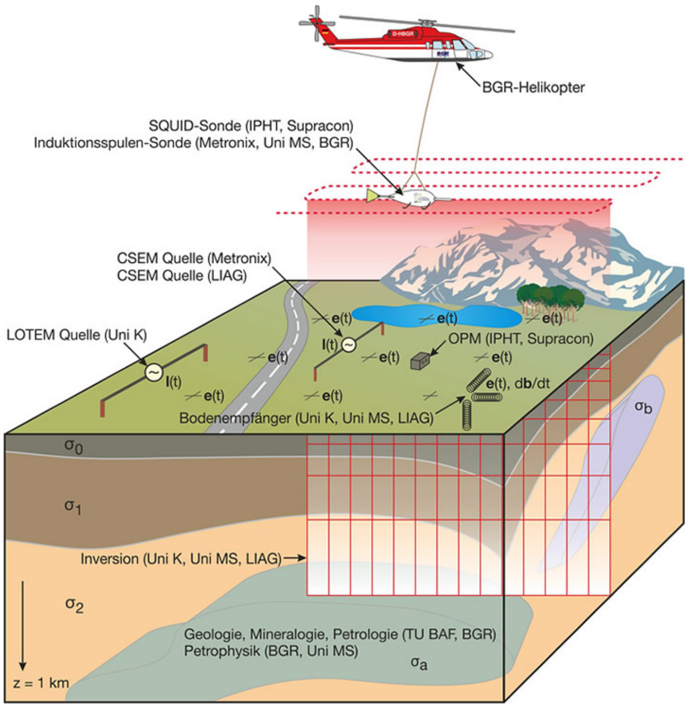

Figure 2.1: Schematic overview of the exploration concept in DESMEX project. Both the ground based measurement (E.g. LOTEM and CSEM) and the semi-airborne receiver systems are included.

transmitter (Tx) and airborne receivers (Rx). In order to obtain the complementary information of the subsurface and reach a considerable penetration depth, ground-based electric field receivers are also deployed. Aiming at validating the novel semi-airborne method, various geological and geophysical studies were carried out (e.g., Rochlitz et al., 2018, 2019; Steuer et al., 2015). Among these applied EM methods, the long offset transient electromagnetic measurements (LOTEM) are supposed to provide validation to the semi-airborne method, with a focus towards deep structures, and deliver a 2D subsurface model Mörbe (2019). As introduced earlier, the focus of this thesis is semi-airborne and LOTEM measurement. The observed data of semi-airborne and LOTEM in the frame of DESMEX are planed to be inverted jointly, and a final superior resistivity model results form joint inversion are expected. Due to the high resolution for the shallow structures, the field data of the HEM survey (Steuer et al., 2015) are also considered in the 1D modeling and inversions. In the following sections, the measuring configurations and details characteristics are concisely introduced for each EM surveys, respectively.

2.5 Long offset transient electromagnetic method

LOTEM is an active electromagnetic method used for the exploration of the subsurface resistivity distribution in great depths. In a LOTEM survey, an alternating current is transmitted by using a grounded dipole. The generated electromagnetic field diffuse in the earth based on the principle of electromagnetic induction. In distances of typically 1-10 km, the earth responses are measured (Mörbe, 2019). For ensuring the generated electromagnetic fields have enough energy, the source moment could be enlarged by increasing the transmitter length and the current. However, the transmitter length is commonly limited by topography, accessibility, as well as the required time and efforts for installation. The current in the grounded wire is restricted by the resistance of electrodes and cables. Regarding the measuring side, the non-polarising CuCu/SO and AgAg/Cl electrodes were employed as the receivers (Rx) to record the electric field components (Mörbe, 2019). The time derivatives of the magnetic fields were measured by large loops or coils. According to the predicted target depth, the transmitter-receiver separation (offset) is designed. Characteristically, the exploration depth should be less than or equal to the utilized offsets (Haroon, 2012). Because of the large source moment and reliable data quality, the method is typically employed to detect the deep structures down to several kilometers (Haroon et al., 2015). The transmitter and the receivers are commonly deployed following two typical configurations, inline and broadside. For an inline configuration, the receivers are positioned in the extended line of the transmitter dipole. The receivers are located in the perpendicular bisector of the transmitter dipole in a broadside configuration. Figure 2.2a sketches the typical LOTEM broadside configuration. After the transmitter and the receivers are properly deployed, the grounded transmitter sends out a rectangular shaped signal as the source. The commonly used rectangular signals are classified as 50 % or 100% duty cycle. Figure 2.2b shows the example of the transmitted 50 % duty cycle wave function, and the corresponding received electric field. In order to suppress the random noise, the measurements are performed repeatedly for a period. Mörbe (2019) fully details the following data processing steps. The processed LOTEM data can be used in the inversions for deducing the subsurface resistivity distributions, together with data standard deviations or error estimations evaluated in the processing.

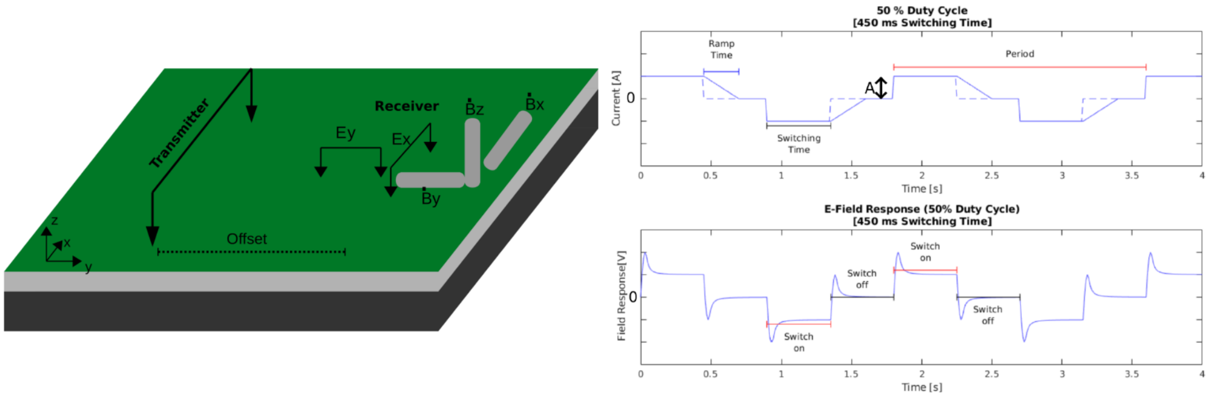

Figure 2.2: Left column: Schematic of a typical LOTEM broadside configuration (after Strack, 1992; Mörbe, 2019); Right column: example for the 50% duty cycle for a switching time of 450 ms (Mörbe, 2019). The upper raw displays the transmitter wave function, and the bottom raw displays the example of received electric field. For a 50% duty cycle, either the switch on and switch off response could be selected theoretically.

Specifically, the data acquired in a typical LOTEM survey are transferred into frequency-domain and evaluated both in frequency- and time-domain (Mörbe, 2019). Such an approach is similar to the widely known CSEM techniques in frequency-domain (Ziolkowski and Slob, 2019). Mörbe (2019) compared the resolution capabilities among the switch on and off transients as well as the transformed LOTEM data in frequency-domain. Kaufman and Keller (1983)and Strack (1992) present the overviews, detailed theory, and practical applications for the LOTEM method, while Ziolkowski and Slob (2019) provides the overview and introductions over CSEM applications.

2.6 Semi-airborne electromagnetic method

Same as LOTEM, semi-airborne is also an active electromagnetic method. In the typical semi-airborne systems, the transmitter is deployed on the earth's surface with the receivers installed on an aircraft. Therefore, in practice, the semi-airborne system combines the advantages of ground-based and airborne techniques. Compared to the measuring system utilized land land-based observing stations like LOTEM, the receivers installed on the aircraft makes the quick covering of a large survey area feasible Seigel (1971). With the need for the large-scaled 3D EM measurements in the further, this character is absolutely a significant virtue. Compared to the common airborne electromagnetic (AEM) systems that have hundreds of meters depth of investigation (DOI), semi-airborne systems have the potentials to achieve the DOI of several kilometers because of the employed ground-based transmitters. Contributed by the large transmitter-receiver separation and possible high-moment source, the DOI of the measurement is effectively extended.

The known earliest semi-airborne development is the TURAIR system proposed by Seigel (1971) in the 1970s. Afterward, several different semi-airborne systems were developed in the following decades. For instance, the FLAIRTEM system introduced by Elliott (1996) and the GREATEM system presented by Mogi et al. (1998, 2009). Smith et al. (2001) compared the performance of some particular airborne, semi-airborne (FLAIRTEM), and the ground-based measurements. They suggested that a semi-airborne survey can be considered as an attractive alternative to ground surveys in situations in which it is difficult to gain access to the ground to acquire data but still possible to deploy transmitters (Smirnova et al., 2019).

As mentioned earlier, the specific semi-airborne system discussed in this thesis is developed in the framework of DESMEX project (Smirnova et al., 2019). The sketch of this system is presented in Figure 2.1. The new semi-airborne performs in frequency-domain. A grounded horizontal electric dipole (HED) with two kilometers length and a current strength of approximately 20 A is employed as the transmitters. the source is operated in the field by the University of Cologne (IGM) or the Leibniz Institute for Applied Geophysics (LIAG) (Smirnova et al., 2019; Mörbe, 2019). The transmitters from the University of Cologne also employed in the LOTEM measurements. The receiving systems are designed by teams from the University of Münster (WWU), the German Federal Institute of Geosciences and Natural Resources (BGR), and Metronix GmbH (Smirnova et al., 2019). Additionally, Schiffler et al. (2017) presented a superconducting quantum interference device magnetometer that measures the three components of the magnetic field. Regarding the measuring, the source signal at one fundamental frequency producing multiple harmonics in the wide frequency range is generated. At these coherent frequencies, the frequency-domain transfer functions (TFs) between the source current and magnetic field components are estimated (Smirnova et al., 2019). More descriptions of technical detailed of this system, as well as the corresponding data processing approaches, are presented by Smirnova et al. (2019).

However, while the semi-airborne system combines part of the virtues of both AEM and land-based CSEM, it also gives up some advantages owned by the other two EM methods. Because the airborne receivers are moving during the measurement, the stacking time for each observed station is not as adequate as that of land-based receiver stations. Compared to, for example, LOTEM, the less data sampling inevitably lead to the reduced data quality of semi-airborne. Reduced data quality limits the largest assailable offsets, and further resulted in the smaller DOI than LOTEM. On the other hand, the particular semi-airborne system considered in this thesis also shows some disadvantaged compared to the typical airborne EM (e.g., HEM). The utilized large dipole moment can extend the DOI of the measurement effectively, but also generates a strong primary field, which dominates the observed responses in the short offsets. That is the reason for acquiring repeated datasets for different source locations over the same flight area, which is aiming at filling in the gaps in data coverage over the source positions (Smirnova et al., 2019). Moreover, the employed large offsets lead to a big footprint, indicating that the measured data is easier affected by the 2D or 3D effects. Different from the typical airborne EM with a small footprint, the 1D inversions of these semi-airborne data may encounter some problems when subsurface structures are complex in the measuring area.

In general, even though the newly developed semi-airborne system in DESMEX may have some weak points, it provides the opportunities to realize the large scale 3D measurements conveniently and quickly even when the terrain is rough. The cooperation or joint inversion between data of semi-airborne and the other EM methods could provide not only superior results but also the potential for the more flexible and adaptable measuring systems (discussed in the later chapter).

2.7 HED solutions for the 1D layered full-space model

Because both the semi-airborne and LOTEM measurements employs horizontal electric dipole as the source, the HEM solutions for the 1D layered model is important. The subsequent brief description of basic theory for HED solutions follows the early work of Weidelt (1986), Kaufman and Keller (1983), Ward and Hohmann (1988) and partly the thesis of Janser (2017) and Haroon (2012).

In source-free regions, both the considered electric and magnetic fields are divergence-free . A divergence-free vector field can be divided into a toroidal and a poloidal part:

$$\mathbf{v} = \underbrace{\nabla \times (\psi_T)\mathbf{e}_z}_{\text{toroidal}} + \underbrace{\nabla \times \nabla \times (\psi_P \mathbf{e}_z)}_{\text{poloidal}}, \tag{2.16}$$

$\mathbf{e}_z$ is an unit vector in vertical direction, and ψ_T and ψ_P are the scalar potentials. Therefore, the electric and magnetic fields could be written as

$$\mathbf{E} \quad = \mathbf{E}_E + \mathbf{E}_M \quad = -\nabla \times (\dot{\varphi}_E \mathbf{e}_z) + \frac{1}{\sigma} \nabla \times \nabla \times (\sigma \varphi_M \mathbf{e}_z) \tag{2.17}$$

$$\mathbf{H} \quad = \mathbf{H}_E + \mathbf{H}_M \quad = \frac{1}{\mu} \nabla \times \nabla \times (\varphi_E \mathbf{e}_z) + \nabla \times (\sigma \varphi_M \mathbf{e}_z). \tag{2.18}$$

The potential φ_T is routinely referred to as TE-mode, which generate no vertical electric field ($E_z = 0$). Similarly, the potential φ_M is TM-mode, which generate no vertical magnetic field ($B_z = 0$). In another word, the TM current is not entirely vertical whereas a vertical current is TM mode. Vice versa, horizontal currents are not entirely TE mode, but TE mode has only horizontal currents. Both these two modes are included by EM fields generated by the HED source. The vertical current flow established by galvanically coupled sources is classified as TM-mode. On the other hand, the HED has a horizontal current systems, which is inductively coupled to the earth and indicates a TE-mode. The the two scalar potentials φ_E and φ_M are the solutions of the following partial differential equations (PDE) (Weidelt, 1986),

$$\nabla^2 \varphi_E = \mu_0 \sigma \dot{\varphi}_E \tag{2.19}$$

$$\nabla(\frac{1}{\sigma} \nabla(\sigma \varphi_M)) = \mu_0 \sigma \dot{\varphi}_M \tag{2.20}$$

Weidelt (1986) applied the partial wave synthesis to solve these in-homogeneous PDEs. By using the inverse Fourier transform, the temporal and horizontal spatial dependencies are transformed to dependencies of frequency ω and horizontal wave number κ, called partial waves (Janser, 2017), which is written as

$$\varphi_{E,M}(\mathbf{r}, t) = \frac{1}{(2\pi)^3} \iiint_{-\infty}^{+\infty} f_{E,M}(z, \kappa, \omega) e^{i(\kappa \cdot \mathbf{r} + \omega t)} d^2 \kappa d\omega, \tag{2.21}$$

where $\kappa = k_x \mathbf{e}_x + k_y \mathbf{e}_y$. The PDEs can be further simplify to the ordinary differential equations (ODE) (Weidelt, 1986):

$$\frac{\partial^2}{\partial z^2} f_{E,M}(z) = \alpha_n^2(z) f_{E,M}(z) \tag{2.22}$$

with $\alpha_n(z) = (\kappa)^2 + i\omega\mu_n\sigma_n$. Here, n is the index for the model layers $n = 1, \cdots, N$. The layer interface lies at $z = h_1 = 0, h_2, \cdots, h_N$, while the z for nth layer should satisfy

$h_n < z < h_{n+1}$. The solution for the equation (2.22) is,

$$f_{E,M}^n = A_n^+ e^{-\alpha_n(z-h_n)} + A_n^- e^{+\alpha_n(z-h_n)} \qquad \text{valid for} \quad h_n < z < h_{n+1}. \tag{2.23}$$

The wave propagation in +z-direction is described by $e^{+\alpha_n(z-h_n)}$ and in -z-direction by $e^{-\alpha_n(z-h_n)}$. Where A is the reciprocal modified impedance, it is defined for TE mode as A_{TE} and TM mode for A_{TM},

$$A_n^{TE} = -\frac{\partial_z f_E(z)}{f_E(z)}. \tag{2.24}$$

$$A_n^{TM} = -\frac{\partial_z f_M(z)}{f_M(z)}. \tag{2.25}$$

With continuity conditions at the boundaries, the recursive equations of every layer from the bottom to the top are expressed as (Haroon, 2012)

$$A_n^{TE} = \alpha_n \frac{A_{n+1}^{TE} + \alpha_n tanh(\alpha_n d_n)}{\alpha_n + A_{n+1}^{TE} tanh(\alpha_n d_n)} \tag{2.26}$$

$$A_n^{TM} = \alpha_n \frac{A_{n+1}^{TM} + \alpha_n \beta_n tanh(\alpha_n d_n)}{\alpha_n \beta_n + A_{n+1}^{TM} tanh(\alpha_n d_n)} \tag{2.27}$$

where $\beta_n = \sigma_{n+1}/\sigma_n$, $n = N-1, \ldots, 1$. The thickness of each layer is denoted by $d_n = h_{n+1} - h_n$. The initial condition for the recursive calculating is $A_N^{TM} = A_N^{TE} = \alpha_N$. By including the source term, the particular solution for the source layer are presented as following for TE mode.

$$\tilde{\varphi}_E(r,z,\omega) = \frac{\mu_0 \tilde{d}(\omega)}{4\pi} \left[\frac{r}{R+|z|} - \int_0^\infty \frac{A_1^{TE}(\kappa,\omega) - \kappa}{A_1^{TE}(\kappa,\omega) + \kappa} e^{\kappa z} \frac{1}{\kappa} J_1(\kappa r) d\kappa \right] \sin\varphi, \tag{2.28}$$

where r denotes the horizontal radius, and and z denotes the vertical height of the receiver position in cylindrical coordinates, $R^2 = r^2 + z^2$. J_1 indicates the Bessel functions.The dipole moment is denoted by $\tilde{d}(\omega)$. Note that, for semi-airborne, the observed quantity is the magnetic field measured within the air-halfspace, where $\sigma = 0$ and $\psi_M = 0$. For TM mode, the solution can be described by the following equation.

$$\tilde{\varphi}_M(r,z,\omega) = \frac{-\tilde{d}(\omega)}{2\pi\sigma_1} \int_0^\infty A_1^{TM}(\kappa,\omega) e^{\kappa z} \frac{1}{\kappa} J_1(\kappa r) \cos\varphi d\kappa, \tag{2.29}$$

The detail derivations can be found in Weidelt (1986), Haroon (2012) and Janser (2017).

2.8 Helicopter electromagnetic method

The helicopter-borne electromagnetic (HEM) system discussed in this thesis is developed by the German Federal Institute of Geosciences and Natural Resources (BGR) (Siemon et al., 2009; Siemon, 2012; Steuer et al., 2009). Figure 2.3 depicts the designs of this system. In order to provide the related background information, the description of HEM presented by Siemon et al. (2009) and Siemon (2012) are concisely summarized in this section.

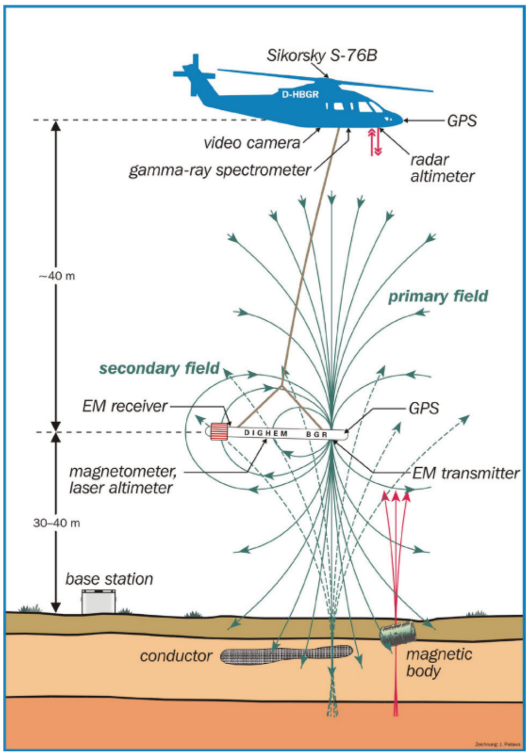

Figure 2.3: BGR's helicopter geophysical system (Siemon et al., 2009)

The airborne electromagnetic (AEM) systems operate in both time- and frequency-domain. Generally, the time-domain AEM systems have a greater DOI than the frequency-domain systems (e.g., Steuer et al., 2009). Contrarily, the frequency-domain system is very suitable for high-resolution near-surface surveys if a helicopter serves as the platform (Siemon, 2012). The HEM systems are employed for numerous applications, such as geologic mapping, mineral prospecting, groundwater exploration, sea-ice thickness measurements, environmental and geotechnical surveys. The BGR frequency-domain HEM systems acquire accurate data in high frequencies and focus on the detection of near-surface information particularly. It utilizes four to six small transmitters and receiver coils having a diameter of about half a meter. The system altitude is around 30 to 40 m above the ground normally (Steuer et al., 2009). The transmitter coil generates the primary magnetic field at a suite of discrete frequencies. The induced eddy currents generate a secondary magnetic field depending on the resistivity distribution. The receiver coils record the secondary magnetic field. The observed responses are related to the expected primary magnetic field. Because the secondary field is much weaker than the primary field, the primary field is bucked out. The resulted relative secondary field is measured in parts per million (ppm) (Siemon et al., 2009). Known from Siemon (2012) and Steuer et al. (2015), the recorded HEM data are at last presented as the in-phase and quadrature components. More technical details about HEM, derivations of basic formulas, as well as abundant application examples are presented by Siemon et al. (2009) and Siemon (2012).

2.9 EM Surveys in eastern Thuringia, Germany

In the framework of DESMEX, various pre-investigations were carried out in the measuring area before the main experiment of the semi-airborne experiment, including the in-Loop transient electromagnetic (TEM) measurements (Ossen, 2017) and radio magnetotelluric measurements (Hauser et al., 2016). The HEM measurements conducted by BGR is also one pre-investigation aiming at finding the suitable areas for the main experiment Steuer et al. (2015); Mörbe (2019). HEM system detected the shallow substructures down to approximately 150 m by using frequencies between 387 Hz and 133 kHz. As mentioned, the HEM survey has a small footprint and the 1D inversions are feasible for the application. According to Steuer et al. (2015), the HEM flight line 17 matches the LOTEM profile (in Figure 2.4b). The and record and results are detailed presented in Steuer et al. (2015). In this thesis, the HEM data in flight line 17 are considered in the 1D inversions, and the 1D modeling studies are performed for the HEM measurement.

The LOTEM survey was conducted in the Thuringian Slate Mountains, Germany, during summer 2016 and 2017 Mörbe (2019), as the important supplementary and validation for the semi-airborne experiment. The LOTEM profile is presented in Figure 2.4b. In LOTEM measurement, six transmitters were employed. Because the targets of this LOTEM measurement are conductors, broadside configuration is utilized. Even though the source signal transmitted by HED dipole includes both tangential electric (TE) and tangential magnetic (TM), the dominating TE Mode in a broadside configuration decides the sensitivity for resistors is relatively low. The transmitter length was around 1 km, and the current strength ranged from 8 to 22 A. Offsets ranged between 300 m and 4921 m, and a total of 170 Ex-field datasets were measured. Vertical magnetic field induction coil

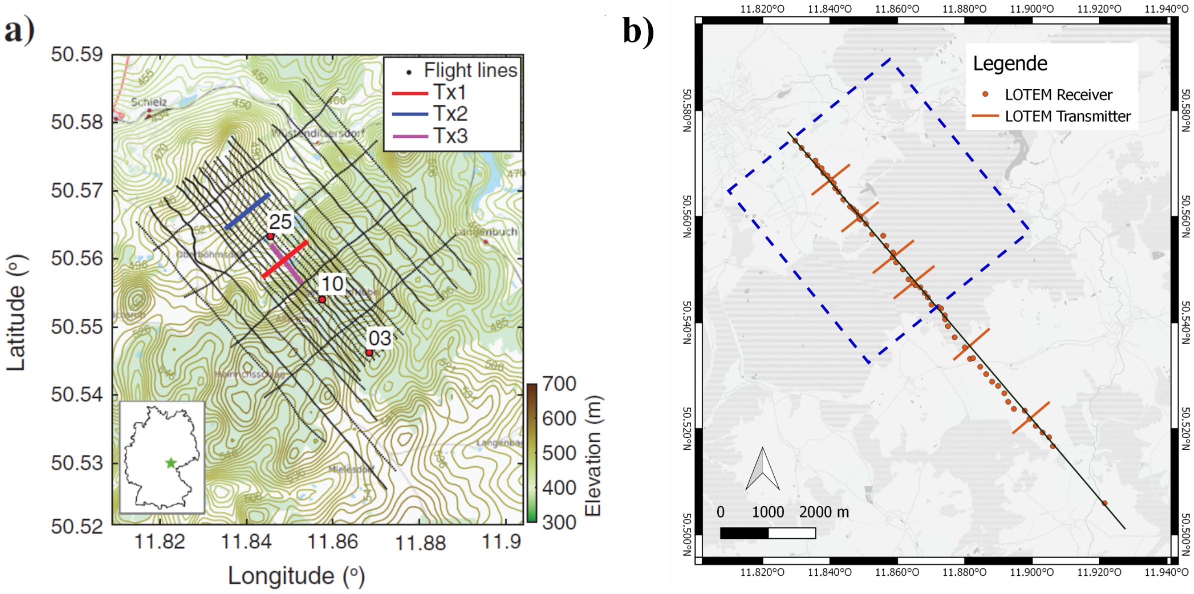

Figure 2.4: Location of the (a) semi-airborne (Smirnova et al., 2019) and (b) LOTEM (Mörbe, 2019) measuring configurations near Schleiz (in eastern Thuringia), Germany in 2016. Part of the LOTEM stations are deployed in 2017 (Mörbe, 2019). In (a), the black dots indicate the flight-lines and the colored lines mark the positions of the transmitters. In (b), red dots and solid lines indicate positions of receivers and transmitters, respectively. The region circled by blue dashes is the semi-airborne measuring area.

data was obtained roughly every 300 m along with the profile. However, due to the time costly set-up, induction coil measurements were skipped in 2017 (Mörbe, 2019). Because of the sparse measuring points, the time-domain magnetic fields from LOTEM measurements are unfortunately not considered in this thesis. For the time-domain transient, the time range is between 2×10^{-5} to 1s. The frequency-domain LOTEM corresponds to 0.25 Hz up to 25 kHz. Due to the short ramp length (around 120 s) of the step off-ramp function, the step on signal is distorted strongly, and the step off transient was recalculated to a switch on response. The recorded voltages are normalized to the transmitter current and the receiver length (Mörbe, 2019). Namely, the LOTEM data considered in this thesis are particularly the step-on horizontal electric fields which are normalized by source current. All the particulars referring to the field set-up of LOTEM and the consequent data processing are provided in Mörbe (2019).

The flight lines of semi-airborne measurements conducted in eastern Thuringia (2016) are provided in Figure 2.4a. Three different transmitters are employed. The two transmitters perpendicular to the LOTEM profile were also employed in LOTEM measurements. Therefore, the transmitter system used in semi-airborne measurement is the same as that of LOTEM. Introduced by Smirnova et al. (2019), the overall covered area of semi-airborne measurement was 7×5km. The flight lines were unevenly spaced. They are densely arranged as 100 m spacing in the vicinity of the transmitter and 300m aside. Usually, the bird altitude is between 40 and 90 m above the topography, and the receiver is moving at a speed of 120 km/h. Time series are separated into 5 s time windows, overlapping by 2.5 s to obtain the data at a certain location. Considering the flight speed, it corresponds to a ground measurement every 150 m or overlapped over 75 m (Smirnova et al., 2019). According to Smirnova et al. (2019), the transfer functions $\mathbf{T}$ are estimated between $\mathbf{B}$ and $\mathbf{I}$ in frequency domain: $\mathbf{B}(f) = \mathbf{T}(f)\mathbf{I}$, where f denotes the frequencies and $\mathbf{T}$ denotes the magnetic field transfer function. Because all the discussed semi-airborne field data in this thesis refer to the transfer function of vertical magnetic fields, Bz is also used to denote the transfer functions in the following text to highlight the essence of the semi-airborne data. The region highlighted by blue dashes in Figure 2.4b is the semi-airborne measurement area in 2016. As can be seen, it overlaps with the LOTEM profile partly. Therefore, the joint inversion presented in this thesis focuses on the overlapping profiles (for semi-airborne, flight line L16).

2.10 Summary and comparison of LOTEM, semi-airborne EM and HEM

This chapter provides the basic theory and background information for this thesis. The general concepts of electromagnetic measurements are introduced briefly. Based on the various EM surveys carried out in the frame of the DESMEX project, this thesis focuses on the joint inversion of the data acquired from HEM, semi-airborne, and LOTEM measurements. Thus the measuring configuration and characteristics, as well as some fundamental formulas, are concisely presented. Important particular details of the EM surveys conducted in eastern Thuringia are provided. For a convenient comparison, Table 2 lists the key information for the considered three EM methods. What has to be specially noted is,

Table 2: Comparison for measuring system of HEM, LOTEM, and semi-airborne.

Method	HEM	LOTEM	semi-airborne
Domain	Frequency	Time	Frequency
Component	In-phase + Quadrature	Ex (Step-on)	Re(Bz)&Im(Bz)
Tx position	Air	Land	Land
Rx position	Air	Land	Air
Tx-Rx separation	$\approx$ 7m	500 to 4000m	500 to 2000m
Freq./time range	0.4 to 200kHz	0.0001 to 1s	10 to 2000Hz

the listed frequency or time range for each method are not the particular values for the

Thuringia survey, but general considerations utilized in this thesis. The frequency range of HEM is the combination of the values provided in Steuer et al. (2015), Steuer et al. (2009) and Siemon (2012). In the work of Steuer et al. (2015) and Steuer et al. (2009), the lowest frequency is around 380Hz. According to Steuer et al. (2009) and Siemon (2012), the largest frequency could reach around 200kHz. Regarding the LOTEM time range, 10^{-4}s is utilized as the earliest time point rather than the 2×10^{-5} s as Thuringia survey. The reason is that the earliest time points are dominated by the system responses (Mörbe, 2019). The semi-airborne data are recorded to around 10 kHz actually. But the data at frequencies larger than 2000 Hz are not considered in this thesis because the high-frequency signal strength is generally low and the transmitter-receiver separation is thus more limited than the low-frequency cases (Becken, personal communication, 2020). These configuration and survey parameters are utilized in the modeling studies in all the following chapters to keep them as close as possible to the field data studies.

3 Inversion theory

By using the forward solutions presented in the last chapter, the synthetic responses can be calculated for HEM, semi-airborne EM and LOTEM. The inversion process iteratively searches for a resistivity model that can interpret the measured EM data, i.e., the previously discussed synthetic response fits the measured data. In this chapter, the basic principles of the used inversion algorithms and techniques are briefly introduced. These basic inversion algorithms are used for both 1D and 2D inversions. Some specific tools for analyzing the model parameter resolution are currently done only using 1D Marquardt inversion (due to the comparably smaller model space). Further details of the inversion schemes utilized in this thesis can be found in various literature. The algorithms employed in the Electromagnetic Universal Inversion package (EMUPLUS) of University of Cologne are described in more detail by for example Scholl (2005) and Yogeshwar (2014). The inversion schemes of the 2D code MARE2DEM are presented in detail in by Key (2016). Additionally, the theory is introduced in Section 5.1 to discuss the major modifications undertaken in this thesis.

3.1 Inverse problem and the cost-function

Inverse theory addresses the reverse problem: starting with data and a general principle, theory, or quantitative model, it determines estimates of the model parameters Menke (2018). Data vector $\mathbf{d}$ of length N denotes the observed or synthetic data sampled at a suited of frequency or time points. In the specific case of this thesis, different components of one EM method could be sampled for the same frequency point. For example, real and imaginary parts of the vertical magnetic field acquired in semi-airborne EM. The data length can be regarded as twice the length of the frequency vector in this case. For joint inversion, the data vector contains data from all the considered EM methods. The model parameters vector $\mathbf{m}$ of length M is consist of the model parameters like resistivity for each layer or element. In 1D Marquardt inversion, the model parameters also include the layer thickness values. The forward operator $\mathbf{F}$ describes the relationship between the data vector $\mathbf{d}$ and model vector $\mathbf{m}$.

$$\mathbf{d} = \mathbf{F}(\mathbf{m}) \tag{3.1}$$

For semi-airborne, HEM and LOTEM, the forward operators $\mathbf{F}$ are all non-linear. Therefore it is not feasible to use the inverse of the forward operator $\mathbf{F}^{-1}$ to calculate a unique model parameter vector. The type of inversion problem is decided by the relationship between N and M in this case. If N > M, the problem is over-determined, and no unique solution exists. If N < M, the problem is under-determined and leads to infinite models, which can be the possible interpretations for the data. The number of electromagnetic data is usually larger than the model parameters, but they are not independent. The determinacy of inverse problems is not simply given by the number of data and model parameters, but by the amount of independent information. This case is considered to be mixed-determined. Some model parameters are well resolved while the others are ambiguously revealed. With the demand to stabilize the inversion and provide meaningful inversion results, prior information is introduced for constraining the problem. Various constraining strategies are utilized by different inversion schemes, but their main target is common: minimizing the data cost-function Φ_d.

$$\Phi_d = \left[\mathbf{W_d}\left(\mathbf{d} - \mathbf{F}(\mathbf{m})\right)\right]^T \left[\mathbf{W_d}\left(\mathbf{d} - \mathbf{F}(\mathbf{m})\right)\right] \tag{3.2}$$

where $\mathbf{W_d}$ denotes weighting matrix consist of reciprocal of error estimations of the data $\mathbf{W_d} = diag(\sigma_1^{-1} \cdots \sigma_N^{-1})$. The data error σ is estimated according to the specific data processing of each EM method (Mörbe, 2019; Smirnova et al., 2019). The whole term $\mathbf{W_d}(\mathbf{d} - \mathbf{F}(\mathbf{m}))$ denotes the residual vector. It is introduced in literature as the following form and usually used to evaluate the data fit at each sampled point (E.g. Gehrmann et al., 2016):

$$r_i = \frac{d_i - F_i(\mathbf{m})}{\sigma_i}; \quad i = 1 \cdots N \tag{3.3}$$

Residuals can be further calculated as the misfit evaluation for the whole dataset:

$$\chi = \sqrt{\frac{1}{N}\sum_{i=1}^{N}\left(\frac{d_i - F_i(\mathbf{m})}{\sigma_i}\right)^2} \tag{3.4}$$

If the error $\sigma_i = 0.01 d_i$ for all the considered data, the resulted value of equation 3.4 equals to Root Mean Square (RMS), which is another widely used evaluation of data misfit. In this thesis, χ is used as measure of the data fit because the error estimations are significantly divergent for different EM methods.

3.1.1 Jacobian matrix

One approach to resolve the non-linear inversion problem is approximating it as linear by calculating its first-order Taylor expansion for small model perturbations Δm around a given model $\mathbf{m}_k$. The higher-order terms in Taylor's expansion are neglected.

$$\mathbf{F}(\mathbf{m}) = \mathbf{F}(\mathbf{m_k}) + \mathbf{J_k}(\mathbf{m} - \mathbf{m_k}) \tag{3.5}$$

where $\mathbf{J_k}$ denotes the derivative of the forward operator with respect to the model parameters.

$$J_{k,ij} = \frac{\partial F_i(\mathbf{m})}{\partial m_j}|_{\mathbf{m}=\mathbf{m_k}} \quad i = 1 \cdots N, \quad j = 1 \cdots M \tag{3.6}$$

This $N \times M$ matrix is usually named as the Jacobian or sensitivity matrix. The absolute value of its entry $|J_{ij}|$ reflects if the data d_i is sensitive to the perturbation of parameter m_j. If the absolute value is small or even close to zero, the variation of model parameter m_j affects the data d_i weakly. In contrast, the model parameter m_j, and the data d_i are connected by the forward operator F strongly. Because the Jacobian matrix is considered as a measure of resolution, it can be further derived to other more intuitive terms, which evaluates the resolution of model parameters in an inversion.

Since the Jacobian matrix is an essential part of the inversion, many efforts are made to improve the calculation method of the Jacobian matrix, especially for 2D and 3D problem (E.g. Farquharson and Oldenburg, 1996; McGillivray et al., 1994). The unknowns in 1D problems are much lesser than those in 2D and 3D problems so that the calculation of the Jacobian matrix is easier. EMUPLUS uses the perturbation approach. One model parameter is perturbed with small variation (e.g., 5% of the value), the responses of the perturbed model are calculated consequently, and the part of entries of the Jacobian matrix corresponding to the perturbed parameter are calculated according to equation 3.6. Therefore a number of M forward calculations are required. The other approach is analytically differentiating the Hankel transform expressions for electromagnetic fields with respect to the conductivity of each layer (Key, 2009). But all the two previous methods are not efficient enough to generate the Jacobian matrix for 2D or 3D problems. In MARE2DEM(Key, 2016), the adjoint reciprocity formula proposed by McGillivray et al. (1994) is utilized. Compared to the direct sensitivity calculations, this approach can significantly reduce the computation time and then accelerate the 2D or 3D inversions. The detail derivation is provided by McGillivray et al. (1994), and some modeling examples are presented by Farquharson and Oldenburg (1996). In this thesis, EMUPLUS is used for all the 1D inversion tasks and MARE2DEM for the 2D inversions. Therefore all the Jacobian matrices for 1D problems are generated by the perturbation approach while the 2D Jacobian matrices are calculated by the adjoint reciprocity formula.

If the joint inversion is applied to data of several different EM methods, all the data are supposed to be interpreted by one set of model parameters. In these procedures, the essential step is the combination of the Jacobian matrix corresponds to different EM methods. The basic forms for cost-function and Jacobian matrix of joint inversion are kept the same as stated in equation 3.2 and 3.6, but their contents are extended (Sudha et al., 2014):

$$\mathbf{d}_{joint} = \begin{pmatrix} \mathbf{d}_{Method1} \\ \mathbf{d}_{Method2} \\ \mathbf{d}_{Method3} \end{pmatrix}; \quad \mathbf{F}_{joint}(\mathbf{m}) = \begin{pmatrix} \mathbf{F}_{Method1}(\mathbf{m}) \\ \mathbf{F}_{Method2}(\mathbf{m}) \\ \mathbf{F}_{Method3}(\mathbf{m}) \end{pmatrix};$$
$$\mathbf{J}_{joint} = \begin{pmatrix} \mathbf{J}_{Method1} \\ \mathbf{J}_{Method2} \\ \mathbf{J}_{Method3} \end{pmatrix} \tag{3.7}$$

Because the date errors are important in the misfit evaluation, the weighting matrix containing data errors $\mathbf{W_d}$ is usually taken into account practically (E.g. Sudha et al., 2014; Key, 2016). From the perspective of joint inversion, the weighting matrix $\mathbf{W_m}$ designed based on the characteristics of different EM methods or model parameters can also be applied. Thus final Jacobian matrix used for subsequent model updating is presented as follows (Sudha et al., 2014).

$$\mathbf{J_w} = \mathbf{W_d J W_m} \tag{3.8}$$

Where the weighting matrix W_m is optional.

3.1.2 Data and model parameter transformation

As stated earlier, the non-linear EM problems are approximately linearised. To increase the linearity of the problem, the data and the model parameters are transformed. The model parameters are transformed logarithmically to $log_{10}(\mathbf{m})$ in both EMUPLUS and MARE2DEM (Haroon, 2016; Key, 2016). Since the data may have a problem of sign-reversals, they could be transformed using the area sine hyperbolic (arsinh) transform, in order to force the dependency to be closer to linearScholl and Edwards (2007). Following Scholl and Edwards (2007) and Haroon (2016), the arsinh-transform on the data vectors and the Jacobian matrix entry are defined as following, respectively.

$$\hat{F}_i(\mathbf{m}) = arsinh(F_i(\mathbf{m})/s) = ln(F_i(\mathbf{m})/s + \sqrt{(F_i(\mathbf{m})/s)^2 + 1}) \tag{3.9}$$

$$\hat{J}_{ij} = \frac{m_j}{\sqrt{F_i^2(\mathbf{m}) + s^2}} \frac{\partial F_i(\mathbf{m})}{\partial m_j} \tag{3.10}$$

The scaling parameter s is set to 1% of the maximal absolute value among a certain data set. Several extreme small values usually occur when a sign-reversal happens. Without a proper transformation, these extreme values will lead to a suite of ill entries in Jacobian matrix and at last result in the non-convergence of the inversion. The scalar 1 in equation 3.9 could buffer the extreme values and lead to a smoother dataset. The sum $F_i^2(\mathbf{m}) + s^2$ in equation 3.10 also prevents the ill entries in transferred Jacobian matrix. The data could also be transformed using the logarithm transformation, thus the entries are (Key, 2016):

$$\hat{J}_{ij} = -\frac{ln10}{m_j} \frac{\partial F_i(\mathbf{m})}{\partial (1/m_j)} \tag{3.11}$$

EMUPLUS includes both log- and arsinh-transform for the data vectors. Specifically, the 1D inversion presented in this thesis uses an log-transform on the data vectors if there is no special notation. The 2D inversions use arsinh-transform for time-domain data vectors while the real and imaginary parts of semi-airborne magnetic field are kept linear in the 2D inversions.

3.1.3 Calibration factor

In the 1D inversions of EMUPLUS, a calibration factor (CF) can be chosen as a free parameter. The CF is treated as a scalar time-independent inversion parameter with which the calculated data is multiplied Hördt and Scholl (2004). Unsatisfactory data fits (E.g. Newman, 1989) were achieved when the calibration factor was fixed to 1 so that the data could not solely be interpreted by the model parameters. The calibration factor could also be used to partly compensate the topography effects (Cai et al., 2018). However, the model space is expanded essentially if CF is not 1. The predicted data is multiplied by a varying CF during the inversion iterations, meaning that a series of datasets around the true response curve could be used to fit the observed data after shifted by the CF. Therefore a lot more resistivity models could be the potential explanations for the observed data. This expansion of the model space will introduce many more uncertainties to the investigation of the joint inversion, which is based on resolution studies. In this thesis, the CF is always kept as 1.0 for all the inversions.

3.2 Marquardt inversion

The Marquardt-Levenberg method, proposed by Levenberg (1944) and Marquardt (1963), is also named as damped least squares inversion. It is relevant for many electromagnetic applications with sharp resistivity contrasts. During the processes of Marquardt inversion, both the resistivity and thickness of a distinct number of layers are inverted. Based on the unconstrained objective function in equation 3.2, an additional term including model update is added.

$$\Phi = [\mathbf{W_d}(\mathbf{d} - \mathbf{F}(\mathbf{m}))]^T [\mathbf{W_d}(\mathbf{d} - \mathbf{F}(\mathbf{m}))] + \beta^2 \Delta\mathbf{m}^T \Delta\mathbf{m} \tag{3.12}$$

Where β^2 is the Lagrange parameter trading off between the data misfit term and the model update term. The corresponding damped least square solution is

$$\Delta m = (\mathbf{J_w}^T \mathbf{J_w} + \beta^2)^{-1} \mathbf{J_w}^T \mathbf{W_d}(\mathbf{d} - \mathbf{F}(\mathbf{m})) \tag{3.13}$$

Marquardt inversion is suitable for depicting the resistivity contrasts, but its result depends on the starting model and can be trapped in a local minimum during the optimization process (Moghadas et al., 2015). Selecting a proper starting model according to the previously obtained Occam inversion is a widely used approach to overcome this drawback. Checking the Marquardt inversion results of a series of starting model designed systematically is also an alternative.

3.2.1 Singular value decomposition

The singular value decomposition (SVD) is relevant in deriving the inverse of the weighted Jacobian matrix J_w. It is also the basic theory of eigenparameter statistical analysis, which can be use to study the correlation of parameters (Edwards, 1997). The $N \times M$ Jacobian matrix can be split up as

$$\mathbf{J_w} = \mathbf{USV}^T \tag{3.14}$$

Where both the $N \times N$ matrix $\mathbf{U}$ and $M \times M$ matrix $\mathbf{V}$ are orthogonal. They have the property that (Edwards, 1997):

$$\mathbf{U^T U} = \mathbf{V^T V} = \mathbf{V V^T} = \mathbf{I} \tag{3.15}$$

Matrix U spans the data space and contains the N eigenvectors of $\mathbf{J_w J_w^T}$. Correspondingly, matrix $\mathbf{V}$ contains the N eigenvectors of $\mathbf{J_w^T J_w}$. $N \times M$ diagonal matrix S contains the singular values of $\mathbf{J_w}$ as $(\lambda_1, \lambda_2, \cdots, \lambda_N)$. The J_w in equation 3.13 is substituted by the decomposition in equation 3.14, then the damped least square solution are rewritten as

$$\Delta\mathbf{m} = \mathbf{V}\underbrace{(\mathbf{S}^2 + \beta^2\mathbf{I})^{-1}\mathbf{S}^T\mathbf{S}}_{\mathbf{T}}\mathbf{S}^{-1}\mathbf{U}^T\mathbf{W_d}(\mathbf{d} - \mathbf{F}(\mathbf{m})) \tag{3.16}$$

Where the diagonal matrix $\mathbf{T}$ includes the damping factor β

$$T_{ii} = \frac{S_{ii}^2}{S_{ii}^2 + \beta^2} = \frac{(S_{ii}/S_{11})^2}{(S_i i/S_{11})^2 + (\beta/S11)^2} = \frac{\lambda_i^2}{\lambda_i^2 + v^2} \tag{3.17}$$

Therefore v is the threshold for relative singular values. The relative singular values are sorted in decreasing order, and the parameter combinations with singular values smaller than v are less important for the data fitting. (Hördt, 1992). If a second order Marquardt technique is applied (Sudha et al., 2014), the entries of $\mathbf{T}$ become

$$T_{ii} = \frac{\lambda_i^4}{\lambda_i^4 + v^4} \tag{3.18}$$

3.2.2 Eigenvalue analysis

As stated earlier, expected changes of the data leaded by a small variation of model parameters can be described by the Jacobian matrix. The relationship depicted by equation 3.6 can also written as

$$\Delta\mathbf{F}(\mathbf{m}) = \Delta\mathbf{d} = \mathbf{J_w}\Delta\mathbf{m} \tag{3.19}$$

After the SVD decomposition is applied on $\mathbf{J_w}$

$$\Delta\mathbf{d} = \mathbf{U}\mathbf{S}\mathbf{V}^T\Delta\mathbf{m}$$
$$\mathbf{U}^T\Delta\mathbf{d} = \mathbf{S}(\mathbf{V}^T\Delta\mathbf{m})$$

$$\Delta\mathbf{d}^* = \mathbf{S}\Delta\mathbf{m}^*; \quad \Delta\mathbf{d}^* = \mathbf{U}^T\Delta\mathbf{d}, \quad \Delta\mathbf{m}^* = \mathbf{V}^T\Delta\mathbf{m} \tag{3.20}$$

Where $\Delta\mathbf{d}^*$ is the linear combination of $\Delta\mathbf{d}$ and $\Delta\mathbf{m}^*$ is the linear combination of $\Delta\mathbf{m}$. $\Delta\mathbf{d}^*$ and $\Delta\mathbf{m}^*$ are termed eigenparameters and eigendata, respectively (Edwards, 1997). Because $\mathbf{S}$is a diagonal matrix, $\Delta\mathbf{d}^*$ and $\Delta\mathbf{m}^*$ relate to each other uniquely. Thus how the eigenparameters are determined by the data could be understood. Consequently, the resolution of the original parameters is analyzed based on the matrix $\mathbf{V}$ and the eigenparameters. Stated by Edwards (1997), the standard errors of eigenparameters are the reciprocal of the corresponding eigenvalues $\mathbf{S}^-1$ if the model parameters are logarithmically transformed. The rough standard error of original model parameters can be calculated using the entries of the V-matrix

$$\Delta_{max}(m_j) = \sum_{k=1}^{M} \left| \frac{V_{jk}}{S_{kk}} \right| \tag{3.21}$$

Because the theory is valid for the linear approximation, the precisely computed error bound needs to be smaller than unity. If the standard error predicted to be larger than unity, a nonlinear technique is needed for finding the correct error bound(Edwards, 1997).

Based on SVD decomposition and eigenvalue analysis, a conventional manner is employed to interpret the resolution characteristics of one Marquardt inversion result in this thesis. The entries of the V-matrix are depicted as circles with various sizes and face color. The circle with larger size indicates a larger absolute value of the entry, while white face color means the entries are positive, and black denotes negative terms. The error estimation of eigenparameters, as well as original model parameters, are displayed for the corresponding columns and rows, respectively. By analyzing the resulted plotting, if an original model parameter is resolved or not can be understood. The detailed derivations of the eigenparameter statistical analysis are provided by Edwards (1997), and more applications can be found in Haroon (2016).

3.2.3 Importance

An alternative approach, termed model parameter importance in literature, is also employed to described the resolution of a specific model parameter in 1D Marquardt inversion. Following Sudha et al. (2014), the parameter importance is defined as

$$Imp(m_j) = \sqrt{[(\mathbf{VT})(\mathbf{VT})^T]_{jj}}, \quad j = 1 \cdots M \tag{3.22}$$

The value of importance lies between 0 and 1. If a model parameter has the importance close to 1, the model parameter is considered as well resolved. Contrarily, a model parameter is regarded as poor resolved if its importance value close to 0.

3.2.4 Equivalent models

Because of the diffusive nature of the electromagnetic field and the mixed-determined inversion problem, the models that can interpret one set of electromagnetic data are usually not unique. If the responses of two resistivity models are identical within a certain error bound, these two models are equivalent. A group of equivalent models is also referred to as equivalence. In some cases, the measured electromagnetic fields depend on the product of resistivity and thickness (ρh) or their ratio (ρ/h) rather than the independent value of each of them. This may result in many different model parameter combinations achieving similar data fitting (Haroon, 2016). On another hand, if a model parameter plays no role in deciding the observed data, any value is possible to be revealed for this parameter in the inversion, and an infinite number of equivalences are generated. With the demand to evaluate the equivalent models for one inversion result, a Hybrid Marquardt Monte Carlo scheme is implemented in EMUPLUS (Scholl, 2005). The parameters of starting models are varied within a predefined percentage range, and a suite of inversion results are computed by using the Marquardt algorithm. If an inversion result has a satisfactory data fitting, this resistivity model is considered to be equivalent. If a model parameter is revealed as a similar value in all the equivalence, it is regarded as well resolved. Otherwise, the dataset used in inversion has a poor resolution for the model parameter.

3.3 Occam inversion

Different from the Marquardt inversion, which usually reveals resistivity variation as a sharp contrast, Occam inversion is widely used when the desired solution is smooth. If no reliable prior information is available, the solution with smoothness constrains could be a prudent choice. Constable et al. (1987) introduced the smoothness constraint as a stabilization term in the objective function:

$$\Phi = \left[\mathbf{W_d}\left(\mathbf{d} - \mathbf{F}(\mathbf{m})\right)\right]^T \left[\mathbf{W_d}\left(\mathbf{d} - \mathbf{F}(\mathbf{m})\right)\right] + \lambda \mathbf{m}^T \mathbf{R}^T \mathbf{R} \mathbf{m} \tag{3.23}$$

where $\mathbf{R}$ describes the smoothness constrain. Note that the model parameters include only the resistivity, the layer thickness or element size are not the free parameters in a Occam inversion. With the demand to allow the model to be as flexible as possible while the complexity explicitly is suppressed (Constable et al., 1987), two different definitions of roughness are presented.

$$R_1 = \int \left(\frac{\partial \rho}{\partial z}\right)^2 dz; \quad R_2 = \int \left(\frac{\partial^2 \rho}{\Delta z^2}\right)^2 dz \tag{3.24}$$

The first order roughness R_1 corresponds to the first derivative of resistivity with respect to the depth. It is applied to aim at finding a model with the smallest gradient of $\rho(z)$. The second-order roughness R_2 tries to minimize the variation of the gradient $\rho(z)$, which means that a model with the smallest overall curvature will be found by roughness R_2.

In a 1D inversion, roughness R_1 can be expressed as

$$R_1 = \begin{pmatrix} 1 & -1 & 0 & \cdots & 0 \\ 0 & 1 & -1 & \cdots & 0 \\ \vdots & & \ddots & \ddots & \\ 0 & 0 & 0 & 1 & -1 \end{pmatrix} \tag{3.25}$$

In EMUPLUS, both roughness R_1 and R_2 are implemented. The Occam inversion result calculated by these two roughnesses could also be used as an evaluation for the resolution of model parameters. A typical example is that the inversions used two roughness often reveal the deep structures differently, indicating that the DOI of inverted data is not able to reach such a depth. The Lagrange factor λ trades off between the data misfit and the model roughness. A large λ enhances the weighting of model roughness, which means that the inversion prefers a smoother model rather than a smaller data fitting and vice versa for a small λ. λ starts with an arbitrarily high value defined by the user. In the subsequent iterations, the inversion searches for a λ, which minimizes the misfit (Constable et al., 1987). Practically, a proper λ could be found by multiplying a cooling factor to decrease its value during the inversion, like the strategy described by the L-curve criterion (Hansen and O'Leary, 1993).

Different from Marquardt inversion, the starting model of the Occam algorithm is usually set to homogeneous (E.g.300 $\Omega \cdot m$). A larger number of layers is often required. Specifically, the 1D resistivity models with 20 layers are usually used for the inversion of a single EM method. Because the different EM methods considered in joint inversion could have a significantly divergent resolution to different layers, 50 layers are employed for 1D joint inversion. The thickness of the layers grows logarithmically with increasing depth. The layer just beneath the earth's surface has the minimum thickness, while the thickness value is determined based on the resolution of the used EM methods.

4 1D joint inversion of HEM, LOTEM and semi-airborne data

For many geophysical problems the subsurface structures are often considered as stratified layers with no horizontal boundaries. Firstly the problem is tried to be resolved as a 1D case (e.g., Key, 2009; Yogeshwar, 2014; Haroon, 2016). The 1D resistivity models are a great simplification of the real earth subsurface in many cases. However, such 1D studies provide valuable knowledge and preliminary models for the following research, which is often computational challenging. Moreover, the 1D forward and inversion modeling are much easier realized and less time-consuming. Compared to multidimensional modeling with significant computational load, a series of systematical 1D modeling studies are feasible in a short time. This advantage provides the chance to get a deep insight into the resolution of one dataset, as well as the occurring equivalence problem. The resolution of one inversion result and the possible equivalence play an important role in the subsequent interpretation. Therefore, the development and analysis of joint inversion are started in this thesis from the 1D case for HEM, semi-airborne, and LOTEM.

In this chapter, the characteristics of each involved EM method are investigated from the perspective of 1D modeling. Based on the resolution and the DOI of different EM surveys, the effects and advantages of 1D joint inversion are discussed in detail. Different weighting schemes are tested to be applied to the 1D joint inversion. These aim at improving the resolution of the results and ensuring optimal convergence. Finally, the field data acquires in eastern Thringia (2016) are inverted using the developed 1D joint inversion. The outcome, some challenges and problems are discussed in detail.

Note that EMUPLUS is employed for all the 1D inversion and modeling within this thesis. Most of the inversion techniques described in the last chapter are implemented in the algorithm.

4.1 Semi-airborne solution for 1D layered resistivity model

With the demand to apply 1D joint inversion on HEM, LOTEM and semi-airborne data, a 1D semi-airborne forward modeling algorithm in frequency-domain is required firstly. Here, the semi-airborne concept can be viewed as a standard frequency-domain CSEM with the receivers positioned in the air at a known altitude (Smirnova et al., 2019). Therefore, standard CSEM modeling codes can be routinely used. Janser (2017) developed a forward modeling code based on the algorithm of Weidelt (1986) in the presence of a 1D-layered subsurface model and embedded it in EMUPLUS. The transmitter can be polygonal-shaped loop sources as well as extended dipole sources. Magnetic field and voltage response receivers can be set at an arbitrary position on the earth's surface and also in the air-halfspace. The theory and step-by-step derivations for the algorithm are described in detail by Janser (2017).

Based on the 1D forward modeling code of Janser (2017), frequency-domain solutions are extracted before the transformation into time-domain is applied. Thus both the frequency-domain and time-domain solution is feasible in EMUPLUS. Afterward, the forward modeling code of semi-airborne is embedded in the joint inversion frame of EMUPLUS.

4.1.1 Verification for the semi-airborne 1D solution

Prior to performing modeling studies and inversions, the accuracy of the 1D semi-airborne solutions should be verified. In frequency-domain, the 1D solutions calculated by EMUPLUS are compared to the results of the algorithm EM1DW from WWU Münster (Becken, personal communication). Semi-airborne responses are calculated for a 1D three-layer resistivity model. The resistivities of the three layers are 300, 10, and 300 $\Omega \cdot m$, respectively. With the demand to verify the modeling solutions for more cases, the thicknesses of the top two layers are varied in the comparison. Figure 4.1a and b display the comparisons between EMUPLUS and EM1DW for semi-airborne solutions at offsets of 500 m and 1500 m. The thickness of both the top two layers is 250 m for (a) and (b). The relative differences between the two solutions are always smaller than 1%, indicating the very good fitting. For the case that both the two top layers have thicknesses of 100 m, the verification is presented in Figure 4.1c and d. The fitting of the solutions between two 1D codes is also high when the offset is 500 m. Nevertheless, the sign reversal encountered at offset 1500 m decreases the accuracy for some frequencies. As relative differences in (d) suggest, the misfits between solutions of both codes are increased around the sign reversal. Excluding the sign reversals, the relative differences between two 1D solutions are smaller than 2%, which is a satisfactory level. Referring to the semi-airborne solutions calculated by EMUPLUS in time-domain, Janser (2017) had presented the code validations for various configurations and model parameters, and the solutions always show sufficient accuracy.

Additionally, the effects of receiver altitude in semi-airborne data are investigated based

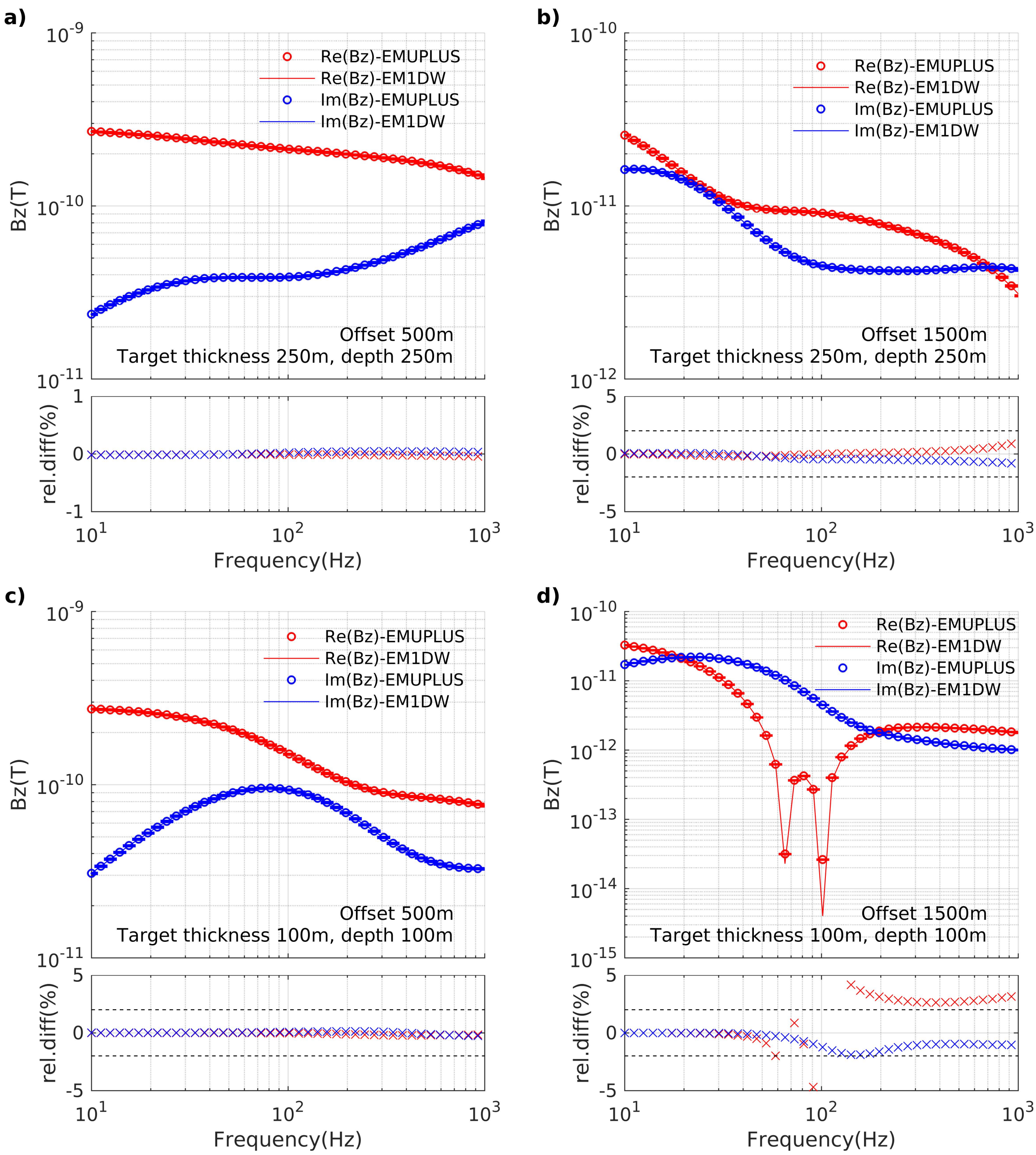

Figure 4.1: Semi-airborne frequency-domain 1D solution calculated by EMUPLUS and EM1DW. (a) and (b) display the solutions for offset 500 m and 1500 m respectively when target has both thickness and depth of 250 m. (c) and (d) display the solutions for offset 500 m and 1500 m respectively when target has both thickness and depth of 100 m. The transmitter has 1000 m length and the broadside configuration is used. The altitude of the receivers are 40 m. Relative differences of the real and imaginary parts are displayed at the bottom of each plot while the black dashes indicate the relative difference of -2% and 2%.

on the same 1D resistivity model utilized in Figure4.1 a. The comparisons are attached in Figure A.1 and A.2 for frequency- and time-domain, respectively. Indicated by the modeling, the effects of receiver altitude are significant and should be fully considered in the studies of semi-airborne data.

4.2 One-dimensional modeling studies

The following modeling studies are carried out, aiming at gaining the detailed insights of resolution characteristics of HEM, semi-airborne, and LOTEM measurements. Moreover, for CSEM applications like semi-airborne and LOTEM, the geometry of the transmitter-receiver offset must be taken into account for any estimations of exploration depth (Mörbe, 2019), which is also an important aspect of the resolution. The results of these modeling studies provide essential information for the design of subsequent joint inversions.

As presented in the last section, semi-airborne modeling is installed in EMUPLUS. The 1D forward modeling algorithm from Siemon (2012) is also introduced in EMUPLUS by Sudha et al. (2014). The LOTEM modeling in EMUPLUS is widely used for many years (Scholl, 2005; Mörbe, 2019). In order to compare the resolution difference of these three EM methods, the modeling studies are conducted systematically based on the 1D resistivity model sketched in Figure 4.2. The subsurface of the 1D resistivity model

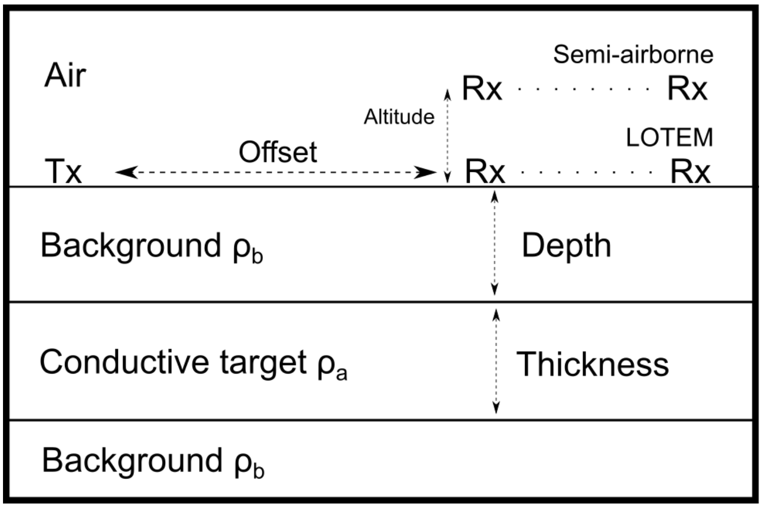

Figure 4.2: Sketch of the 1D resistivity model discussed in this section.

consists of three layers. The target of the EM surveys here is the conductive layer with resistivity ρ_a, which is embedded in background rocks with resistivity ρ_b. In this section, the values of ρ_a and ρ_b are fixed as 10 and 300 $\Omega \cdot m$, respectively. This resistivity structure is designed according to the typical 1D inversion results of LOTEM data acquired in eastern Thuringia (Mörbe, 2019). With the demand to examine the resolution variations when the target has different sizes and locations, the thickness and the buried depth of the conductive layer are changed during the modeling studies. The broadside configuration is always employed for both the LOTEM and semi-airborne surveys. The receivers at a series of different offsets are deployed on the earth's surface. The magnetic field sensors of semi-airborne measurements are positioned in the air with a fixed altitude of 40 m in this section.

4.2.1 Approaches used for the resolution studies

In order to evaluate the resolution by a given data set to the parameters of the investigated resistivity model, three methods are utilized. The first approach is the eigenvalue analysis based on SVD decomposition, which is introduced in the last chapter. The second approach bases only on forward modeling. The misfit space for a particular resistivity model as a function of perturbations to a pair of model parameters is plotted (Key, 2012). In another word, the equivalence domain of the target model parameter variation is presented as colored heat maps (Haroon, 2016). This test is performed by generating noisy synthetic data for a series of perturbed models and then computing the data misfit χ with the true model response. An example is shown in Figure 4.3a. Specifically, the heat map presented in (a) is calculated for a HEM dataset (same as Figure 4.6d). The target layer

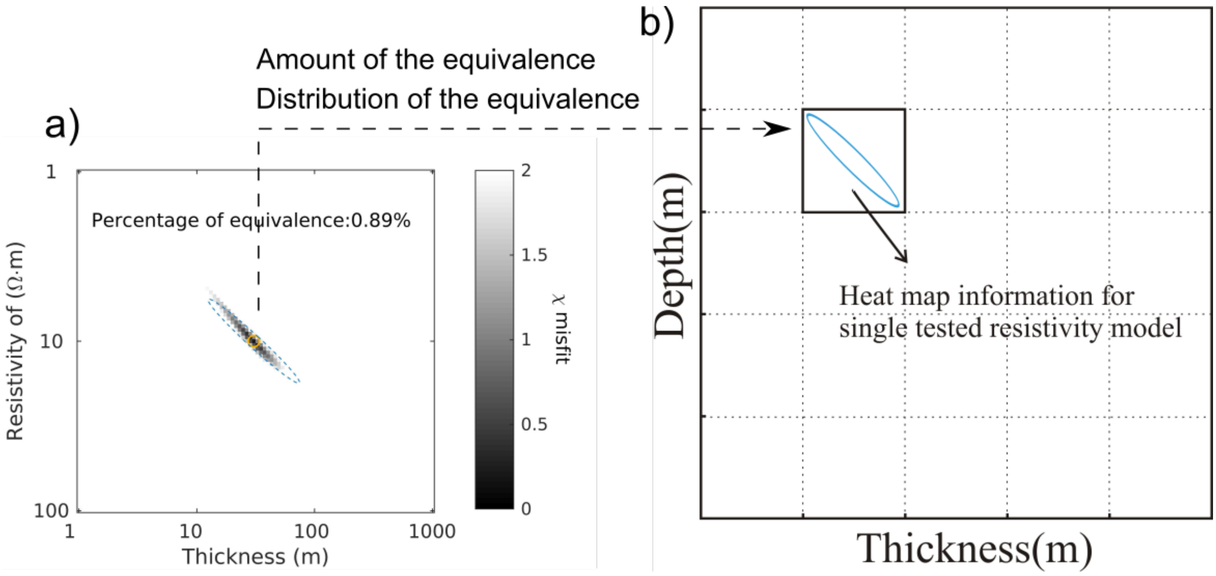

Figure 4.3: The concept for the summary of heat maps for the resolution study. a) An example of a heat map of a single tested model and b) the summary of information of heat maps as a function of target buried depth and target thickness for a suite of tested models.

has a resistivity of 10 $\Omega \cdot m$, a thickness of 30 m, and buried depth of 75 m. The data error estimation is set as 2% for all the synthetic HEM data. Misfit space is presented as a function of perturbations to the thickness and resistivity of the conductive target layer. The resistivity models providing responses with misfit χ smaller than 2.0 are accepted as equivalent models. For the test in 4.3a, searching for equivalence is performed for resistivity values vary from 1 to 100 $\Omega \cdot m$, and the thickness varies from 1 to 1000 m. 91 and 100 values are logarithmically equally spaced between the limits for resistivity and thickness, respectively. Among the total 9100 pairs of resistivity and thickness, 81 pairs of them lead to the resistivity models having misfit χ smaller than 2.0. Therefore 0.89% of the tested 1D models belong to the equivalence domain of the true model. As one can see, only the equivalences are colored in Figure 4.3a. The distributions of the equivalence also provide important information. In this example, the region of low misfit is linear between the thickness and resistivity. Compared to the true values highlighted by the orange circle, the equivalent models always have smaller resistivity and thickness simultaneously or larger resistivity and thickness at the same time. This relationship illustrates the fact the HEM data resolve the resistivity-thickness ratio of conductive target better than the individual value of resistivity or thickness. Contrarily, for a resistive target, the resistivity-thickness product will be resolved (Key, 2012). Note that this test describes a highly constrained problem, the background resistivity, and the buried depth of the target layer are always fixed.

One single heat map provides the resolution characters of one dataset to one pair of parameters in an individual 1D resistivity model. If the resolution capability of an EM method or a measuring configuration is supposed to be investigated, a large number of heat maps correspond to target layers with various buried depth and thickness should be examined systematically. For convenient analysis, the information included by a group of heat maps is summarised by the approach shown in Figure4.3b. A big map is created for storing the information of all the examined heat maps. The horizontal axis of this map indicates the variation of target thickness, while the vertical axis indicates different target buried depth. Thus the map can present the resolution characters for target layers with different thicknesses and buried depths simultaneously — one cell stores the information of one tested 1D model. Two parts of resolution information are extracted from an individual heat map and stored in the big map. Firstly, the percentage of equivalence is depicted as colored code. The percentage of equivalence is an important term because it describes directly if the tested two model parameters can be resolved. Different color indicates a different equivalence amount, suggesting the resolution variance intuitively. Secondly, the shape of the low misfit region is simulated by an ellipse. For example, the ellipse denoted by a blue dash in Figure 4.3a. The half major and minor axis of the ellipse are defined as follows:

$$a = \frac{\sqrt{C_\rho^2 + C_T^2}}{2}; \quad b = \frac{C}{a\pi}; \quad \Phi = arctan(\frac{C_\rho}{C_T}) \tag{4.1}$$

Where the a and b denotes the half major and minor axes of the ellipse, respectively. C denotes the percentage of equivalence in an individual heat map, which can be understood as the area of the colored low misfit region; C_ρ denotes the ratio between the number of possible resistivity values among the equivalence and the total number of tested values. For example, in Figure4.3a, 23 tested resistivity values between 4 and 15 $\Omega \cdot m$ occur in the equivalence. Since total number of tested resistivity values are 91, $C_\rho = 23/91 = 0.2527$. C_ρ can also be understood as the length of the low misfit area in the Y-direction. C_T shares the same concept with C_ρ, but it is the measure of thickness. Similarly, C_T can be understood as the length of the low misfit area in the X-direction. Therefore the half major axis a of the ellipse can be calculated by the Pythagoras theorem, and the minor axis b is calculated according to the area and the half major axis of the ellipse. Moreover, the dipping angle of the major axis is also gained by C_ρ and C_T. However, because the area of the colored low misfit region is usually too small, the plotted ellipses are not readable. Thus the sizes of the ellipses are enlarged to fit the length of the cells in the big map.

$$a^{'} = \frac{\sqrt{2}}{2}; \quad b^{'} = \frac{b}{a}a^{'} \tag{4.2}$$

Where the enlarged half major and minor axes $a^{'}$ and $b^{'}$ are used for plotting practically. The examples can be found in the next section (e.g., Figure 4.4). By reading this summary of the heat maps, one can easily understand how the resolution of the target layer parameters vary as a function of the buried depth and the layer thickness. The range of depth and thickness of examined 1D models are decided according to the DOI of each EM method. Note that The resolution information given by heat maps always focuses on the two investigated model parameters. Thus this approach still has its limitations, which will be discussed in the next sections.

4.2.2 Modeling studies for HEM

The resolution characteristics of the HEM survey are investigated in this part. Because the transmitter-receiver separation doesn't vary significantly during the HEM survey, the DOI of HEM is not decided by the offset and, therefore, relatively stable. As stated earlier, the 1D resistivity model studied in this section has background resistivity of 300 $\Omega \cdot m$ and a 10 $\Omega \cdot m$ target conductor. The resolution capability of HEM data for the conductor is firstly investigated by a group of heat maps. The heat maps are generated for the 1D models contain target layers with the buried depth vary from 2.5 to 150 m, and the thickness between 4 to 100 m. During the forward modeling, the error estimations of the synthetic HEM data are assumed to be 2%. The information about heat maps are summarised in Figure 4.4 as described above. Illustrated by the percentage of accepted

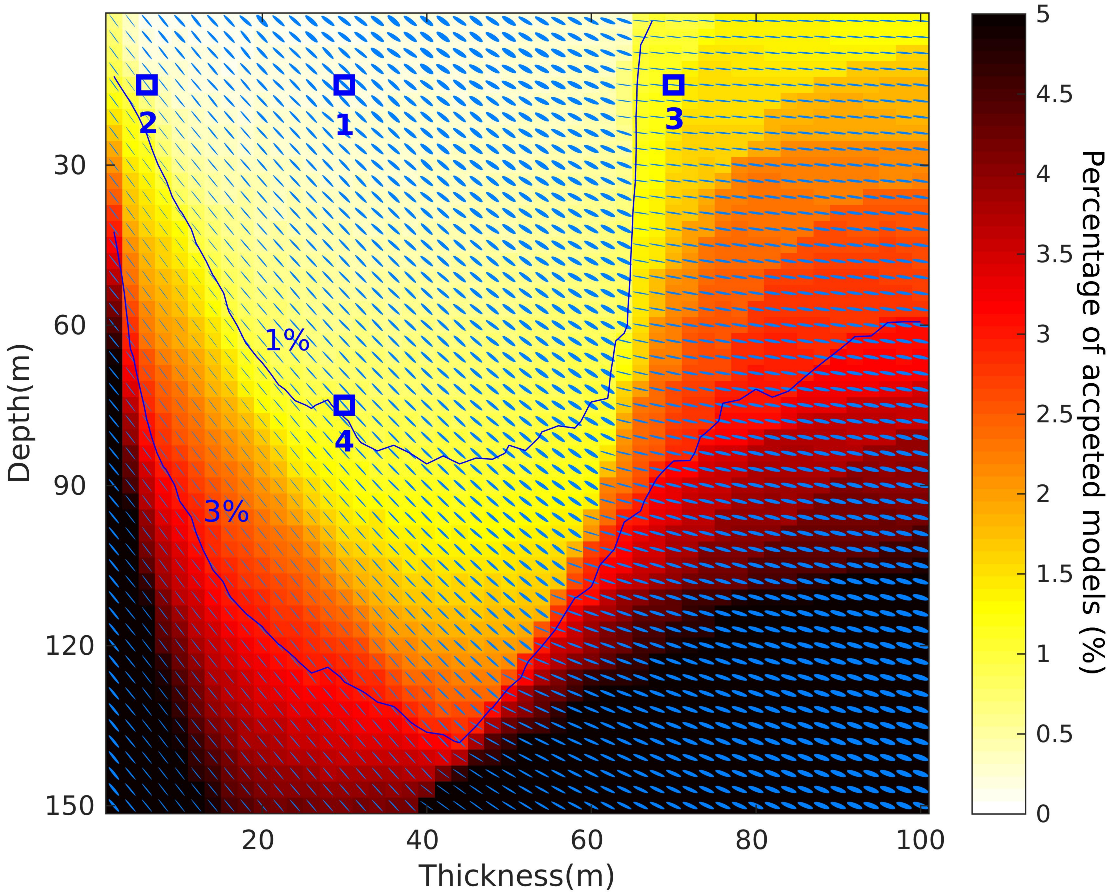

Figure 4.4: Summary of resolution studies for HEM. The error estimation is set as 2%. The resolution of HEM data to the four particularly highlighted 1D models are further analysed.

models (or equivalence), the HEM dataset can resolve the resistivity and thickness best for the target conductors with thickness 20 to 60 m and buried depth down to 60 m (the region colored as white). The resolution will reduce if the layer thickness is too thin or too thick, or it is buried too deep. According to this summary of heat maps, four 1D models are selected for further analysis, which are highlighted by the blue squares. The synthetic data of these four models are inverted by Occam and Marquardt algorithms, respectively. It is important to mention that, the starting model for Marquardt inversion is selected based on the Occam inversion results, which is a routine operation in 1D inversions of EM data (Moghadas et al., 2015; Cai et al., 2018). Figure 4.5 displays the

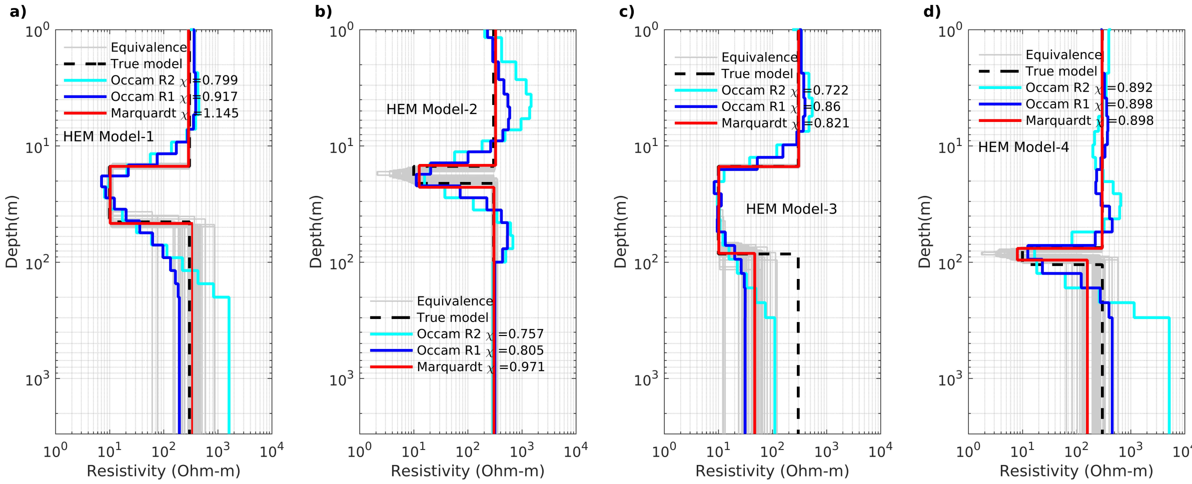

Figure 4.5: 1D inversion results of HEM synthetic data. The results are correspond to the four models highlighted in Figure 4.4. (a) Model-1; (b) Model-2; (c) Model-3; (d) Model-4.

corresponding inversion results as well as the equivalent models. Moreover, the heat maps and the eigenvalue analysis for the Marquardt inversion results are provided in Figure 4.6 and 4.7 for the four models, respectively. Subsequently, the resolution characters will be analyzed for the highlighted four models one by one.

For Model-1, the conductive layer has a thickness of 30 m, and it is buried at a depth of 15 m. In Figure 4.5a, the true 1D model is depicted by the black dash. Both Occam and Marquardt inversions describe the overburden and the target conductor. The resistivity and thickness of the conductor are clearly revealed in all the equivalence. The heat map and SVD analysis support this high resolution of determining the individual value of resistivity and thickness. As shown in the heat map (Figure4.6a), the equivalence with low misfits are limited in a small region, indicating that the resistivity value is well constrained around 10 $\Omega \cdot m$ by the data, and the thickness is limited around 30 m. In Figure4.7a, $log\rho_i$ denotes the logarithmically transformed resistivity of ith layer, and $logd_i$ demotes that for thickness. The ΔMax of $log\rho_2$ and $logd_2$ provided by the eigenvalue analysis suggest that these two model parameters have the max error bound 3% and 7%, respectively. To sum up, all the analyses support the conclusion that the HEM survey provides a high resolution for detecting the substructures in Model-1. The conductive target layer in Model-2 has the same buried depth as Model-1, but its thickness is reduced to 6 m. In the summary of the heap maps (Figure 4.4), the Model-2 locates on the left of Model-1. There number of equivalence for Model-2 increases; thus, it is colored in light yellow. The

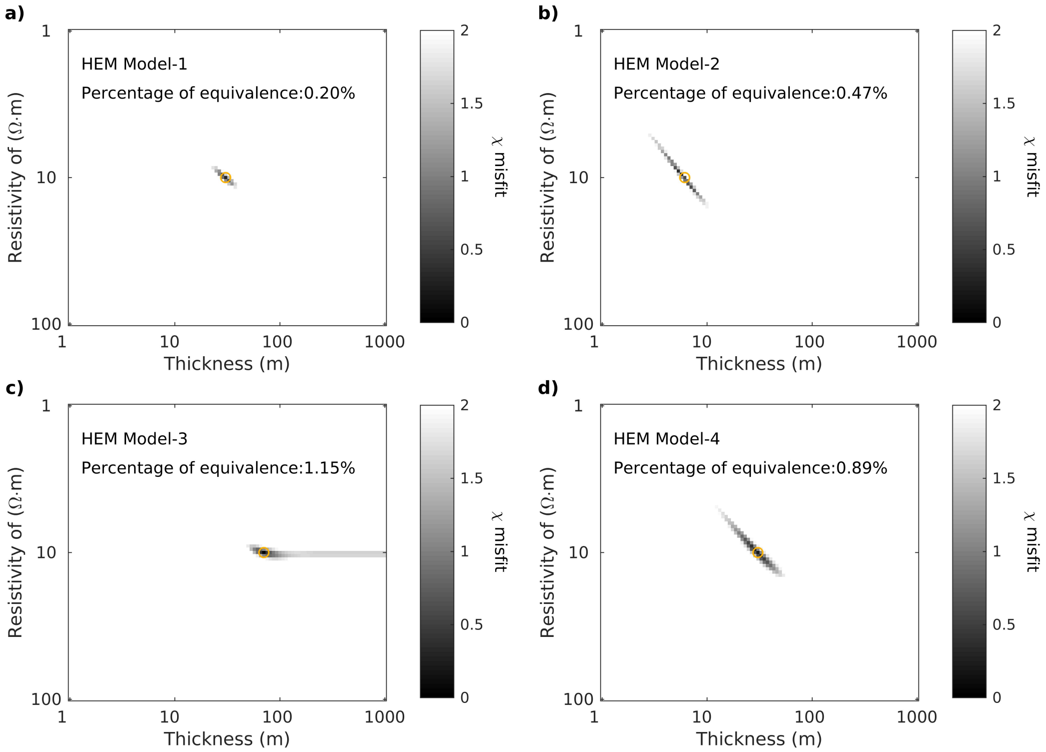

Figure 4.6: Modeling studies investigating the resolution of HEM data to the resistivity and thickness of conductive layers. The results are correspond to the four models highlighted in Figure 4.4. (a) Model-1; (b) Model-2; (c) Model-3; (d) Model-4.

sharp ellipse indicates the resistivity-thickness ratio generally decides the equivalence distribution. The specific individual heat map is given in Figure 4.6b. The inversion results show the same conclusion (Figure 4.5b). Even though the target layer is well described by Occam and Marquardt inversion, the equivalence suggests that resistivity and thickness of the thin layer are hard to be determined uniquely. The error estimations of these two model parameters are provided in Figure 4.7b as 23% and 25%, respectively. The analysis results of Model-2 fit the common knowledge of EM measurements — the thinner layer is more difficult to be resolved. On the other hand, Model-3 shows a special case. Usually, a thick conductive layer causes strong anomalous fields in the measured data, and the parameters of the thick layer are easy to be resolved. It is a good example that, compared to Model-2, the thicker conductor of Model-1 can be resolved better. However, Figure 4.4 shows that Model-3 has more equivalence than Model-2. The flat, sharp ellipse provides the explanation. In the specific heat map of Model-3, the resistivity of the conductor is constrained around 10 $\Omega \cdot m$, but all the thickness values from 70 (the true value) to 1000 (or even more) lead to the sufficient data fitting. This poor resolution for thickness is also demonstrated by the inversion results in Figure 4.5c and eigenvalue analysis in Figure 4.7c. The equivalent Marquardt inversion results show that the lower boundary of the thick conductor is hardly determined. And the maximum error bound (ΔMax) for $logd_2$ of Model-3 is 42%. The reason for the poor resolution of the thick conductor

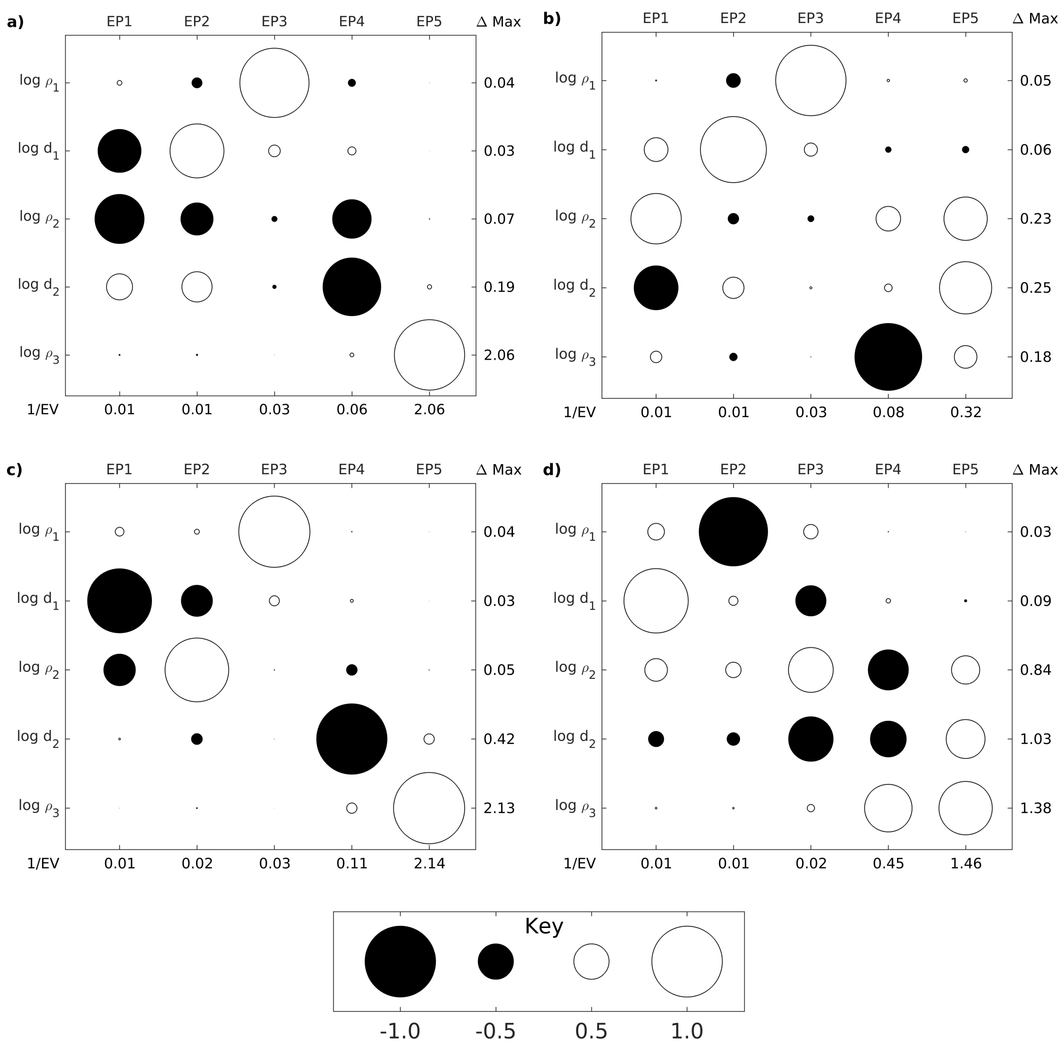

Figure 4.7: SVD analyses for the Marquardt inversion models displayed in Figure 4.5.The results correspond to the four models highlighted in Figure 4.4. (a) Model-1; (b) Model-2; (c) Model-3; (d) Model-4.

in Model-3 is the limited DOI of the HEM survey. The EM fields decay quickly in the conductive media of the thick layer, and most of the energy of transmitted EM fields can not reach the lower boundary. Naturally, the basement in Model-3 can not be resolved either. Indicated by the summary of the heat maps (Figure 4.4), no matter how the buried depth is, the resolution of the lower boundary of the conductor decrease dramatically if its thickness reaches around 65 m. Model-4 has the as same thickness with the Model-1, but it is buried much deeper (75 m). It shows another typical characteristic of the EM measurement. The anomalous signals caused by a deeper target is usually weaker, and it is more challenging to be resolved. The inversion results for the synthetic data of Model-4

(Figure 4.5d) show a high amount of equivalent models. The low misfit region in the heat map (Figure 4.6d) is as long as that for Model-2, but wider. The wider equivalence distribution indicates that the resolution for resistivity-thickness ratio also decreases. The eigenvalue analysis for the Marquardt result of Model-4 (Figure 4.7d) not only provides large error estimations for the $log\rho_2$ and $logd_2$, but also the evenly distributed entries of V-matrix. This SVD analysis indicates that these two model parameters are decided by complex linear combinations of the eigenparameters and highly inter-correlated with each other.

To sum up, the HEM survey has a promising resolution for the shallowly buried conductors. In the specific case of this modeling study ($\rho_a = 10\Omega \cdot m \quad \& \quad \rho_b = 300\Omega \cdot m$), the HEM survey has a high resolution for the conductors with a thickness between 10 to 60 m and buried depth down to around 60 m. If the conductive layer is too thin or too deep, the resolution is reduced. If the conductive layer is too thick, the lower boundary is difficult to be detected.

4.2.3 Modeling studies for LOTEM

The LOTEM measurement considered in this thesis includes only the step-on responses of the horizontal electric field (Ex). For step-on Ex transient, a strong primary field superimposes the inductive field response. Therefore the measured field data are offset dependent. As introduced earlier, the exploration depth can be approximately evaluated by the diffusion depth for time-domain surveys. But with the demand to design the joint inversion, which can fully take advantage of the benefits of each EM method, studies of LOTEM DOI for the specific case in this thesis is performed. Because the error estimation plays a vital role in the practical DOI, 1% error estimation is used to all the synthetic LOTEM data in this section based on the error estimation of the LOTEM field data. The resistivity of anomalous layer and background is kept as before for the continuity of the resolution studies — resistivity is 300 $\Omega \cdot m$ for background and 10 $\Omega \cdot m$ for the conductor. The offset, buried depth and thickness for the target conductor are varied during the modeling studies naturally. Figure 4.8 displays the comparison between the Ex responses of background and the 1D model with the target conductive layer. For the target has a buried depth of 700 m and thickness of 100 m, the anomalous signals in the Ex transient occurs after the 10^{-3}s. The anomalous field distributions diverge for different offsets. In the subsequent modeling, the data misfit caused by the anomalous signals is used as a measure for the DOI. For examining the continuous variations of the anomalous field as a function of the offsets, the residuals at a series of offsets are plotted

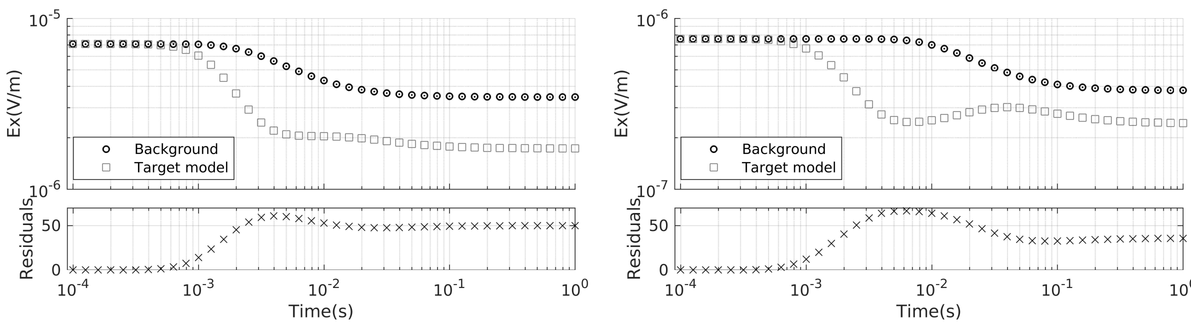

Figure 4.8: LOTEM horizontal electric field (Ex) for the half-space (circles) and 1D resistivity model including a conductive target layer (squares). The target layer is buried at 700 m depth and has thickness of 100 m. (a) and (b) show the response at offset 2350 m and 5000 m, respectively.

in Figure 4.9 a to c for the target layer buried at different depth. There are three points evident from these figures. Firstly, by comparison between (a), (b), and (c), the common knowledge is validated again that the conductor buried in shallow layers causes much stronger anomalous signals than a deeply buried target. Secondly, the time at which the second layer is first detected is independent of the offsets. The conclusion is presented by Spies (1989) for the magnetic field in the transient electromagnetic method. Thirdly, for a deep structure, the short offsets may not have the capability to detect the anomaly. For example, in Figure 4.9 c, the offsets smaller than 500 m show no information from the target layer buried at 1300 m depth. The relationship between the anomalous field distributions and the offset is further summarised. The residuals at each time point in a) to c) are summed up to χ as a measure for the anomaly information in the whole transient. Thus the χ variations at different offsets are displayed for the target layers locate at a suite of continuously increasing depth. The results are presented in Figure 4.9 d to f for the conductors with different thicknesses. As predicted, for the same buried depth, thicker conductor causes stronger anomalous fields and leads to a larger χ. For a certain thickness, if the target is buried deeper, the χ will decrease. Regarding the variation with offsets, the χ increases only for some cases with increasing offset. For example, in Figure 4.9 d, when the target is buried at depth 100 m, the χ changes little with the increasing of the offsets. When the target is buried at depth 1600 m, a larger offset can receive more anomalous signals and result in a larger χ. For the specific case here ($\rho_a = 10\Omega \cdot m \& \rho_b = 300\Omega \cdot m$), a conductor with 50 m thickness can lead to the $\chi = 10$ at a depth of 1600 m if the offsets are larger than 2000 m. In other words, LOTEM measurement could effectively detect a 50 m thick target in a depth of 1600 m if the offset is large enough, and the data error is 1%.

From another perspective, the detectable anomalous fields don't mean the target can be

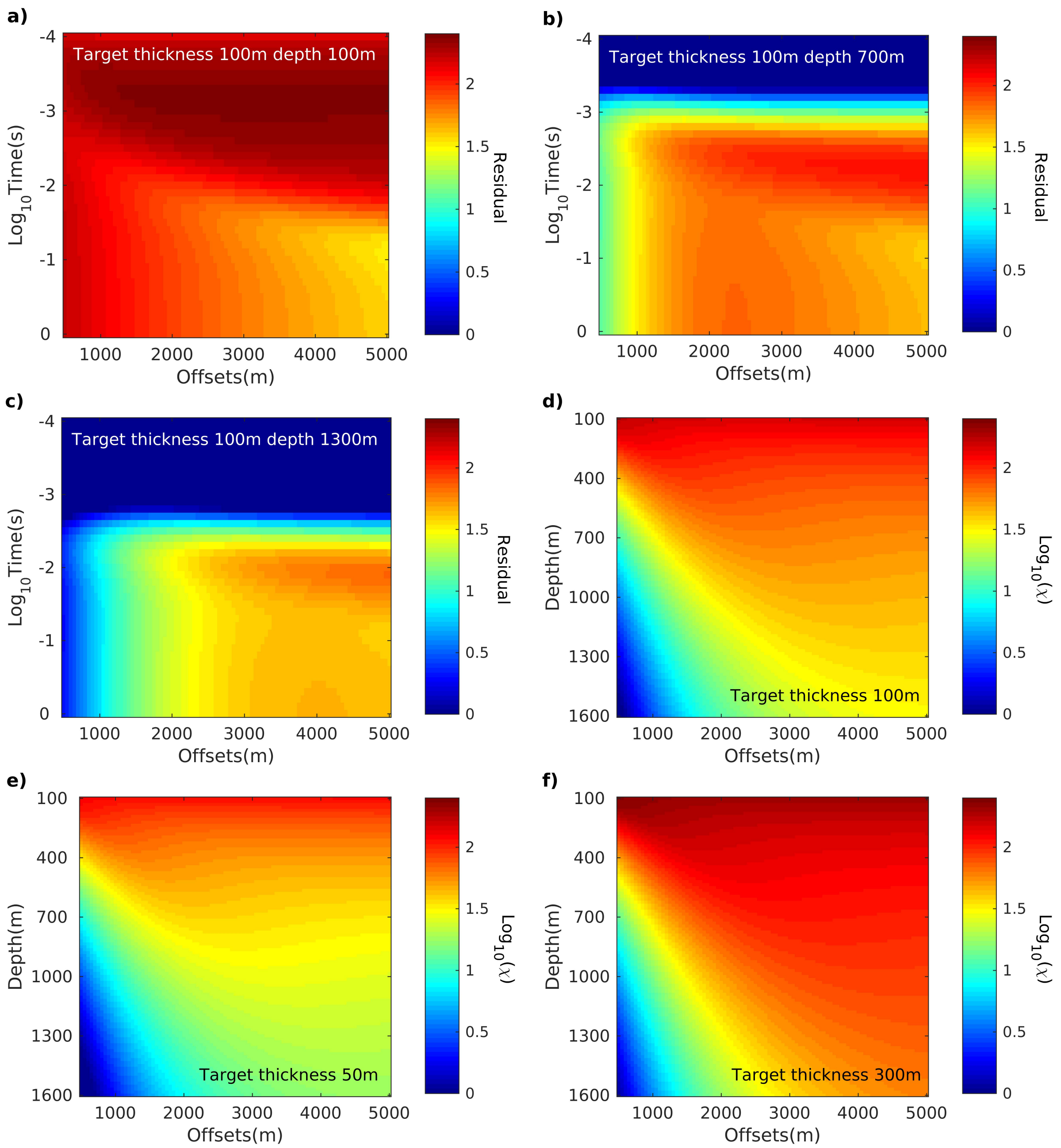

Figure 4.9: Sensitivity of LOTEM horizontal electric field (Ex) for a conductive target layer. Residual between responses of target model and background model are calculated by using logarithm transformation, and presented in (a), (b) and (c) for buried depth 100, 700 and 1300 m, respectively. (d), (e) and (f) are χ misfits varying as a function of different transmitter-receiver separations and buried depth for target thickness of 100, 50, and 300 m, respectively.

revealed with a high resolution. The summary for heat maps is consequently performed for the LOTEM (Figure 4.10). Each single heat map considers only the target resistivity and thickness. The offset is selected as 3000 m. For getting close to the realistic situation, 2% Gaussian noise is added in the synthetic data. In general, it is more difficult to resolve the parameters of a conductive layer if it is thicker or buried deeper. Moreover, the boundary of less equivalence domain is approximately linear between the thickness and target depth, like the 1% boundary denoted by the solid blue line. Overall, for the 3000 m offset and the 2% noise level, the conductors with a thickness larger than 100 m and depth smaller than 600 can be well resolved. However, this is just the conclusion suggested by the heat maps. The depth variation is not considered in each heap map. Therefore the

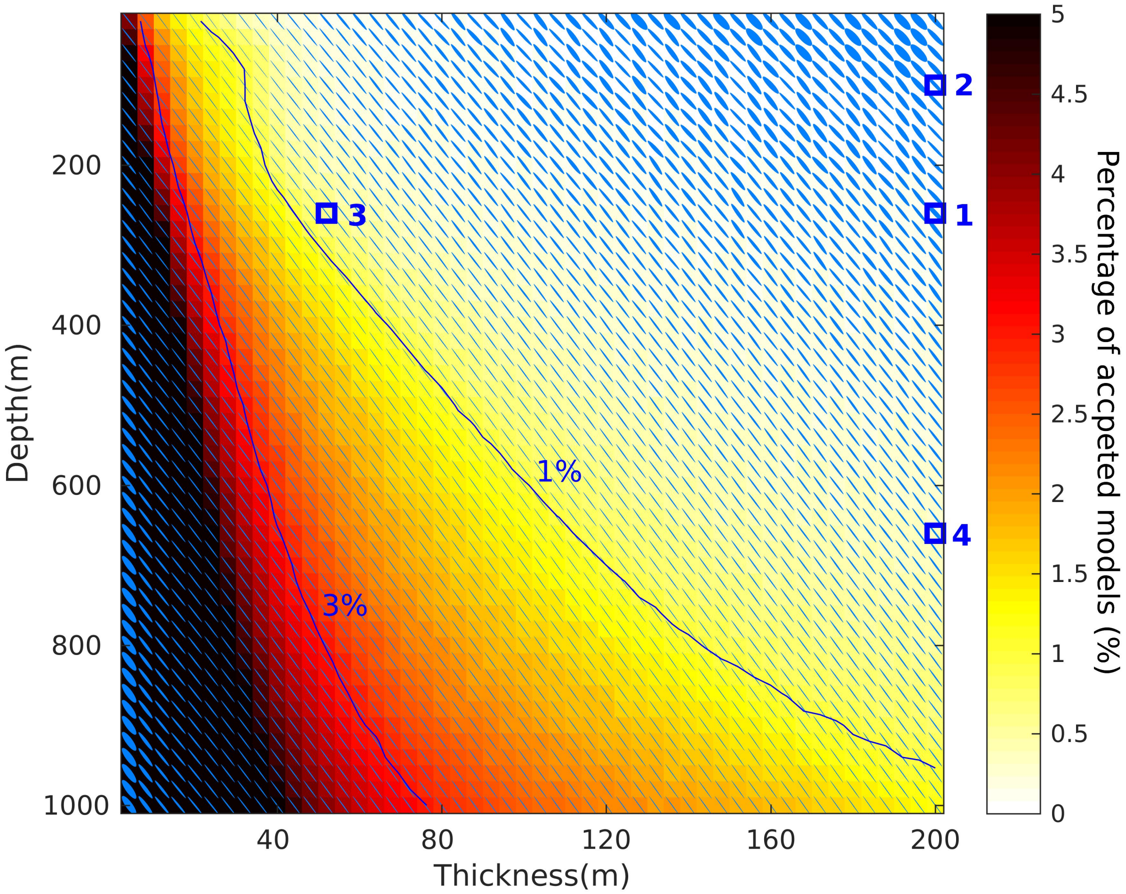

Figure 4.10: Summary of resolution studies for LOTEM Ex component. The offset is 3000 m. 2% Gaussian noise is added in the synthetic data. The resolution of LOTEM Ex components to the four particularly highlighted 1D models are further analysed.

inversions on synthetic data and the corresponding eigenvalue analysis are carried out for the complementary information. Similarly, four models are selected for further studies. The Model-1 is the best revealed one. It has a thickness of 200 m and buried depth 250 m. The Occam and Marquardt inversion results depict the true model perfectly, and no obvious divergent model parameters are resolved among the equivalence. The particular heat map for Model-1 (Figure 4.12a) shows a very small low misfit region while all the error estimations of the major model parameters are smaller than 5%. The resolution

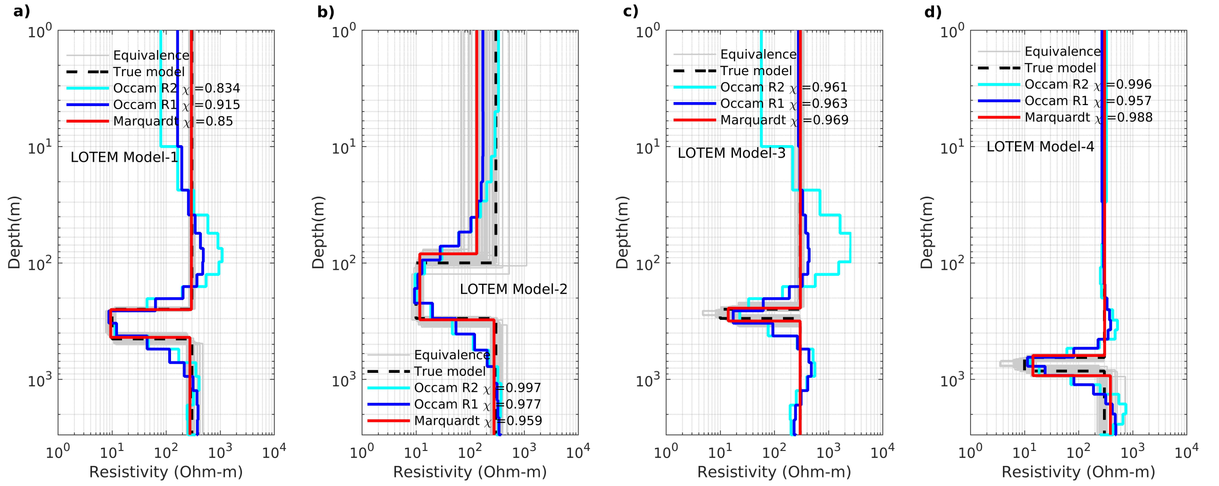

Figure 4.11: 1D inversion results of LOTEM synthetic electric fields. The results are correspond to the four models highlighted in Figure 4.10. (a) Model-1; (b) Model-2; (c) Model-3; (d) Model-4.

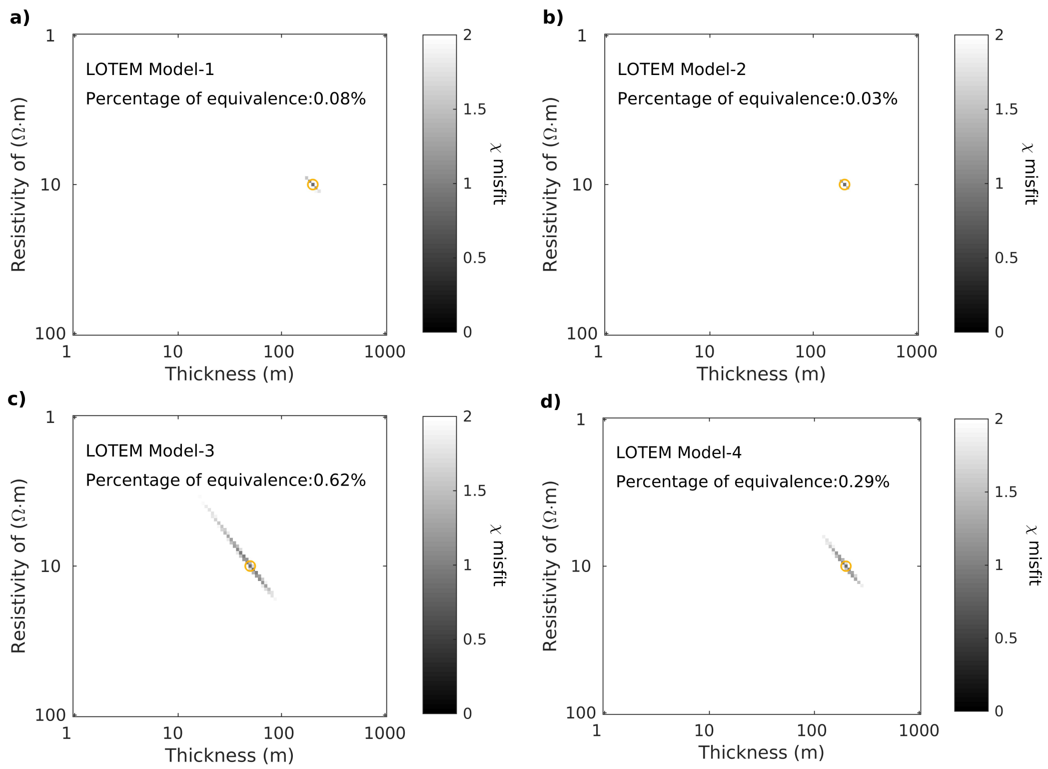

Figure 4.12: modeling studies investigating the resolution of LOTEM Ex to the resistivity and thickness of conductive layers. The results are correspond to the four models highlighted in Figure 4.10. (a) Model-1; (b) Model-2; (c) Model-3; (d) Model-4.

reduction led by the small thickness and the large buried depth is validated by Model-3 and

4, respectively. The target layer can be clearly recovered by the inversions (Figure 4.11c and d), but the equivalences show a series of different resistivity-thickness combinations. Compared to Model-1, the ΔMax of $log\rho_2$ and $logd_2$ for Model-3 and 4 (Figure 4.13c and d) are significantly larger. Illustrated by the particular heat maps (Figure 4.12c and d), the equivalence distributions for Model-3 and 4 are dominated by the resistivity-thickness ratio. To summarise, the resolution variations suggested by Figure 4.10 are validated in the cases of Model-1,3 and4. On the other hand, the equivalence domain described in the specific heat map of Model-2 (Figure 4.12b) is even smaller than that of Model-1. But the better resolution for the conductor in Model-2 is not true. As the inversion results of Model-2 (Figure 4.11b) shows, the resistivity of overburden is poor resolved. The upper boundary of the conductor, or the lower boundary of overburden, is also not determined perfectly. The eigenvalue analysis for Model-2 shows that the error estimation of $log\rho_2$ and $logd_2$ increase a bit compared to Model-1, while the error bound for $log\rho_1$ is 40%. In other words, the poor resolution of overburden also negatively affects the resolution of the target layer. For validation, the resolution studies performed as a heat map is also applied to the first layer (overburden) of Model-1 and 2. As Figure 4.14 shows, the resistivity and thickness of the 1st layer in Model-1 are highly constrained by the LOTEM data. In comparison, the top layer thickness of Model-2 is no longer constrained so well, while the possible values of its resistivity range from 160 to 530 $\Omega \cdot m$. Because the offset utilized here is 3000 m, for complementary, a similar resolution study is conducted for the case of offset 500 m (Figure A.5). Suggested by the modeling examples of Model-2 and Figure A.5, the step-on signal of the LOTEM horizontal electric field do not have a good resolution for the shallow layers. Because of the superimposed system responses, the very short LOTEM offsets are not considered in this thesis. Good resolution is not the reason for the well-resolved top layer in the Marquardt inversion results of Model-1,3 and 4. They are revealed well because the layer number is fixed as three for the Marquardt inversions (based on the Occam inversion results). Because the top layer for these three models are thick enough and affect the data significantly, they can be well constrained by the data in turn. If the thick top layers are divided into the smaller shallow layers, the resolution for them will decrease significantly. The Occam inversion results calculated by different roughness in Figure 4.11c are a good example. The inversion result of roughness 2 deviates obviously from the true model while the data fitting is still ideal. A similar case could also happen for HEM theoretically, for example, the shallow layers revealed by Occam inversions in Figure 4.5b. However, these poor resolutions for shallow layers are never presented by the heat maps, which is one important drawback. Overall, supplemented by the inversions and SVD analysis, the resolution studies guided by the summary of heat maps provide an integrated insight for the resolution characters of LOTEM horizontal

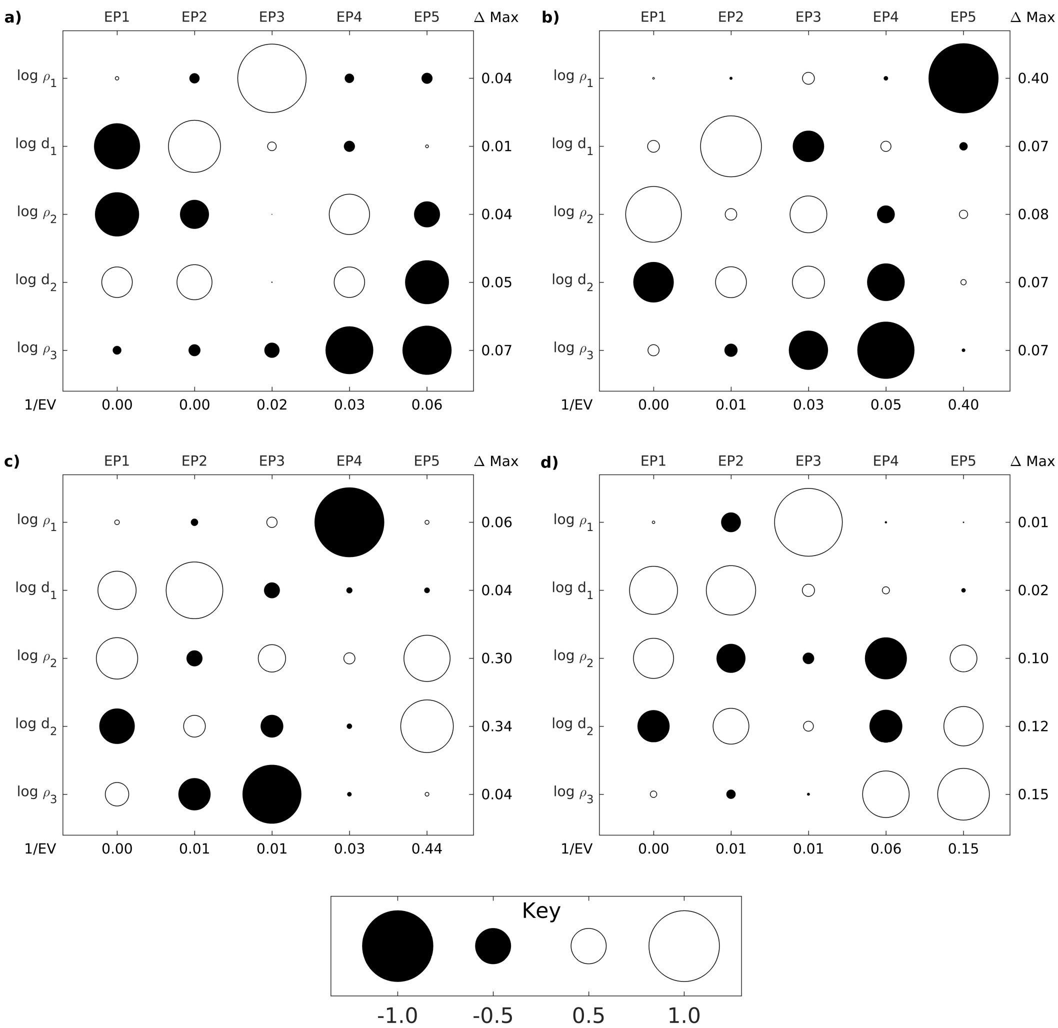

Figure 4.13: SVD analyses for the Marquardt inversion models displayed in Figure4.11.The results are correspond to the four models highlighted in Figure 4.10. (a) Model-1; (b) Model-2; (c) Model-3; (d) Model-4.

electric fields. In addition, one may notice that the ellipses for the very shallow part in Figure 4.10 are not continuous in the roundness. The reason is the equivalence domain for these models are too small. Thus the effects of 2% Gaussian noise appear. Moreover, the summary of heat maps for other offsets (e.g., 1000 and 2000 m) and Gaussian noise (1%) are attached in Figure A.7 for supplementary. With the demand for reducing the computation load, the tested parameters in each heat map are no longer logarithmically equally spaced. The linear spacing is utilized instead, while the conductor resistivity varies from 1 to 25 $\Omega \cdot m$, and the thickness varies from 1/10 to 3 times of the true value. Because both the total tested region and the step size for parameter perturbations are reduced, the number of equivalent models increase. The plotting of the ellipses uses equation 4.1.

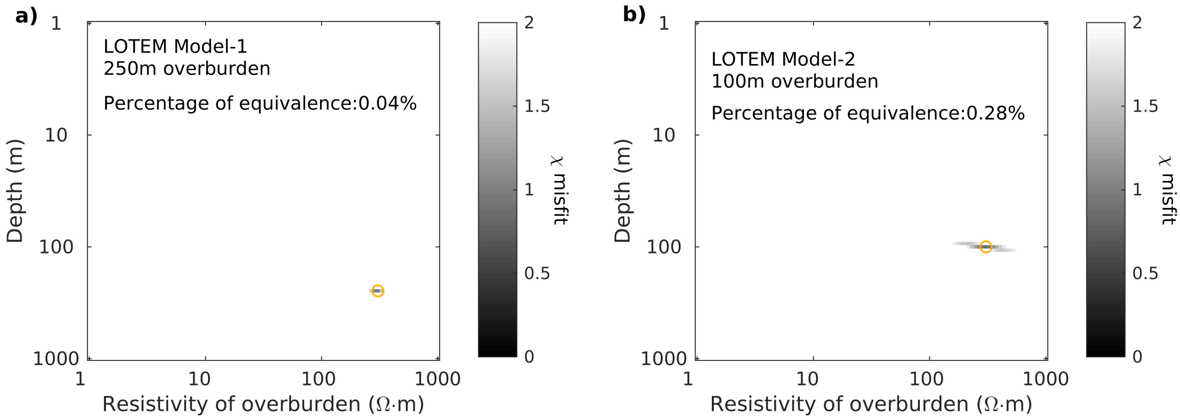

Figure 4.14: modeling studies investigating the resolution of LOTEM Ex to the resistivity and thickness of the overburden. The results are correspond to the (a) Model-1 and (b) Model-2 highlighted in Figure 4.10.

4.2.4 Modeling studies for Semi-airborne EM in frequency-domain

Same as the case for step-on LOTEM electric field, the DOI is one important aspect of the semi-airborne resolution characteristic. But different from the step-on responses in LOTEM, the noise level plays an essential role in the semi-airborne data. According to Smirnova et al. (2019), the noise level is frequency-dependent, and it is defined according to the amplitude. The error estimates from the data processing show a noise level of 20% of the amplitude at lower frequencies (10 Hz), and decrease to 1% at higher frequencies (1000 Hz) (Smirnova et al., 2019). This noise level should be considered when evaluating if the anomalous fields can be effectively observed in the modeling studies. Smirnova et al. (2019) discussed the DOI problem of semi-airborne data by presenting the 3D modeling tests. Since the detail modeling results can be found in the publication, only two major opinions from Smirnova et al. (2019) are introduced in this section. Firstly, with the increasing depth of the target conductor, the frequencies which can reflect the anomalous signals become narrow. Secondly, the response of the anomalous field becomes weaker as the anomaly is buried deeper. In the example of Smirnova et al. (2019), the amplitude of the anomalous field is above the noise threshold (approximately 0.1nT) when the conductor is at a depth of 911 m. Therefore, it can be expected that one can detect a sufficiently large conductor at a depth of approximately 900 m by using offsets of 2 to 3km.

Similarly, the resolution capability of semi-airborne data to the parameters of the target conductor is investigated. For guiding the consequent modeling studies on the particular models, the summary for heat maps is firstly performed for the semi-airborne configuration with 1500 m offset. According to the instruction and real data example from

Smirnova et al. (2019), an average error and noise estimations of 5% is utilized — 5% Gaussian noise is added in the semi-airborne synthetic data. Figure 4.15 presents the summary of heat maps. The 1D conductors with buried depth smaller than 150 m are not considered here because of the effects of thin overburden discussed in the last section, as well as the possible sign reversal problems (Figure 4.1d). As evident in the figure, the variation of the resolution of semi-airborne data is similar to that of LOTEM. The resolution decrease with the increasing of the target buried depth and the reduction of the layer thickness. However, compared to the LOTEM case, the resolutions of semi-airborne are reduced in general. Same as before, four particular 1D models are analyzed in detail. The model, including the best-resolved conductor, is selected as Model-1. The conductor thickness is 200 m, and the buried depth is 150 m. Certainly, the inversion results are perfect (Figure 4.16a), and the good resolution for this conductor is confirmed by the SVD analysis (Figure 4.18a). The thickness of the conductor is reduced to

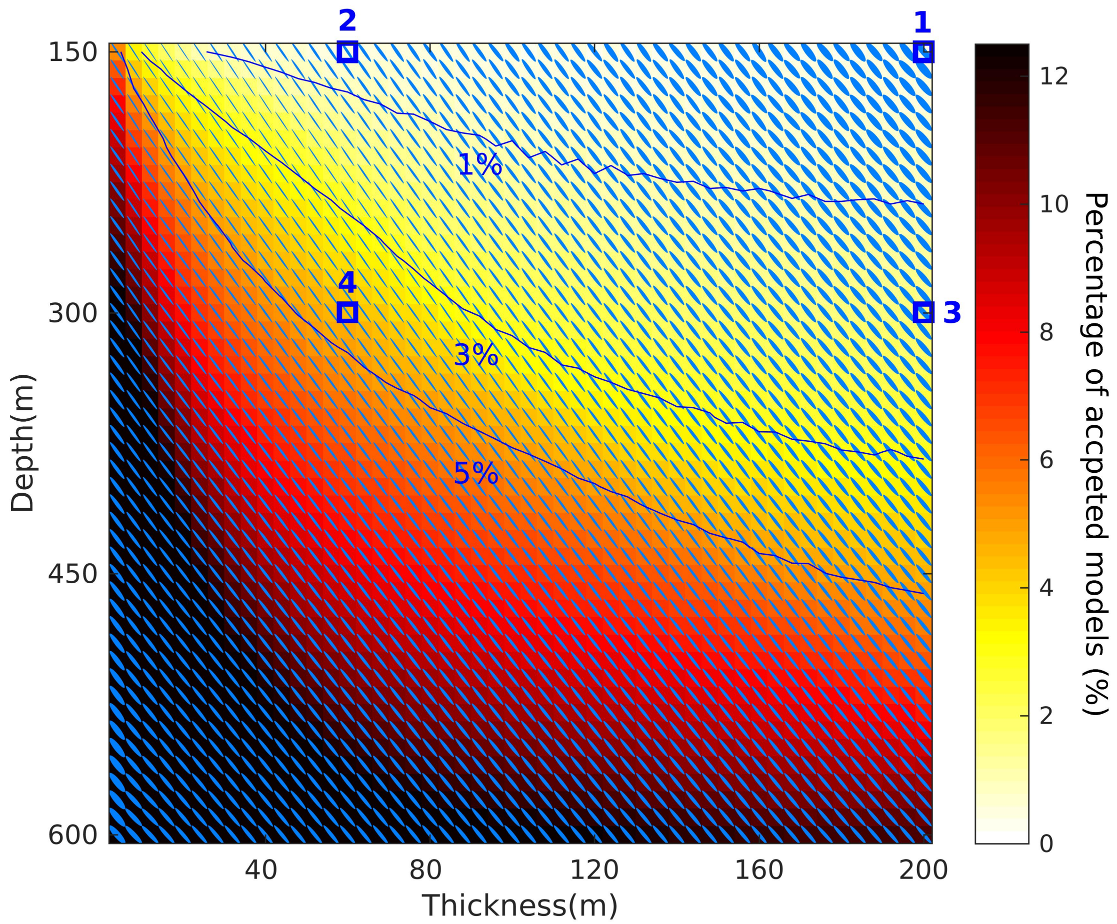

Figure 4.15: Summary of resolution studies for Semi-airborne Bz component. The offset is 1500 m. 5% Gaussian noise is added in the synthetic data. The resolution of semi-airborne data to the four particularly highlighted 1D models are further analysed.

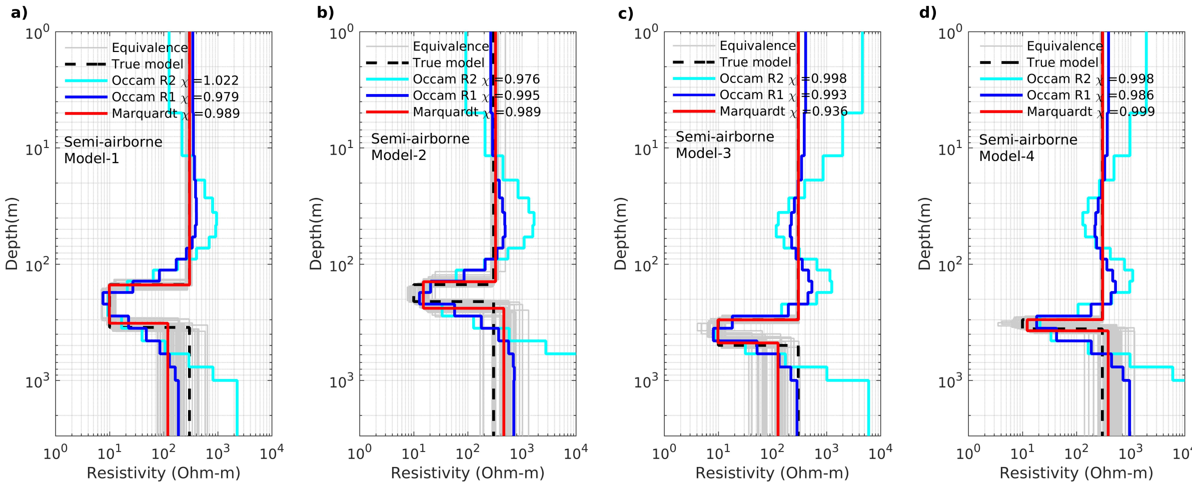

Figure 4.16: 1D inversion results of semi-airborne synthetic data. The results are correspond to the four models highlighted in Figure 4.15. (a) Model-1; (b) Model-2; (c) Model-3; (d) Model-4.

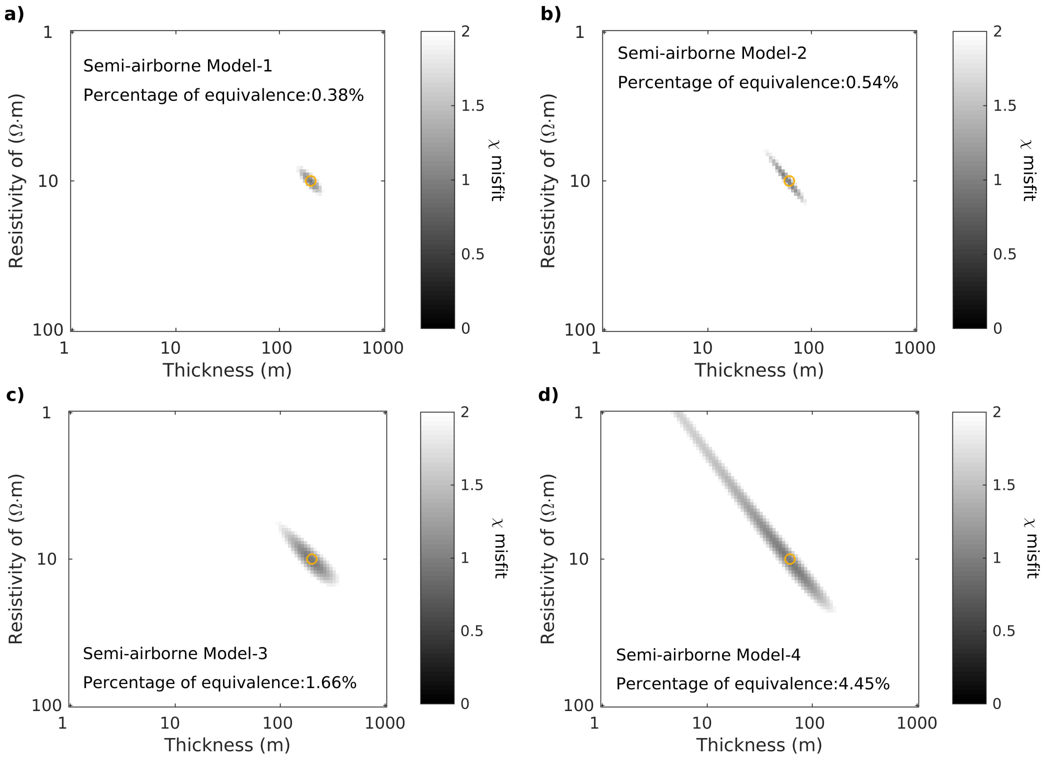

Figure 4.17: modeling studies investigating the resolution of semi-airborne data to the resistivity and thickness of conductive layers. The results are correspond to the four models highlighted in Figure 4.15. (a) Model-1; (b) Model-2; (c) Model-3; (d) Model-4.

60 m for the nest test (Model-2). In the inversion results of Model-2 (Figure 4.16]b), the resistivity of equivalence show larger deviations from the true value than the case for Model-1. Particular heat map for Model-2 (Figure 4.17b) indicate larger equivalence

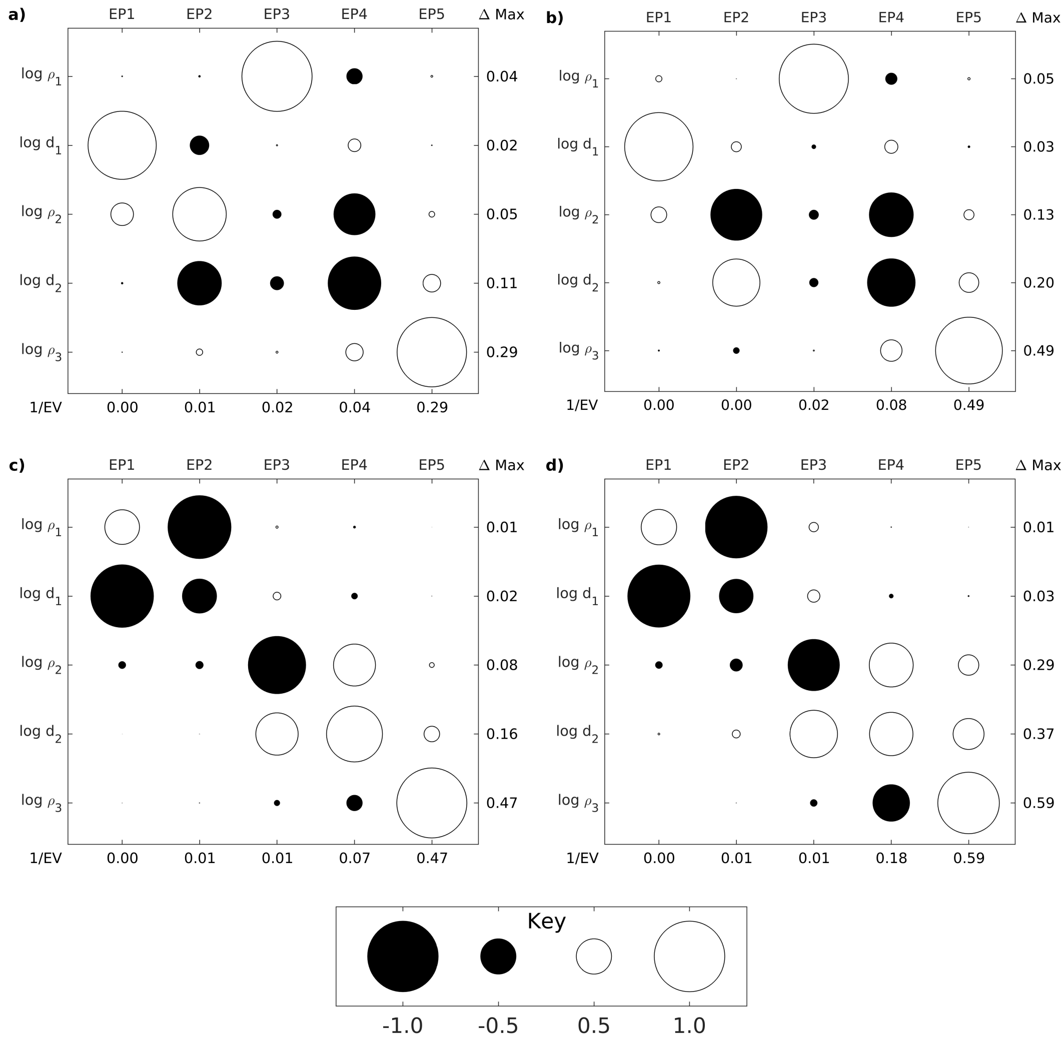

Figure 4.18: SVD analyses for the Marquardt inversion models displayed in Figure4.16.The results are correspond to the four models highlighted in Figure 4.15. (a) Model-1; (b) Model-2; (c) Model-3; (d) Model-4.

domain. The resistivity-thickness ratio also constrains the equivalences. The valuable point is, compared to a similar study for LOTEM (Figure 4.12c), the equivalence domain is significantly shorter. This character could help reduce the equivalence domain in joint inversion. The V-matrix in the eigenvalue analysis of Marquardt inversion for Model-2 (Figure 4.18b) is quite similar to that of Model-1, but the values of ΔMax increase obviously. Model-3 has the same layer thickness as Model-1 but a larger buried depth of 300 m. Its individual heat map (Figure 4.17c) shows not only the larger equivalence domain but also a wider distribution than those of Model-1 and 2. This wide low misfit region means the resolution of semi-airborne data to the resistivity-thickness ratio decreases either. The more irregularly distributed equivalence supports this point in the inversion results (Figure 4.16 c). Correspondingly, the V-matrix of the Marquardt inversion result of Model-3 has quite a different pattern form the Model-1 and 2. It is worthy to note that this pattern of resolution reducing is different from that of LOTEM. In the LOTEM case, the constraint from the resistivity-thickness ratio is still strong down to 650 m depth (Figure 4.12d). At last, the conductor in Model-4 includes both the reduced thickness and increased buried depth. The inversions still recover the conductor clearly, but the resolution for its parameters are already poor. The specific heat map of Model-4 (Figure 4.17]d) displays a significantly large equivalence domain, and the SVD analysis also suggests the large error bounds for the model parameters (Figure 4.18]d).

To summarise, the semi-airborne has similar resolution characters to the LOTEM generally, but the overall resolution for the model parameters is reduced. In other words, the equivalence domain of semi-airborne data is usually larger than a matched LOTEM case. The key factor that leads to this reduced resolution is the relatively large error estimation. If the error or noise in the data can be reduced further, the resolution will improve significantly (Figure A.8). On the other hand, the observed magnetic field of semi-airborne shows some valuable different resolution capabilities from the LOTEM electric field. The most important, for a similar conductor, LOTEM and semi-airborne data have differences in the equivalence domains, which are beneficial in the joint inversions.

4.2.5 Summary of resolution characteristics of three EM methods

According to the resolution studies in the last sections, the joint inversion strategy can be developed for the HEM, LOTEM and semi-airborne. The resolution characteristics of these three EM methods are approximately sketched in Figure 4.19 according to summaries of heat maps for each individual method (Figure 4.4, 4.10 and 4.15). In this sketch, the horizontal axis denotes the variation of target conductor thickness, and the vertical axis denotes its buried depth. The thickness increase in the right direction, while depth increases downward. Generally, the three EM methods share the same basic laws. If the target conductor is too thin or is buried too deep, no method has a good resolution for it. Surely, HEM can resolve thinner targets in shallow layers better than the LOTEM and semi-airborne. And the LOTEM can usually detect the deepest target. On the other hand, the diverse resolution of these three EM methods provides a large space for the joint inversion. Firstly, HEM has a high resolution for the shallow layers. The joint inversion of HEM and LOTEM or semi-airborne can help the other two methods to constrain the shallow structures better and result in better resolution for the deep regions. If the conductor is too thick for the HEM, the LOTEM or semi-airborne can determine the lower boundary of the conductor in a joint inversion. Next, for a conductor locate out of the DOI of HEM, the joint inversion of semi-airborne and LOTEM will be applied. Known form the modeling studies in the last two sections, both LOTEM and semi-airborne can perfectly resolve a conductor with thickness 200 m and buried depth around 200 m. Therefore, it can be deduced that there is a group of the conductors having the proper size and buried depth can be resolved perfectly by both LOTEM and semi-airborne. If the buried depth of the conductor further increases, the resolution for it is naturally decreased. Both LOTEM and semi-airborne can not perfectly resolve the parameters of the target individually. But because the equivalence domain is different between two datasets, the joint inversion can effetely reduce the possible equivalence and result in the better-resolved parameters. However, for an even deeper conductor, both EM methods have large equivalence domains. In this case, the joint inversion has the possibility to reduce the equivalence domain further, but can no longer lead to the ideal resolution. At last, the target drops out of the DOI of semi-airborne and can be reluctantly detected by LOTEM only. In general, the joint inversion takes more data into account. The resolution is never expected to be poorer than any considered individual dataset. Additionally, sometimes the joint inversion can reveal the true substructures better than each single method inversion. These possible situations are marked as B̈etter Jointïn Figure 4.19. Note that this sketch is just an approximate evaluation, even though it is supported by the summaries of heat maps.

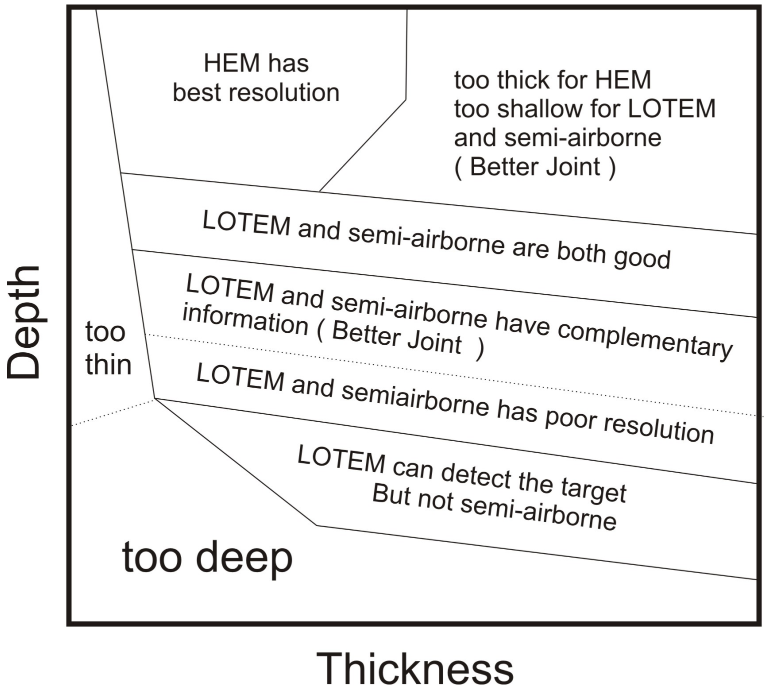

Figure 4.19: Summary of resolution characteristics for HEM, LOTEM and semi-airborne EM.

4.3 Application of 1D joint inversion on synthetic data

4.3.1 1D joint inversion of HEM and LOTEM (or semi-airborne) data

The 1D joint inversion is firstly applied to the synthetic data of HEM and LOTEM. A 1D resistivity model contains two conductive layers that are considered in this section. As depicted as a black dash in Figure 4.20a, the first conductive layer has a thickness of 15 m and is buried in the top 30 m. The second conductive layer is buried much deeper. Its upper boundary is 650 m away from the earth's surface. The resistivity of conductors and the background are still kept as 10 and 300 $\Omega \cdot m$, respectively. The 1D inversion on HEM data can resolve the first layer perfectly, but can not detect the second layer (Figure 4.20a). A three-layered staring model is used in the Marquardt inversion, and the data is fitted ideally. Figure 4.20b shows the SVD analysis for the Marquardt inversion result, while the data fitting is attached in Figure A.9. The SVD analysis result and the ideal data fitting demonstrate that the HEM data has no resolution to the second conductive layer totally.

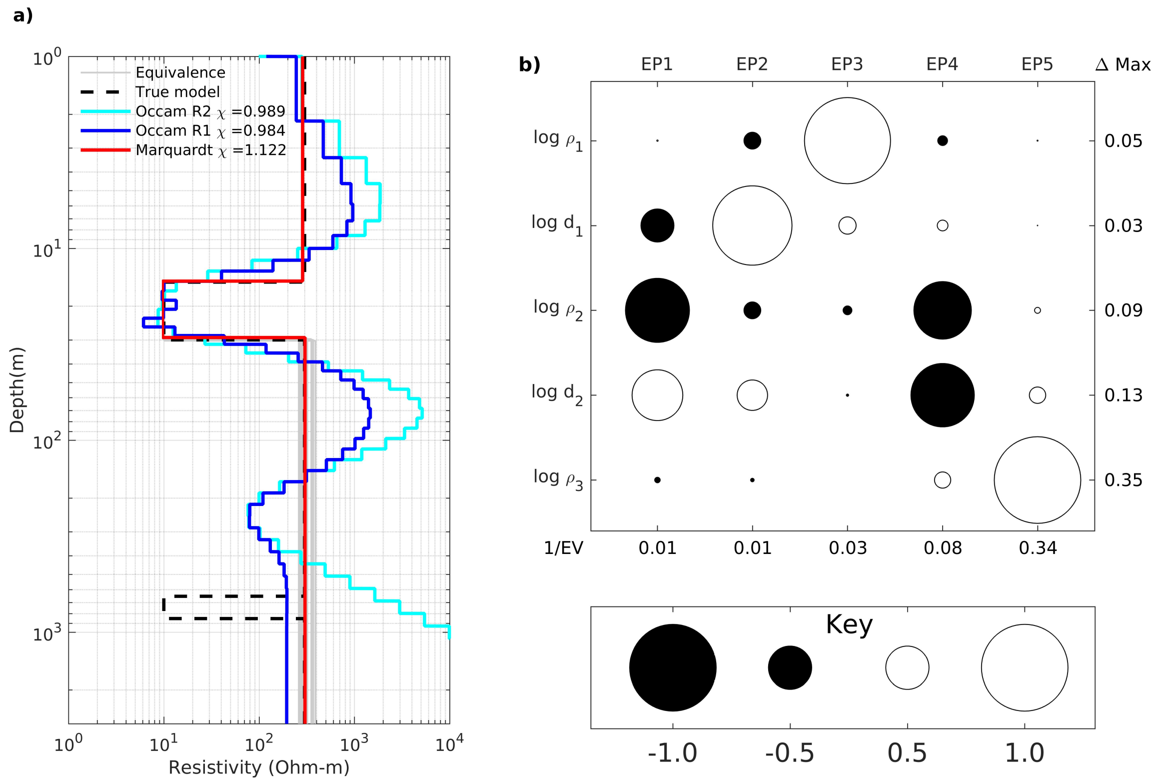

Figure 4.20: (a) Inversion result of HEM synthetic data and (b) the SVD analysis for the Marquardt inversion result.

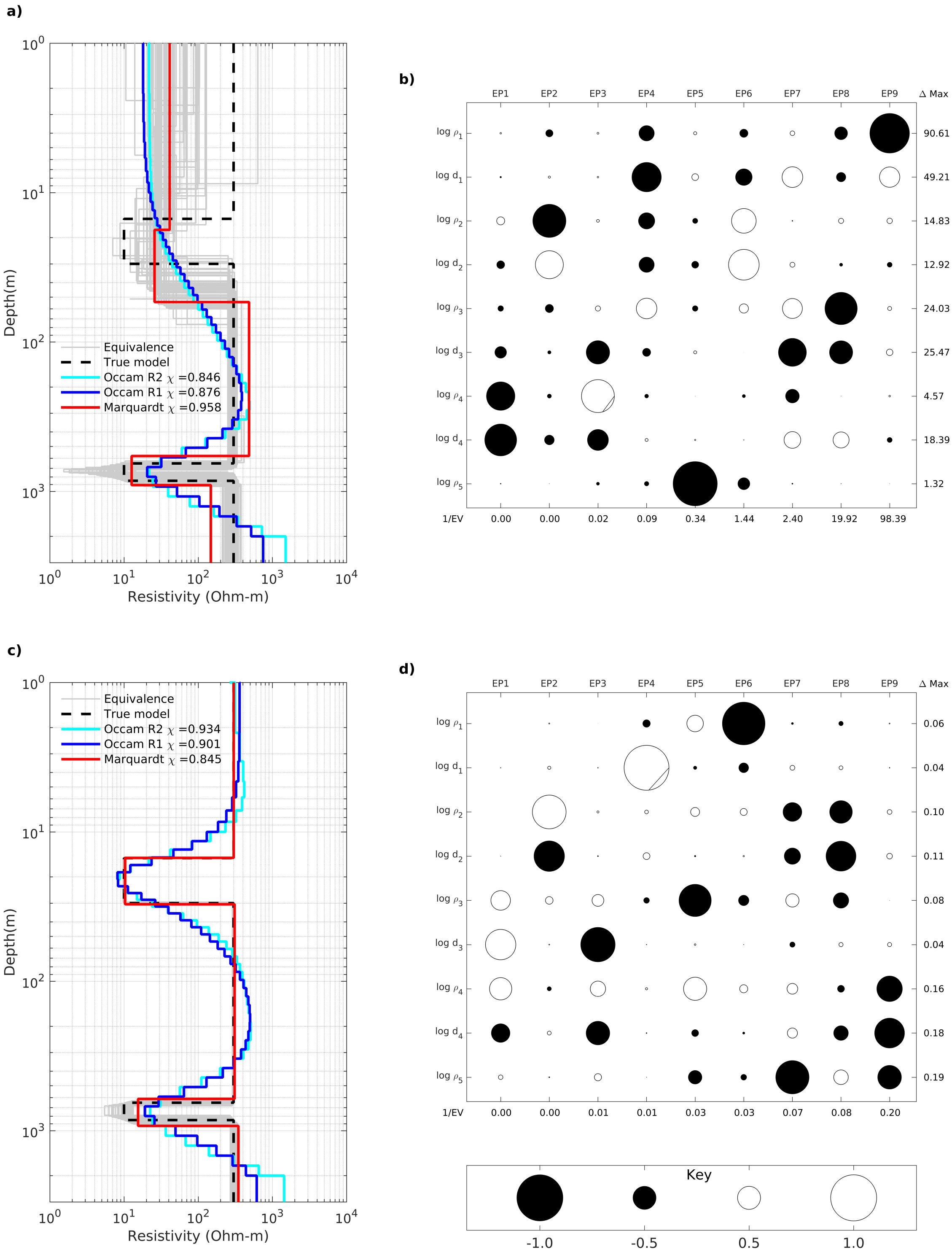

Figure 4.21: Inversion result of LOTEM single method (a) and the joint inversion results with HEM data (c). The SVD analysis for the each Marquardt inversion result are displayed in (b) and (d), respectively. The offset for LOTEM measurement is 3000 m.

Contrarily, the LOTEM data discover the second layer, but failed in resolving the first layer (Figure 4.21a), even though the data misfit is ideal. The parameters of the second layer are also not well determined. The resistivity and thickness values are significantly distinct among the equivalent models. The SVD analysis also suggests poor resolutions for all the model parameters (Figure 4.21b). No ΔMax is smaller than 1.0, indicating no error bound can be reliably determined. However, after two datasets are inverted jointly, both the two conductors are ideally described (Figure 4.21c). Not only the first layer is entirely revealed by HEM data, but the parameters of the second conductor in the deep region are also resolved much better. All the error estimations for the model parameters presented by the SVD analysis (Figure 4.21d) are much smaller than 1.0. The shallow layers are constrained by HEM data, leading to a smaller equivalence domain, and resulting in a better resolution of the second layer. The data fitting of these inversions are attached in the appendix (Figure A.9). Note that 2% Gaussian noise is added in the synthetic data for both HEM and LOTEM. Moreover, because the advantage shown by the 1D joint inversion of HEM and semi-airborne data are similar, the part of synthetic inversion modeling studies are also put in the appendix (Figure A.11 and A.12).

4.3.2 1D Joint inversion of semi-airborne and LOTEM data

Subsequently, the 1D joint inversion is applied to the synthetic semi-airborne and LOTEM data. The true resistivity distribution is denoted by the black dash in Figure 4.22a. As can be seen, the 1D resistivity model considered in this time also has two conductive layers. The first layer is 200 m deep, and the second layer is more than 1000 m deep. 5% Gaussian noise is added in the semi-airborne synthetic data. A typical offset 1500 m is used for modeling the semi-airborne data. The semi-airborne single method inversion resolves the first conductor well, but reveal a conductive basement rather than discover the second layer. The corresponding SVD analysis (Figure 4.23) indicates the poor resolutions for all the model parameters locate deeper than depth 300 m. The LOTEM data is calculated

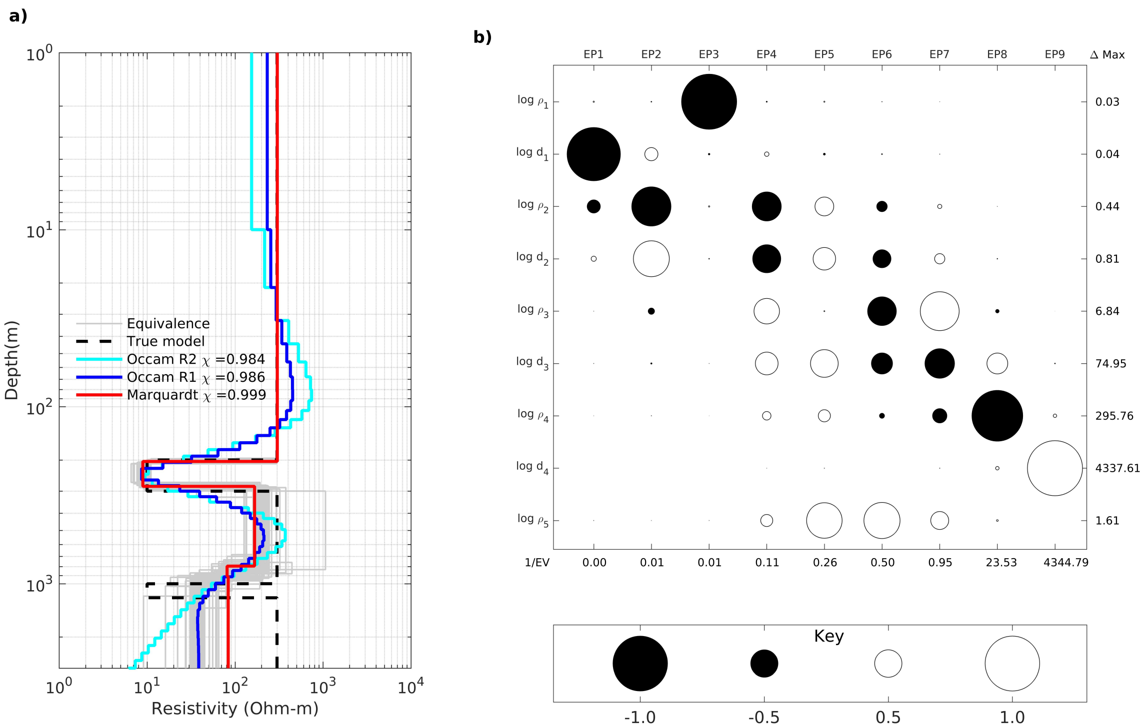

Figure 4.22: (a) Inversion result of semi-airborne synthetic data and (b) the SVD analysis for the Marquardt inversion result. The offset is 1500 m.

by using an offset of 3000 m and contain 2% Gaussian noise. The larger DOI decides that the LOTEM data can reveal both the conductors (Figure 4.23a). The joint inversion results (Figure 4.23c) do not show any improvement over the LOTEM single method inversion results. Nevertheless, a comparison between the SVD analyses (Figure 4.23b and d) suggests that the error estimation (ΔMax) for the model parameters are reduced after the semi-airborne data are taken into account in the inversion. The data fitting for these 1D inversions are attached in Figure A.14.

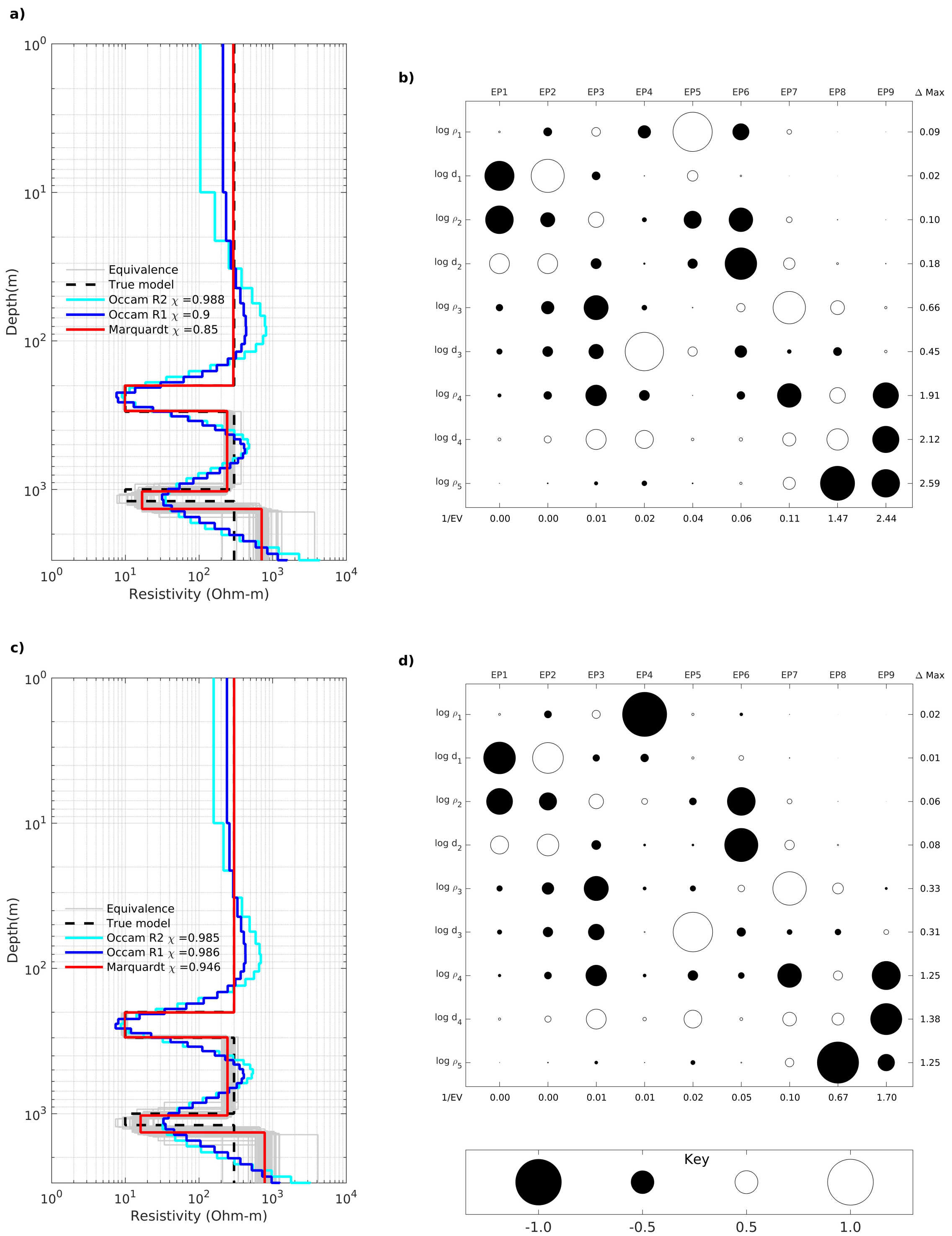

Figure 4.23: Inversion result of LOTEM single method (a) and the joint inversion results with semi-airborne data (c). The SVD analysis for the each Marquardt inversion result are displayed in (b) and (d), respectively. The offset for LOTEM measurement is 3000 m, and 1500 m for semi-airborne.

4.3.3 1D Joint inversion of the data from three EM methods

The final step for the 1D joint inversions on synthetic data is inverting the datasets form all the three EM methods simultaneously. In Figure 4.24, the complex 1D resistivity model depicted by a black dash is a simulation for the Marquardt inversion result of field data (Figure 4.31d). The real offsets in the field measurement are also utilized in this synthetic modeling. LOTEM has offset as 1208 m, and semi-airborne has offset as 1209 m. The synthetic data of this 1D model are firstly inverted for HEM, LOTEM and semi-

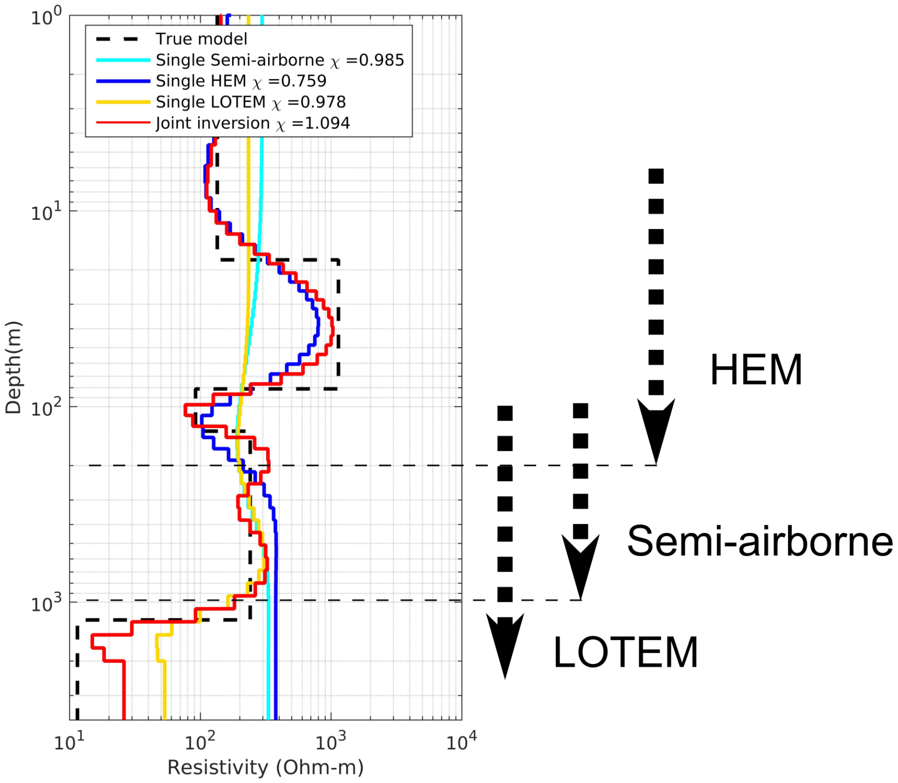

Figure 4.24: HEM, LOTEM and Semi-airborne single method inversion results and three methods joint inversion results for synthetic data. The inversion results are calculated by Occam algorithm with roughness 1 (Constable et al., 1987).

airborne EM methods individually. A dark blue solid line indicates the HEM inversion result, it reveals the structure above 100 m depth well. The solid yellow line shows the LOTEM inversion result, it recovers the deepest conductive body but not the structure in shallow layers. Semi-airborne inversion result can reveal the substructure between 100 m to 1000 m. The joint inversion result is noted by the solid red line, finely resolving the complex 1D resistivity model.

4.4 Weighting schemes for 1D joint inversion

As shown in the synthetic studies in the last section, the joint inversion combines the advantages of different EM methods. Therefore it achieves a higher resolution than inverting the data of each EM method individually. However, joint inversion can encounter some specific problems because of the diverse characteristics of different EM methods. The common essence of these problems is the different weights of the considered EM methods in the Jacobian matrix (see equation 3.7). They lead to diverse influences on the model update and, at last, the final inversion results. In other words, the final result of joint inversion maybe not equally influenced by the data come from different methods, which is not satisfactory in some cases. For example, Commer and Newman (2009) found that the number of data points of each dataset relates to calculated gradients in a joint 3D non-linear conjugate gradient (NLCG) inversion of marine MT and CSEM data. The more numerous CSEM data cause the influence of the MT data on the imaging outcome to become insignificant. In order to achieve a balanced data influence, dataset with the smaller amount of data points is then up-weighted by applying a factor $w = \sqrt{N_1/N_2}$, where N_1 and N_2 denote the number of data points for 2 different datasets while $N_1 > N_2$. Commer and Newman (2009) also mentioned that such a method is likely to achieve a balanced data influence only when both data methods are characterized by similar intrinsic sensitivities. Meqbel and Ritter (2015) designed another weighting scheme for the 3D inversion using the NLCG approach. They found the ratio between the norms of total and individual data gradients gives the contribution of each individual dataset for the total gradients. Because the data gradient vectors are different, the contribution of each individual dataset for the total gradients diverse, then influence the final inversion results unequally. They applied a balance based on the data gradients and improved the 3D joint inversion result of MT and CSEM. For the inversions adopting the linear least square technique, the weighting schemes are usually applied to the Jacobian matrix. Candansayar and Tezkan (2008) multiplied a diagonal matrix as weighting factors on the original Jacobian matrix (E.g. $\mathbf{W_m}$ in equation 3.8). If the effect of some data on a given parameter is needed to be changed, the related diagonal element of the matrix is modified to a value between 0 and 1. The approach is essentially a down-weighting scheme. Kalscheuer et al. (2013) further tested the weighting scheme devised according to the reciprocal of the second norms of the Jacobian matrices of each dataset. Sudha et al. (2014) designed a weighting scheme based on the diverse depth of investigation (DOI) of each EM method for the joint inversion of RMT, HEM and TEM.

As evident in the last section, the three EM methods considered in this thesis have significantly diverse DOI and sensitivity characteristics. Here it is investigated that if the application of weighting schemes could further improve the resolution of joint inversion. For answering this question, the effects of applying a DOI weighting scheme (Sudha et al., 2014) in 1D joint inversion are analyzed firstly. Note the 1D inversions applied in this thesis use only Occam and Marquardt algorithms. The weighting is realized by the product of the Jacobian and weighting matrix. Following Sudha et al. (2014), the importance and SVD eigenvalue analysis is employed to evaluate the performance of the DOI weighting scheme. Afterward, the newly developed weighting scheme is tested in the 1D joint inversion of semi-airborne and LOTEM data. It will be discussed, consequently, if the new weighting scheme is well-performing or delivers valuable results.

4.4.1 Importance of the equivalence

As stated, the importance (equation 3.22) and SVD eigenvalue analysis (Section 3.2.2) are employed by Sudha et al. (2014) to evaluate the performance of DOI weighting scheme. However, in the practice of analyzing the weighted 1D joint inversion results, the Importance values are found to be distinctly different among equivalence in many cases. In order to understand why equivalent models provide significantly diverse resolution indicators, a small test is conducted. The black dash (overlapped by the solid blue line) in Figure 4.25a shows a 1D resistivity model. Two 10 $\Omega \cdot m$ conductive layers are embedded in the 300 $\Omega \cdot m$ background. A 100 m thick resistive layer is surrounded by the two conductive layers, which is challenging to be revealed by the EM methods. The detailed model parameters can be found in the third row of the Table 3. A LOTEM broadside configuration with offset 2000 m is employed for this test. For calculating the Importance of the model parameters, 1 % Gaussian noise is added to the synthetic LOTEM data calculated for the three-layer case. The data are inverted by the Marquardt algorithm. Naturally, the inversion converged in one iteration with no change for the model parameters. The resulted importance values are displayed in the fifth row of the Table 3. One of its equivalent model (red line in Figure 4.25a) is generated via Marquardt inversion by using a new starting model. In the new starting model, the resistivity of the layer lies between two conductive zones are changed to 50 $\Omega \cdot m$ while the other parameters are kept the same as the true model (seventh row of the Table 3). Synthetic data of the true model has inverted again by inputting this new stating model, and the inversion converged in one iteration too. The eighth row of Table 3, as well as the red line in Figure 4.25a, display the inversion result. Figure 4.25b and c show the data fitting and the residuals for these two inversion results. Even though the residuals show slight differences, the data fitting has to be regarded as perfect for both. Thus the two inversion results are

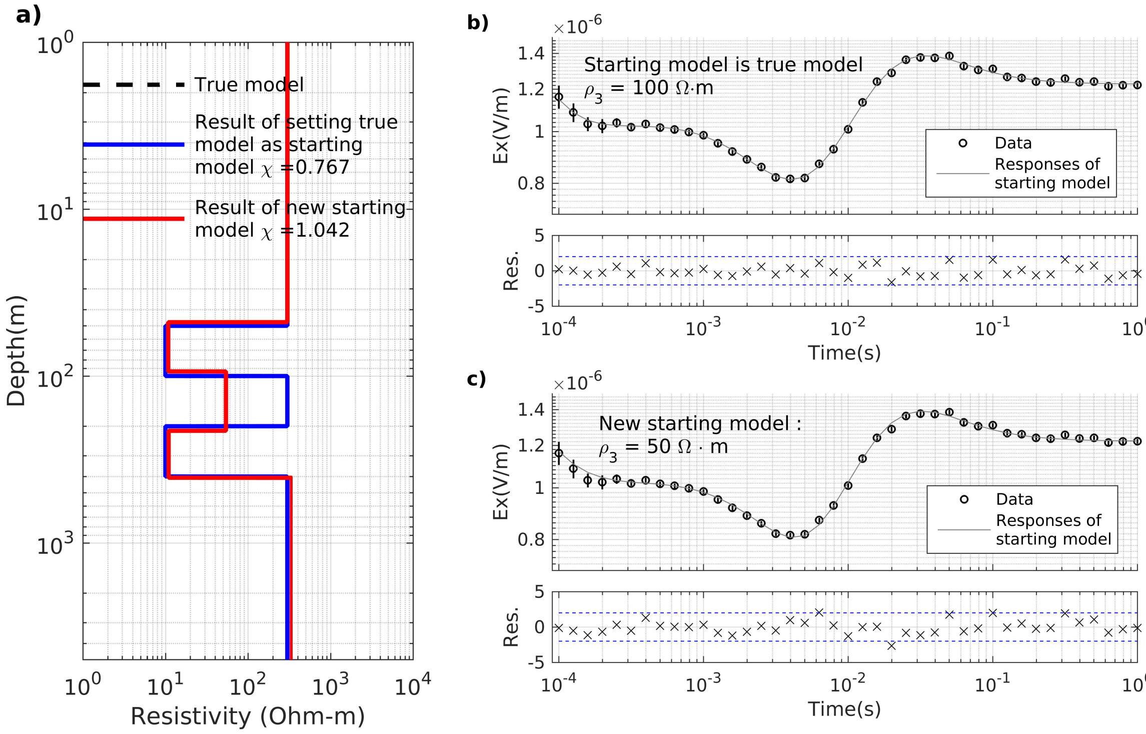

Figure 4.25: Equivalent models which having different Importance values. (a) the equivalent models generated by using different starting models in Marquardt inversion ; (b) and (c) the data fitting for the two equivalent models, respectively.

equivalent. However, the responses of the two starting models are not totally the same, the slight deviations lead to a different Jacobian matrix and thus result in the distinct Importance values which are displayed in the fifth and last rows of Table 3 respectively. Known for comparison, some of the Importance values jump from 0.2 or 0.3 to around 0.7 or 0.8, indicating significantly different resolution for the model parameters. Since the SVD eigenparameter analysis bases also on the Jacobian matrix, it has the same problem. Considering these terms are used to evaluate the resolution of one inversion approach in this section rather than one individual inversion result, it is more logical that more the possible analyses of the resolution are taken into account. An example displays the importance and the ΔMax for a suite of equivalence is provided in the next section.

4.4.2 Weighting scheme based on depth of investigation

The analysis for the weighting scheme effects is conducted based on the DOI weighting because HEM and LOTEM considered in this thesis have dramatically different DOI. Another reason is the DOI weighting scheme is the only one applied in 1D joint inversion in the literature mentioned above. The DOI weighting scheme proposed by Sudha et al.

Table 3: Importance for the equivalent models displayed in Figure 4.25.

Parameters	ρ_1	ρ_2	ρ_3	ρ_4	ρ_5	d_1	d_2	d_3	d_4
Starting model $\rho_3 = 300\Omega \cdot m$									
Starting	300	10	300	10	300	50	50	100	200
Result	300.0	10.0	300.0	10.0	299.9	50.0	50.0	100.0	200.0
IMP	0.031	0.771	0.176	0.736	0.207	0.398	0.508	0.806	0.749
Starting model $\rho_3 = 50\Omega \cdot m$									
Starting	300	10	50	10	300	50	50	100	200
Result	300.9	10.8	54.1	10.9	340.9	47.6	46.6	118.9	194.2
IMP	0.040	0.775	0.358	0.850	0.699	0.782	0.651	0.895	0.721

(2014) consists of two parts. Firstly, The data number balance introduced by Commer and Newman (2009) is applied for the joint inversion of HEM, RMT and TEM. Because datasets of three EM methods are included, the up-weighting factor for data number balance is defined as $\sqrt{(\sum N_k)/N_k}$ where k is the index of each individual dataset. The second part is the down-weightings designed according to the diverse DOI of considered EM methods. The minimum and maximum DOI of each EM method are chosen following Spies (1989). For an individual EM method, the model parameters lay in its DOI will be weighted as 1.0. Otherwise, it will be down-weighted (approximately 50-75%).

In this section, the same DOI weighting scheme is applied to the 1D joint inversion of HEM and LOTEM data. HEM datasets have 10 data points, while LOTEM transient includes 41 data. Therefore Jacobian matrix of HEM will be up-weighted five times by the data number balance. As evident by the modeling studies earlier, the largest DOI of the HEM survey employed in this thesis is around 150 to 200 m. Thus the Jacobian matrix of HEM will be down-weighted for the parameters locate at a depth larger than 200 m. From the perspective of LOTEM, the resolution for the resistivity structures buried in the top 100 m is usually unsatisfactory. The Jacobian matrix of LOTEM will be down-weighted for the model parameters located in the top 100 m. Specifically, the down-weighting factors are 30% for HEM and 50% for LOTEM in this example. The synthetic examples of non-weighted and weighted 1D joint inversion of HEM and LOTEM data are presented in Figure 4.26a and d. LOTEM data are simulated by using broadside configuration with offset 2000 m. 1% Gaussian noise is added for both the LOTEM and HEM synthetic data.

Figure 4.26b displays the model parameter importance for the equivalence shown in (a). The grey circles denote the importance for normal equivalent models, while the purple signs "+" mark the importance values obtained by inputting the true model as the starting model. Note that the importance marked by signs "+" corresponds not to Marquardt inversion result denoted by solid red line but to the true model denoted as a black dash in (a). The Marquardt inversion result in a solid red line belongs to normal equivalence. The inversion results obtained by using true models as the starting model is specified because the true model is the most special one among the equivalent models. It is meaningful to see how the importance will behave when the true model is revealed. Similarly, the values of ΔMax calculated by SVD eigenparameter analysis are displayed in (c) for non-weighted joint inversion. The Importance and ΔMax for weighted joint inversion are presented in (e) and (f), respectively. For weighted joint inversion, resolution evaluations for normal equivalence are denoted as black circles while the results calculated by inputting true model as the starting model is denoted as an orange circle. The purple signs "+" from non-weighted joint inversion are also presented together for convenient comparison.

As discussed in the last section, the Importance and ΔMax can behave differently for different equivalent models. Displaying the Importance and ΔMax for a series of the equivalent model could provide a more general view for evaluating the performance of the weighted joint inversion scheme. In this case, not only the values but also the deviations of Importance and ΔMax could be used as the evaluation for the model parameter resolution. If the Importance and ΔMax of one model parameter vary significantly, the resolution for this parameter is not stable and therefore, can be regarded as poor. A typical example is the resistivity of the layer located in the middle of two conductive zones ($log\rho_3$). This general view provides by equivalence makes analysis results more stable and reliable. But this approach is still not perfect. The possible bias of sampling the equivalence may lead to misunderstanding. Moreover, it makes it more difficult to define the boundary between good and poor resolution. Anyway, this approach is useful in comparing the variation of Importance and ΔMax led by the weighting schemes.

It has to be admitted that the weighed joint inversion results in Figure 4.26b do not show advantages visually over the non-weighted inversion results in a. However, the comparison of Importance and ΔMax clearly suggests that the resolution of 1D joint inversion is significantly improved by the application of DOI weighting. In Figure 4.26e, most of the importance values calculated by using the true model as a starting model for weighted inversion (orange circles) are larger than the ones of non-weighted inversion (purple signs +). Regarding the ΔMax, the weighted ones are smaller than the non-weighted ones, indicating the smaller error bounds of model parameters are achieved by using DOI weighting. The comparison of the resolution evaluations provided by the other equivalence suggests the same conclusion — the DOI weighting improves the resolution of model parameters, especially for the shallow layers.

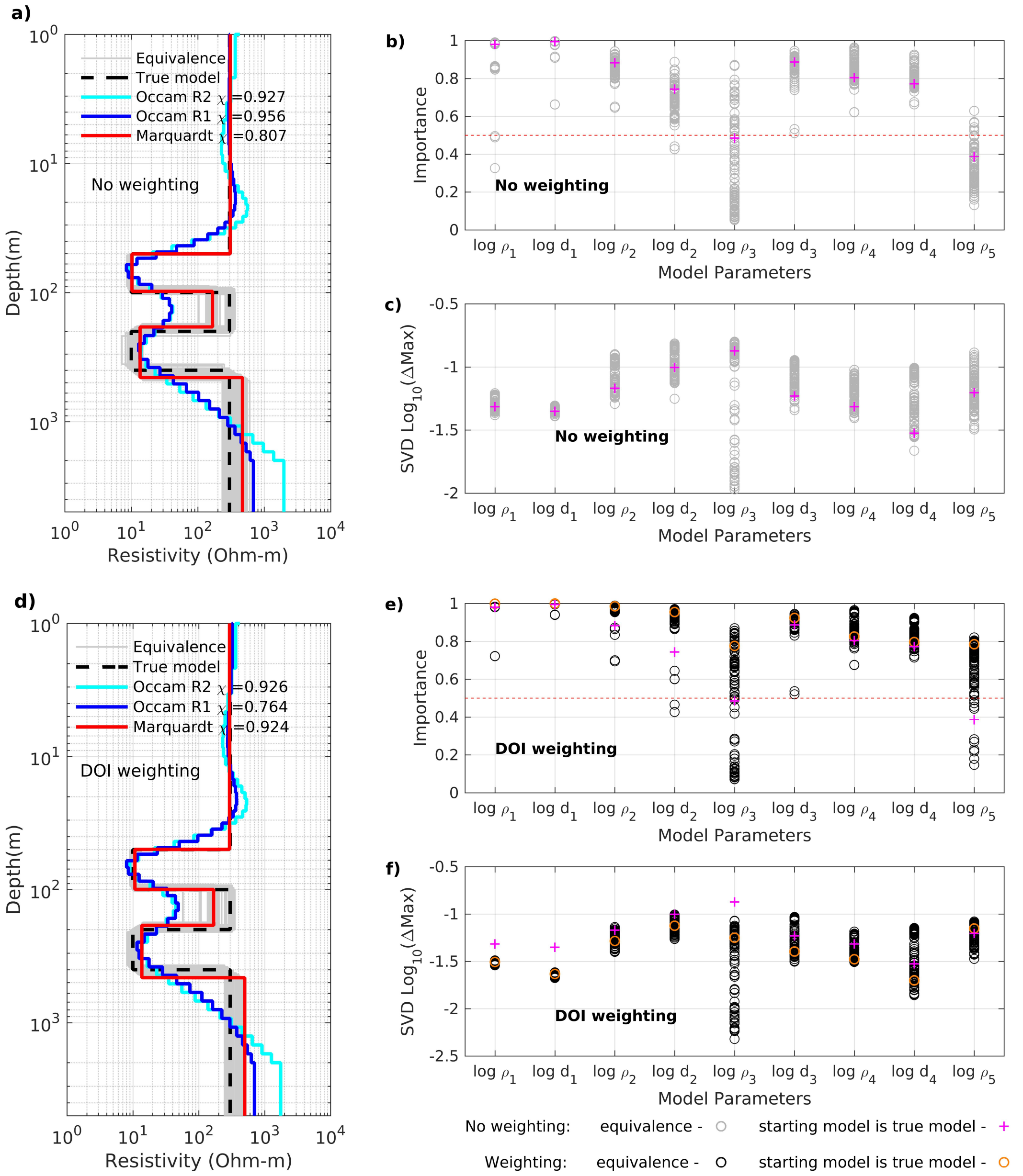

Figure 4.26: Comparison between the non-weighted and weighted 1D joint inversion of HEM and LOTEM synthetic data. (a) the non-weighted joint inversion results, (b) and (c) display the Importance and ΔMax for the non-weighted joint inversion, respectively; d) the DOI weighted joint inversion results, (e) and (f) display the Importance and ΔMax for the DOI weighted joint inversion, respectively.

The next question is how the DOI weighting scheme improves the Importance and ΔMax. As stated above, the DOI weighting is consists of two parts or three steps: data number balance, down-weighting of HEM for deep structures, and down-weighting of LOTEM for shallow layers. Subsequently, a modeling test is conducted to investigate which steps contribute to the improvements of Importance and ΔMax (Figure 4.27). The three steps of DOI weighting are added into the application one by one. For calculating the importance shown in Figure 4.27a, only the data number balance is applied in the joint inversion. Same as before, the Importance values of equivalence are displayed as black circles while the orange circles indicate the ones calculated by inputting the true model as the starting model. For comparison, the Importance values obtained via setting true model as starting model are also attached for the non-weighting (purple signs +) and full DOI weighting (light blue x) joint inversion. In other words, the purple, blue, and orange markers are consistent in all images for comparison. Known form Figure 4.27a, after the application of only data number balance, the Importance values of the true model already get very close to the ones obtained by full DOI weighting and far away from the non-weighted ones. This result indicates that the data number balance plays a major role in the improvements achieved by DOI weighting. Figure 4.27b shows the importance calculated by applying data number balance and HEM down-weighting. Compared to (a), no variation can be observed in (b), suggesting that the HEM down-weighting does not affect the Importance. At last, the LOTEM down-weighting is added into the weighted joint inversion (Figure 4.27c). The slight deviations of true model importance left by applying only data number balance are compensated. Moreover, the Importance values of equivalence are almost the same among these three plotting, indicating again that the contribution of data number balance dominates the improvements led by DOI weighting. It is important to note that this conclusion is a specific one for the current synthetic example. It will be demonstrated in the next section that the up-weighting realized by data number balance can generally improve the Importance and ΔMax, but the down-weighting based on DOI may play more roles in other cases. Actually, the down-weighting based on DOI introduced by Sudha et al. (2014) is also aiming at compensating the side effects led by the up-weighting of data number balance.

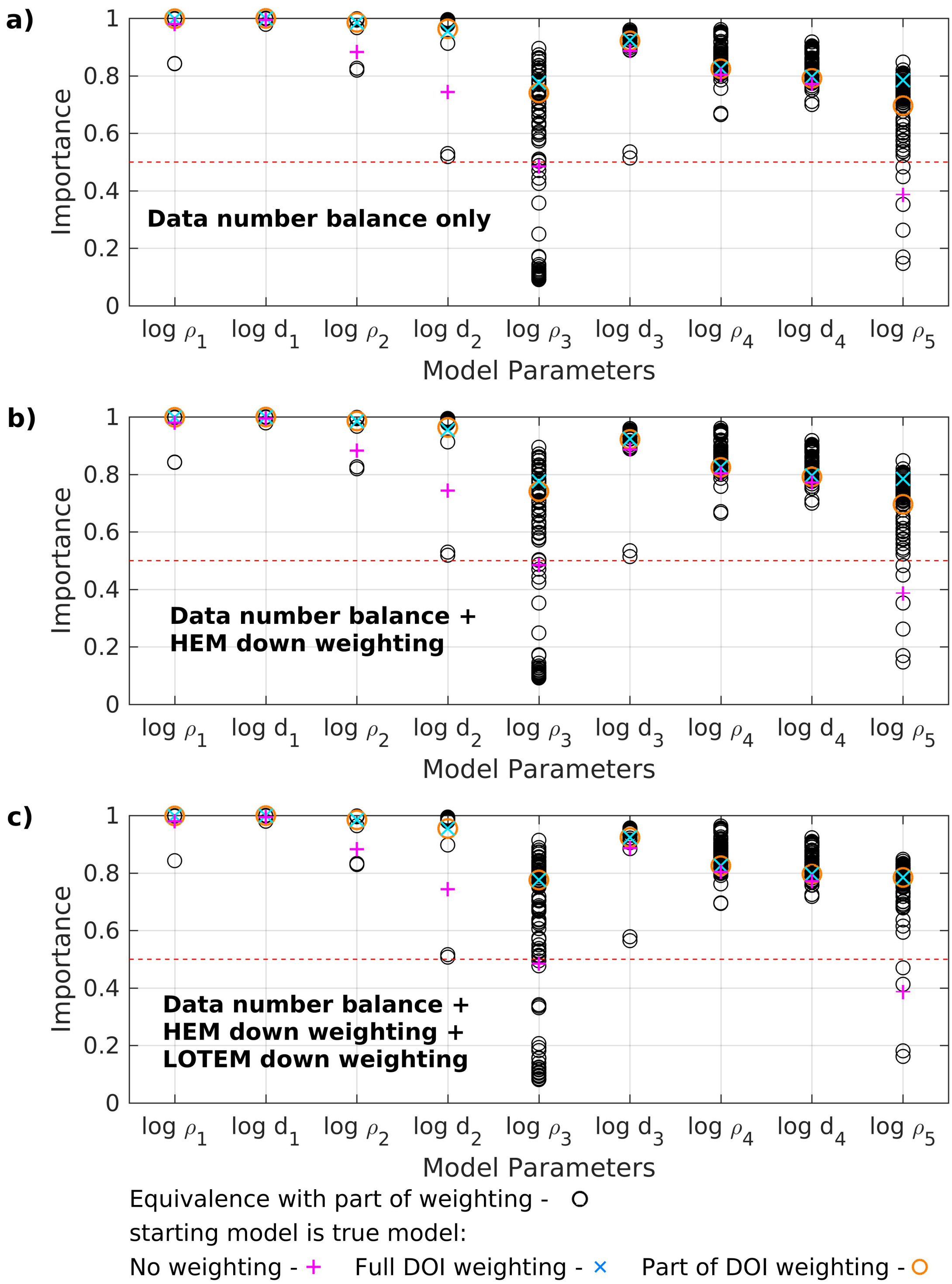

Figure 4.27: The Importance calculated by partly applying DOI weighted joint inversion on HEM and LOTEM synthetic data. (a) only data number balance is applied, (b) data number balance and HEM down-weighting are applied, (c) full DOI weighting is applied.

4.4.3 Relationship between weighting and Jacobian matrix

As found in the last section, the improvements of Importance and ΔMax achieved by DOI weighting are mainly contributed by the data number balance, which is an up-weighting scheme. In this section, it is discussed why the up-weighting can improve these resolution evaluations. As stated earlier, both the Importance and eigenvalue analysis are calculated according to the Jacobian matrix. The Importance is calculated according to V-matrix and the T-vector, which is decided by the eigenvalues. ΔMax is the rough error estimation of model parameters, which is the product of the V-matrix and the reciprocal of eigenvalues (error bound for eigenparameters). Therefore, the eigenvalues play an important role in deciding the values of Importance and ΔMax. The relationship between the Frobenius norm of the Jacobian matrix and the eigenvalues can be expressed as the following equation:

$$||\mathbf{J_w}||_F^2 = \sum_{j=1}^{M}\sum_{i=1}^{N}|J_{ij}|^2 = trace(\mathbf{J_w^*}\mathbf{J_w}) = \sum_{j=1}^{M}\lambda_j^2 \tag{4.3}$$

Where the $\mathbf{J_w^*}$ denotes the conjugate transpose of $\mathbf{J_w}$ and the λ_j are the eigenvalues. It is assumed that the data number N is larger than the number of model parameters M, which is the typical case for the 1D EM geophysical problem. As evident by this equation, the sum of the square of eigenvalues will certainly increase if any entry of the Jacobian matrix is up-weighted while no additional down-weighting is applied. Because the sum is increased, at least one eigenvalue has a large absolute value. For a common case, it is quite likely that a large part of the eigenvalues are increased. The large eigenvalues lead to the small error bound of eigenparameters and thus the possible decrease of ΔMax. Because the calculation of Importance uses the normalized eigenvalues (equation 3.18 and 3.22), it is more difficult to analyze how the Importance is improved by up-weighting from a similar view. Nevertheless, the following synthetic example also supports the argument that it is easy to realize the improvements of Importance and ΔMax by applying up-weightings. Two different up-weighting schemes are designed for synthetic modeling according to the norm of the Jacobian matrix of each dataset. Assuming the total number of datasets inverted jointly is K. And k is the index of each dataset. Thus the weighting factor for kth dataset w_k can be defined as equation 4.4. The $\mathbf{J}$ denotes the Jacobian matrix weighted by only data errors $\mathbf{W_d}$. In the first weighting scheme (Type-1, equation 4.4), $\mathbf{J}_l$ and N_l denote respectively the Jacobian matrix and the number of data for each considered datasets l, which include also the target dataset k. $\mathbf{J}_k$ and N_k indicate the

Jacobian matrix and data number of specific target dataset k.

$$w_k = \sqrt{\frac{\sum_{l=1}^{K} ||\mathbf{J}_l||_F / N_l}{||\mathbf{J}_k||_F / N_k}}; \quad l = 1, 2, \cdots, k, \cdots, K \tag{4.4}$$

This weighting scheme is aiming at pulling the norm of the Jacobian matrix of different datasets to the same level by the sum of them. Obviously, it is an up-weighting scheme. A similar balance could be realized by the ratio between the norms of the total and individual Jacobian matrix, which is expressed as equation 4.5 (Type-2).

$$w_k = 1 + \sqrt{\frac{||\mathbf{J}_T||_F / N_T}{||\mathbf{J}_k||_F / N_k}} \tag{4.5}$$

$\mathbf{J}_T$ and N_T indicate the Jacobian matrix and data number include all the considered datasets. Because this ratio could be smaller than 1 for some datasets and therefore results in a down-weighting, a constant factor 1.0 is added to ensure the up-weighting. These two weighting schemes are tested on the 1D joint inversion of semi-airborne and LOTEM synthetic data. Both LOTEM and semi-airborne use broadside configuration with offset 2000 m. 5% Gaussian noise is added for semi-airborne synthetic data and 1% Gaussian noise for LOTEM. The 1D resistivity model employed for this test is presented in Figure 4.28a together with the non-weighted joint inversion results of its synthetic data. In general, all of the resistivity structures are depicted by both Occam and Marquardt inversions except the basement (ρ_5). Figure 4.28b and c show the Importance and ΔMax for each model parameter in the Marquardt inversions. The first two layers are resolved quite well while the resolution for the model parameters start to decrease obviously from the 3rd layer. The 3rd layer is the resistive layer surrounded by two conductive layers. The Importance values for its resistivity (ρ_3) and thickness (d_3) evenly distributed in the range from 0.1 to 0.8. Regarding the 4th layer, the second conductive layer, its Importance values range from 0 to 0.55 for the thickness (d_4) and from 0 to 0.6 for the resistivity (ρ_4).

The two up-weighting schemes mentioned above are applied to the same datasets. Figure 4.29 shows the inversion results as well as the corresponding Importance and ΔMax for the model parameters. Even though no improvements can be visually observed in the inversion results displayed in a) and d), the Importance provided in b) and e) suggest better resolutions for parameters of 3rd as well as 4th layers. For ρ_3 and d_3, most of the equivalence show high resolution with the Importance values larger than 0.8. For ρ_4, and a large part of the equivalence have Importance values larger than 0.6. The Importance

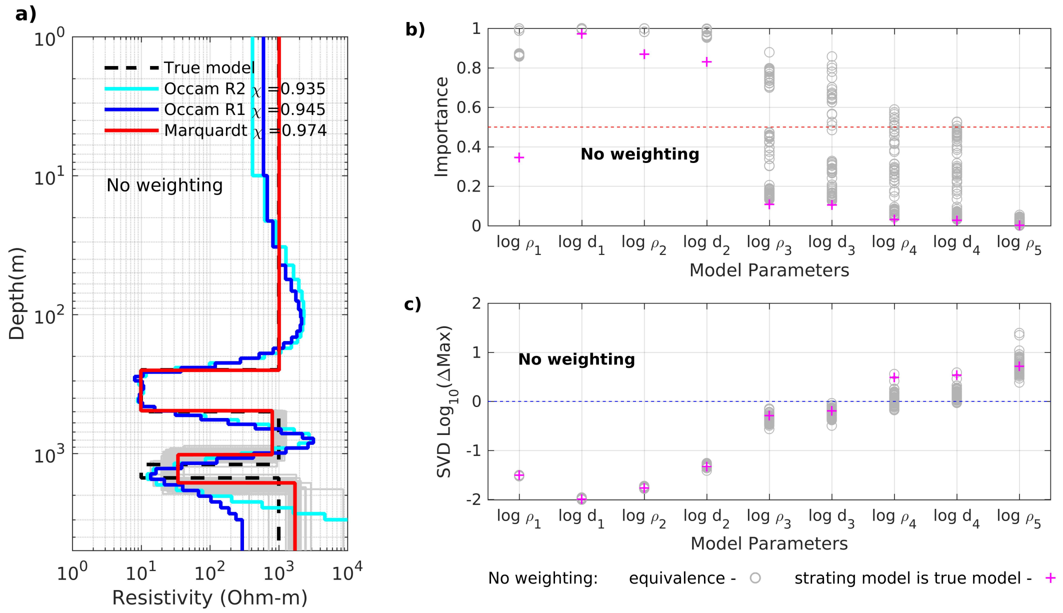

Figure 4.28: Non-weighted 1D joint inversion of semi-airborne and LOTEM synthetic data. (a) the non-weighted joint inversion results, (b) and (c) display the Importance and ΔMax for the non-weighted joint inversion, respectively.

values calculated by inputting the true model as a starting model also suggest slight improvements. The same conclusion can also be derived according to the ΔMax. All of the calculated error bounds for the model parameters decrease.

The evidence presented thus far supports the idea that the improvements of the Importance and ΔMax could be generally achieved by applying an up-weighting on the Jacobian matrix. However, it is a question that if such improvements are meaningful. As stated earlier, the Importance and ΔMax are calculated based on the Jacobian matrix. When a weighting factor w is multiplied on the Jacobian matrix, its entry can be rewritten as

$$wJ_{ij} = w\frac{\partial F_i(\mathbf{m})}{\partial m_j} = w\frac{(F_i(\mathbf{m}+\Delta\mathbf{m}) - F_i(\mathbf{m}))/\sigma_i}{\Delta m_j} = \frac{F_i(\mathbf{m}+\Delta\mathbf{m}) - F_i(\mathbf{m})}{\sigma_i/w}\frac{1}{\Delta m_j} \quad (4.6)$$

Where the σ_i is the standard deviation of the ith data point. The term σ_i/w plays the same role as the standard deviation. When a up-weighting is applied, σ_i/w will be divided by a $w > 1$, therefore $\sigma_i/w < \sigma_i$. In this case, the data standard deviation can be regarded as reduced. If a down-weighting is applied, the $w < 1$ will lead to $\sigma_i/w > \sigma_i$, which equals to a enlarged data standard deviation. Reducing data standard deviation will naturally enhance the resolution of model parameters in the inversion and vise versa. Commer and Newman (2009) mentioned this point and stated that the up-weighting scheme aiming at data number balance assumes that one has a high confidence in the original standard

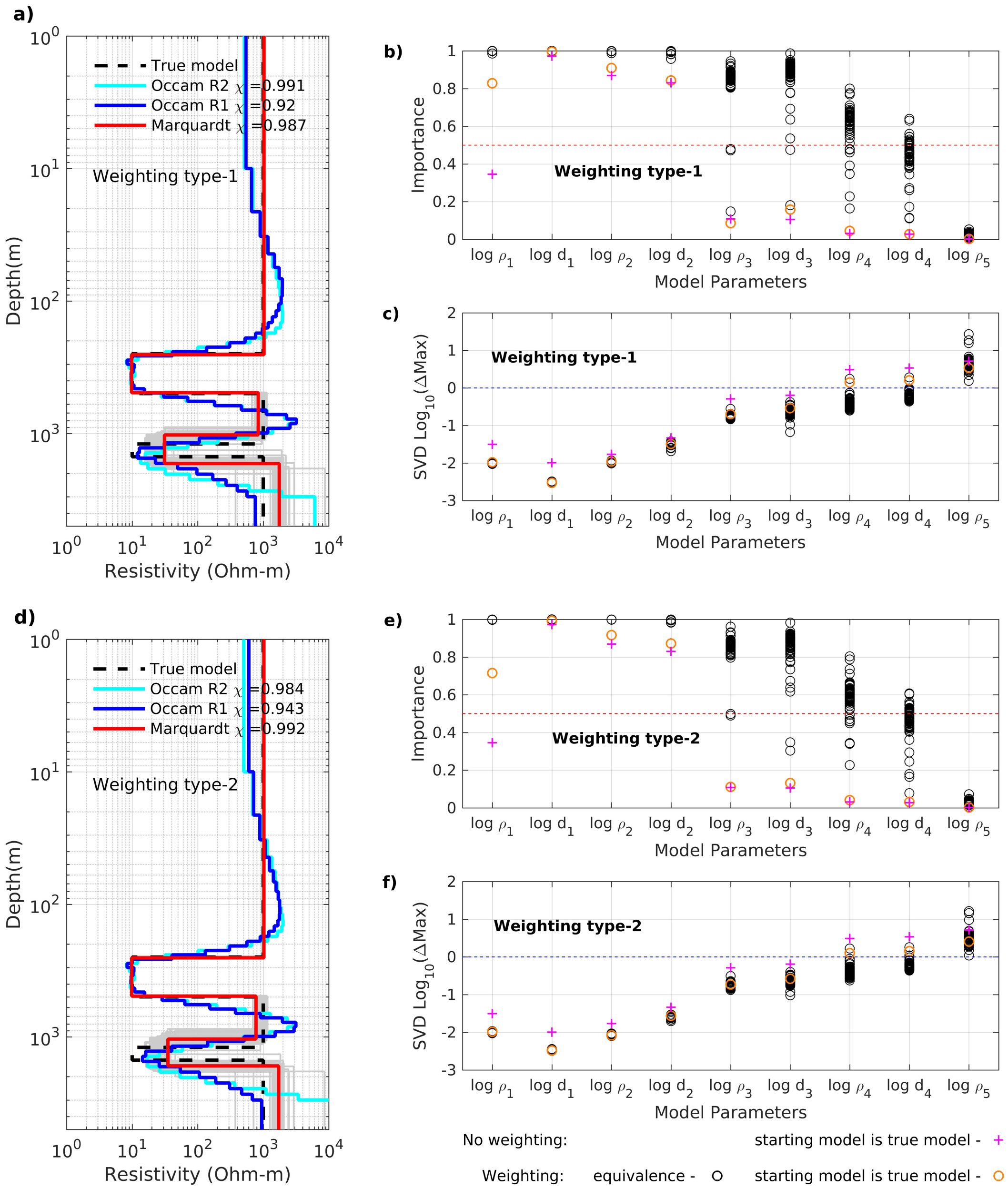

Figure 4.29: Two types of weighted 1D joint inversion of semi-airborne and LOTEM synthetic data. (a) the Type-1 weighted joint inversion results, (b) and (c) display the Importance and ΔMax for Type-1 weighting, respectively; d) the Type-2 weighted joint inversion results, (e) and (f) display the Importance and ΔMax for Type-2 weighting, respectively.

deviations of the measurements. Sudha et al. (2014) introduced the down-weighting based on DOI to reduce the influence of up-weighting when the target region is out of the DOI of one certain EM method.

According to the discussion above, one can find a dilemma. Up-weighing will lead to larger Importance and smaller model parameter error bounds (SVD ΔMax), while the data standard deviations can be regarded as reduced. Down-weighing is helpful in many cases, but it leads to smaller Importance and larger ΔMax in eigenvalue analysis. Therefore, if the resolution variations are evaluated based on the Importance and eigenvalue analysis, the derived conclusion for most of the cases is — up-weighing improve the resolution, while down-weighting decreases the resolution. Thus the question is if the joint inversion should be down-weighted? In many realistic cases, people need down-weighting to find a more satisfactory model (e.g., Candansayar and Tezkan, 2008; Sudha et al., 2014). Considering both up- and down-weighting have their practical values in some cases, a more reasonable answer is that using Importance and ΔMax to evaluate the performance of a weighted joint inversion is doubtful. Weighting schemes are applied to a joint inversion aiming at selecting a biased resistivity model. This procedure can be considered as introducing some additional information to constrain the inversion further while the constraining can not be realized by the data and the original inversion algorithm themselves. However, from the perspective of Importance and ΔMax, these bias or prior information equal only to the variation of data standard deviations.

Unfortunately, the weighted 1D joint inversion algorithms discussed in this section are never applied to the field data because most of the field data include strong 2D or 3D effects, which are not suitable for the 1D joint inversion. The details of 2D effects are discussed in the following sections.

4.5 Application of 1D joint inversion on field data

In the last sections, the resolution characteristics of each EM method are investigated, and the advantages of 1D joint inversions are shown in synthetic studies. Subsequently, the 1D inversions are applied to the field data acquired in eastern Thuringia, Germany. The data for each EM methods are firstly inverted individually, and the results are compared. Afterward, the HEM, semi-airborne, and LOTEM field data are tried to be inverted jointly. Examples of 1D joint inversion results are presented and analyzed.

4.5.1 1D inversion results of each single EM method

Figure 4.30 compares the 1D inversion results of HEM, LOTEM and semi-airborne field data acquired along with the profile shown in Figure 2.4b. The HEM data is measured in the survey in 2015. The helicopter survey (Steuer et al., 2015; Mörbe, 2019) covered a flight area of in total of 445 square kilometers. The selected profile shown in Figure 4.30a is directly along with the LOTEM profile, and it is recorded as Flight line 17 in Steuer et al. (2015). More details of this HEM survey are presented by Steuer et al. (2015). The LOTEM Occam R1 inversion results are provided by Mörbe (2019) and displayed in b). There are six transmitters employed in the LOTEM surveys in eastern Thuringia so that Mörbe (2019) presented the LOTEM 1D inversion results for six profiles actually. Compared with semi-airborne inversion, the LOTEM results are shown only for the profile, which shares the same transmitter with the semi-airborne survey. As depicted in Figure 2.4b, the semi-airborne survey conducted in 2016 has a smaller length in profile direction than that of LOTEM. Thus the scale of the semi-airborne 1D inversion section in c) is enlarged for the clear presenting. Data misfits are attached for each station in the subplot of c). The black dash in the figure marks the related area for the results of each EM survey.

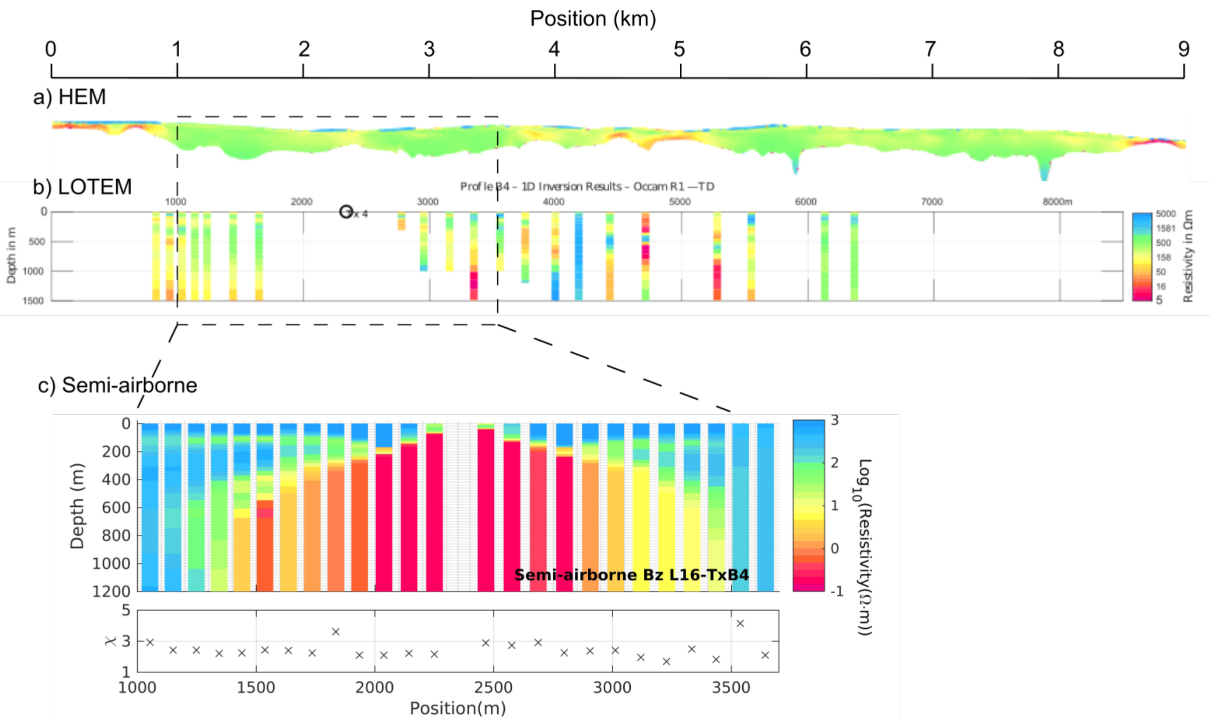

Figure 4.30: 1D Inversion result of HEM,LOTEM and semi-airborne single method inversions.

At first glance, the resistivity distributions described by each EM method are quite different. HEM measurement has a small footprint, and it is suitable for 1D inversion. Therefore the 1D inversion results of HEM data are reliable theoretically and practically. In the target area (region circled by a black dash), a conductive zone is pointed out at a horizontal position around 2.4km by the HEM results. For semi-airborne and LOTEM, one important negative factor is the multidimensional character of the subsurface in the measuring area. The LOTEM data provide little information around the transmitter because the system response dominates the step-on horizontal electric fields in this region. Nevertheless, the LOTEM 1D inversions still suggest the possible conductive bodies in the deep structures. The additional 1D inversion results of LOTEM data can be found in Mörbe (2019). The semi-airborne 1D inversions in c) show significant continuities. The data misfit χ stably locates around 3 for most of the stations. A large conductive zone lies between the horizontal position 1500 to 3500 m is indicated by the semi-airborne data, which is comparable to the conductive region described by the HEM survey at 2400 m. It is worthy of mentioning that, because of the limited DOI, the resistivity distributions around the transmitter in c) are not reliable for the deep layers. In general, all of the 1D inversion results indicate the possible conductive structures in the subsurface of the measured area. But the detailed resistivity distributions for deep structures are not fitted among them.

4.5.2 1D joint inversion example of field data

In the next step, the 1D joint inversion is applied to the field data acquired along with the LOTEM profile (Figure 2.4b). Figure 4.31 shows one successful example of the 1D joint inversion, including the data of all the three EM methods. The LOTEM and semi-airborne measurements use the same transmitter named as B4. The selected LOTEM station has an offset of 1208 m, and the semi-airborne station has an offset of 1209 m. The closest HEM measuring point to this LOTEM station is selected for the 1D joint inversion, and it is recorded as 21997 by Steuer et al. (2015). Figure 4.31a and b display the single method inversion results for semi-airborne and LOTEM data, respectively, and Figure 4.32 provides the corresponding data fitting achieved in 1D Marquardt inversion. The resistivity distributions in Figure 4.31a and b show similarities in shallow layers but divergences in deep layers. Considering the DOI of these two datasets are different, one more test is carried out to check if the Marquardt inversion results of each side are equivalent. The synthetic semi-airborne data of LOTEM Marquardt inversion results are compared to the original semi-airborne field data and vice versa. The comparison is shown in Figure 4.33. In (a), the semi-airborne response of the LOTEM Marquardt

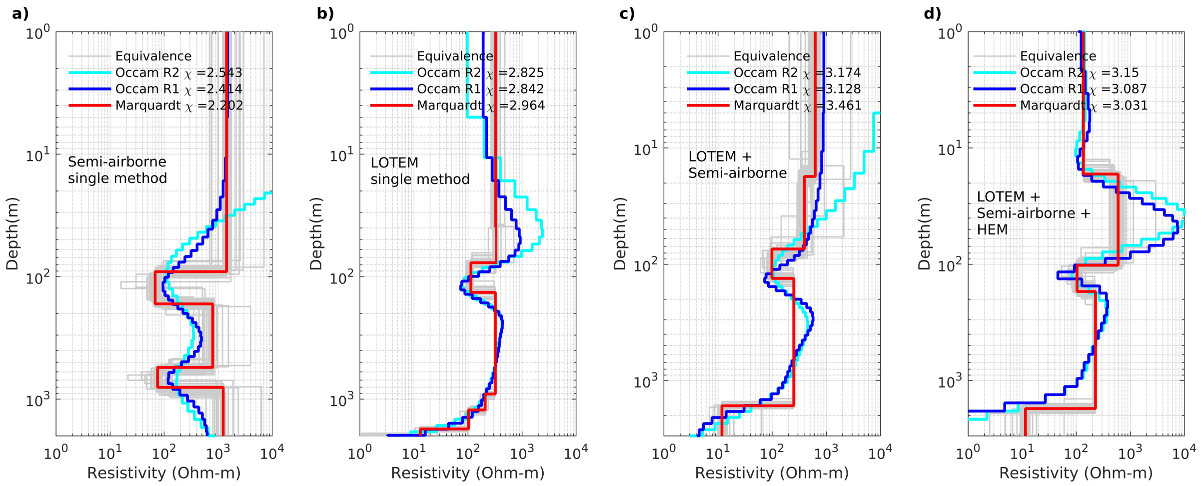

Figure 4.31: Inversion results for field data of a selected station. Transmitter B4 is employed in LOTEM and semi-airborne survey (2016).(a) Semi-airborne single method inversion, data from station L16Tx1032, offset is 1209.03 m. (b) LOTEM single method inversion, data from station 04, offset is 1208.11 m. (c) Semi-airborne and LOTEM joint inversion results. (d) HEM, semi-airborne and LOTEM joint inversion results. HEM data comes from Line17.1 Record 21997. Lowest relative error is set as 1% in inversions.

result fits well with the field data generally, except the real part of Bz in frequencies larger than 300Hz. In this case, from the perspective of semi-airborne field data, the resistivity model obtained by LOTEM Marquardt inversion could be even regarded as an equivalent model reluctantly. The comparison from the LOTEM side displayed in (b) shows the obvious distinction in the late time, indicating that LOTEM data do not agree with the deep structures revealed by semi-airborne Marquardt inversion. Even

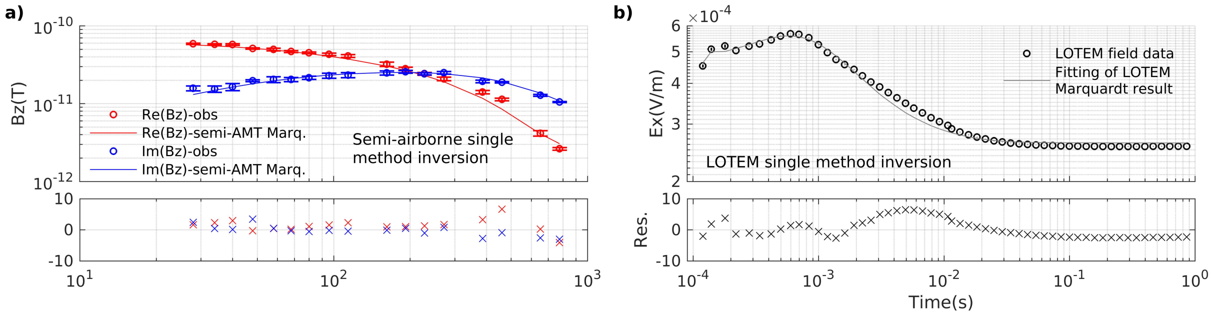

Figure 4.32: Data fitting for the 1D Marquardt inversion results presented in Figure 4.31a and b.

though the singe method inversion results show some difference, the 1D joint inversion of these two datasets converged (Figure 4.31c). The HEM data are added in the 1D joint inversion subsequently and the results are displayed in Figure 4.31d. Compared to the single method inversions in (a) and (b), the total data misfits increased slightly in both

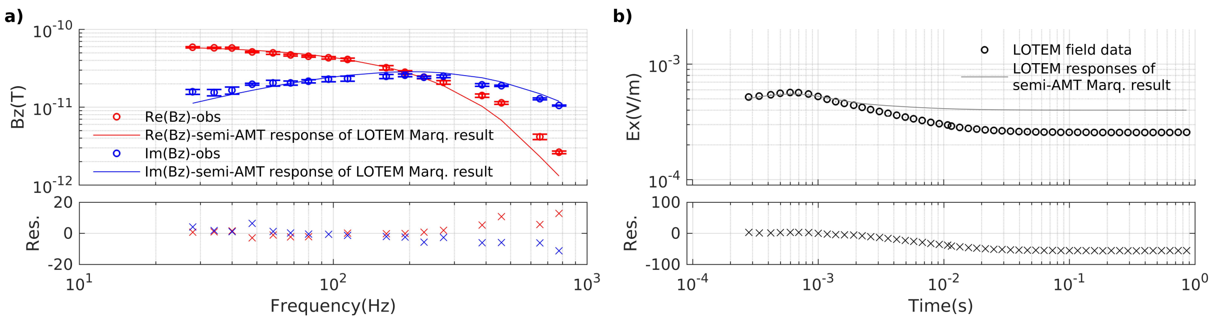

Figure 4.33: (a) The comparison between synthetic semi-airborne data of LOTEM Marquardt inversion result (Figure 4.31b) and the original semi-airborne field data at station L16Tx1032; (b) the comparison between synthetic LOTEM data of semi-airborne Marquardt inversion result (Figure 4.31a) and the original LOTEM field data at station 04.

(c) and (d). Considering the χ values increase at most 13% (Marquardt result in (c)) and the data misfitting presented in Figure A.16 is acceptable, the 1D joint inversions in (c) and (d) are regarded as successful. The joint inversions present their advantages also in these two examples. Firstly, the information from semi-airborne and LOTEM data are combined and result in a good resolution for the deep structures in (c). Given the fact that the Marquardt inversion result of only LOTEM data is an equivalent model from the perspective of semi-airborne field data (Figure 4.33a), it is reasonable that the deep structures revealed in (c) are similar to those displayed in (a). On the other hand, because additional datasets are taken into account in the joint inversions, their extended Jacobian matrices are essentially different from those of the inversions considering only one dataset. Therefore the resolution variations indicated by Importance and SVD eigenvalue analysis are meaningful. Figure 4.34 displays the Importance and ΔMax of the equivalence for the joint inversions include semi-airborne and LOTEM data in (a) and (b), as well as those for joint inversion consider all three EM methods. Suggested by Figure 4.34a and b, the 1D joint inversions of semi-airborne and LOTEM data (Figure 4.31c) resolve the deep substructures well, especially the fourth layer. However, the shallow layers can not be well resolved by only semi-airborne and LOTEM data. After the HEM data join the 1D inversion, the resolution for shallow layers is significantly improved. The resistivity of the first layer is nearly determined, and the resistive second layer is clearly revealed. However, the 1D joint inversions encounter convergence problems for most of the LOTEM and semi-airborne data acquired in this region, because of the multidimensional character of the substructure. The difficulty in 1D joint inversions happens even though the 1D inversions of each single EM method show a good convergence and a good data fitting. An example is shown in Figure 4.35. Same as that in the successful case above, the LOTEM station in this example also used the transmitter B4. The offset of the selected LOTEM station is 905 m. The closest semi-airborne station to the LOTEM

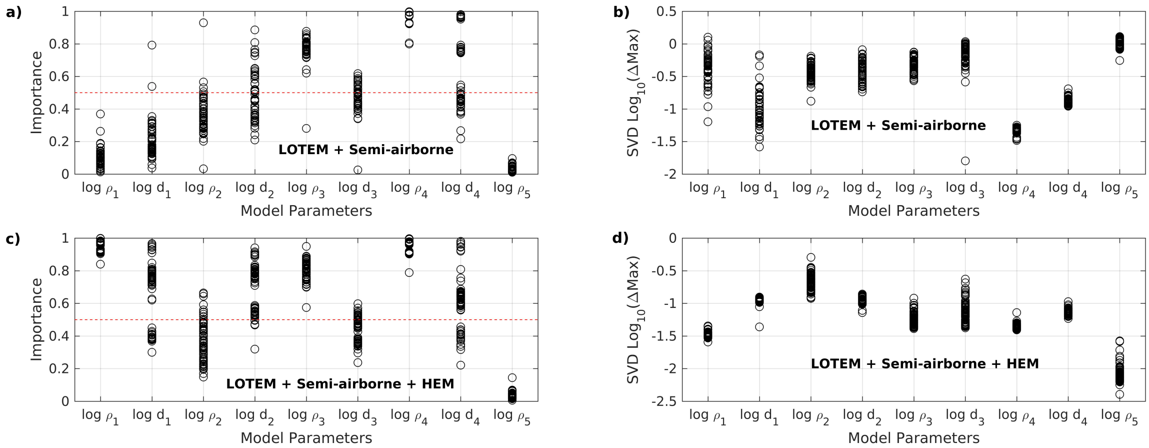

Figure 4.34: Importance and model parameters error bounds (SVD ΔMax) for the 1D joint inversions. (a) and (b) display the Importance and ΔMax for semi-airborne and LOTEM joint inversion (Figure 4.31c), respectively; (c) and (d) display the Importance and ΔMax for HEM, semi-airborne and LOTEM joint inversion (Figure 4.31d), respectively.

station is chosen for the 1D joint inversion, which has an offset of 918 m. The inversion results of each single dataset are presented in Figure 4.35a and b. Figure 4.36 shows the satisfactory data fitting acquired in Marquardt inversions for each single method inversion. However, distinct resistivity distributions are revealed by the dataset from different EM methods. Moreover, the 1D joint inversion of these two datasets can not achieve a satisfactory convergence — compared to the single method inversions, the data misfits χ of joint inversions increase around 100%, significantly larger than the 13% in the successful example. Subsequently, the comparison the same as that shown in Figure 4.33 is carried out also for the data of this station. Both Figure 4.37a and b show distinctively divergence, indicating that the two Marquardt inversion results calculated by each individual dataset contain essentially different resistivity information. As stated earlier, the difference between 1D single method inversions and the non-convergence of 1D joint inversions may leaded by the multidimensional character of the substructure in measuring area. The detailed investigations for this aspect are presented in the next section.

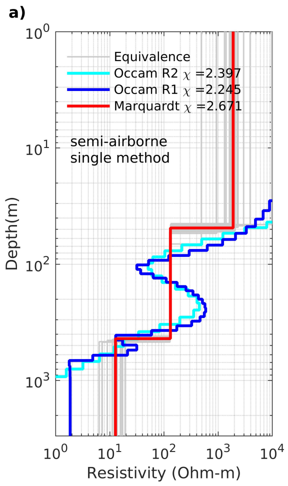

Figure 4.35: An example of convergence problem in 1D joint inversion. Transmitter B4 is employed in LOTEM and semi-airborne survey (2016).(a) Semi-airborne single method inversion, data from station L16Tx1029, offset is 918 m. (b) LOTEM single method inversion, data from station 06, offset is 905 m. (c) Semi-airborne and LOTEM joint inversion results. Lowest relative error is set as 1% in inversions.

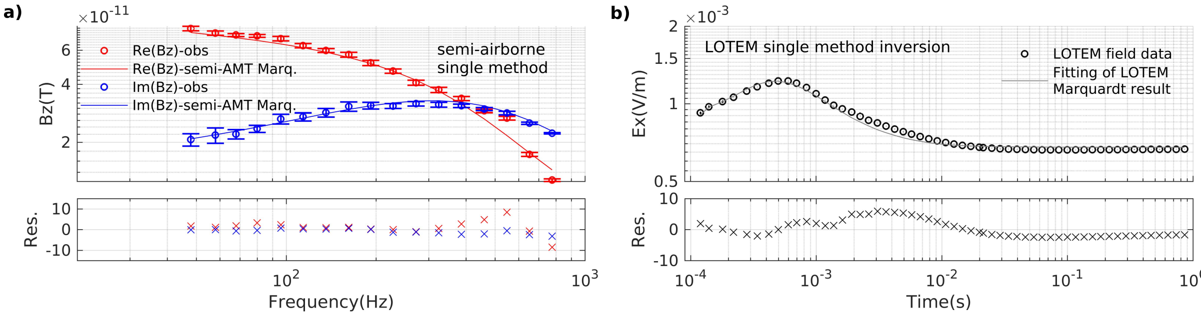

Figure 4.36: Data fitting for the 1D Marquardt inversion results presented in Figure 4.35a and b.

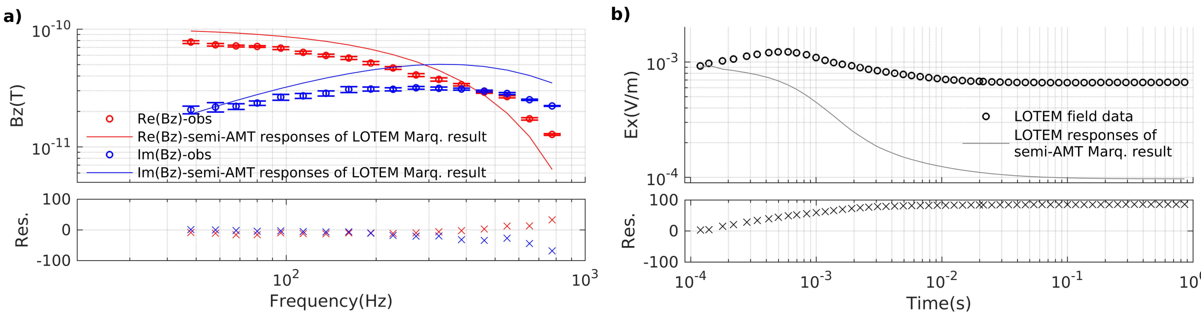

Figure 4.37: [

Comparison of 1D Marquardt inversion results for LOTEM station 06](a) The comparison between synthetic semi-airborne data of LOTEM Marquardt inversion result (Figure 4.35b) and the original semi-airborne field data at station L16Tx1029; (b) the comparison between synthetic LOTEM data of semi-airborne Marquardt inversion result (Figure 4.35a) and the original LOTEM field data at station 06.

4.6 2D effects in 1D inversion

As mentioned in the last section, the 1D joint inversions for the field data encounter convergence problems for a large part of the measuring areas. For most of the stations, each single EM method (e.g., semi-airborne or LOTEM) 1D inversion can show a good convergence and a good data fitting. However, the 1D resistivity models depicted by the well-fitted data show significant divergence for different EM methods(e.g., Figure). The consequent 1D joint inversions of these field data often do not converge. It is widely known that the 1D inversions could be affected by many factors, such as 2D and 3D effects or even anisotropic and IP effects. Among these factors, the 2D effects in 1D joint inversion are one of the most important but easy ones to be investigated. In this section, how the

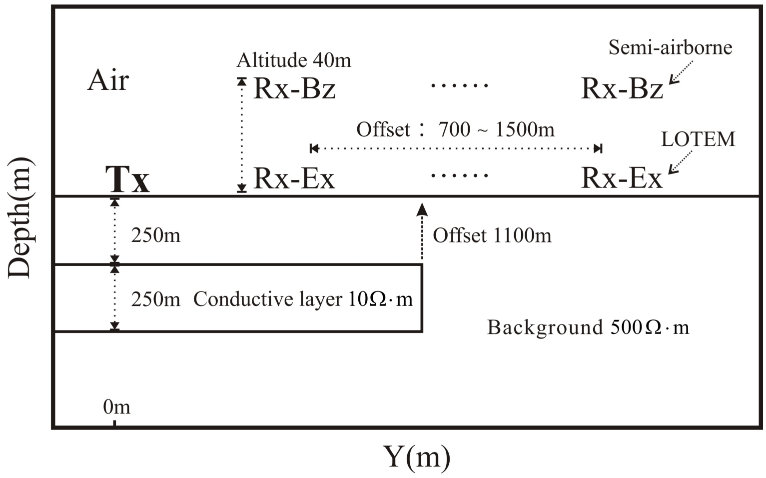

Figure 4.38: Sketch of the 2D resistivity model and the measuring set-up. 2D boundary locates at offset 1100 m.

2D effects hinder the 1D joint inversion is studied. 1D joint inversions are applied on the synthetic LOTEM and semi-airborne data of a 2D model (Figure 4.38). The 2D forward calculations are realized by using MARE2DEM (Key, 2016). The validations of the 2D modeling code are presented in the section 5.1.5 and 5.1.6. As depicted in Figure 4.38, in the 2D resistivity model, a conductive layer of 10 $\Omega \cdot m$ is embedded in the background of 500 $\Omega \cdot m$. The conductive layer has a thickness of 250 m, and it is buried 250 m under the earth's surface. The left horizontal boundary of this layer is infinity extended, while the right boundary is 2D and locates in the middle of this model (horizontal position Y = 1100 m). Aiming at investigating joint inversion, both semi-airborne and LOTEM measuring configurations are employed. They use one same transmitter locates at the horizontal position of 0 m, above the conductive layer. The broadside configuration is used for both EM methods. For simplification, a point source is simulated in this modeling study. Nine receivers are deployed at the same horizontal positions for LOTEM and semi-airborne measurements separately. The offsets vary from 700 to 1500 m with an interval of 100 m. Altitude for all semi-airborne receivers is 40 m. Gaussian noise of 5% is added into the semi-airborne 2D synthetic data for this model, while the Gaussian noise for LOTEM horizontal electric field is 2%.

The results of 1D single method inversions of LOTEM and semi-airborne 2D synthetic data are presented as the 2D sections in Figure 4.39a and b, respectively. Figure 4.39c presented the results of the 1D joint inversions. By comparing the 1D inversion results in Fig 4.39, how the 2D effects hinder the 1D joint inversion can be understood. When receivers locate above conductive layer and far away from 2D boundary (e.g., offset 700 m), all single inversions and joint inversion reveal the target layer well with promising data fitting. While the LOTEM inversion result shows nearly no 2D effects, the 1D inversion of semi-airborne data is already suffered from 2D effects. Instead of the deep resistive structure, very conductive deep layers result from the semi-airborne data. The joint inversion result at this station is closer to the LOTEM inversion result. When receivers get close to the 2D boundary (e.g., offset 1200 m), both LOTEM and semi-airborne single inversions converge with good data fitting but present obviously different inversion results. Semi-airborne single inversion cannot reveal the target layer already. Joint inversion cannot converge data at these stations because of LOTEM and semi-airborne data containing totally different subsurface information from the 1D perspective. When receivers locate far away from the 2D conductive layer (e.g., offset 1500 m), LOTEM single method inversions still reveal conductive bodies due to long offset and the location of the transmitter. Semi-airborne single inversion cannot converge due to 2D effects. Therefore, joint inversion cannot converge either since no 1D model can fit the semi-airborne data at these stations.

As evident by the modeling studies above, 1D joint inversion is problematic when the 2D effects are strong in the data. 2D effects in the data of different EM methods lead the 1D inversion to different directions, generating different artificial structures. These divergences can never be accepted by a single 1D resistivity model. Then the 1D joint inversion can not converge. Therefore, the 2D joint inversion is necessary for these cases. With the demand to interpret the field data acquired in eastern Thuringia, Germany, the algorithm for the 2D joint inversion is developed in the next chapter.

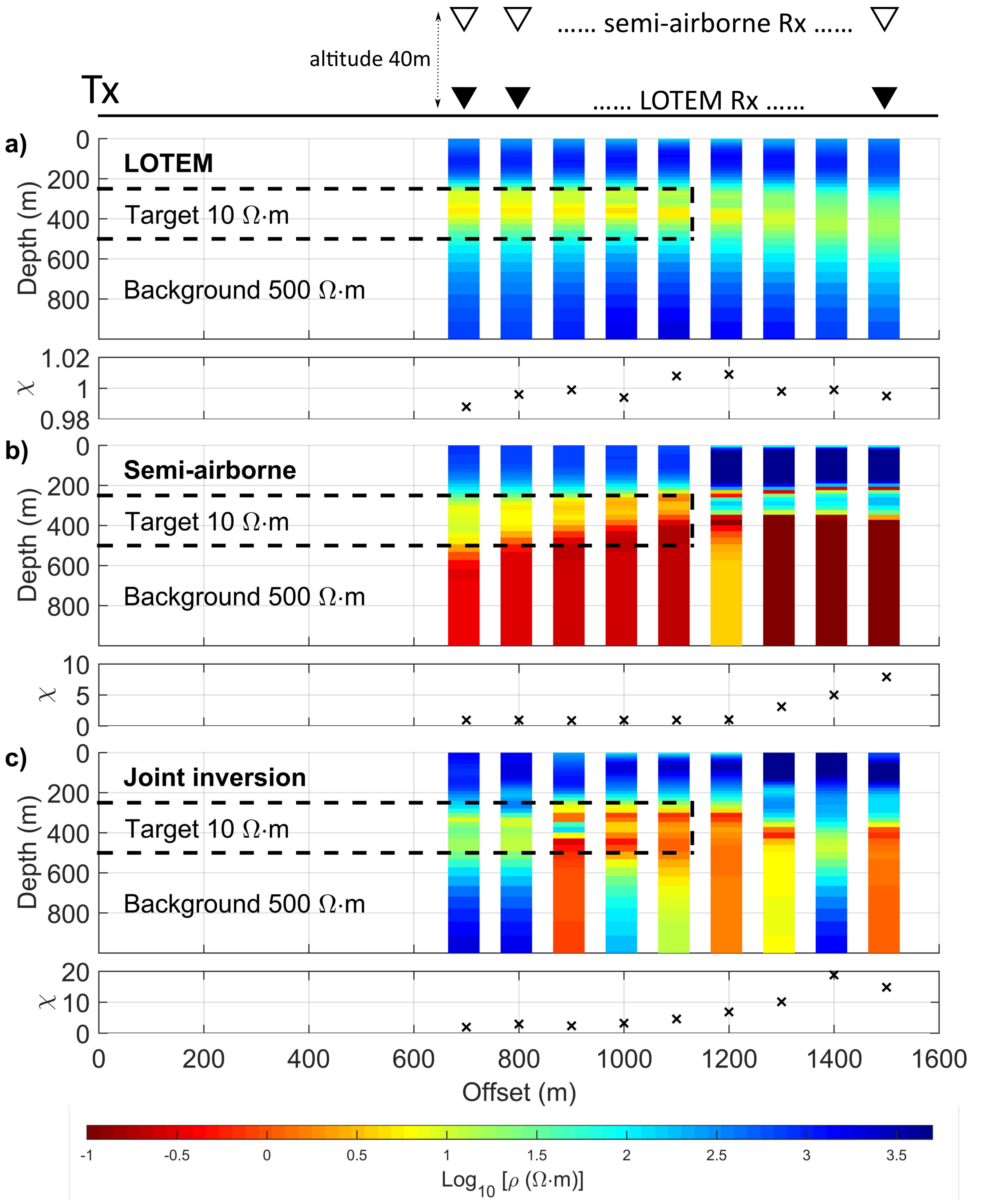

Figure 4.39: 1D inversion results for 2D synthetic data. (a) LOTEM; (b) Semi-airborne; (c) Joint inversion. The data misfits are displayed for each station.

4.7 Summary of 1D modeling studies

In this chapter, the 1D joint inversion of HEM, LOTEM and semi-airborne is firstly tried to be resolved in 1D cases. Studying the resolution characteristics from a 1D perspective provides valuable insights regarding the advantages and disadvantages of each individual EM method. According to these modeling studies, the benefits of a 1D joint inversions are motivated and also demonstrated using synthetic data. In the first step, the inversion Kernel was extended for the joint inversion and the 1D forward operators for semi-airborne data in frequency-domain were developed and installed in EMUPLUS. The forward modeling part was realized by Janser (2017). In order to guarantee accurate modeling results, the 1D semi-airborne solutions of EMUPLUS are verified by comparison with the results of algorithm EM1DW from WWU Münster (M. Becken, personal communication, 2018). The relative differences between the solutions from both codes are smaller than 1% when there is no sign reversal in the magnetic responses. Next, modeling studies are carried out systematically in order to investigate the individual resolution characteristics of HEM, LOTEM and semi-airborne. With the demand to ensure the results are comparable, the studied 1D resistivity model is kept as three-layered, and the resistivity for the conductor and the background is always set as 10 and 300 $\Omega \cdot m$, respectively. Based on this assumption, the resolutions of the data from different EM methods are studied for the conductors with various thicknesses and buried depth. For the synthetic data of a certain 1D resistivity model, the inversions with Occam and Marquardt algorithms are applied. The SVD analysis and the equivalence domain of the target conductor (heat map) are used for evaluating if the parameters of the target layer are well resolved. In general, these systematical inversions and analyses are guided by summaries using heat maps. The summary of equivalence in heat maps describe the variation of the equivalence domain as a function of the continuously changing thickness and buried depth of the target conductor.

Based on these modeling studies, valuable insights are obtained for the resolution characteristics of the three EM methods. HEM data has a very high resolution for the shallow layers. But because of the limited depth of investigation (DOI), HEM data has less resolution for the structures below 150 to 200 m (depends on the resistivity). Moreover, a thick conductor at shallow depth can also reduce the DOI of HEM. LOTEM can provide the deepest information among these three EM methods because it benefits from the high data quality at large offsets using land-based stations with sufficient stacking time. Semi-airborne has the potential of a DOI down to 1000m depth. Because of the relatively large data standard error, the semi-airborne data usually have reduced resolution compared to the LOTEM. But the equivalence domain of the semi-airborne and LOTEM often present distinct characteristics. Both the LOTEM and semi-airborne data can not resolve the shallow structures well. The joint inversions take advantage of each EM method and can better reveal the complex 1D resistivity distributions. The HEM data can well constrain the shallow layers and helps the semi-airborne or LOTEM data to resolve deep structures better. The different equivalence domains of the semi-airborne and LOTEM data usually lead to a better resolution for the target layer than each individual data-set.

Additionally, different weighting schemes for joint inversion are studied. Based on the proposed weighting schemes, it is investigated how these weighting between different EM methods can improve the joint inversion results. The relationship between the weighted Jacobian matrix and the resolution is evaluated, for example, SVD analysis.

Both up- and down-weighting strategies have their practical benefits in an interpretation and for the convergence. However, the weighting should not influence the resolution and is therefore considered as insignificant to improve, for example, importance or SVD analysis results.

At last, the 1D inversion is applied to the field data acquired in eastern Thuringia, Germany. For a few selected stations, the 1D joint inversion successfully converged. However, for most of the stations, the joint inversion encounters convergence problems even though each single method inversion shows a good convergence and good data fitting. The presence of 2D effects that distort the data differently for each method is one of the possible reasons. Therefore, 2D effects in 1D joint inversion are further investigated. The results indicate that strong 2D effects will lead to different artificial structures in the inversion for the data of different EM methods, and result in the non-convergence of the 1D joint inversion.

5 2D joint inversion of LOTEM and semi-airborne data

Because a 1D joint inversion may not be feasible when strong 2D effects are present in the data measured by each EM, a 2D interpretation by forward and inverse modeling is required. This is the case for most of the data acquired in eastern Thuringia, Germany in 2016. To apply a 2D joint inversion on LOTEM and semi-airborne EM data, the open-source Fortran code MARE2DEM (Key, 2016) is adapted. MARE2DEM is used as the preferable 2D algorithm within this thesis for several reasons. Firstly, it provides comprehensive modeling possibilities for land-based CSEM data. Moreover, an unstructured triangle mesh is implemented so that the topography along profiles can be simulated precisely. The finite length of the transmitter is also considered in the code. The semi-airborne concept is similar to standard ground-based frequency-domain CSEM except that the receivers are positioned in the air Smirnova et al. (2019). In MARE2DEM, the position of receivers can be determined arbitrarily. After some adjustments of the algorithm for the wavenumber selection and mesh design, it provides accurate semi-airborne EM data in the required frequency range. Secondly, time-domain solutions were implemented recently by Haroon et al. (2018). With the latter new implementation, the modeling and inversion of LOTEM data in time-domain are feasible. This provides the foundation for further development towards a joint inversion of time-domain and frequency-domain EM data significantly. Thirdly, the code originally supports the joint inversion of MT and CSEM data, which means a frame for joint inversion exists already. This frame could be extended to include also time-domain modeling. At last, a high efficient parallel algorithm is implemented. Due to that, the is code suitable for the inversion of a large amount of LOTEM and semi-airborne EM field data using multiple transmitters.

The first section of this chapter briefly describes the basic theory of the 2D forward modeling algorithms used in MARE2DEM. Afterward, the 2D forward solutions for semi-airborne data as well as frequency- and time-domain LOTEM data are validated. The original MARE2DEM forward operators are described by the authors in details(Key and Ovall, 2011; Key, 2016). Therefore, this thesis addresses the main key points and not the full theoretical background. The implementation of the time-domain forward solutions is introduced by Haroon et al. (2018). The adjustment for semi-airborne modeling and the realization of the joint inversion for frequency- and time-domain data are described in detail. Before extensive 2D modeling studies, the code validation is crucial to ensure the forward responses are accurate and reliable. The second section is the main focus of this chapter. It includes various 2D synthetic studies of semi-airborne and LOTEM joint inversion. It also includes the 2D joint inversion of field data and an elaborate discussion.

Because the original time-domain LOTEM field data was also evaluated/processed in frequency-domain (Mörbe, 2019), the content of the 2D modeling studies and joint inversion is divided into two parts, in order to separate frequency- and time-domain LOTEM modeling. For each part, synthetic studies and field data inversions are conducted. The 2D synthetic studies aim at investigating the advantage of the 2D joint inversion. Semi-airborne EM and LOTEM single method inversions, as well as joint inversion, are applied to various 2D synthetic models with different configurations. This is done to investigate resolution capabilities and to compare how well model features are reproduced. Different data-sets, mesh designs, and constraining conditions were tested to reach a satisfactory inversion result with optimal convergence.

The Semi-airborne field data is inverted in frequency-domain for one flight line. The LOTEM field data is inverted in both time- and frequency- domain. However, only the Ex components are considered in this thesis. The inversion for large scale LOTEM field data using multiple components is presented by Mörbe (2019). Here, the focus is on the joint inversion of LOTEM field data together with semi-airborne data. The results are compared and discussed in detail for each single method inversion and the joint inversion. Further analysis is presented to explain the similarities and differences between the results. Finally, possible 3D effects are also investigated by simple forward modeling studies.

5.1 2D forward/inversion algorithm MARE2DEM

The governing equations that used to describe the 2D electromagnetic geophysics problems in MARE2DEM are Maxwell equations(Key and Ovall, 2011; Key, 2016).

$$\nabla \times \mathbf{E} - i\omega\mu\mathbf{H} = \mathbf{M_s} \tag{5.1}$$

$$\nabla \times \mathbf{H} - \sigma\mathbf{E} = \mathbf{j_s} \tag{5.2}$$

where $\mathbf{j_s}$ and $\mathbf{M_s}$ denote the 3D electric and magnetic source terms, respectively.
MARE2DEM can describe the anisotropic problem, but in this thesis, only isotropic earth is considered, so σ denotes isotropic conductivity. Because 2D cases are considered here, σ is constant in the x-direction. The differential problems are transferred into the wavenumber-domain in x-direction by using Fourier Transformation for the resolving, while the y-direction is kept in spatial-domain. After (Key and Ovall, 2011), the differential equations can be written as

$$-\nabla \cdot (A\nabla\mathbf{u}) + C\mathbf{u} = \mathbf{f} \quad in\,\Omega \qquad \mathbf{u} = \mathbf{0}\ on\ \delta\Omega \tag{5.3}$$

where Ω indicates the model domain and $\mathbf{u} = (\hat{E}_x, \hat{H}_x)$. $\mathbf{u} = \mathbf{0}$ on $\delta\Omega$ indicates the boundary conditions that the EM fields are zero at the outer boundary $\delta\Omega$. $\mathbf{f} = (f_1, f_2)$ denotes the source terms. The coefficients A and C matrix are

$$R = \begin{pmatrix} 0 & -1 \\ 1 & 0 \end{pmatrix} \qquad A = \lambda \begin{pmatrix} \sigma I & ik_x R \\ ik_x R & i\omega\mu I \end{pmatrix} \qquad C = \begin{pmatrix} \sigma & 0 \\ 0 & i\omega\mu \end{pmatrix} \tag{5.4}$$

The EM fields in the wavenumber-domain can be obtained via the solution of 5.3, and afterward, be converted into spatial-domain fields using the inverse Fourier transform.

In order to describe the adjustment and modification made in this thesis for MARE2DEM better, concepts of the adaptive refinement method and parallel forward computations approach are mentioned in this thesis. The Fast Occam inversion algorithm used in MARE2DEM is an important factor that decides final inversion results, so it is also introduced briefly. Some other important algorithms used in MARE2DEM, like the adjoint reciprocity formula for computing EM sensitivities, are not repeatedly stated in this thesis. Detailed descriptions for them can be found in Key and Ovall (2011) and Key (2016).

5.1.1 Adaptive refinement method

One of the obvious advantages of MARE2DEM is its adaptive mesh refinement. Iterative mesh refinement is guided by a goal-oriented error estimator that considers the relative error in the strike aligned fields and their spatial gradients. Key and Ovall (2011) describes the detailed algorithm for calculating the goal-oriented error estimator. Local error indicator μ_τ for each element in a mesh could be produced according to the goal-oriented error estimation method. Then, a fraction α of the elements with the largest errors are refined. For a newly refined mesh, forward calculation and the local error indicators μ_τ are computed, and again the α elements with the largest error estimates are refined. The iterations keep going until the functional error is less than the tolerance.

All the required EM solutions are calculated based on the final accepted mesh. How well the mesh is refined directly decide the accuracy of the forward modeling results. For semi-airborne modeling, the receivers are positioned in the air, which is much more resistive than rocks or marine sediments. Due to the high resistivity of the air, the accuracy problem could occur for semi-airborne forward modeling. This problem and the corresponding alternative solution are discussed in subsection 5.1.5.

5.1.2 Parallel forward computations

Message Passing Interface standard (MPI) is used for the parallel forward computations in MARE2DEM. The computations are carried out using the data decomposition scheme presented in Key and Ovall (2011). A manager–worker framework is employed. Input transmitter, receiver, frequency, and even wavenumber arrays are divided into smaller subsets and reassemble to form some refinement groups. Each refinement group corresponds to a small modeling task. The manager processor maintains a queue of all modeling tasks and assigns the next task to the next available worker processors by MPI broadcasting (Key, 2016). Assigned refinement groups are modeled in parallel using the goal-oriented adaptive finite element method. That means each of the refinement groups has its unique mesh, and a suite of different refined meshes are produced during this parallel computation. This dynamic task-queue-based approach offers much better load balancing among the processors than if the tasks were instead preassigned to each processor (Key, 2016). After all the worker processors return the wavenumber-domain solutions, the manager processor applies the inverse Fourier transform to convert them into spatial-domain fields. The joint inversion of frequency- and time-domain data are designed based on this parallel computation strategy, so it is also illustrated in Figure 5.1. It should be mentioned that the fragments of the Jacobian matrix are calculated by these worker processors according to adjoint reciprocity formula and afterward gathered and assembled to result in the total Jacobian matrix by the manager processor.

5.1.3 Inversion method and the roughness norm for the unstructured grid

After the forward modeling is completed by the parallel computations, the manager processor calculates the total Jacobian matrix and starts the consequent inversion procedures. MARE2DEM uses the fast Occam inversion approach for the inversion. This modification is aiming at reducing the computation cost. Compared to the widely known Occam inversion (Constable et al., 1987), which uses a full dynamic search over the parameter μ to fine the model having optimal data misfit as well as model roughness, the fast Occam accepts the first model found with a sufficient misfit reduction and finish the current iteration. Otherwise, the full dynamic search like the original Occam scheme will be executed. Key (2016) mentioned that, for typical MT and CSEM inversions, a RMS misfit reduction threshold of about 15% was found to perform well. Examples or illustrations for the performance of fast Occam are presented by Key (2016) and also by Mörbe (2019).

The roughness norm for the unstructured mesh is included in the following objective function (simplified from Key (2016)).

$$U = \parallel \mathbf{Rm} \parallel^2 + \mu^{-1} \parallel \mathbf{W}(\mathbf{d} - F(\mathbf{m})) \parallel^2 \tag{5.5}$$

where $\mathbf{m}$ is the model parameters vector, the second term at the right hand is fit of forward response $F(\mathbf{m})$ to the observed data $\mathbf{d}$ and the $\mathbf{W}$ is diagonal weighting matrix consists of inverse standard deviations of the data. $\parallel \mathbf{Rm} \parallel^2$ is the model roughness, its minimization will steer the inversion away from producing spurious structures (Key, 2016). For the finite-element unstructured mesh, this term can be calculated by the following equations.

$$\parallel \mathbf{Rm} \parallel^2 = \sum_{i=1}^{m} A_i \left[\sum_{j=1}^{N(i) w_j} \left(\frac{\Delta m_{ij}}{\Delta r_{ij}} \right) \right] \tag{5.6}$$

where

$$\Delta m_{ij} = m_i - m_j, \tag{5.7}$$

$$\Delta r_{ij} = \sqrt{(y_i - y_j)^2 + (z_i - z_j)^2}, \tag{5.8}$$

$$w_j = \frac{A_j}{\sum_{k=1}^{N(i)} A_k} \tag{5.9}$$

A_i is the area of the parameter or element i, $N(i)$ is the number of the neighbouring elements of element i. The distance Δr_{ij} between elements are calculated according to centre of each element. An additional modification on equation 5.8 can be used to introduce the different smoothness in horizontal or vertical directions.

$$\Delta r_{ij} = \sqrt{(\frac{y_i - y_j}{w_{hv}})^2 + (z_i - z_j)^2} \tag{5.10}$$

If the horizontal to vertical weight $w_{hv} > 1$, the smoothness in horizontal direction is enhanced and vice versa for $w_{hv} < 1$.

5.1.4 Realisation of joint inversion for frequency- and time-domain data

As mentioned in the introduction part of this chapter, the time-domain LOTEM field data from eastern Thuringia are transferred into frequency-domain. In the studies of Mörbe (2019), the 1D inversion results for the LOTEM data in both domains show similar results. Mörbe (2019) also applied the 2D inversion on both frequency- and time-domain LOTEM data-sets. The results show similar overall resistivity distributions, while some small but obvious discrepancies exist. In order to investigate the joint inversion of LOTEM and semi-airborne data from more aspects, both the frequency- and time-domain LOTEM data-sets are taken into account in this thesis.

In order to apply joint inversion on semi-airborne data in frequency-domain and LOTEM data in time-domain, MARE2DEM was modified. As mentioned above, Haroon et al. (2018) implemented the time-domain solutions in MARE2DEM. This step is realized via transferring frequency-domain solutions into time-domain by using inverse Fourier Transformation. Before the forward modeling, a suite of frequencies required by the transformation are calculated according to the needed time points as the inputs for the following frequency-domain calculations. Afterward, frequency-domain solutions are computed by the same procedures used in the original code of (Key, 2016). The sensitivity matrix is firstly calculated in frequency-domain by using the adjoint reciprocity formula (Farquharson and Oldenburg, 1996) and then transferred into time-domain. The procedures for calculating time-domain solutions are illustrated in the right part of Figure 5.1. In the implementation of Haroon et al. (2018), CSEM modeling can be either time-domain or frequency-domain, calculating the data for both domains simultaneously or parallel is not feasible. The reason is the frequency-domain calculations required by time-domain modeling use the same groups of dummies and arrays, which are used by frequency-domain modeling. For avoiding confliction, the frequency-domain calculations for time-domain modeling should be distinguished from the calculations of frequency-domain modeling. Therefore, an extra group of dummies and arrays are created to store the parameters and frequency-domain solutions for time-domain modeling. The corresponding frequency-domain calculation tasks are also divided into smaller ones and packed as refinement groups. From the view of manager–worker framework, the manager processor sends the information of a certain refinement group to a worker processor together with a logical flag which marks if the current group belongs to frequency- or time-domain modeling. Because the frequency-domain calculations are essentially the same for both frequency- or time-domain modeling, the logical flags play no role in the works of worker processors. After the manager processor receives the results from worker processors, it checks the logical flag and judges if or not the solutions of the current refinement group belongs to time-domain modeling and should join the consequent inverse Fourier Transformation. For an inversion case, the time-domain Jacobian matrix resulted from inverse Fourier Transformation are combined with the frequency-domain Jacobian matrix and used for the following calculations of model update. The transformation of the Jacobian matrix is also performed by parallel computations Haroon et al. (2018). Figure 5.1 illustrates these procedures in detail. It is worth noting that this joint inversion scheme is originally used in MARE2DEM for the joint inversion of MT and CSEM, so the version of MARE2DEM in this thesis can invert MT, CSEM and TDEM data jointly.

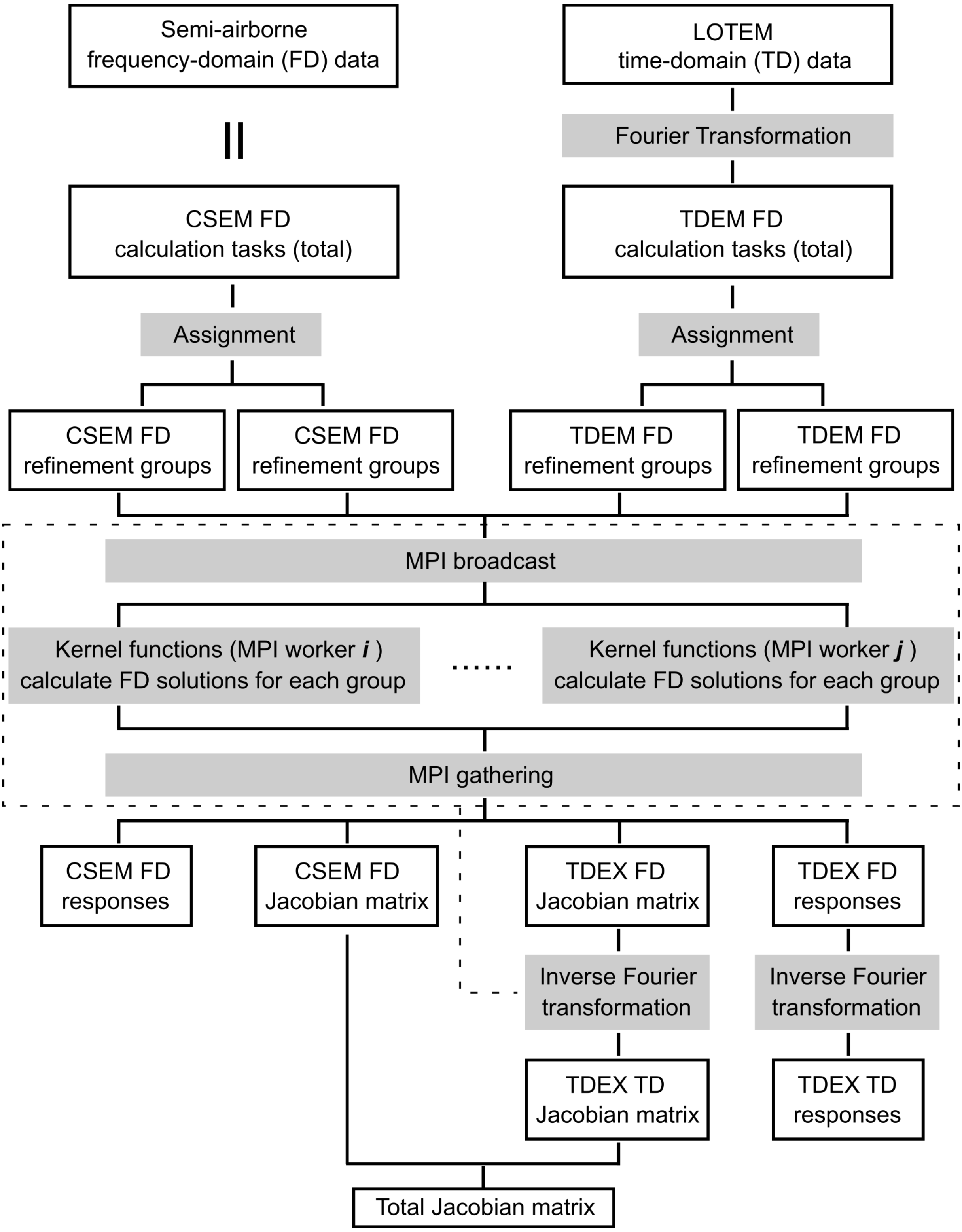

Figure 5.1: Schematic for the realisation of the joint inversion of frequency-domain and time-domain data in MARE2DEM.

5.1.5 Verification for semi-airborne numerical solutions of MARE2DEM

In this section, the accuracy of the numerical solutions calculated by MARE2DEM is verified by comparing to the 1D solutions of EMUPLUS (verified in section 4.1.1). The 1D resistivity model used in verification is designed according to main resistivity distributions shown in the 2D inversion result of Mörbe (2019). Background resistivity of the model is set to 500 $\Omega \cdot m$. A conductive layer of 10 $\Omega \cdot m$ and 250m thickness is buried 250m beneath the surface. Regarding semi-airborne measuring configuration, the transmitter has 1000m length and the broadside set-up is employed. The receivers are positioned in the air with an altitude of 40m. The offsets vary from 500m to 1500m. Figure 5.2 indicates not only the sketch of the 1D resistivity model used in verification but also the unrefined mesh input as the initial mesh for forward modeling in MARE2DEM. In the forward modeling, this raw frame is broadcast, and each of the worker processors finishes the consequent refinements of the mesh.

Since the receivers are positioned in the air, several additional adjustments are needed for

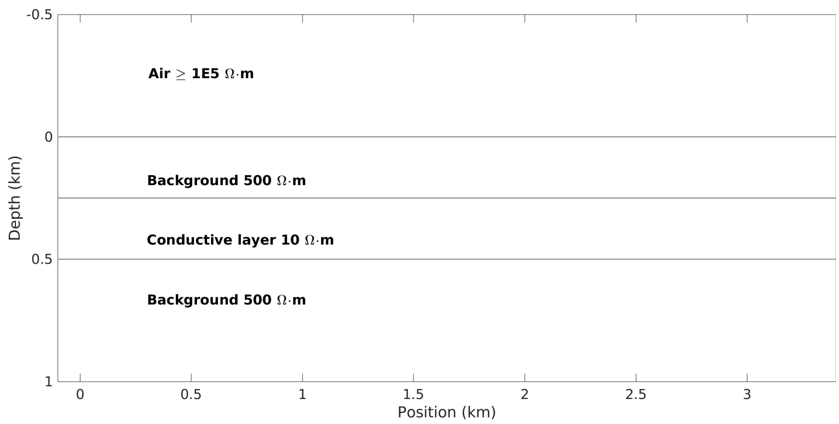

Figure 5.2: Unrefined mesh input as the initial mesh for forward modeling. The unrefined mesh frames the subsurface structure simply, final meshes for solution calculating are generated adaptively (E.g. Figure5.4 and 5.5).

the solutions accurate enough. Firstly, the wavenumber selection for numerical modeling has an effect on the accuracy of solutions. For MARE2DEM, a wavenumber range can be defined by users in the input file. After a suite of systematically testings or trails, the wavenumber range of 10^{-4} to 10^{6} m^{-1} are decided to be used for the following semi-airborne 2D modelings in this thesis. In the testings, a range smaller than 10^{-4} to 10^{6} m^{-1} could lead to the reduced accuracy of the solutions.

Another causal factor that contributes to the modeling accuracy is the quality of the adaptively generated mesh. For semi-airborne modeling, a possible relationship between air resistivity and the mesh quality is noticed. In Figure 5.3, semi-airborne solutions calculated by using air resistivity of 10^5 and 10^6 $\Omega \cdot m$ are displayed together with the corresponding 1D solutions calculated by EMUPLUS. The raw mesh shown in Figure 5.2 is used as the initial input for the numerical forward modeling. When the air resistivity of 10^5 $\Omega \cdot m$ is used (Figure 5.3a), the relative differences between 1D solutions and the 2D numerical solutions are almost smaller than 3%. If the air resistivity is changed to 10^6 $\Omega{\cdot}m$ (Figure 5.3b), the relative differences increase obviously. The largest value of relative differences could be 10%, and the curve of Bz responses show apparent oscillations.

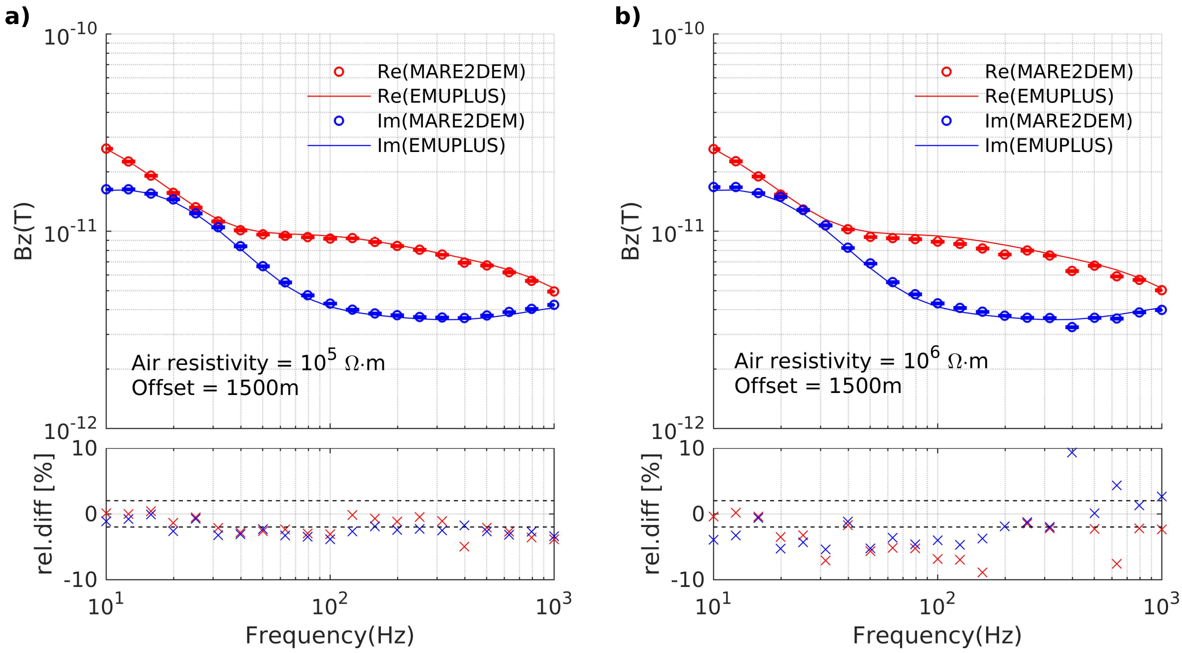

Figure 5.3: Comparison of semi-airborne 2D solutions when different air resistivity is used in the modeling. The air resistivity is set as a) $10^5 \Omega \cdot m$ and b) $10^6 \Omega \cdot m$. Transmitter length is 1000m and the offset is 1500m. Rx altitude is 40m. Unrefined raw mesh shown in Figure 5.2 is input as initial mesh.

For understanding the relationship between large air resistivity and the reduced accuracy of numerical solutions, the meshes generated by using air resistivity of 10^5 and 10^6 $\Omega \cdot m$ are compared. Figure 5.4 and 5.5 display two selected examples. Note again that the raw mesh in Figure 5.2 is used as the initial mesh here. All displayed meshes are generated when the frequency is set as 10Hz. Figure 5.4 compares the mesh generated with different air resistivity for wavenumber vectors range from 10^{-5} to 2.5×10^{-5} m^{-1} and Figure 5.5 for 3.3×10^{-3} to 8.5×10^{-3} m^{-1}. From both of the comparisons, one can found that the mesh is relatively more densely refined when the air resistivity is set as 10^5 $\Omega \cdot m$.

Obvious examples could be found in the regions highlighted by blue dashes. Even the

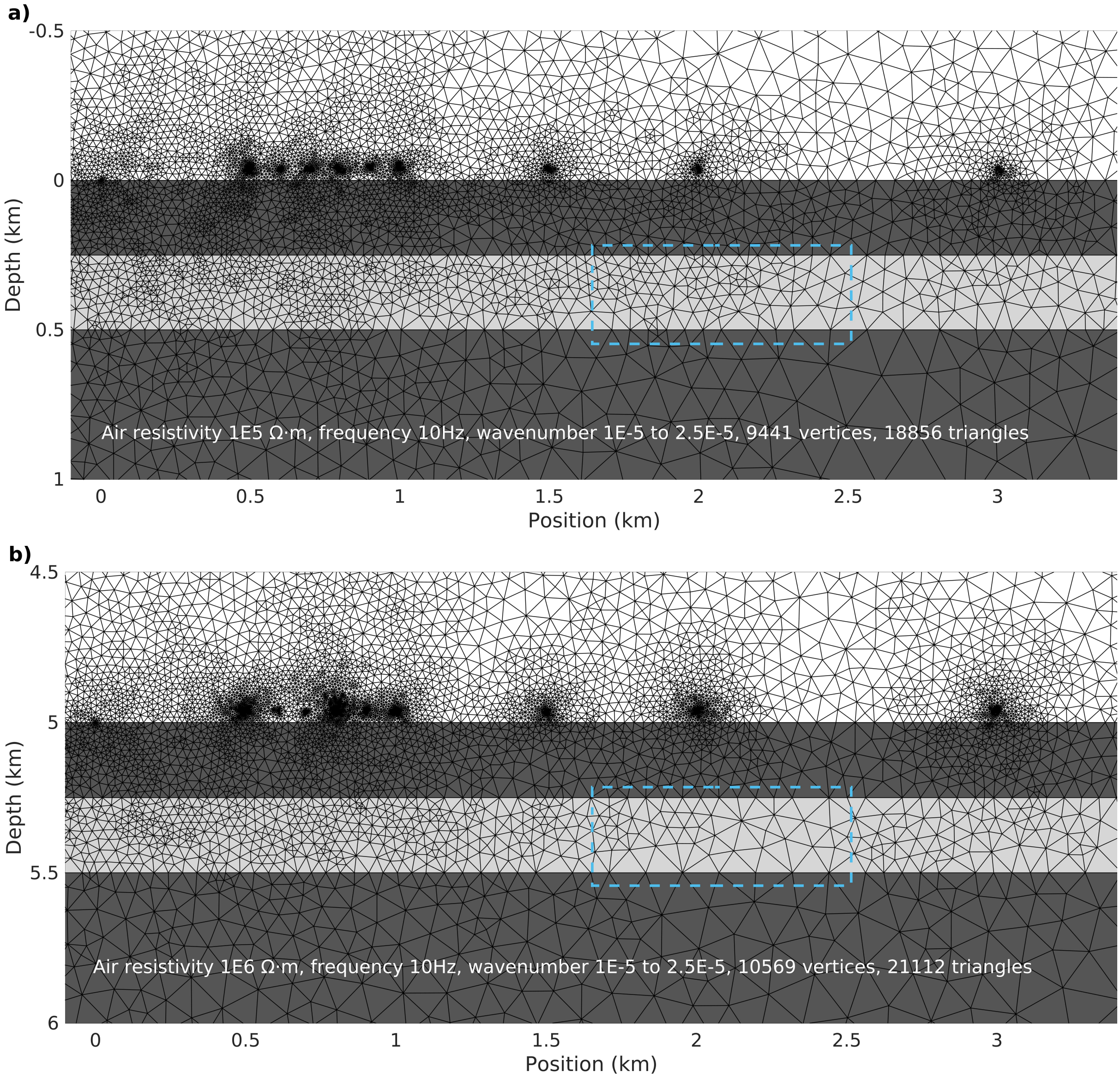

Figure 5.4: Comparison of final refined mesh when different air resistivity is used in the modeling. The air resistivity is set as a) $10^5 \Omega \cdot m$ and b) $10^6 \Omega \cdot m$. The frequency is 10Hz, wavenumbers range from 10^{-5} to 2.5×10^{-5}. Unrefined raw mesh shown in Figure 5.2 is input as initial mesh.

meshes generated with air resistivity of $10^6\ \Omega \cdot m$ have more vertices and triangles, the refinements are more focus in the air layer rather than the subsurface structure. The regions include resistivity contrasts can not get enough refinements, resulting in the obvious oscillations in the curves. Because the amount of produced meshes are too large for analysis, the reasons are still not confirmed for why the large air resistivity can result in the poorly refined mesh. Here, one possible hypothesis is presented. As mentioned in section 5.1.1, when the mesh is not refined enough, and the solution is not stable, large fields lead to large errors. The elements having the top 5% large errors are refined in the next refinement iteration. If the resistivity of air becomes larger, the slightly stronger fields lead the refinements to further concentrate on the region around the receivers, resulting in the meshes get less refined in subsurface structures. However, using a relatively low air resistivity (e.g., $10^5\ \Omega \cdot m$) in the modeling can not be satisfactory when the demand for joint inversion of semi-airborne and LOTEM is considered. Deviations are introduced in the LOTEM solutions when the air resistivity is set as $10^5\ \Omega \cdot m$ (see Section 5.1.6).

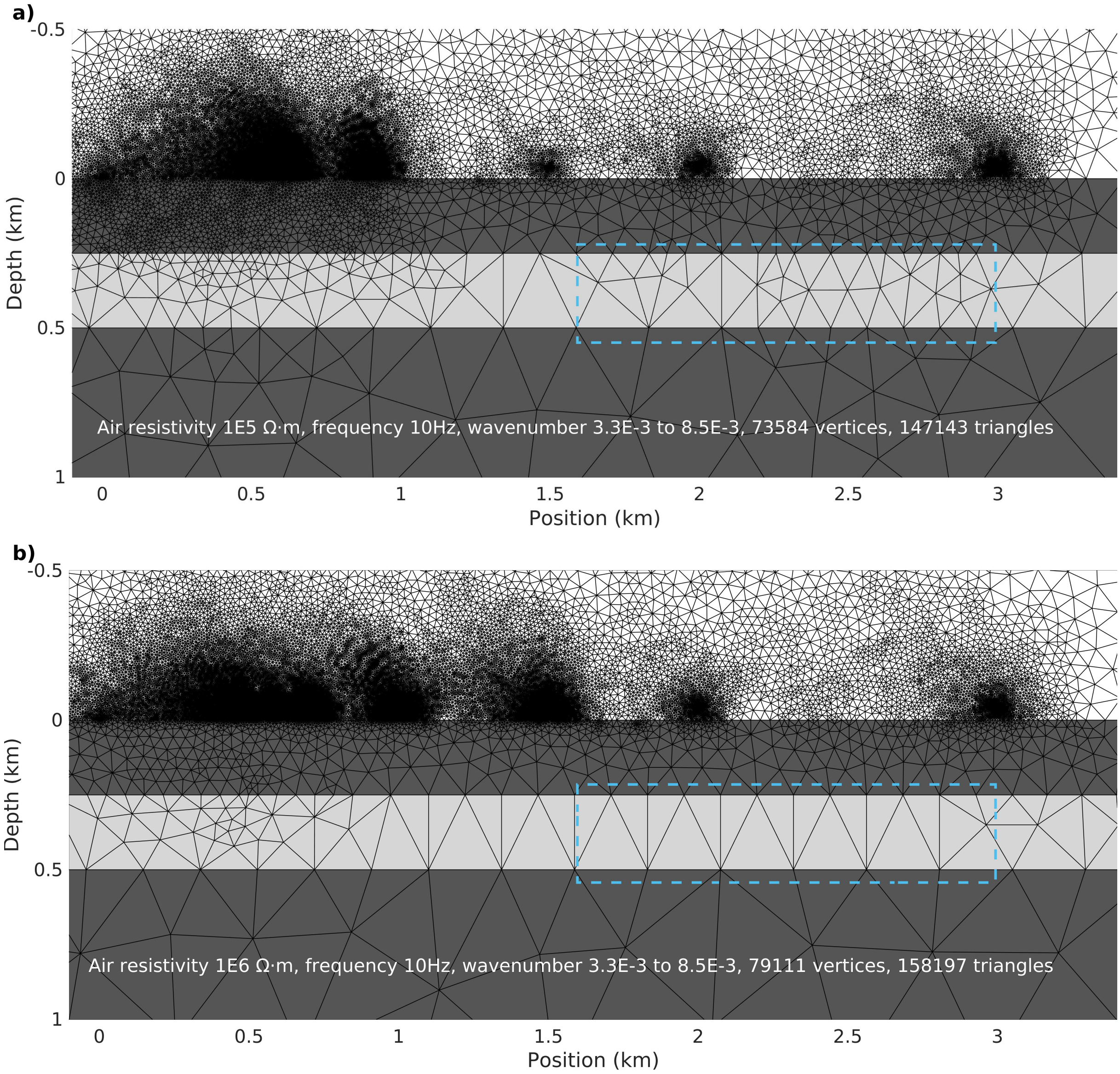

Figure 5.5: Comparison of final refined mesh when different air resistivity is used in the modeling. The air resistivity is set as a) $10^5 \Omega \cdot m$ and b) $10^6 \Omega \cdot m$. The frequency is 10Hz, wavenumbers are 3.3×10^{-3} to 8.5×10^{-3}. Unrefined raw mesh shown in Figure 5.2 is input as initial mesh.

On the other hand, with the knowledge that the reduced accuracy of semi-airborne solutions is led by the mesh problems, an alternative solution can be used to improve the modeling accuracy when the air resistivity is maintained as $10^6\ \Omega \cdot m$. The mesh can be refined previously by the users before it is input for the further adaptive refinements. Considering that the previous refinements are necessary for inversion, this alternative approach is acceptable for forward modeling too. Figure 5.6 displays the previously refined mesh for the same 1D resistivity model shown in Figure 5.2. Note that the air resistivity

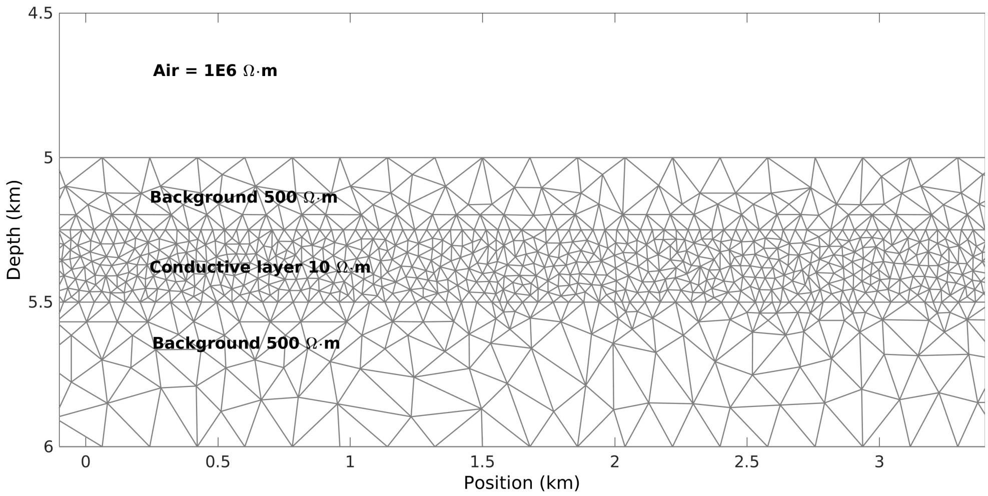

Figure 5.6: Previously refined mesh input as the initial mesh for forward modeling of MARE2DEM. The mesh is refined by user before input as initial mesh and it will be further refined adaptively during the modeling.

here is set as $10^6\ \Omega \cdot m$. The corresponding forward modeling results are presented in Figure 5.7, showing their significantly improved accuracy. The relative differences between 1D solution and numerical solution of MARE2DEM are always smaller than 2%. As mentioned, the previously refined mesh is usually required in inversion, so the high accuracy of semi-airborne modeling can be ensured in the following works of this thesis.

5.1.6 Verification for LOTEM numerical solutions of MARE2DEM

Mörbe (2019) presents the verification for LOTEM numerical solutions of MARE2DEM in frequency-domain. In this section, the time-domain LOTEM solutions calculated by MARE2DEM are verified via the comparison with the 1D solutions of EMUPLUS. Same as the case for semi-airborne, the EM responses used for comparison are calculated based on the 1D model shown in Figure 5.2. Transmitter length is 1000 m, and the receivers are deployed on land with offsets vary from 500m to 1500m. Because of the land-based receivers, it is not necessary to previously refine the mesh for LOTEM forward modeling.

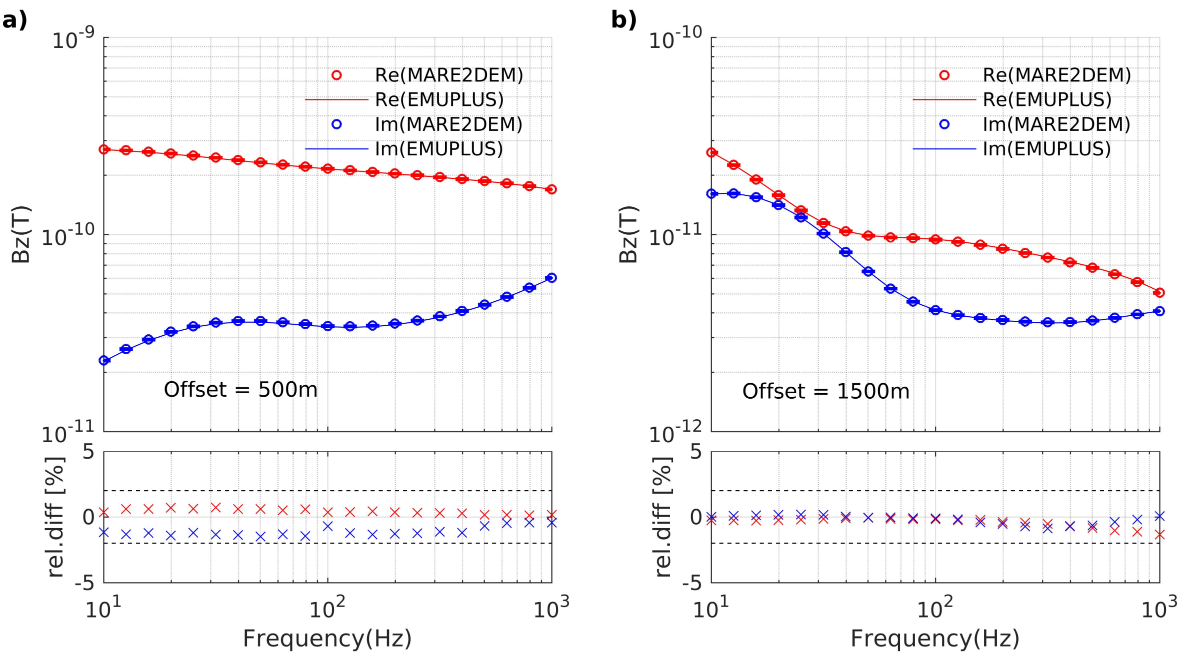

Figure 5.7: Validation of the semi-airborne 2D solution when pre-refined mesh is used in the modeling. The air resistivity is $10^6 \Omega \cdot m$. 2D solutions for offset equals 500m (a) and 1500m (b) are displayed.

For inversion modeling, the previous refinement applied by users and the adaptive refinement afterward could ensure the high accuracy of LOTEM numerical solutions.

Nevertheless, considering the demand for joint inversion of semi-airborne and LOTEM data, the setting of air resistivity is worthy of attention. In LOTEM and semi-airborne measurements, the air is actually considered as the insulator with an infinitely large resistivity. From the perspective of semi-airborne modeling, a relatively low air resistivity of $10^5\ \Omega \cdot m$ can improve the mesh refinements and result in accurate solutions while introducing no extra deviations. (see Section 5.1.5). Conversely, the $10^5\ \Omega \cdot m$ air layer causes deviations in the modeling of time-domain LOTEM data. Figure 5.8 compares the LOTEM numerical solutions calculated by MARE2DEM when different air resistivity are used in the modeling. A large enough air resistivity of $10^9\ \Omega \cdot m$ is used in the calculation, and the corresponding solutions are considered as the standard values (circles in Figure 5.8). When the air resistivity is set as $10^5\ \Omega \cdot m$, at most 10% relative differences are introduced in the solutions range from 10^{-4} to 10^{-3}s, meaning this relatively low air resistivity is not suitable for the required LOTEM modeling.

Fortunately, together with the previously refined mesh, the air resistivity of $10^6\ \Omega \cdot m$ can provide stable and accurate semi-airborne solutions. And $10^6\ \Omega \cdot m$ is also large enough for the calculation of LOTEM responses. Figure 5.9 shows the verification of LOTEM numerical data calculated when the air layer is set as $10^6\ \Omega \cdot m$. Between 1D solutions and the numerical results, the relative differences are always smaller than 2%.

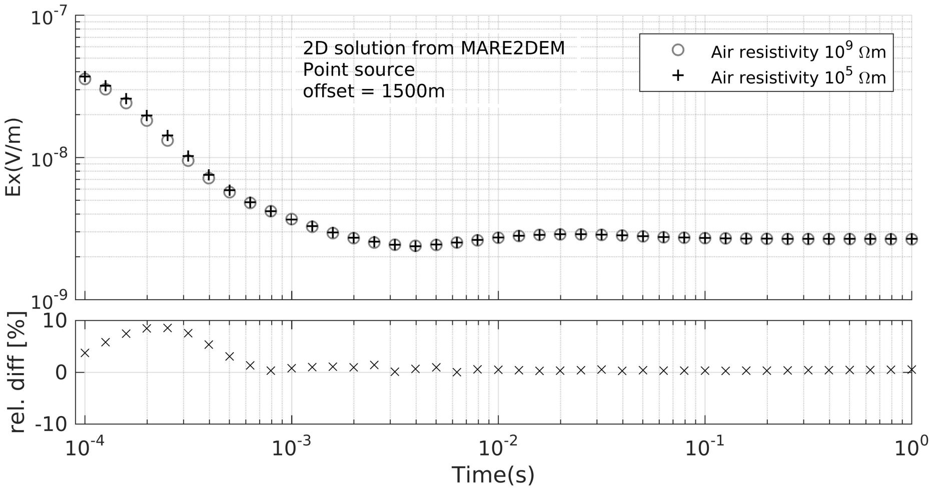

Figure 5.8: LOTEM numerical solutions calculated when different air resistivity are used in the modeling. The offset is 1500m and a point source is used for the calculation.

In order to guarantee the numerical modeling accuracy in the consequent studies, air resistivity is always set as $10^6\ \Omega \cdot m$, and wavenumber range of 10^{-5} to $10^6\ m^{-1}$ is utilized to fulfill the requirements of both semi-airborne and LOTEM modeling. For forward modeling tasks, the previously refined meshes are input.

5.2 2D joint inversion of semi-airborne and LOTEM data in frequency-domain

As mentioned before, time-domain LOTEM field data are transferred into frequency-domain by Mörbe (2019). From another aspect, the original MARE2DEM algorithm can fulfill both the inversion tasks of semi-airborne and frequency-domain LOTEM data. For comparison with the results calculated by time-domain LOTEM data, the 2D joint inversions are also applied to the semi-airborne data and frequency-domain LOTEM data. The content in this section includes the inversions for a synthetic model and the field data from eastern Thuringia. The analyses for the field data inversion results are presented as well.

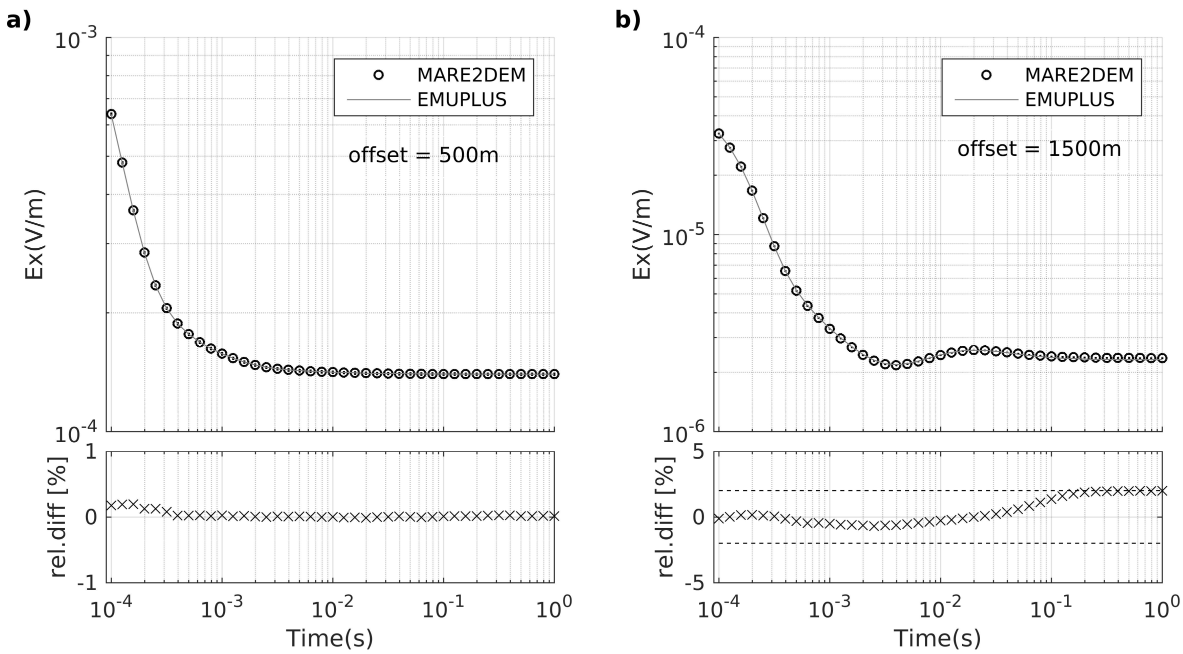

Figure 5.9: Validation of the LOTEM 2D solution in time-domain. The air resistivity is $10^6\ \Omega \cdot m$. Tx length is 1000m. 2D solutions for offset equals 500m (a) and 1500m (b) are displayed.

5.2.1 Application of 2D joint inversion on synthetic data

As the preparation for inverting field data, the 2D inversions are firstly applied to the data of a synthetic model. One of the purposes of this step is validating the 2D (joint) inversion algorithms for frequency-domain modeling. Moreover, the characteristics of 2D inversions for each individual EM methods can be investigated in this step, as well as for joint inversion. Because the true model is known, the performance of 2D inversions can be understood straightforward.

The synthetic model (Figure 5.10) is designed based on inversion results of field data in the next section (Section 5.2.2). It consists of the 1000 $\Omega \cdot m$ background and four conductive targets. Three small conductive bodies with the resistivity of 10 $\Omega \cdot m$ locate close to the earth's surface. Their buried depths range from 20m (the shallowest point at position 0.6km) to around 100m, and the thicknesses are 100m. A large conductive structure with the resistivity of 100 $\Omega \cdot m$ is buried at a depth around 700m while its thickness is 500m. The measuring configurations are the same as those employed in the field measurements and the real topography and are considered here. The transmitters used in semi-airborne measurements are denoted as big white circles, and the small yellow ones denote the transmitters used for LOTEM measurements. Regarding the receivers, the white ones in the air are used for semi-airborne, while the yellow ones on land are LOTEM stations. The same denotation is utilized for the plotting in the following of this thesis. Semi-airborne Bz component and LOTEM Ex components are simulated for the 2D resistivity model. Gaussian noises are added in the synthetic data before the inversions are applied. Semi-airborne data have 5% Gaussian noise, while LOTEM data have 2% Gaussian noise for amplitude and noises around 2 degrees for phase.

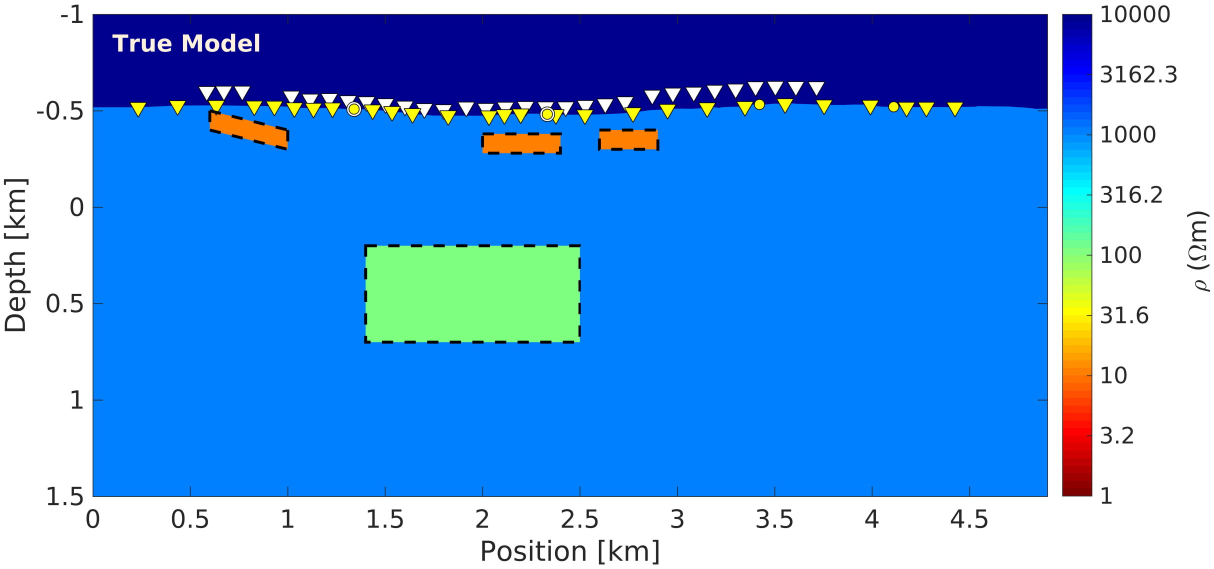

Figure 5.10: The 2D resistivity model used for the modeling study of semi-airborne and LOTEM joint inversion in frequency-domain.

The mesh for the 2D inversion is displayed in Figure 5.11. The real topography is considered, and the surface of the earth is defined around -500m in the vertical axis. This mesh is also used for the inversions taking all the LOTEM field data along with the profile into account in the next section. Therefore it has a length of around 9km in the horizontal direction. Considering the resolution of EM measurements usually decrease with increasing depth, the approximate triangle length is defined differently for different depths. For the triangle cells above -400m depth, the length is set to around 20m so that the topography and the shallow structures around the earth's surface can be simulated precisely. From -400 to -200m depth, the length of triangles is set to 30m approximately, and the value increases to 50m for the depth range of -200 of 0m. The length of triangle cells beneath the depth of 0m is set as 100m.

The 2D inversions are computed by the Cologne High Efficient Operating Platform for Science (CHEOPS). Usually, 60 to 100 processors are employed for these computations. The 2D inversion results are presented for semi-airborne (Figure 5.12a) and LOTEM (Fig-

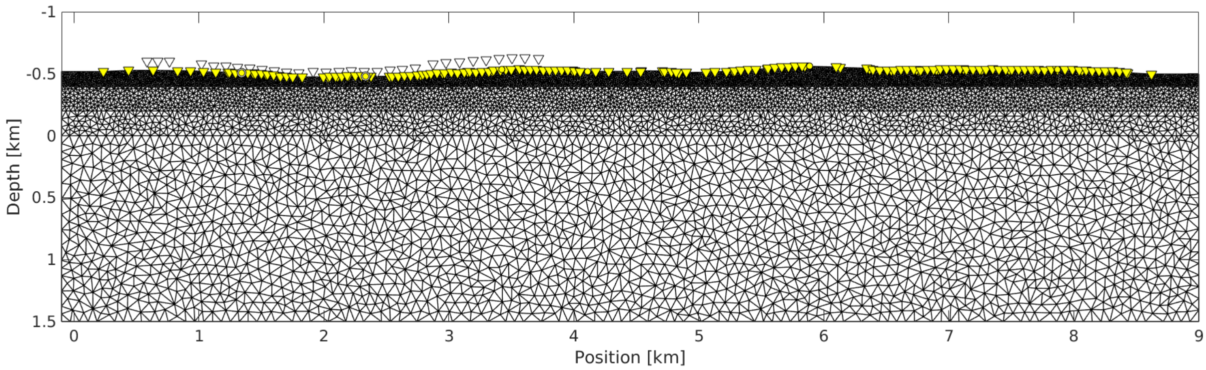

Figure 5.11: The mesh used for the 2D inversion which takes the LOTEM data of the whole profile into account.

ure 5.12b) single method inversions together with the consequent joint inversion (Figure 5.12c).

All of the three 2D inversions reveal all the conductive targets. However, some discrepancies between them still indicate the resolution differences. For the two shallow conductive targets lay between the horizontal position of 2 to 3km, LOTEM and joint inversion results clearly describe the boundaries, and the two bodies are distinguished from each other perfectly. In the semi-airborne inversion result, the two bodies are linked to each other by a conductive region with 100 $\Omega \cdot m$, which turns out to be a small artificial structure. For the deep target body, the inversion of only the LOTEM Ex components do not reveal the upper boundary of the deep structure clearly. The conductive region is extended to the depth around 0m at the horizontal position at 1.5km. On the other hand, semi-airborne inversion shows the worst resolution for the lower boundary of the deep structure. The lower boundary is extended to 1000m depth while the true depth is 700m. The joint inversion obviously presents the best result, and both the upper and the lower boundaries are clearly recovered.

In this synthetic study, the joint inversion algorithms of MARE2DEM in the frequency-domain is validated. Both LOTEM and semi-airborne single method inversions show the conductive targets but with different resolutions. The joint inversion combines the advantages of both EM methods and leads to the result better than the single method inversions.

Additionally, the same synthetic study is applied to the 2D model with the deep conductive target buried at a depth of 1400m. The 2D resistivity model and the corresponding inversion results are presented in Figure B.1 in the appendix. This example highlights the

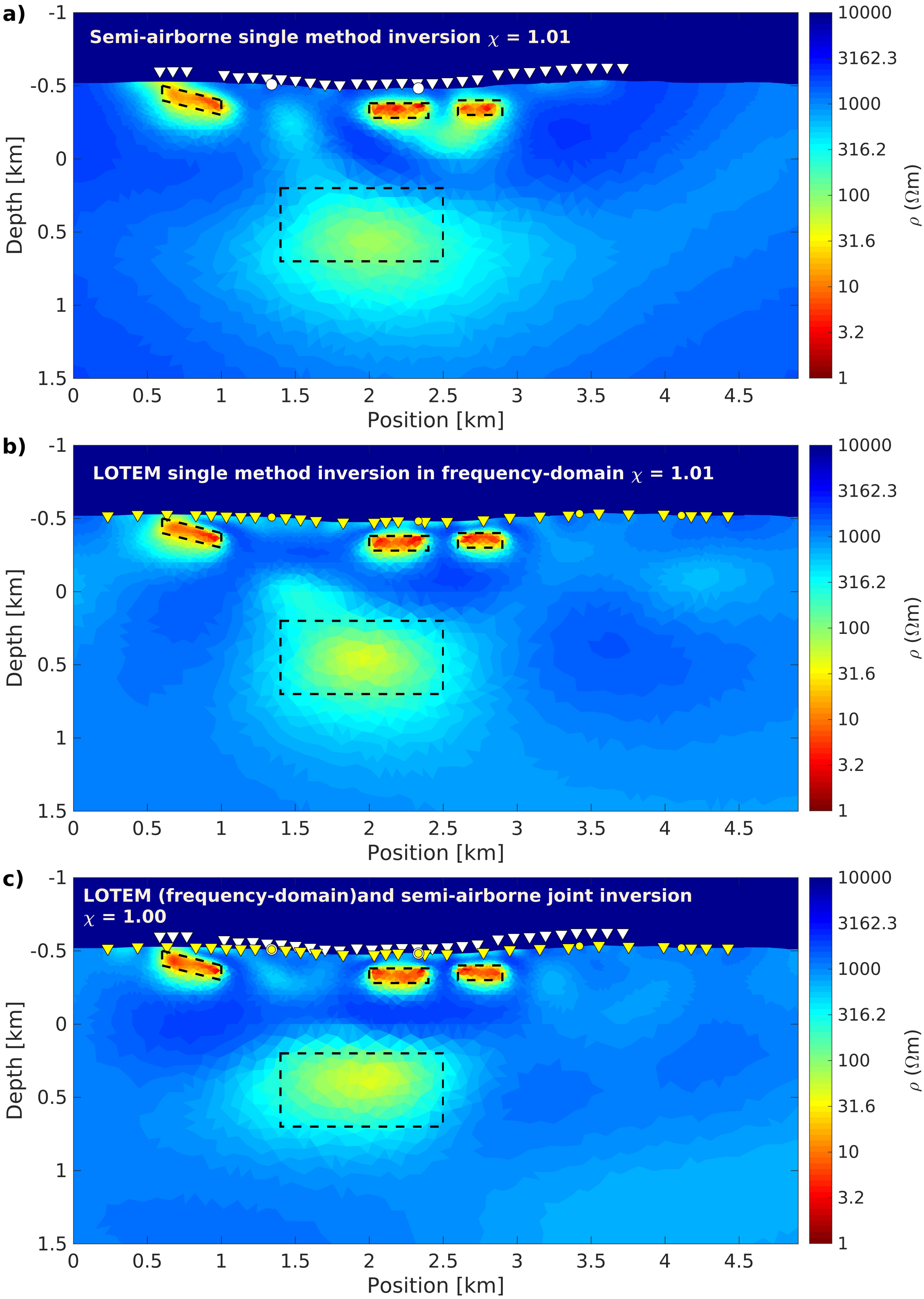

Figure 5.12: 2D inversion results for synthetic data of model in Figure 5.10. Results are displayed for the inversions of (a) semi-airborne data individually, (b) LOTEM data in frequency-domain individually and (c) LOTEM and semi-airborne data jointly.

advantage of LOTEM measurement in deep structure detection. Because the LOTEM stations are land-based, the long stacking times improve the data quality significantly. High-quality electric field data (Ex) can be measured at an offset of 4000m (Mörbe, 2019), which makes the detection of structures deeper than 1000m possible. Because the semi-airborne data also include some information from deep layers and can contribute to the constrain of shallow layers, the joint inversion result still shows better resolution than that of LOTEM single method inversion.

5.2.2 Application of 2D joint inversion on field data

In this section, the 2D inversions are applied to the field data measured in eastern Thuringia, Germany (Figure 2.4). The inversion mesh in Figure 5.11 is utilized for all the inversions in this section. Before the joint inversion, the semi-airborne field data are inverted individually. At the first beginning, all the possible data are considered in the 2D inversion. However, the 2D inversion can not converge properly and results in the unsatisfactory data misfit (AppendixB.2: Figure B.2). The possible reasons could be the distortion of the data led by some unconsidered factors like 3D effects or anisotropic, or the error bounds are not estimated perfectly for all of the data. Known from Smirnova et al. (2019), due to the moving receivers in the air, the semi-airborne data have relatively large standard deviations, and the error estimations could be challenging in some cases. Therefore, the first step is selecting the data used in the 2D inversion. Some parts of data are considered to be not suitable to join the 2D inversion for the following four reasons.

Firstly, the data measured in the vicinity of the transmitters are not used in the inversion. For frequency-domain semi-airborne EM, the recorded data are dominated by the transmitter effects when the receivers are too close to the transmitter. In the 3D inversions of Smirnova et al. (2019), repeated data sets over the fixed flight area are acquired, but for different source locations. This approach allows the gaps in data coverage over the source positions to be filled. Practically, using data obtained with the first transmitter, the gap at the second source position can be filled and vice versa. Therefore, Following Smirnova et al. (2019), all the semi-airborne data acquired with offsets smaller than 500m are not taken into account in this thesis.

Secondly, the data from remote receivers are also removed. As, presented in Smirnova et al. (2019), the amplitude of the semi-airborne responses decays with the increasing offsets. For large offsets, the measured data are relatively week and close to the noise level. In order to reduce the possible uncertainties, only the data from offsets smaller than 1500m are considered in this thesis. Note that the threshold of 1500m may not be the best one. In the research of Smirnova et al. (2019), the data from offset 1800m are also taken into account.

The third unused part is the data measured in high frequencies. The high-frequency signal strength in general may be low and therefore the offset is more limited. On another hand, the high-frequency data provide less information for the interesting depth because of the limited skin depth (also demonstrated by Smirnova et al. (2019)). Therefore, in this case, inverting high-frequency data may increase the data misfits while introducing little new information in the inversions. In the following inversions, data acquired in frequencies larger than 1000Hz are not utilized.

At last, the data acquired in low frequencies are also not considered. According to Smirnova et al. (2019), the semi-air data usually have large uncertainties in low frequencies. The error estimate for low frequencies could be 20% of the amplitude. Because of the low data sample rate, the quality and error estimations of this part of data maybe not perfect. Here, the data for frequencies larger than 58Hz are considered. Smirnova et al. (2019) uses the data also from 28Hz.

The final decision of data selection is presented in Figure 5.13. Gray crosses denote all the measured data of Tx-B3 and black dots for those of Tx-B4. Purple squares and orange circles denote the selected data for Tx-B3 and B4, respectively. The selected data correspond to frequencies range from 58 to 1000 Hz, and offsets range from 500 to 1500m. However, even though the four reasons mentioned above are reasonable, the final data selection in Figure 5.13 may not be the best one. The exact threshold for each aspect is decided independently based on personal experience. Compared to the data-sets selected by Smirnova et al. (2019) (E.g. Figure 5.32), the data from one low frequency (28Hz), one high frequency (1096Hz), and 3 remote receivers around Y-4000m are not used. Contrarily, data from 10 more frequencies in the middle are taken into account. The 2D inversion for the selected data converges well. The inversion result is displayed in Figure 5.14b, and the data fit is presented in Figure 5.15. As shown in Figure 5.15a and b, all the residuals are smaller than 10. One of the worst fitted stations (highlighted in a and b by the purple rectangles) is displayed in 5.15c, showing an acceptable data fitting too. Additionally, the variation of data misfits as a function of iterations is presented in 5.15d for the inversion of selected data-sets (orange line) and all the possible data. Obviously, after the selection of the data, the 2D inversion converges much better. It is worth mentioning that the data selection in Figure 5.13 is further validated accidentally by the studies of 3D effects in

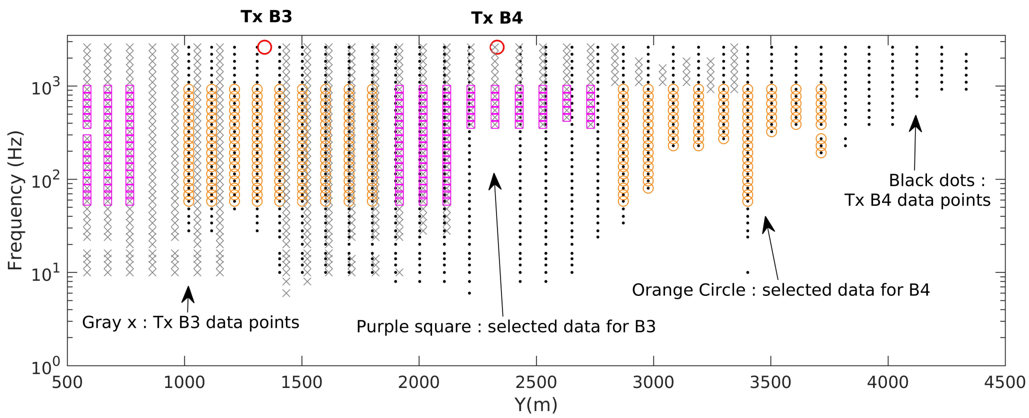

Figure 5.13: Semi-airborne data distribution along the LOTEM profile.

Section 5.4. The 2D inversion result calculated by the data-sets of Smirnova et al. (2019) (Figure 5.31a)) shows very high similarity with the results displayed in Figure 5.14b.

Because of the good data fitting, the 2D inversion result in Figure 5.14b is considered to be significant. Consequently, some different inversion parameters are tested in order to validate the 2D inversion result further. Similar to the ideas of checking equivalence or different roughness norms in 1D inversion, if one structure shown in the inversion result is unimportant, it is possible that the structure shifts significantly or disappears when the inversion parameters are changed. Therefore, different regularization values and horizontal-vertical weight (w_{hv} in equation 5.10) are tested. For the result shown in Figure 5.14b, the Lagrange value begins from 5 and end with 1.15. The horizontal-vertical weight is set as 3, meaning that the horizontal smoothness is enhanced three times than the vertical smoothness. Additionally, starting Lagrange value ranges from 5 to 50, and horizontal-vertical weight ranges from 1 to 100 are tested. In these results, the shape of the conductive bodies may change, but the main resistivity distribution always stays the same. One example is presented in Figure B.3 for the inversion result calculated by using the starting Lagrange Value of 10 and the horizontal-vertical weight of 10. Considering the huge computations costs for the similar tests and the fact that the regularization values and horizontal-vertical weights do not significantly change the main resistivity structures in this example, the Lagrange Value always starts from 5 for the following 2D inversions in this thesis and the horizontal-vertical weight is always set to 3. On another hand, one different mesh is also utilized for the inversion of semi-airborne field data. The inversion result maintains similar resistivity distributions, which will be further discussed in the next section.

In Figure 5.14b, four conductive structures can be obviously distinguished. They are

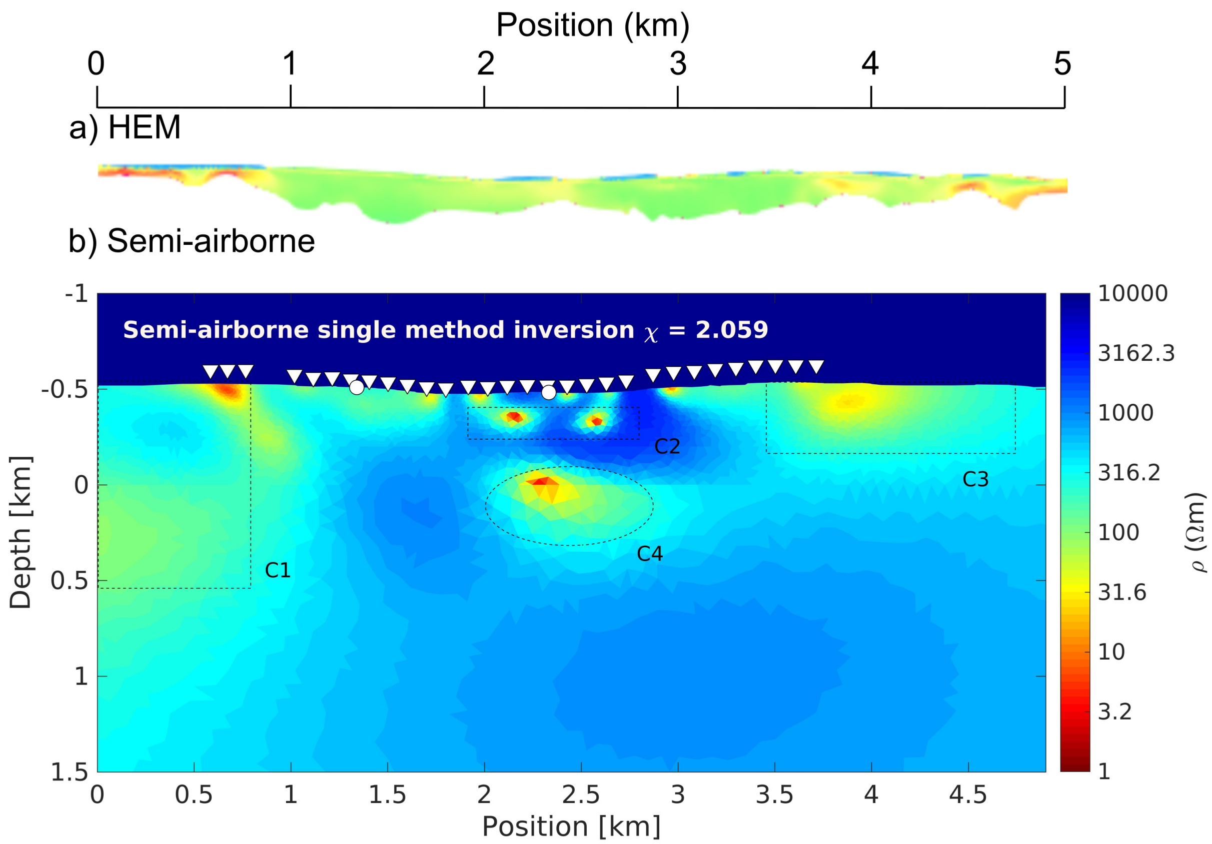

Figure 5.14: Comparison between (a) the 1D inversion results of HEM data (Steuer et al., 2015) and (b) the 2D inversion result of semi-airborne field data.

highlighted by the black dashes and marked as C1 to C4. For validating these detected structures, the HEM profile (selected from Figure 4.30a) in this region is attached as Figure 5.14a. Known from the comparison, the conductive structures C1 and C3 can be validated by HEM measurement. A conductive region is also detected by HEM measurement around the horizontal position of 2.5km, which may correspond to C2 in the semi-airborne result. C4 locates at a depth of around 500m (beyond the DOI of HEM). For the positions of conductive structures in shallow layers, it is promising to see that the results of HEM and semi-airborne fit well with each other. However, it is still a question that if the shapes or resistivity distributions of these shallow conductive structures are true. Moreover, based on Figure 5.14, if C4 is a true structure can not be confirmed yet.

Next, the horizontal electric fields (Ex) measured by the LOTEM survey are inverted individually. The large mesh shown in Figure 5.11 is used for taking all the LOTEM data along with the profile into account. A large amount of data points is one of the reasons for the large data fit of LOTEM inversion. The LOTEM inversion result is the same as that shown by Mörbe (2019), although the mesh is different. However, from the perspective of

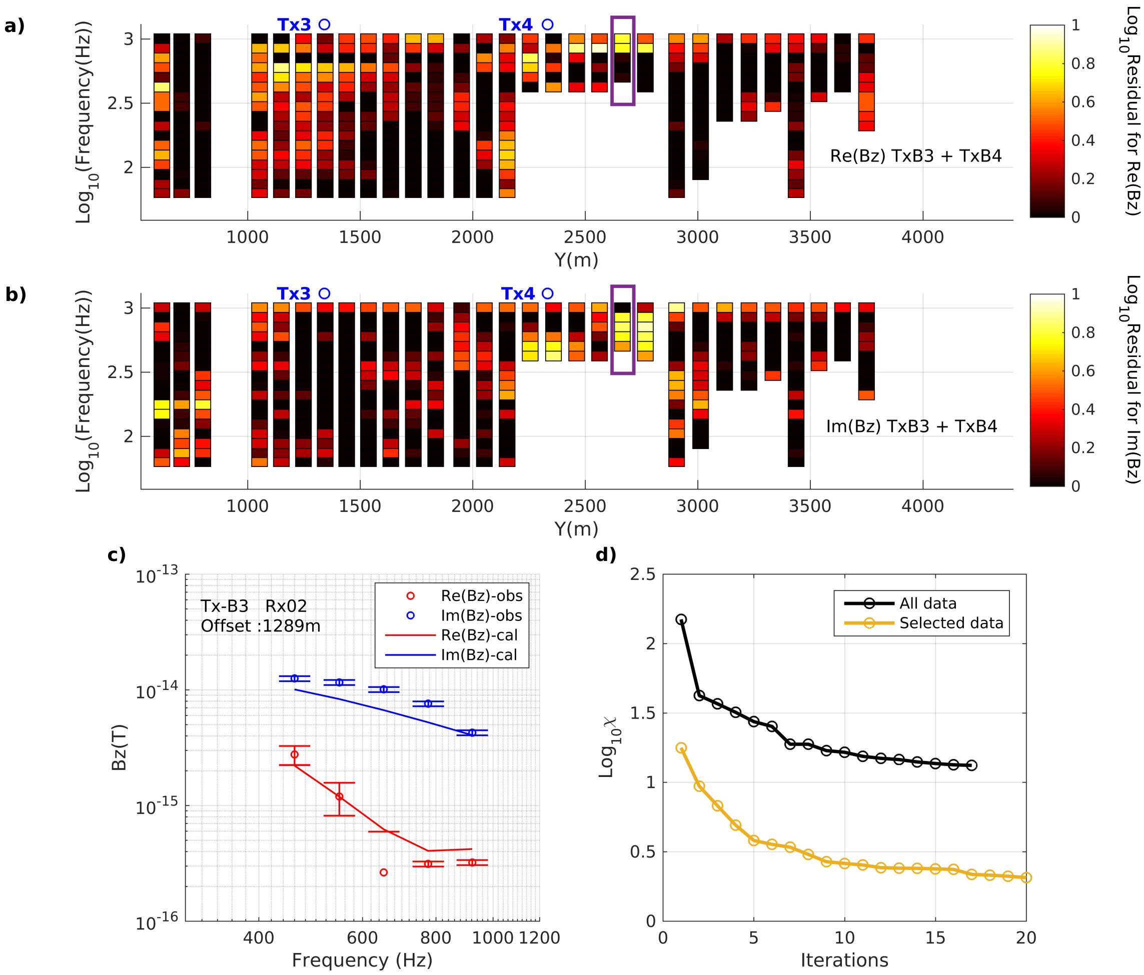

Figure 5.15: Data fitting for the semi-airborne single method inversion result in Figure 5.14b. Residuals of the inversion are displayed for (a) real part of Bz and (b) imaginary part of Bz; (c) shows one of the worst data fitting which is also highlighted in (a) and (b) with purple rectangle; note that the field data put into MARE2DEM for inversion are normalised by transmitter length;(d) shows the decreasing of data misfits as a function of iteration numbers for the 2D inversion result in Figure 5.14b and B.2a.

joint inversion (the main focus of this thesis), the interesting area should be kept the same as the region for the semi-airborne measurement. Therefore the LOTEM single method inversion result is displayed in Figure 5.16 for the same area as that in Figure 5.14b. The same black dash for highlighting conductive structures C1 to C4 in Figure 5.14b are also presented in Figure 5.16 for convenient comparison. There are still conductive structures in the highlighted regions of C1 to C3, but the resistivity distributions are obviously different. For example, the C2 is no longer consist of 2 small conductive bodies. The isolated C4 in Figure 5.14b disappears in the LOTEM inversion result. Instead, a continuous conductive zone around 100 $\Omega \cdot m$ occurs on the left side of C4's original position. It is worthy of mentioning that the significant conductive body locates beneath C3 is the main target in the inversion of Mörbe (2019). Because the semi-airborne measurements in 2016 did not cover this area, this structure is not discussed in this thesis.

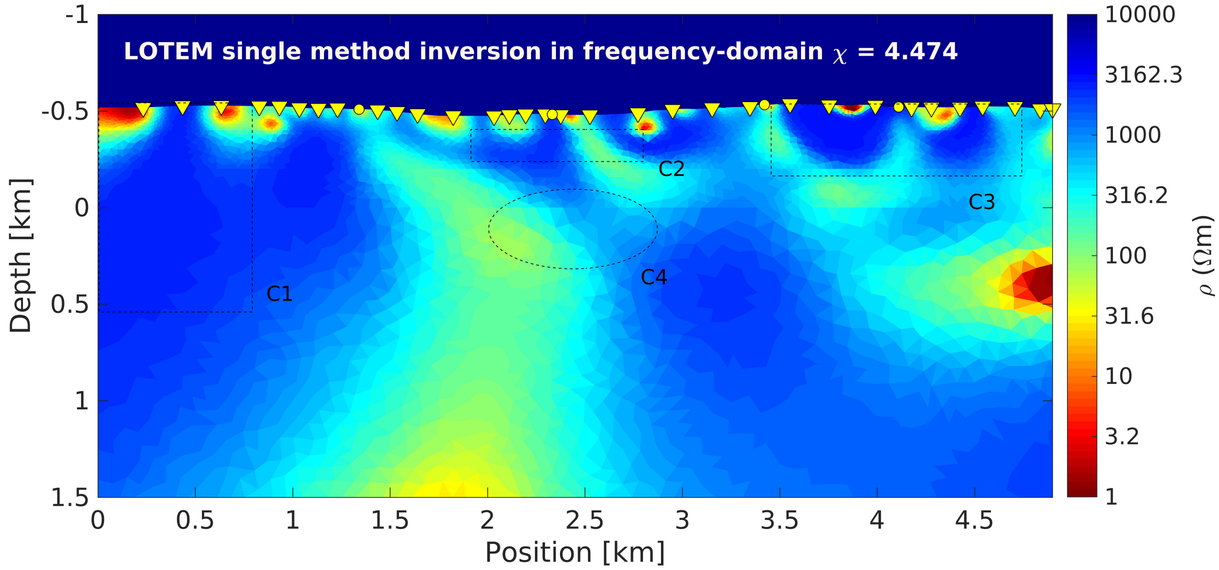

Figure 5.16: 2D inversion result of LOTEM field data in frequency-domain.

The 2D joint inversion is consequently applied to the semi-airborne data and LOTEM data. The inversion result is displayed in Figure 5.17, together with the highlighting of C1 to C4. Because the value of data misfit χ of joint inversion is only 0.04 larger than that of LOTEM single method inversion, it can be regarded that both semi-airborne and LOTEM data can be interpreted by the inversion result. The misfit of semi-airborne data in the joint inversion is presented as residuals in Figure B.4. Compared to the inversion of only LOTEM data, one outstanding variation is the two small conductive bodies in C2 appear again. Regarding C1 and C3, the effects of taking semi-airborne data into account is also obvious. The distribution of the conductive zone beside C4 is slightly changed, but the isolated conductive body in the semi-airborne inversion result is still missing. In general, the joint inversion result is affected by both semi-airborne and LOTEM data in shallow layers and dominated by LOTEM data in deep parts.

The next question is if the joint inversion result in Figure 5.17 already presents the true resistivity distributions in the subsurface of the measuring field. In another word, if the model is the true model is a question. The validation of the LOTEM data inversion result from the view of geology is presented by Mörbe (2019). In this thesis, this question is investigated from the view of joint inversion. Figure 5.18 shows the plan for the following testing. The 2D resistivity model in Figure 5.17 is regarded as the "True model", then the predicted data or calculated data of this model can be regarded as the "observed

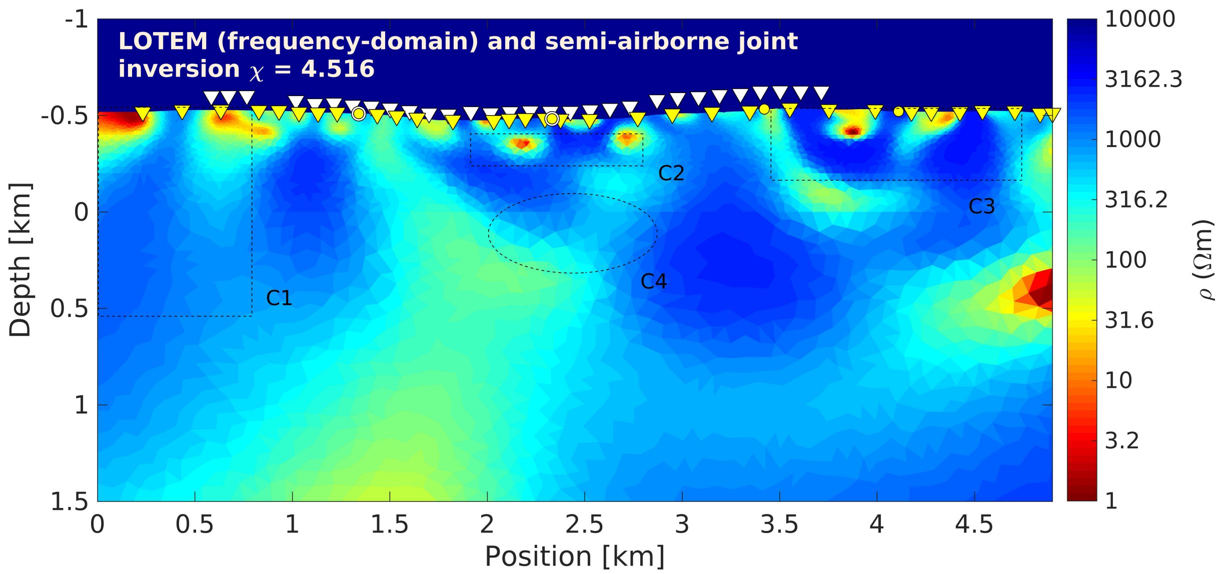

Figure 5.17: 2D joint inversion result of semi-airborne data and frequency-domain LOTEM data.

data". These synthetic "observed data" include semi-airborne data as well as LOTEM data, and they are inverted, respectively. Because there is no 3D, anisotropic, or IP effects are included in the synthetic "observed data", the difference between semi-airborne and LOTEM single method inversion results are purely leaded by the resolution difference of these two EM measurements. Afterward, the single method inversion results of synthetic "observed data" are compared to those of true field data (Figure 5.14 and 5.16). By these steps, the two following questions can be answered:

- if the predicted semi-airborne and LOTEM data-sets have different resolutions for the "True model" (Figure 5.17)?
- if the resolution differences exist, can they explain the discrepancies between the 2D inversion results of field data of semi-airborne (Figure 5.14) and LOTEM (Figure 5.16)?

Gaussian noises are added in the predicted data before single method 2D inversions are

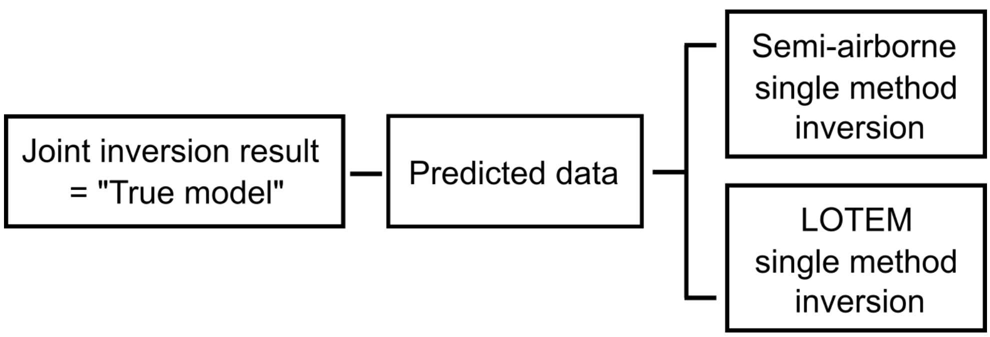

Figure 5.18: Schematic for the sensitivity testing of semi-airbrone and LOTEM single method inversion.

applied: 5% for semi-airborne data, 2% for LOTEM amplitude and around 2 degree for LOTEM phase. The inversion results are displayed in Figure 5.19a for semi-airborne and b for LOTEM.

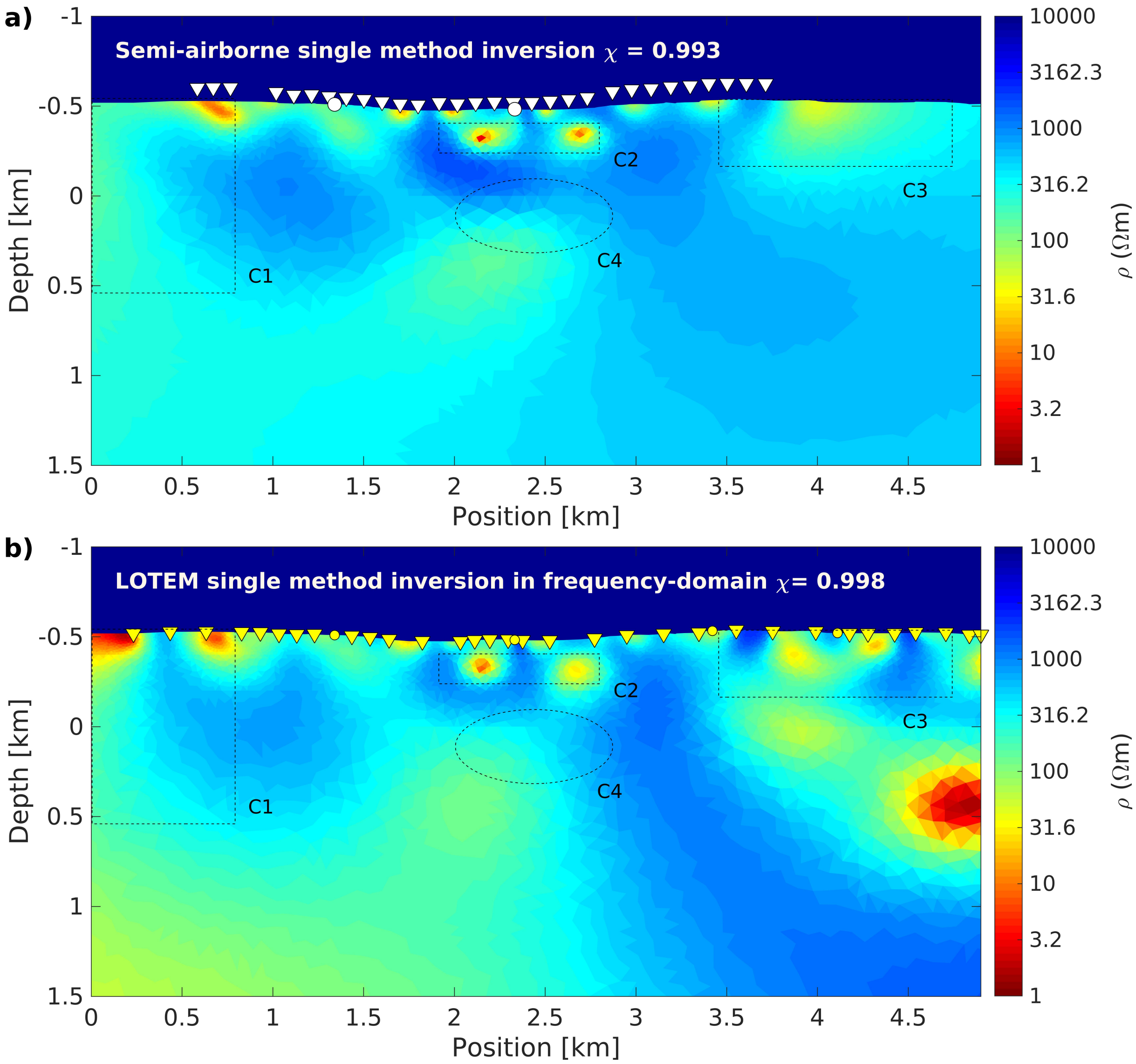

Figure 5.19: Semi-airborne (a) and frequency-domain LOTEM (b) single method inversion results for the predicted data of field data joint inversion results shown in Figure 5.17.

By comparing Figure 5.19a and b, the resolution differences between semi-airborne and LOTEM measurements for the "True model" can be investigated. The two results are similar at first glance, especially for the deep structures (beneath 0m) on the left side of the horizontal position 3km. Regarding the big conductive body under C3 in 5.19b, it is validated again that it can not be detected by the semi-airborne configurations employed here. However, the resolutions difference can be noticed when the small structures are checked. The C1 and C3 in the two figures are obviously different. Considering the position of the receivers, the differences between C1 and C3 are largely decided by the measuring configurations. There is no semi-airborne receiver close to horizontal positions of 0.2km and 4.3km. Naturally, the corresponding two small conductive bodies close to the earth's surface can not be revealed in semi-airborne inversion results. The C2 structure is consists of two small conductive bodies in both results, but it turns out that semi-airborne inversion has a better resolution for the right small conductive body. Therefore, it is a fact that there are resolution differences between the predicted semi-airborne and LOTEM data-sets.

However, these resolution differences can only partly explain the discrepancies between the 2D inversion results of field data for semi-airborne and LOTEM single method inversions. For C1 and C3, the resistivity distributions are highly similar between Figure 5.19a and Figure 5.14, also similar between Figure 5.19b and Figure 5.16. Therefore, the same as discussed in the last paragraph, semi-airborne and LOTEM inversions reveal C1 and C3 differently because the receiver positions are different. But the different resolution or measuring configurations can not be the explanations for divergences for C2 and C4. The two small conductive bodies are revealed by the inversion of predicted LOTEM data for "True model" (Figure 5.19b) but not in the field data inversion result (Figure 5.16). Moreover, the isolated conductive body in C4 revealed by semi-airborne field data doesn't appear in Figure 5.19a. Instead, the deep structures similar to LOTEM results are revealed.

Because the inversion results in Figure 5.19 are different from the corresponding single method inversion results of field data in several aspects, the joint inversion result in Figure 5.17 can not be regarded as true resistivity distributions in the real world. The unexplained divergences between field data inversion results may be caused by some other factors.

5.3 2D joint inversion of semi-airborne data and LOTEM time-domain data

In this section, the 2D joint inversions are applied to the semi-airborne data (in frequency-domain) and the LOTEM data in time-domain. Conventionally, the LOTEM data are acquired in time-domain and also processed and inverted in time-domain (E.g.Strack et al. (1990); Haroon et al. (2015)). The advantages of time-domain methods are also introduced by several previous researchers (E.g.Strack (1992); Streich (2016); Zhdanov (2010)). The detailed comparison between the inversions of frequency- and time-domain LOTEM data is presented by Mörbe (2019). In this thesis, in order to investigate the effects of 2D joint inversion from an additional aspect, the LOTEM data in time-domain are also taken into account. The time-domain data are modeled individually or jointly by the steps described in Figure 5.1. Transient includes 24 time points range from 0.0005 to 0.4s are used for the time-domain 2D inversion in this section (Mörbe, 2019). Because the frequency-domain solutions correspond to around 120 frequencies are required to calculate the time-domain data for 24 time points, the time-domain modeling is much more time consuming than the frequency-domain modeling. Similar to the last section, the 2D inversions are firstly applied to the synthetic data and then the field data from eastern Thuringia, Germany.

5.3.1 Application of 2D joint inversion on synthetic data

By conducting the synthetic studies, the resolution characteristics of semi-airborne and time-domain LOTEM data can be compared, and the effects of consequent joint inversion can be investigated. Because the 2D joint inversion on frequency- and time-domain data are newly implemented in MARE2DEM, the algorithm needs to be validated first. For this step, a canonical 2D resistivity model is considered (Figure 5.20). A 2D conductive layer with a thickness of 100m is buried 250m beneath the earth's surface. The resistivity of the conductive layer is 10 $\Omega \cdot m$, while the background is 300 $\Omega \cdot m$. The deep structures start to change at a depth of 650m. A resistivity contrast is set at the horizontal position of 0km. The basement is 50 $\Omega \cdot m$ on the left side and 1000 $\Omega \cdot m$ on the right side. As discussed in the last section, the resolution differences shown in the inversion results of two EM measurements is decided not only by the measured EM field (e.g., Bz and Ex), but also by the employed measuring configurations. In order to focus on the resolution differences caused by the measured EM field, the horizontal positions of the receivers are set to be the same for semi-airborne and the LOTEM. Naturally, the LOTEM receivers are land-based, and the semi-airborne receivers have an altitude of 40m. Two same transmitters are also employed for both methods. The same as before, 5% Gaussian noise is added on the semi-airborne synthetic data, while 2% Gaussian noise is added on LOTEM horizontal electric fields in time-domain. Note that the same inversion mesh is used in following 2D inversions, the starting Lagrange value and the horizontal-vertical weight are always set as 5 and 3, respectively.

Figure 5.21 displays the results for the 2D inversions of only semi-airborne magnetic field (a), only LOTEM electric field (b) and both of them (c). All of these three inversion results have ideal data misfit (χ close to 1.0) while display different resistivity distribu-

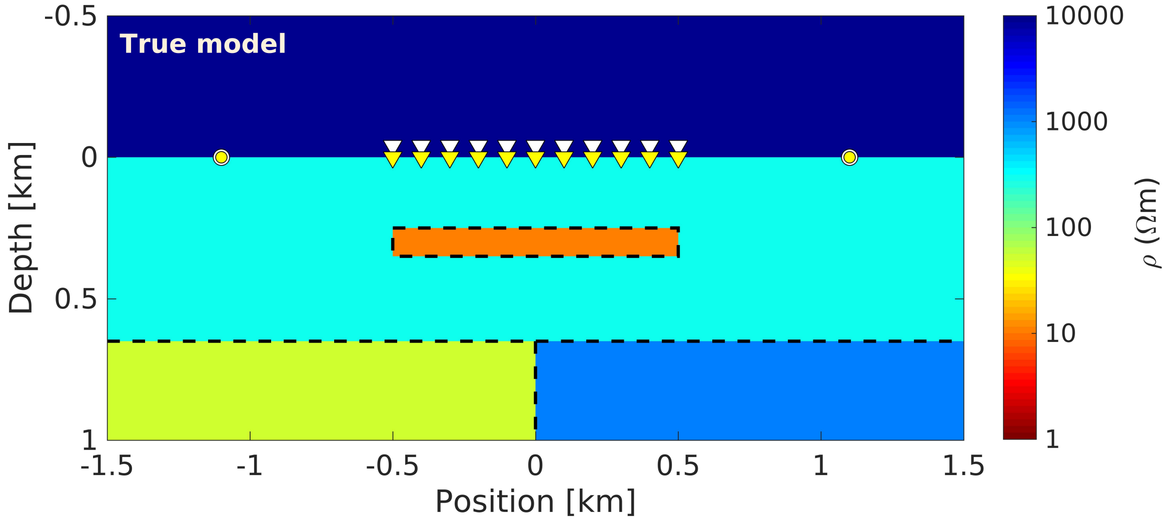

Figure 5.20: The first 2D resistivity model used in the modeling study for the joint inversion of semi-airborne and LOTEM time-domain data.

tion, indicating that the joint inversion of frequency- and time-domain data performs well. Known from the comparison of Figure 5.21a and b, the resolution differences are obvious between the inversions results of the Bz component from semi-airborne and Ex component from LOTEM. For the shallow conductive layer, semi-airborne inversion result shows significantly better resolution. The upper boundary and both the horizontal boundaries are revealed perfectly. Compared to semi-airborne, the inversion result of LOTEM horizontal electric fields shows the weakness in revealing all these three boundaries. Because of combining the different resolutions of these two components, the joint inversion of them shows a significantly promising result (Figure 5.21c). Not only the upper and horizontal boundaries of the shallow conductive layer are perfectly described, but also the lower boundary is recovered. Moreover, the resistivity basement on the right side of the model is perfectly revealed in Figure 5.21c. The rectangle-like boundary is clearly shown, and the resistivity is also restored to the true value of 1000 $\Omega \cdot m$. Unfortunately, the resistivity contrast is not pronounced as good as the resistive side for the conductive side. In general, the resolution of the joint inversion result is significantly better in comparison to the inversions use single EM component.

The second synthetic model shown in Figure 5.22 is designed based on the inversion results of field data. The three small conductive bodies buried in the shallow part are designed according to the C1 to C3 structures that occur not only in the field data inversion results in the last section but also in the 3D inversion of semi-airborne field data (Figure 5.30, Smirnova et al., 2019). The 2D joint inversion applied to semi-airborne and time-domain

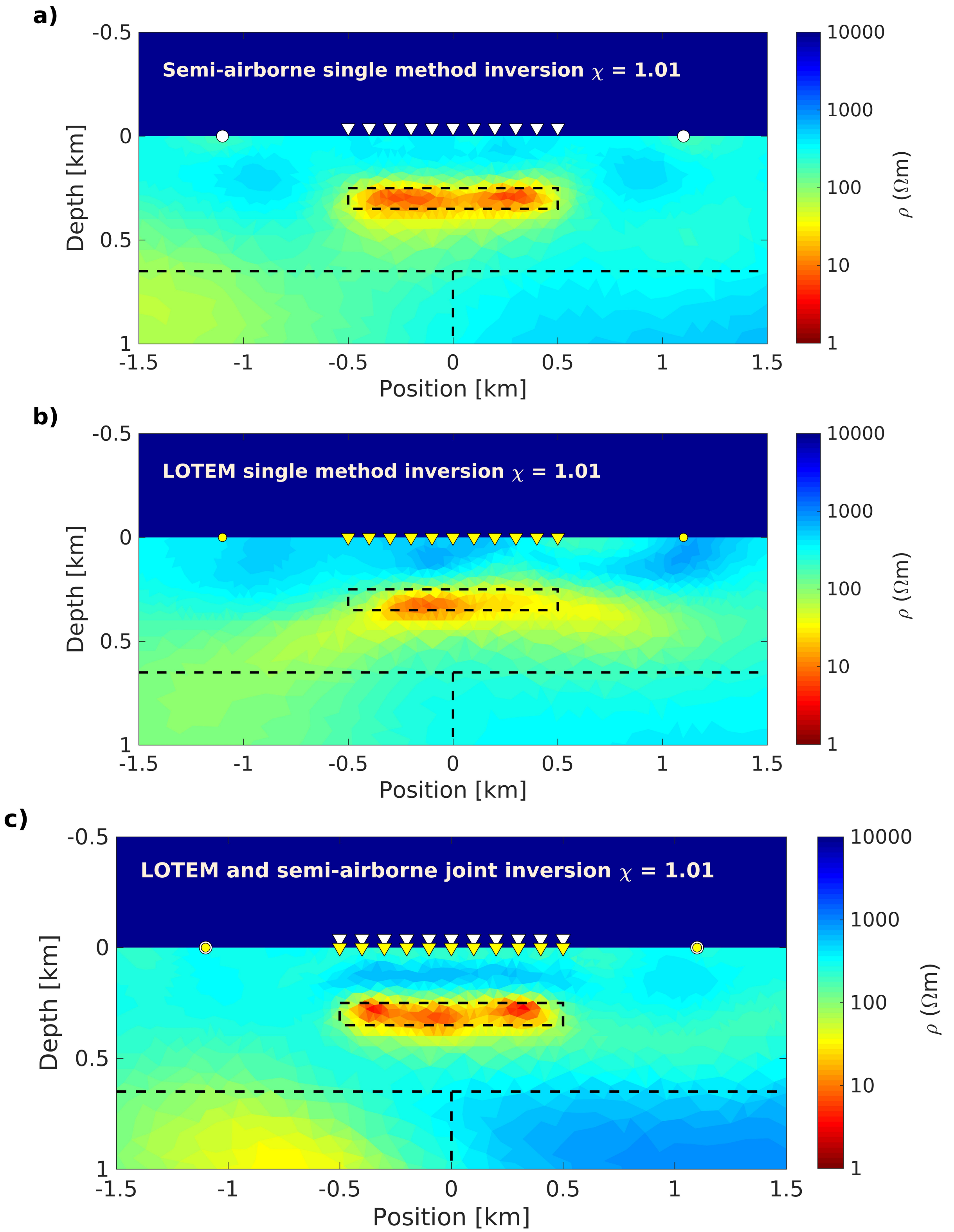

Figure 5.21: 2D inversion results for the synthetic data of model shown in Figure 5.20. Results are displayed for the inversions of (a) semi-airborne data individually, (b) LOTEM time-domain Ex individually and (c) LOTEM and semi-airborne data jointly.

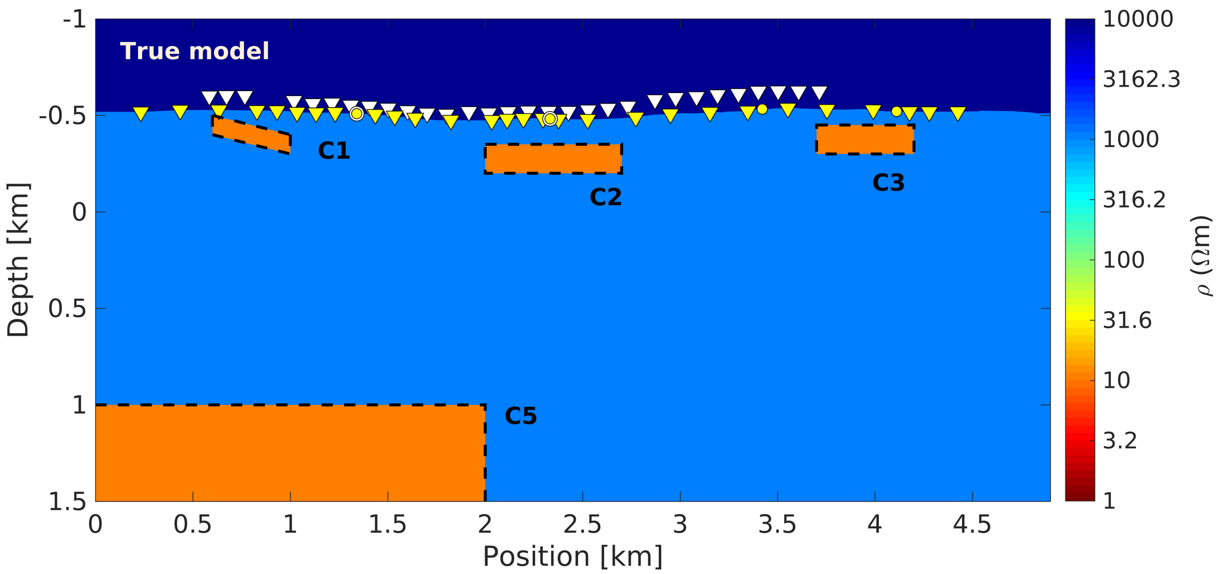

Figure 5.22: The second 2D resistivity model used in the modeling study for the joint inversion of semi-airborne and LOTEM time-domain data. The topography and the field measuring configurations are taken into account.

LOTEM data in the next section also proves the existence of these three structures. Thus they are also referred to as C1, C2 and C3 in this synthetic study. The big conductive body lies between horizontal position 0 to 2km is buried around 1500m depth below the earth's surface. It is a rough simulation of the deep structure revealed by the 2D inversion of time-domain LOTEM field data (Figure 5.27b and c). In order to distinguish it from the C4 presented by semi-airborne field data inversion (e.g., Figure 5.14), this deep conductive body is denoted as C5. All of the conductive bodies have a resistivity of 10 $\Omega \cdot m$, and the background resistivity is kept as 1000 $\Omega \cdot m$. For simulating the cases of real measurements, the 2D topography is considered and the measuring configurations the same as the field set-ups in eastern Thuringia are employed. Same as the setting of Gaussian noise used earlier, semi-airborne synthetic data have 5% Gaussian noise, and the LOTEM Ex components have 2%.

Figure 5.23 displays the results of the 2D inversions applied to synthetic data. For the semi-airborne (a), the inversion uses 20 iterations to fit the synthetic data with an ideal $\chi = 1$. All the shallowly buried conducted bodies C1 to C3 are generally discovered. As predicted, the deep conductive structure C5 is not revealed. What is out of expectation is that an artificial conductive body appears above the original position of C5. The reason for the occurrence of this artifact could be the slight effects of C5 in the semi-airborne data. Although C5 is too deep to be revealed by semi-airborne measurements here, it has a weak influence on the semi-airborne data. The distortion led by C5 can not be fitted by only C1 to C3. Instead of revealing C5, the artifact is created by inversion procedures to compensate for the distortion. For a similar reason, the conductive structures of C1 are also extended. Although the precise positions are different, the artifact just above C5 shows similarity with C4 revealed by semi-airborne field data — an isolated round conductive body locates below C2 and between the horizontal position of 2 to 2.5km. This artificial conductive body could be a potential explanation for the C4 revealed by semi-airborne field data. If C5 does not exist in the true model, the artificial conductive body will not exist (see Figure B.7).

The result of 2D inversion considering only the LOTEM time-domain electric field is unsatisfactory either (Figure 5.23b). The data misfit reached $\chi = 1.35$ at 27th iteration but dropped very slowly afterward. The presented figure is the result of the 34th iteration, indicating the data misfit dropped only 0.04 after seven more iterations. The reason for the difficulty of achieving an ideal χ is also obvious. An artifact with resistivity 30 $\Omega \cdot m$ appears between the horizontal position of C1 and C2 (at depth 0m). Moreover, C1 is not fully revealed on the right side but extended on the left side, while the shape of C2 is distorted. On the other hand, even though the rectangle-like boundary and the true resistivity value of C5 are not precisely revealed, the existence and position of C5 are correctly discovered.

Because two sets of data are taken into account, the 2D joint inversion started with a large data misfit and costs more iterations to reach the satisfactory value. The χ reached as 1.46 at iteration 34 and further dropped to 1.11 at iteration 40 (see Figure B.8). For a comparison with LOTEM single method inversion, Figure 5.23c presents the result at iteration 34. Better than the result shown in Figure 5.23b, a resistivity model closer to the true model is recovered by joint inversion, although the data misfit is larger. All C1 to C3 are perfectly revealed, with no obvious artificial structures connected to them. The resistivity of the conductive zone between C1 and C2 is reduced to 300 $\Omega \cdot m$ and thus could be considered as background compared to the 10 $\Omega \cdot m$ targets. The lowest recovered resistivity of C5 drops to 30 $\Omega \cdot m$, closer to the true value than that provided by the inversion of only LOTEM data. Unfortunately, the rectangle-like boundary of C5 is still not clearly described. Obviously, in this synthetic example, the 2D joint inversion result shows a significant advantage over the single method inversions.

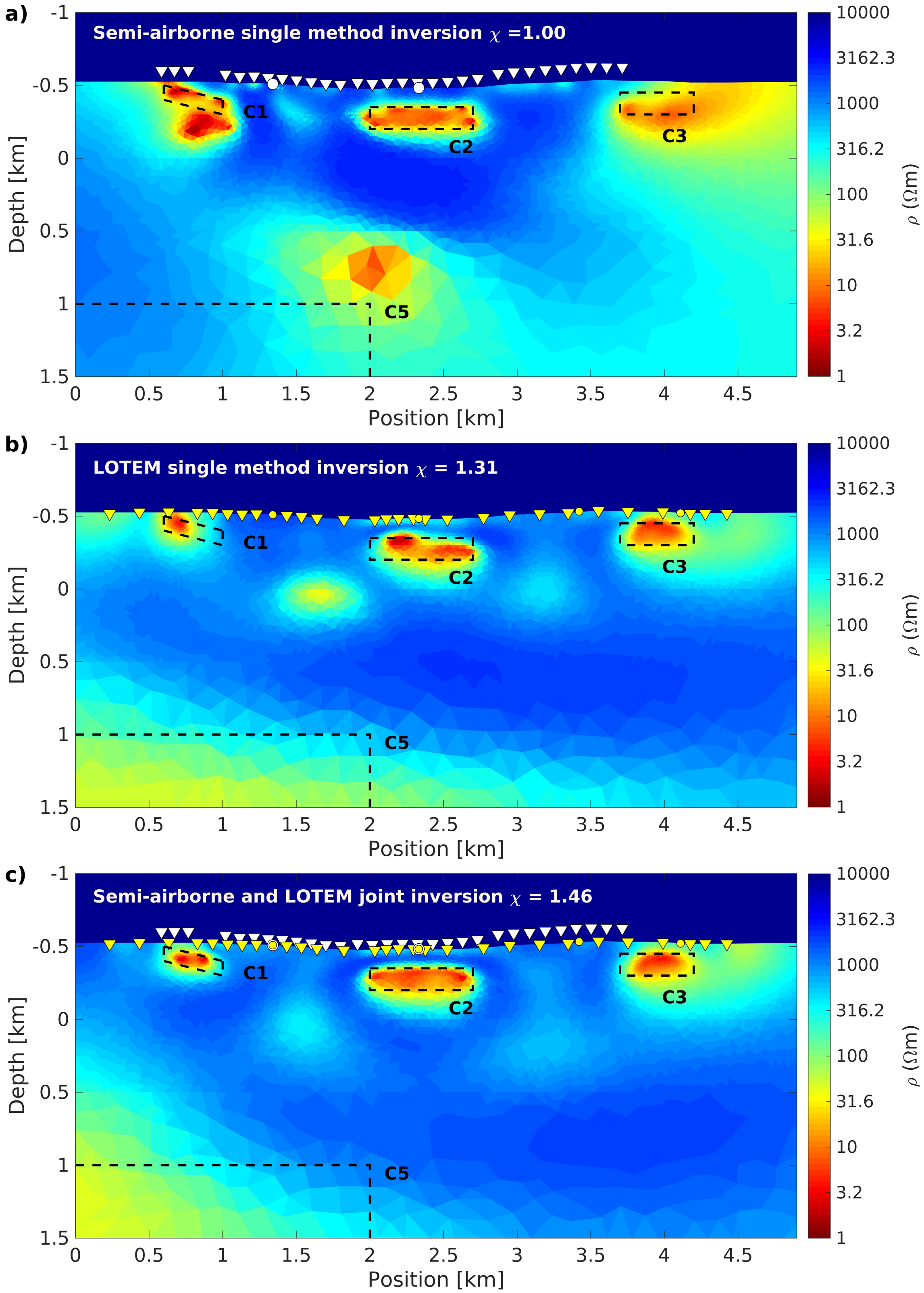

Figure 5.23: 2D inversion results for the synthetic data of model shown in Figure 5.22. Results are displayed for the inversions of (a) semi-airborne data individually, (b) LOTEM time-domain Ex individually and (c) LOTEM and semi-airborne data jointly.

5.3.2 2D joint inversion with reduced LOTEM configuration

As introduced earlier, semi-airborne measurement is faster and more convenient than LOTEM measurement. On the other hand, taking LOTEM data into account could improve the general resolution of inversion results, especially for the deep structures. However, the 2D joint inversion thus includes plenty of data, resulting in the huge computation cost and the slowly dropping data misfits (e.g., 5.23c). From the perspective of accelerating field works, reducing the LOTEM stations employed in joint inversion is considered. The key problem is the possibility to maintain the advantages of joint inversion while the number of LOTEM stations is reduced. Therefore, an additional test for answering this problem is carried on based on synthetic studies in the last section. The data of LOTEM stations with offset smaller than 1500m are no longer considered in the 2D joint inversion of the synthetic data of the model in Figure 5.22. Figure 5.24 displays the comparison between the configurations (a) includes all the LOTEM stations utilized in the previous joint inversion (Figure 5.23c) and the reduced one (b). As stated, the LOTEM stations

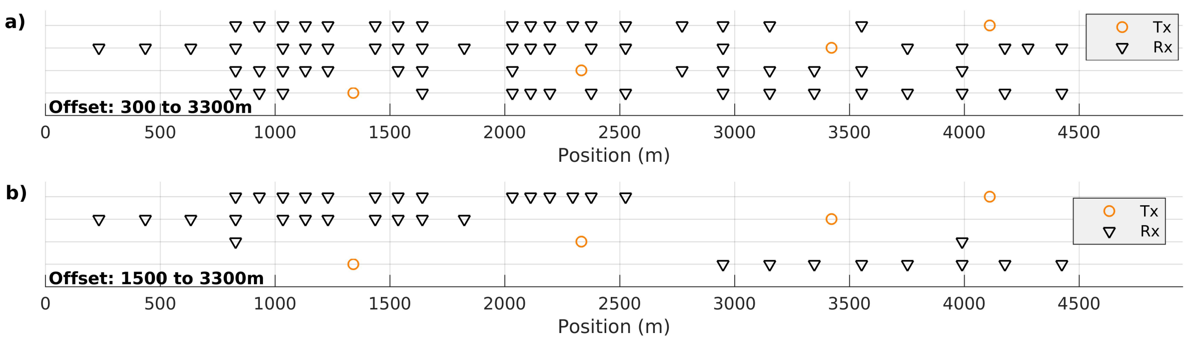

Figure 5.24: Comparison of the configurations includes all the LOTEM stations (a) and the reduced one (b).

with offset smaller than 1500m are removed. Although the total measured locations along the profile are the same between (a) and (b), nearly half of the LOTEM measurements are no longer conducted, and the number of LOTEM data used in the joint inversion is reduced from 1704 to 840. The horizontal electric fields (Ex) recorded by the remained LOTEM stations are inverted jointly with the full semi-airborne dataset. The data misfit χ of 2D joint inversion decreased to 1.17 after 30 iterations, much faster than the 2D joint inversion considering all the LOTEM data. The inversion result is displayed in Figure 5.25.

Although half of the LOTEM data are removed, all the shallow targets (C1 to C3) are still perfectly depicted by the joint inversion result. The C5 is still clearly revealed by the contribution of LOTEM data at offsets larger than 1500m. Compared to joint inversion

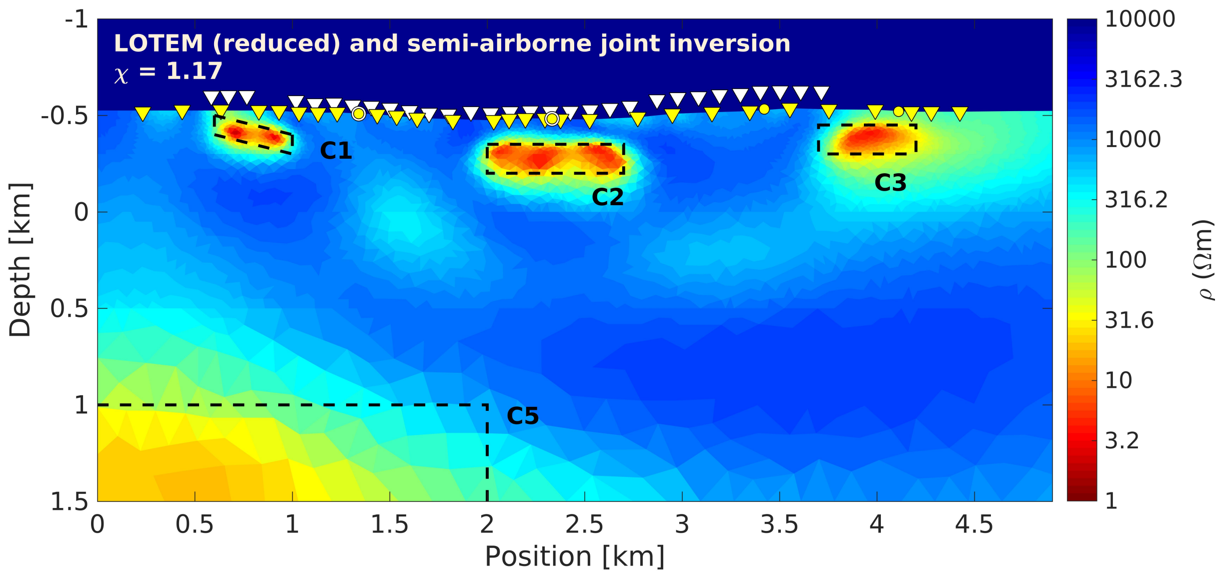

Figure 5.25: 2D joint inversion results for the synthetic semi-airborne and LOTEM data of model shown in Figure 5.22. The reduced LOTEM configuration in Figure 5.24b is employed.

using all LOTEM data (Figure 5.23c), no resolution reduction is observed in this synthetic example. However, considering more data bring more information, usually, it is a commoner sense that reducing data leads to a decrease of resolution. Overall, as evident by this testing, the more flexible measuring configurations are possible for joint inversion or measurement compared to the EM surveys using only one method.

5.3.3 Application of 2D joint inversion on field data

After the synthetic modeling, the time-domain LOTEM field data are inverted jointly with the semi-airborne field data. The semi-airborne field data used in this section is exactly the same as those used in Section 5.2. On the other hand, because the time-domain modeling needs much more computation time, the LOTEM field data from the receivers far from the measuring area of semi-airborne are no longer considered. Practically, the receivers with horizontal positions larger than 4500m are not taken into account. The receivers are selected according to the comparison of the predicted data of the 2D inversions for all frequency-domain LOTEM data individually (Figure 5.16) and jointly (Figure 5.17). Relative differences between the LOTEM predicted data in frequency-domain are attached in Figure B.5 and B.6 for all the transmitters.

Since the modeling area is reduced, it is no longer necessary to use the large mesh (Figure 5.11), which is designed to invert all the LOTEM data along with the profile. The new mesh presented in Figure 5.26 is designed for the following 2D inversions. Because the length of the area needs fine refinement is reduced in the horizontal direction, the mesh for deep structures can be better refined than that in the previous version (Figure 5.11). The areas meshed by triangles with the length of 20 m and 30 m are extended to the depths of -300m and 0m, respectively. Between the depth of 0m and 500m, the triangles have an approximate length of 50m. After this modification, the finely refined mesh with the largest cell length of 50m is used to invert the structures buried in the first 1000m depth (depth -500 to 500m in the figures), including the C4 revealed by 2D inversion of semi-airborne field data.

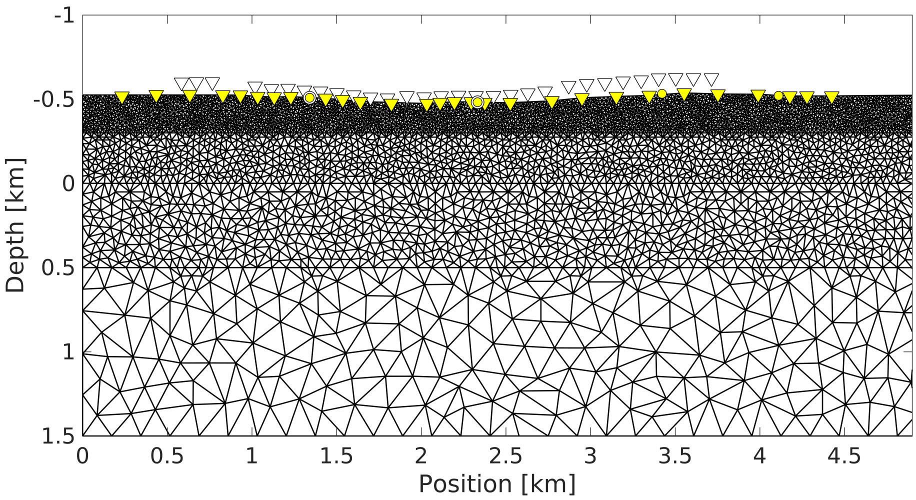

Figure 5.26: The mesh used for the 2D inversions which focus on the area covered by the semi-airborne measurements in 2016, eastern Thuringia.

The semi-airborne field data are inverted by using the new mesh, and Figure 5.27a presents the result. Compared to the result (Figure 5.14) calculated by using previous mesh, the main resistivity distributions show nearly no change. All of C1 to C4 are clearly revealed, validating again that the 2D inversion result of semi-airborne field data is stable. However, there is still one slight variation worth the attention. The most conductive part of C4 is no longer revealed as 1 $\Omega \cdot m$ but at most 10 $\Omega \cdot m$, while the position of the most conductive point also shows a visible shifting to the deep-right direction. This small variation indicates that C4 is the most unstable structure in the result, in other word, the most unimportant one.

LOTEM field data in time-domain are also inverted independently (Figure 5.27b). As mentioned, only the receivers located in the semi airborne measuring area are taking into account. Therefore the big conductive body locates beneath C3 in Figure 5.16 is not

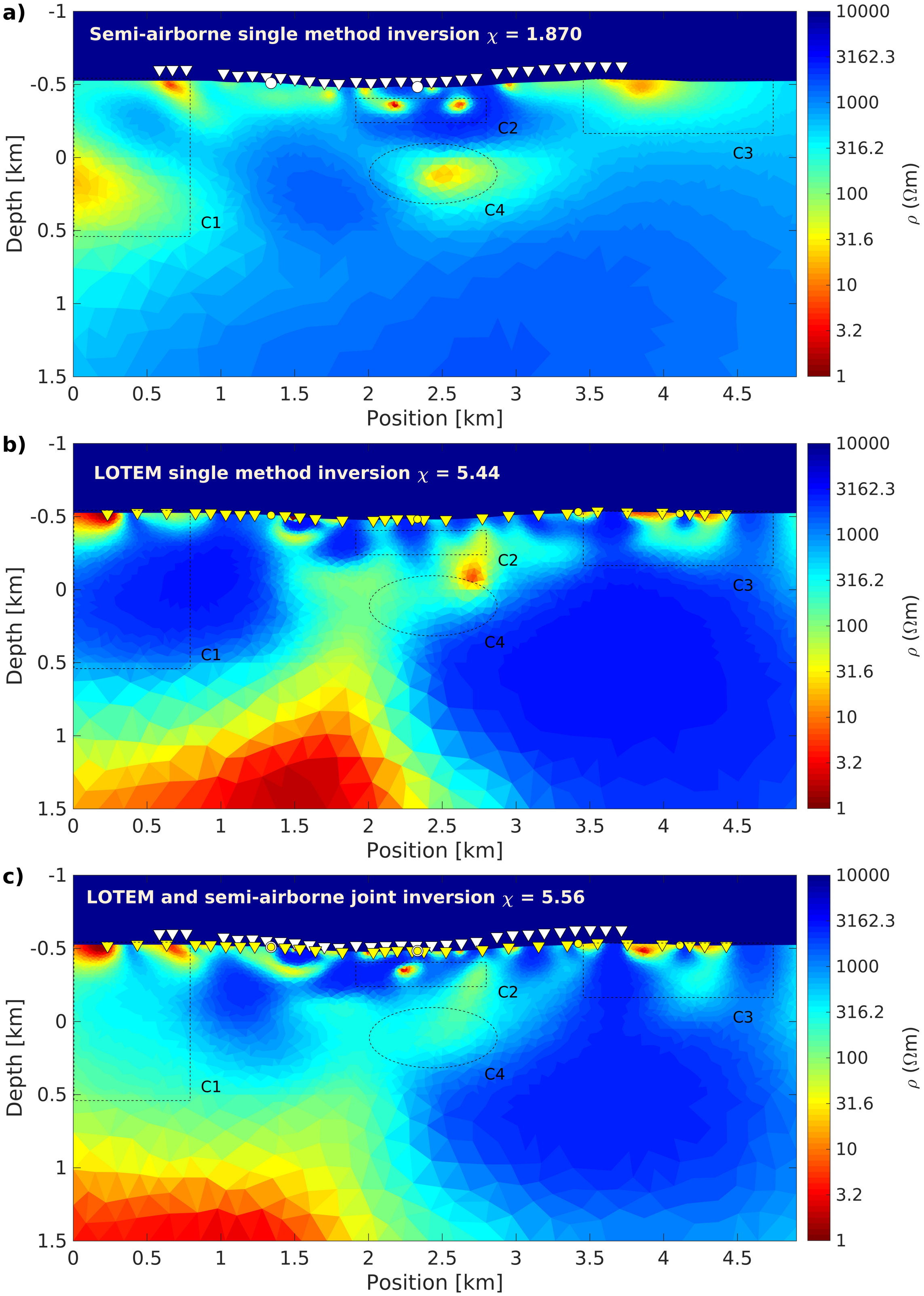

Figure 5.27: 2D inversion results for the field data acquired in eastern Thuringia, Germany. Results are displayed for the inversions of (a) semi-airborne data individually, (b) LOTEM time-domain Ex individually and (c) LOTEM and semi-airborne data jointly.

discovered here. Even though many LOTEM receivers are not taken into account, the resistivity distributions in the interested area (horizontal position 0 to 4.5km) are highly similar to those shown by Mörbe (2019), especially the huge conductive structure lies between the horizontal position of 0 to 2.5km and beneath the depth of 1km. This huge conductive structure is also shown in some iterations of the 2D inversion for frequency-domain LOTEM data (Mörbe, 2019). Regarding the other small conductive structures, the C1 and C3 are stably revealed as usual. The C2 and C4 in the semi-airborne 2D inversion result are not detected here, but there are still many conductive structures locate in this area. It can confirm that some conductive bodies exist in this region. The doubtful point is the specific distributions of them. On the other hand, one may notice that the data misfit of time-domain inversion is apparently larger than that of frequency-domain inversion (Figure 5.16). This difference is led by the form of the data (e.g., amplitude & phase or Ex in time-domain), which is demonstrated by Mörbe (2019).

The consequent 2D joint inversion result is displayed in Figure 5.27c. The total data misfit increases only 0.12 compared to the LOTEM single methods inversion. The individual data misfit for semi-airborne and LOTEM are 3.75 and 6.21, respectively. Similar to the case in frequency-domain, the joint inversion result (c) shows effects led by both semi-airborne and LOTEM. The small conductive body at the most left side in C1 is detected by LOTEM data, while the shape of another shallow conductive body (at the horizontal position around 0.7km) is close to that revealed by semi-airborne single method inversion. The two small conductive bodies are restored because of the effects of semi-airborne data, but one of them are merged into the continuous conductive zone pronounced by LOTEM inversion. Naturally, the deep structures are dominated by the influence of LOTEM data.

Moreover, the validation planed in Figure 5.18 is also conducted for the 2D joint inversion result obtained by using LOTEM time-domain data. Because the LOTEM single method inversion result is highly similar to the joint inversion result, the individual LOTEM inversion is not repeatedly conducted. 2D inversion is applied individually to the semi-airborne predicted data (with 5% Gaussian noise) of the model shown in Figure 5.27c. Figure 5.28 presents the inversion result. As expected, C1 and C3 are not fully discovered because of the measuring configurations. And both the small conductive bodies included by C2 are revealed. Compared to the 2D inversion result of field data, what significantly different are C4 and the deep structures. C4 merges into the conductive zone connecting with the deep structures below the depth of 0.5km. Contrarily, both the conductive zone and the deep conductive structures are never presented in the inversion of semi-airborne field data. The 2D joint inversion result in Figure 5.27c, therefore, can not fully present

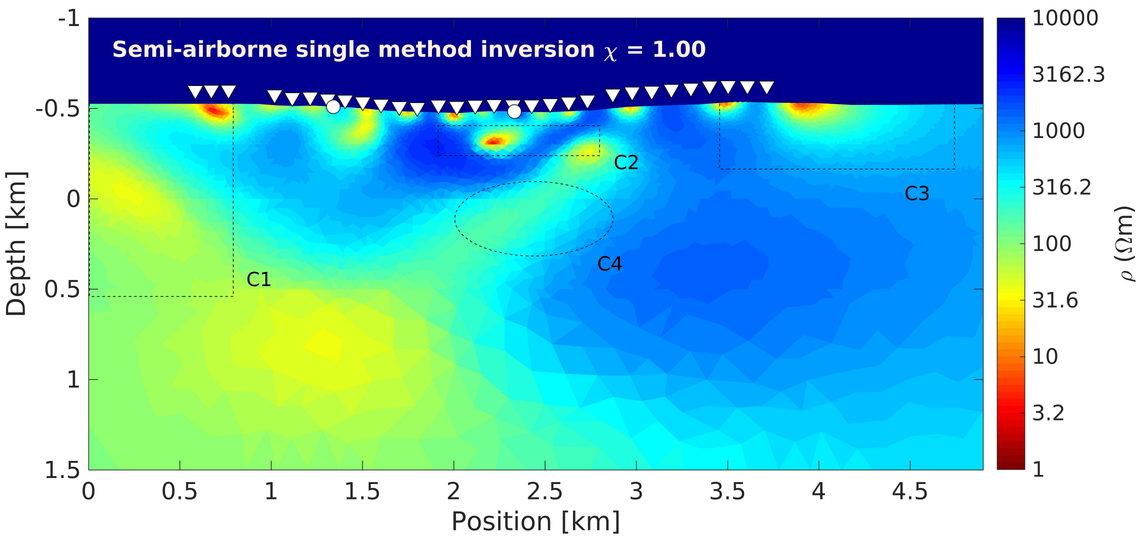

Figure 5.28: 2D inversion for semi-airborne predicted data of joint inversion result in Figure 5.27c.

the real resistivity distribution of the subsurface of the measuring field. Otherwise, the divergence between Figure 5.27a and 5.28 is not logical.

5.4 3D effects

Even though a large part of the resistivity distributions revealed by the 2D inversions of semi-airborne and LOTEM field data are similar or explicable, some obvious divergences exist. As evident in the sections above, these divergences can not be explained by the resolution differences between semi-airborne and LOTEM measurements. Therefore the factors never considered in previous researches could be the true reasons, such as the effects caused by anisotropy, induced polarization or 3D resistivity distributions. Due to limited conditions, only 3D effects are investigated roughly in this thesis. Figure 5.29 shows the plan for investigating the 3D effects in the 2D inversions of semi-airborne data. Because the joint inversion with 2D LOTEM data is the focus of this thesis, the data of one profile are extracted from the 3D semi-airborne field data. The 2D semi-airborne data are also inverted individually afterward (Figure 5.27a). On the other hand, Smirnova et al. (2019) applied the 3D inversion to the semi-airborne data of all profiles and obtained a 3D resistivity model. The 2D cross-section locates in the same position as the LOTEM profile is extracted from the 3D inversion result and presented in Figure 5.30.

Compared to the 2D field data inversion results, the resistivity structures depicted in Figure 5.30 also include C1 to C3, but not C4. Because many unconsidered factors could lead to this divergence are included in the field data, no further information can be known

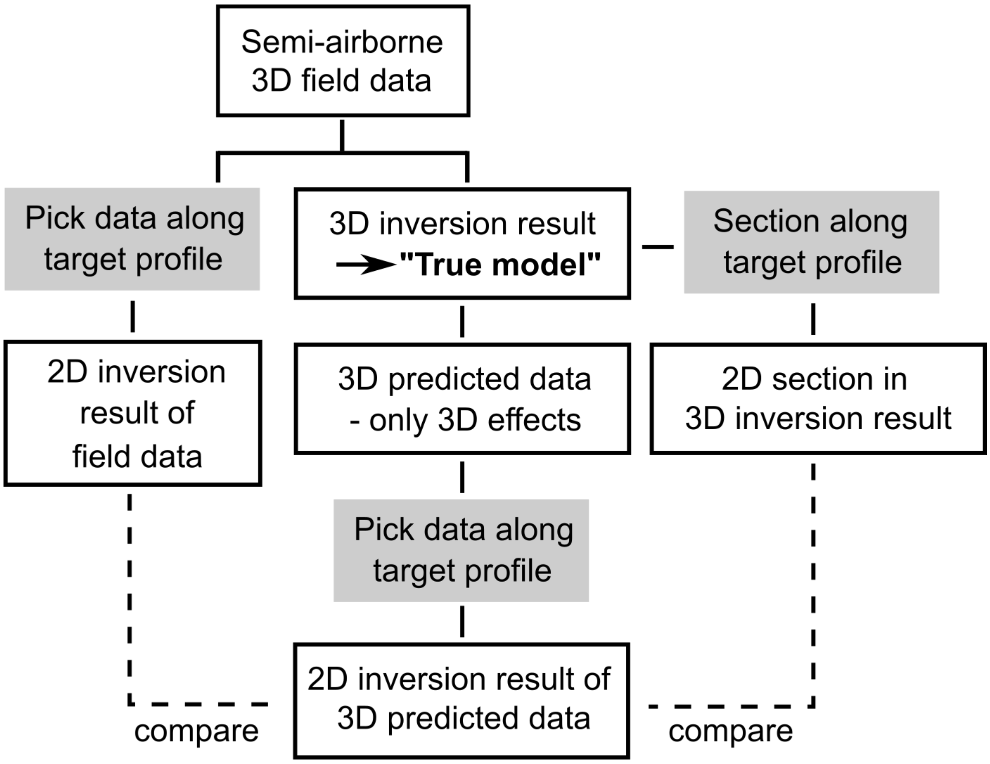

Figure 5.29: Plan of investigation for the 3D effects in the 2D inversions of semi-airbrone data.

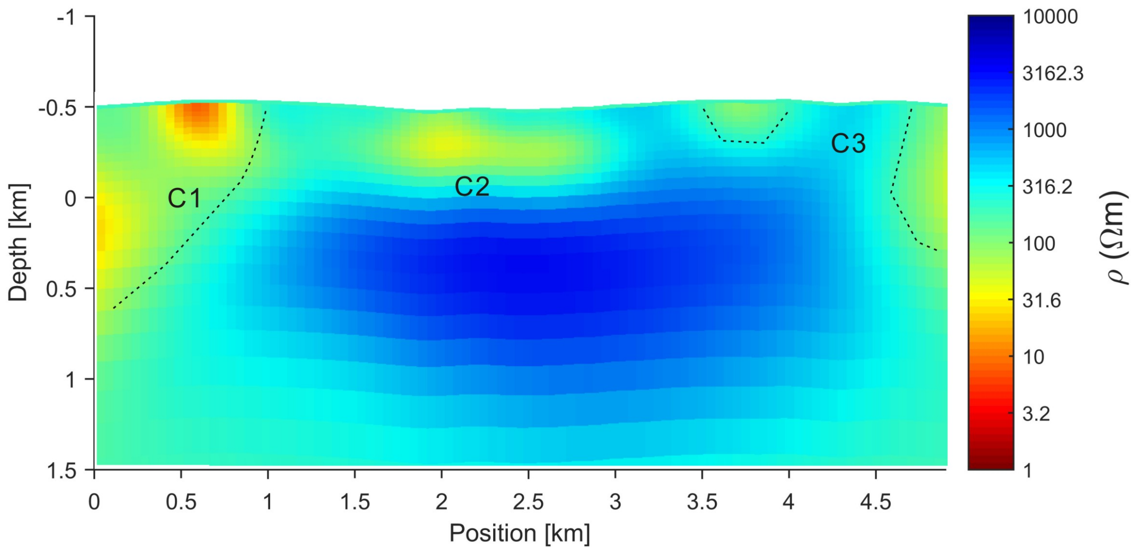

Figure 5.30: A 2D cross section of the 3D inversion result of semi-airborne EM field data. The position of this section is the same as that of LOTEM profile. (Smirnova et al., 2019 and Moerbe, 2019)

by this comparison. In order to rule out the other factors (e.g., anisotropic, IP effects), the 3D resistivity model provided by 5.30 is regarded as the "True model". The predicted data along the LOTEM profile of this 3D model are extracted for the 2D inversion. Because the predicted data are calculated by the known 3D model, it can be guaranteed that these data include no other unconsidered factors that could influence the 2D inversion result. Even the measuring system is perfectly simulated, and no system errors exist in the data.

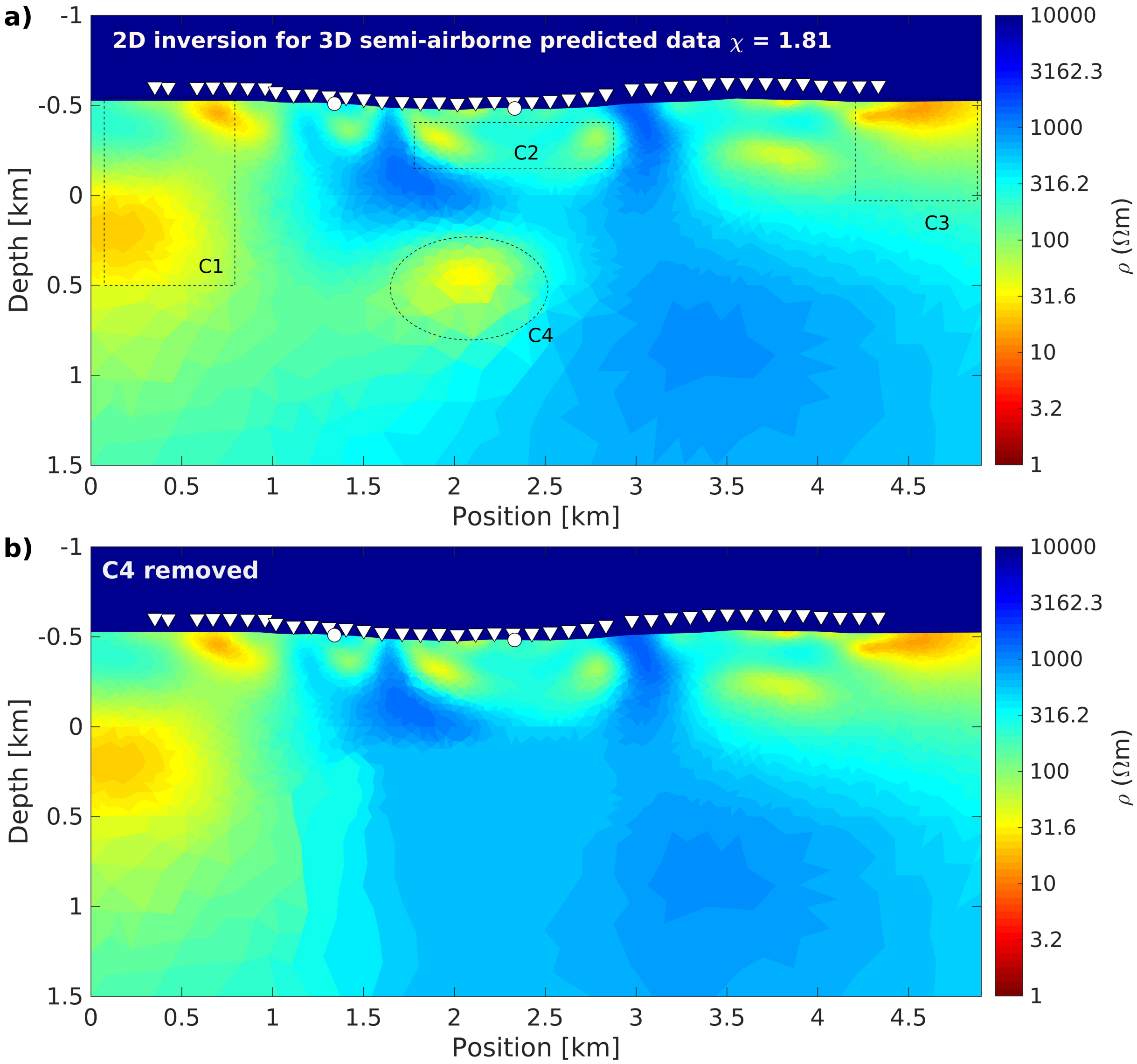

Figure 5.31: (a) 2D inversion results of the 3D predicted data; (b) the 2D resistivity model with C4 removed form (a).

Figure 5.31a displays the 2D inversion result for these predicted data. Significant similarities are shown between the inversion results of extracted 3D predicted data and the 2D field data. Not only all the C1 to C3 are revealed, but also the C4. Compared to the 2D inversion of field data, the C4 is shifted, but there is no conductive structure in the same position as the true model here (Figure 5.30). Moreover, different from the continuously extended 2D layer in C2 of true model, the C2 is revealed as two small conductive bodies in Figure 5.31a, like the case of 2D inversion of field data. Because C4 is an obvious artificial structure here, the forward modeling is conducted for the 2D resistivity model without it (Figure 5.31b). Figure 5.32 displays the relative difference of the responses

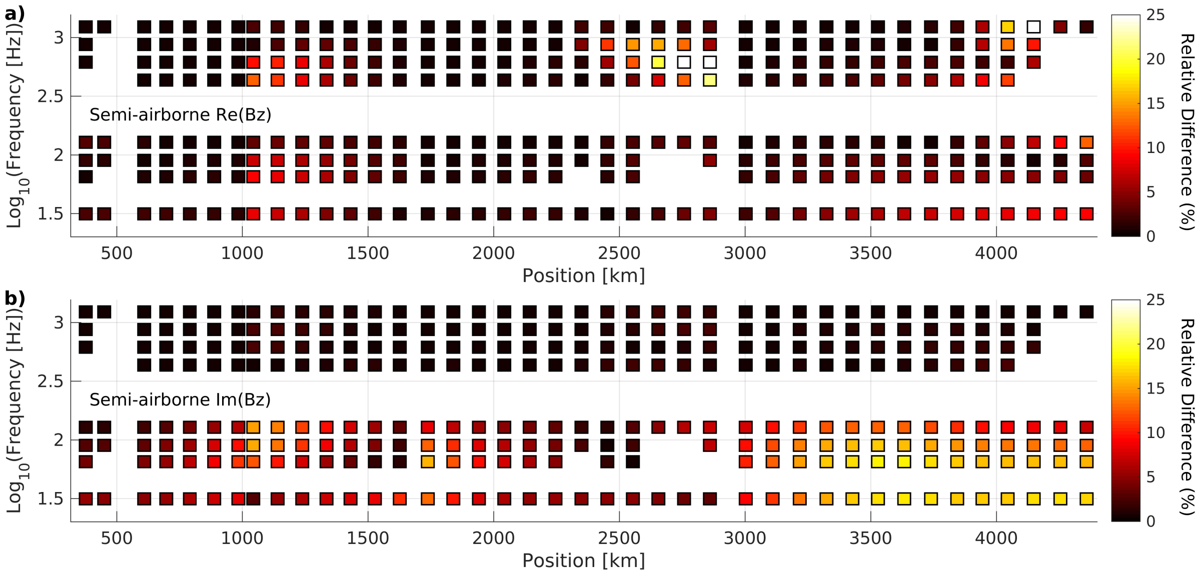

Figure 5.32: Comparison for calculated data between the two resistivity model displayed in Figure 5.31 a and b.

between the 2D model with or without C4. The widely spread relative differences around 20% pronounce that the C4 structure significantly affects the data. In this case, two possible factors could be reasons for this divergence. 3D effects surely could be one possible reason. Considering the transmitter has a finite length of around 1000, the information which leads to the revealing of C4 probably comes from the 3D structures outside of the 2D section shown in Figure 5.30. Another possible reason is the combined effects of the inversion algorithm and the resolution of the semi-airborne survey. A structure similar to C4 can also be observed in the synthetic modeling presented in Figure 5.23.

5.5 Summary of 2D modeling studies

Because the 1D joint inversion encounters convergence problems for the semi-airborne field data and the measured LOTEM electric field data acquired in eastern Thuringia (2016), a 2D joint inversion is required. The open-source Fortran code MARE2DEM (Key, 2016) is adopted to tackle this requirement. Firstly, the joint inversion of time- and frequency- domain data is realized based on the time-domain solutions implemented by Haroon et al. (2018) within MARE2DEM. Secondly, optimal parameter settings are investigated for ensuring the accuracy of the semi-airborne and LOTEM 2D forward solutions. A wide wavenumber range of 10^{-4} to 10^{6} m^{-1} is tested and utilized for the semi-airborne 2D modeling. The mesh used for forward modeling is manually refined before automated adaptive refinements to ensure the accuracy of semi- airborne solutions when the air resistivity is 10^{6} $\Omega \cdot m$. The high air resistivity value also works for accurate LOTEM forward solutions. Both the semi-airborne and LOTEM 2D solutions are verified with 1D forward solutions.

The time-domain LOTEM field data are also processed in frequency-domain (Mörbe, 2019). Therefore, the 2D modeling and joint inversions are applied to both the LOTEM data in frequency- and time-domain. The synthetic studies suggest that the semi-airborne and LOTEM surveys (in both domains) have distinctly different resolutions for the detection of subsurface resistivity distributions. These resolution diversities are lead by different observed quantities as well as the different measuring configurations. The 2D joint inversions can combine the advantages of both EM methods and provide the inversion results with higher resolutions than the ones obtained by inverting each dataset individually.

The semi-airborne field data involved in 2D inversions are selected carefully. Different regularisation parameters, spatial weights, and meshes are tested in the 2D inversions of semi-airborne field data, demonstrating that the inversion result is stable. The LOTEM horizontal electric fields observed on the same profile in eastern Thuringia are inverted by using the same meshes utilized by semi-airborne 2D inversion. Although the used mesh and inversion parameters vary, the LOTEM 2D inversion results obtained here are almost the same as those shown in previous works (Mörbe, 2019). Distinct divergences are observed among the results acquired by inverting semi-airborne and LOTEM field data individually. According to the synthetic studies, part of divergences can be explained by the different resolutions between two EM surveys. The 2D joint inversion results of two field datasets show the combining characteristics of both individual inversions while the data misfits are satisfactory. However, the subsequent synthetic studies indicate that the 2D joint inversion results still have a distance from the ideal interpretations for the resistivity distribution of the measuring area. The calculated data of the 2D joint inversion results are inverted individually for semi-airborne and LOTEM. The corresponding results do not show the distinct divergences observed in the field data inversion results. Additionally, the possible 3D effects in 2D inversions are investigated. Predicted semi-airborne data of a 3D resistivity model provided by Smirnova et al. (2019) is inverted in 2D. The result shares high similarity with the inversion result of field data.

In overall, the 2D joint inversion of semi-airborne and LOTEM data are realized and show significant advantages than the singe method inversions. But the 2D joint inversion results on the field data are not perfect because many possible influencing factors (such as anisotropy, IP, unrecord system error) are still not considered in current works.

6 Conclusions and outlook

The focus of this thesis is the development and elaborate investigation of joint inversion algorithms for deep semi-airborne EM and LOTEM data. HEM data are also considered, but only in the 1D case. While each individual EM method has its limitations, the joint inversion tries to combine the advantages of all the considered EM methods. The aim is to acquire superior inversion results in terms of model resolution for the interpretation of subsurface resistivity distributions. The developed 1D and 2D joint inversion algorithms are applied to field data measured in a former antimony mining area in eastern Thuringia, Germany. According to the joint inversion results, the advantages and limitations of 1D and 2D joint inversion on semi-airborne and LOTEM data are discussed in detail.

Firstly, the joint inversion algorithms are developed and investigated for 1D cases. The 1D forward and inverse modeling algorithms for semi-airborne EM data in frequency-domain are developed, and the accuracy of the solutions is verified. Using the originally available 1D forward modeling and inversion algorithms for HEM and LOTEM, the 1D joint inversion including all three types of datasets is realized and proved to be feasible. Prior to the application on field data, systematic modeling studies are performed to deepen the understanding of individual resolution characteristics of each method, i.e. HEM, LOTEM and semi-airborne. Based on the 1D inversion results as well as the subsequent resolution analysis, the advantages and disadvantages of each individual EM method are summarised. The HEM data is superior in terms of data density and at resolving the shallow layers, but has less resolution for the deep substructures compared to the other techniques. Taking the HEM data into account in the joint inversion can not only ensure a high resolution for the shallow structures but also help the other datasets to resolve deep structures better by constraining/reducing the equivalence domains for the shallow layer parameters. Although semi-airborne EM data usually have relatively large error estimations compared to ground-based recordings and thus less resolution to deep structures than LOTEM, the semi-airborne EM survey provides a dense data spatial coverage. Hence, the technique is very powerful at revealing continuous 3D variations of resistivity distributions down to around 1000 m depth. LOTEM has the largest depth of investigation among these three EM methods but a far less data density and was conducted only on one profile. Utilizing the LOTEM data in a joint inversion can significantly help to reveal deep structures better. Moreover, the equivalence domain of the semi-airborne and LOTEM often present distinct characteristics. Combining these distinct characteristics can usually help to constrain the joint inversion further and improve the results. The 1D joint inversion is applied first on synthetic data and presents significant advantages over the single method inversion for selected cases.

However, the application of 1D inversion on the field data is not in general successful. The 1D inversion of the field data from each individual EM method can often reach a satisfactory data misfit, in case no strong data distortion is present. All single inversions of measured data indicate the existence of conductive structures in the subsurface. But, the derived resistivity distributions are ambiguous and inconsistent due to distinct depth of investigations, different spatial resolution, and partly different receiver distributions. Hence, 1D joint inversion encounters severe convergence problems. For most of the observed stations, the 1D inversions of each single EM method show a good convergence and a good data fitting, but the datasets from different EM methods can hardly be simultaneously fitted by using a single 1D resistivity model. Further analyses show that 2D effects in the data are found to be one possible factor that leads to the non-convergence using a 1D approach. For validation, the LOTEM and semi-airborne synthetic data for a 2D resistivity model are inverted using 1D algorithms separately and jointly. The results confirm that the 1D joint inversion is insufficient for 2D affected data. If the 2D effects are strong, the 1D inversion results in artificial structures and a wrong interpretation, although the single method inversion converges. Moreover, the data is affected differently for each method or EM component. Therefore, for the datasets from different EM methods, different artifacts are produced. This results in the non-convergence of the 1D joint inversion.

Naturally, at least a 2D joint inversion is required for the interpretation of observed data from eastern Thuringia. To tackle the 2D joint inversion of LOTEM and semi-airborne data, the open-source 2D modeling code MARE2DEM is modified and adapted. Currently, MARE2DEM can fulfill the 2D joint inversion requirements for frequency- and time-domain data for HED sources using efficient parallel computing. To ensure the modeling solutions are accurate enough, optimal parameter settings are selected for calculating the semi-airborne and LOTEM 2D solutions. Both the semi-airborne and LOTEM 2D solutions are verified by the comparison with 1D solutions. Subsequently, the 2D modeling studies are applied to the semi-airborne and LOTEM synthetic data. As indicated by the inversion results of each individual EM method, the semi-airborne EM and LOTEM techniques have different resolution power to the 2D resistivity distributions. One reason for the resolution distinctions is the different observed quantities between these two EM methods. Vertical magnetic fields are measured in the semi-airborne survey, while only the horizontal electric fields are considered in LOTEM measurements in this thesis. Another factor is the measuring configurations. The semi-airborne survey has a dense and continuous measuring configuration in the space, but the largest offsets are limited. The configuration utilized by LOTEM measurement did not have station coverage as dense as that of semi-airborne in some area, but much larger offsets are feasible. The 2D joint inversion results of the data of both EM methods show obvious advantages in synthetic modeling. Different information contained in the two datasets complement each other in the 2D joint inversion and provide the results with higher resolutions than any inversion result calculated by only one dataset.

At last, the field data are inverted by using the developed 2D modeling algorithm. The semi-airborne field data used for 2D inversion are selected carefully. The stability of the 2D inversion result is validated by using different regularisation parameters, spatial weights, and also different meshes. The LOTEM horizontal electric fields observed on the same profile are inverted by using the same meshes as the semi-airborne data. Even though there are some similarities between the semi-airborne and LOTEM single inversion results, the distinctions between them are also obvious. Part of divergences can be explained by the different resolutions between the two EM techniques, which were also presented in the synthetic studies. The 2D joint inversion results of two field datasets successfully converge, and the data misfits are satisfactory. Characteristics from both individual inversion results can be found in the 2D joint inversion result. Aiming at investigating if the 2D resistivity distributions suggested by joint inversion could be the full explanation for the discrepancies observed in inversion results of each single dataset, the predicted data of 2D joint inversion results are inverted individually for semi-airborne and LOTEM. The corresponding results indicate that the resolution differences between two EM measurements are not sufficient to explain the discrepancies among the 2D inversion results of the field data. Therefore, possible 3D effects are briefly studied to validate the 2D results further. 2D inversion is applied to the predicted semi-airborne data of the 3D resistivity model derived from semi- airborne field data. The 2D inversion result of the predicted data of the 3D model is closer to the 2D inversion result of field data rather than the 2D cross-section of the 3D model provided by Smirnova et al. (2019). The reason could be the 3D effects or the limitation of the 2D inversion and the employed semi-airborne configurations.

Even including the 3D effects, there are still several unconsidered factors, which can be the reasons for the unexplained discrepancies among the field data 2D inversion results. Given the existence of massive black shales in the survey area, it is quite possible that the field data are influenced by anisotropic effects. The IP effects in the LOTEM field data have already been mentioned by Mörbe (2019), yet the modeling and inversions have never taken this factor into account. Given these possible factors, a 3D joint inversion algorithm considering anisotropic and IP effects is required to explain the data fully. Moreover, besides using LOTEM and semi-airborne EM data, the joint inversion could be extended to take other EM methods with various configurations into account.

Reference

Archie, G. E., 1942. The electrical resistivity log as an aid in determining some reservoir characteristics. Transactions of the AIME.

Cai, J., Tezkan, B., Li, Y., 2018. Effects of the sea floor topography on the 1D inversion of time-domain marine controlled source electromagnetic data. Geophysical Prospecting.

Candansayar, M. E., Tezkan, B., 2008. Two-dimensional joint inversion of radiomagnetotelluric and direct current resistivity data. Geophysical Prospecting.

Commer, M., Newman, G. A., 2009. Three-dimensional controlled-source electromagnetic and magnetotelluric joint inversion. Geophysical Journal International 178 (3), 1305–1316.

Constable, S. C., Parker, R. L., Constable, C. G., 1987. Occam's inversion: a practical algorithm for generating smooth models from EM sounding data. Geophysics 52 (3), 289–300.

Edwards, R. N., 1997. On the resource evaluation of marine gas hydrate deposits using sea-floor transient electric dipole-dipole methods. Geophysics 62 (1), 63–74.

Elliott, P., 1996. New airborne electromagnetic method provides fast deep-target data turnaround. Leading Edge (Tulsa, OK).

Farquharson, C. G., Oldenburg, D. W., 1996. Approximate sensitivities for the electromagnetic inverse problem. Geophysical Journal International 126 (1), 235–252.

Gehrmann, R. A., Schwalenberg, K., Riedel, M., Spence, G. D., Spieb, V., Dosso, S. E., 2016. Bayesian inversion of marine controlled source electromagnetic data offshore Vancouver Island, Canada. Geophysical Journal International 204 (1), 21–38.

Hansen, P. C., O'Leary, D. P., 1993. The use of the L-curve in the regularization of discrete ill-posed problems. SIAM Journal on Scientific Computing 14 (6), 1487–1503.

Haroon, A., 2012. The Application of the Long Offset Transient Electromagnetic Method in Perekishkul , Azerbaijan. Master's thesis, University of Cologne.

Haroon, A., 2016. Development of Novel Time-Domain Electromagnetic Methods for Offshore Groundwater Studies : A Data Application from. Ph.D. thesis, University of Cologne.

Haroon, A., Adrian, J., Bergers, R., Gurk, M., Tezkan, B., Mammadov, A. L., Novruzov, A. G., 2015. Joint inversion of long-offset and central-loop transient electromagnetic data: Application to a mud volcano exploration in Perekishkul, Azerbaijan. Geophysical Prospecting 63 (2), 478–494.

Haroon, A., Hölz, S., Weymer, B., Tezkan, B., Jegen, M., 2018. Calculating Time-Domain Controlled Source Electromagnetic Signals with MARE2DEM. In: 3rd Applied Shallow Marine Geophysics Conference.

Hauser, J., Yogeshwar, P., Tezkan, B., 2016. Radiomagnetotellurische Messungen zur Erkundung der oberflächennahen Leitfähigkeitsstruktur bei Schleiz/ Thüringen. Protokoll über die 76. Jahrestagung der Dt. Geophys. Gesellschaft, Münster, Germany.

Hördt, A., 1992. Interpretation transient elektromagnetischer Tiefensondierungen für anisotrop horizontal geschichtete und für dreidimensionale Leitfähigkeitsstrukturen. Ph.D. thesis, Institut für Geophysik und Meteorologie der Universität zu Köln.

Hördt, A., Dautel, S., Tezkan, B., Thern, H., 2000. Interpretation of long-offset transient electromagnetic data from the Odenwald area, Germany, using two-dimensional modelling. Geophysical Journal International 140 (3), 577–586.

Hördt, A., Scholl, C., 2004. The effect of local distortions on time-domain electromagnetic measurements. Geophysics.

Janser, S., 2017. Development of an one-dimensional forward and inverse algorithm for SQUID and coil TDEM data. Master's thesis, University of Cologne.

Kalscheuer, T., Bastani, M., Donohue, S., Persson, L., Aspmo Pfaffhuber, A., Reiser, F., Ren, Z., 2013. Delineation of a quick clay zone at Smørgrav, Norway, with electromagnetic methods under geotechnical constraints. Journal of Applied Geophysics.

Kaufman, A. A., Keller, G. V., 1983. Frequency and transient soundings. Chi-Yu King Roberto Scarpa 207, 7.

Key, K., 2009. 1D inversion of multicomponent, multifrequency marine CSEM data: Methodology and synthetic studies for resolving thin resistive layers. Geophysics 74 (2).

Key, K., 2012. Marine Electromagnetic Studies of Seafloor Resources and Tectonics. Surv Geophys, 135–167.

Key, K., 2016. MARE2DEM: A 2-D inversion code for controlled-source electromagnetic and magnetotelluric data. Geophysical Journal International 207 (1), 571–588.

Key, K., Ovall, J., 2011. A parallel goal-oriented adaptive finite element method for 2.5-D electromagnetic modelling. Geophysical Journal International 186 (1), 137–154.

Levenberg, K., 1944. A method for the solution of certain non-linear problems in least squares. Quarterly of applied mathematics 2 (2), 164–168.

Lippert, K., Tezkan, B., 2019. On the exploration of a marine aquifer offshore Israel by long-offset transient electromagnetics. Geophysical Prospecting.

Marquardt, D. W., 1963. An algorithm for least-squares estimation of nonlinear parameters. Journal of the society for Industrial and Applied Mathematics 11 (2), 431–441.

McGillivray, P. R., Oldenburg, D. W., Ellis, R. G., Habashy, T. M., 1994. Calculation of sensitivities for the frequency-domain electromagnetic problem. Geophysical Journal International.

Meju, M. A., 1996. Joint inversion of TEM and distorted MT soundings: Some effective practical considerations. Geophysics.

Menke, W., 2018. Geophysical data analysis: Discrete inverse theory. Academic press.

Meqbel, N., Ritter, O., 2015. Joint 3D inversion of multiple electromagnetic datasets. Geophysical Prospecting 63 (6), 1450–1467.

Moghadas, D., Engels, M., Schwalenberg, K., 2015. 1D joint multi-offset inversion of time-domain marine controlled source electromagnetic data. Geophysical Prospecting 63 (6), 1334–1354.

Mogi, T., Kusunoki, K., Kaieda, H., Ito, H., Jomori, A., Jomori, N., Yuuki, Y., 2009. Grounded electrical-source airborne transient electromagnetic (GREATEM) survey of Mount Bandai, north-eastern Japan. Exploration Geophysics.

Mogi, T., Tanaka, Y., Kusunoki, K., Morikawa, T., Jomori, N., 1998. Development of grounded electrical source airborne transient EM (GREATEM). Exploration Geophysics.

Moorkamp, M., Heincke, B., Jegen, M., Roberts, A. W., Hobbs, R. W., 2011. A framework for 3-D joint inversion of MT, gravity and seismic refraction data. Geophysical Journal International.

Mörbe, W., 2019. Deep Controlled Source Electromagnetics for Mineral Exploration : A Multidimensional Validation Study in Time and Frequency Domain. Phd thesis, University of Cologne.

Newman, G. A., 1989. Deep transient electromagnetic soundings with a grounded source over near-surface conductors. Geophysical Journal International.

Ossen, D., 2017. Evaluation of TEM Data from Schleiz, Thuringia: 1D Inversion and 2D Modelling. Ph.D. thesis, University of Cologne.

Rochlitz, R., Queitsch, M., Yogeshwar, P., Günther, T., Chwala, A., Janser, S., Kukowski, N., Stolz, R., 2018. Capability of low-temperature SQUID for transient electromagnetics under anthropogenic noise conditions. Geophysics.

Rochlitz, R., Skibbe, N., Günther, T., 2019. CustEM: Customizable finite-element simulation of complex controlled-source electromagnetic data. Geophysics.

Schiffler, M., Chwala, A., Kukowski, N., Meyer, H. G., Meyer, M., Meyer., U., Stolz, R., 2017. Development of new magnetic field sensors for electromagnetic mineral exploration in the DESMEX project. Fruehjahr- stagung der Deutschen Geophysikalischen Gesellschaft.

Scholl, C., 2005. The influence of multidimensional structures on the interpretation of LOTEM data with one-dimensional models and the application to data from Israel. Ph.D. thesis, University of Cologne.

Scholl, C., Edwards, R. N., 2007. Marine downhole to seafloor dipole-dipole electromagnetic methods and the resolution of resistive targets. Geophysics 72 (2), WA39—-WA49.

Seigel, H., 1971. A recent development in semi-airborne electromagnetic prospecting. Exploration Geophysics.

Siemon, B., 2012. Accurate 1D forward and inverse modeling of high-frequency helicopter-borne electromagnetic data. Geophysics.

Siemon, B., Christiansen, A. V., Auken, E., 2009. A review of helicopter-borne electromagnetic methods for groundwater exploration.

Smirnova, M. V., Becken, M., Nittinger, C., Yogeshwar, P., Mörbe, W., Rochlitz, R., Steuer, A., Costabel, S., Smirnov, M. Y., 2019. A novel semiairborne frequency-domain controlled-source electromagnetic system: Three-dimensional inversion of semiairborne data from the flight experiment over an ancient mining area near Schleiz, Germany. Geophysics 84 (5), E281–E292.

Smith, R. S., Annan, A. P., McGowan, P. D., 2001. A comparison of data from airborne, semi-airborne, and ground electromagnetic systems. Geophysics.

Spagnoli, G., Hannington, M., Bairlein, K., Hördt, A., Jegen, M., Petersen, S., Laurila, T., 2016. Electrical properties of seafloor massive sulfides. Geo-Marine Letters.

Spies, B. R., 1989. Depth of investigation in electromagnetic sounding methods. Geophysics.

Steuer, A., Siemon, B., Auken, E., 2009. A comparison of helicopter-borne electromagnetics in frequency- and time-domain at the Cuxhaven valley in Northern Germany. Journal of Applied Geophysics.

Steuer, A., Siemon, B., Pielawa, J., Petersen, H., Vob, V., Balzer, H. U., Plath, C., 2015. Zwischenbericht Hubschraubergeophysik Befliegung DESMEX Teil 1. Tech. rep., Bundesanstalt fuer Geowissenscheften und Rohstoffe.

Strack, K.-M., 1992. Exploration with deep transient electromagnetics. Vol. 373. Elsevier Amsterdam.

Strack, K.-M., Lüschen, E., Kötz, A. W., 1990. Long-offset transient electromagnetic (LOTEM) depth soundings applied to crustal studies in the Black Forest and Swabian Alb, Federal Republic of Germany. Geophysics 55 (7), 834–842.

Streich, R., 2016. Controlled-source electromagnetic approaches for hydrocarbon exploration and monitoring on land. Surveys in Geophysics 37 (1), 47–80.

Sudha, S., Tezkan, B., Siemon, B., 2014. Appraisal of a new 1D weighted joint inversion of ground based and helicopter-borne electromagnetic data. Geophysical Prospecting 62 (3), 597–614.

Telford, W. M., Geldart, L. P., Sheriff, R. E., 1990. Applied Geophysics. Cambridge University Press.

Vozoff, K., Jupp, D. L., 1975. Joint Inversion of Geophysical Data. Geophysical Journal of the Royal Astronomical Society.

Wagner, F. M., Mollaret, C., Günther, T., Kemna, A., Hauck, C., 2019. Quantitative imaging of water, ice, and air in permafrost systems through petrophysical joint inversion of seismic refraction and electrical resistivity data. Geophysical Journal International.

Ward, S. H., Hohmann, G. W., 1988. Electromagnetic Theory for Geophysical Applications. Society of Exploration Geophysicists.

Weidelt, P., 1986. Einführung in die elektromagnetische Tiefenforschung. Lecture Notes.

Yogeshwar, P., 2014. A resistivity-depth model of the central Azraq basin area, Jordan: 2D forward and inverse modeling of time domain electromagnetic data. Ph.D. thesis, University of Cologne.

Zhdanov, M. S., 2010. Electromagnetic geophysics: Notes from the past and the road ahead. Geophysics 75 (5), 75A49—-75A66.

Ziolkowski, A., Slob, E., 2019. Introduction to Controlled-Source Electromagnetic Methods: Detecting Subsurface Fluids. Cambridge University Press.

Appendix A Supplementary for Chapter 4

A.1 Effects of receiver altitude in semi-airborne data

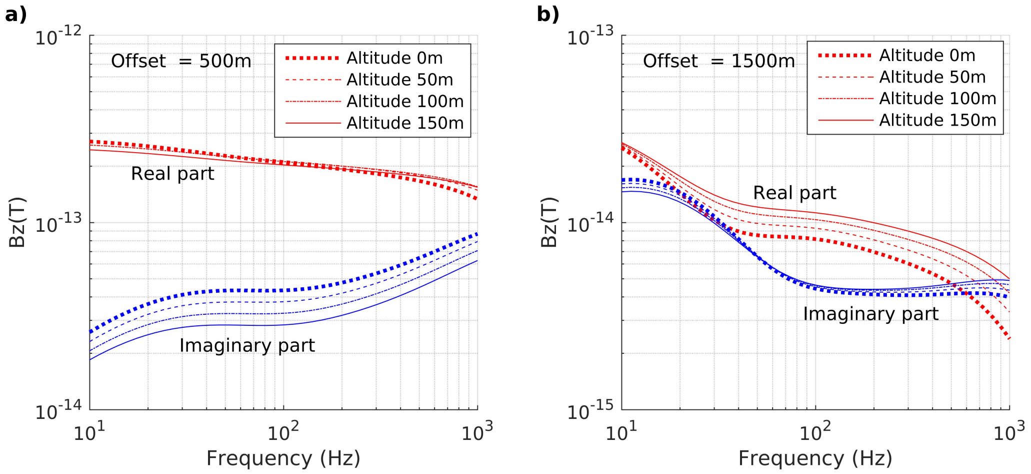

Figure A.1: Semi-airborne frequency-domain 1D solutions for a suite of different receiver altitudes. The three layered 1D resistivity model has resistivity of 300, 10 and 300 $\Omega \cdot m$, respectively. The solutions are calculated for conductive target layer with depth and thickness of 250m. The offset is (a) 500m and (b) 1500m.

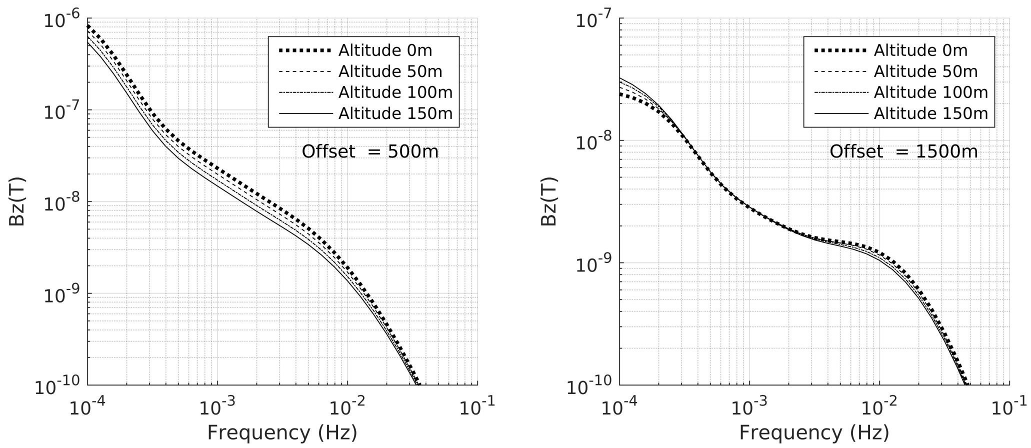

Figure A.2: Semi-airborne time-domain 1D solutions for a suite of different receiver altitudes. The three layered 1D resistivity model has resistivity of 300, 10 and 300 $\Omega \cdot m$, respectively. The solutions are calculated for conductive target layer with depth and thickness of 250m. The offset is (a) 500m and (b) 1500m.

Figure A.1 presents the comparison of the semi-airborne responses at a suite of different altitudes for frequency-domain while Figure A.2 shows the comparison for time-domain. Indicated by the modeling, the effects of receiver altitude vary with the offsets as well as the observed quantities.

A.2 Supplementary for 1D resolution studies

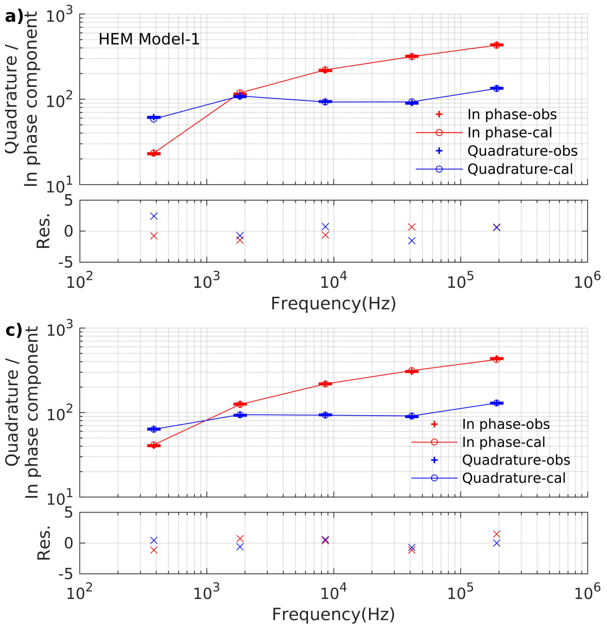

Figure A.3: Data fitting for the 1D Marquardt inversion models displayed in Figure 4.5.The results correspond to the four models highlighted in Figure 4.4. (a) Model-1; (b) Model-2; (c) Model-3; (d) Model-4.

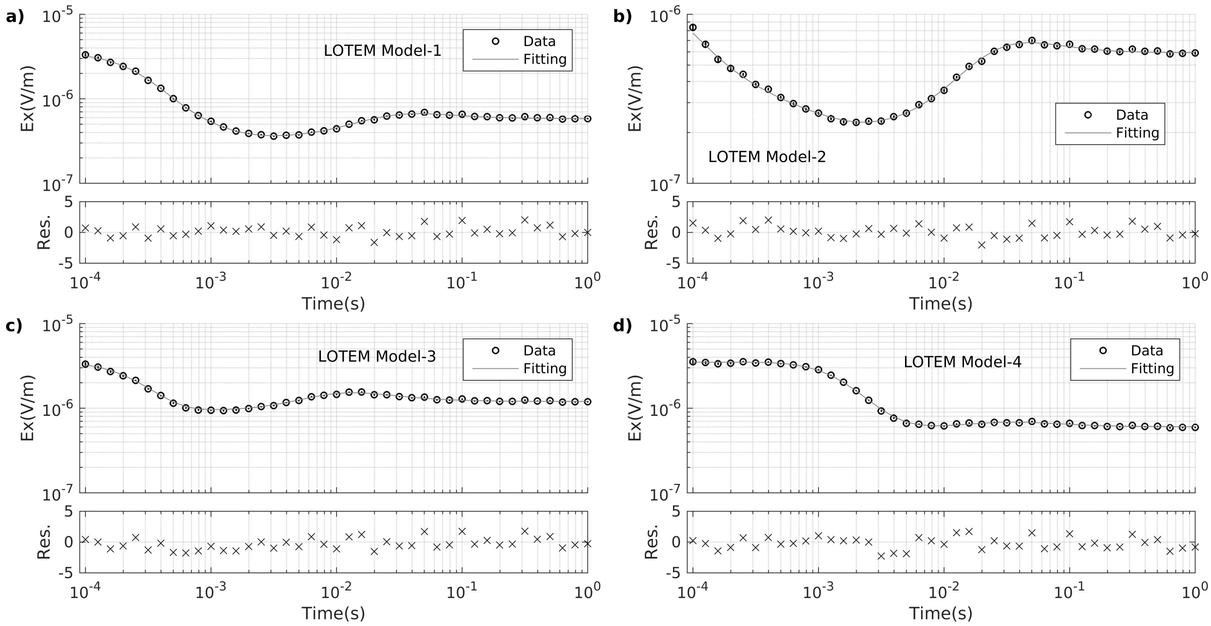

Figure A.4: Data fitting for the 1D Marquardt inversion models displayed in Figure 4.11.The results correspond to the four models highlighted in Figure 4.10. (a) Model-1; (b) Model-2; (c) Model-3; (d) Model-4.

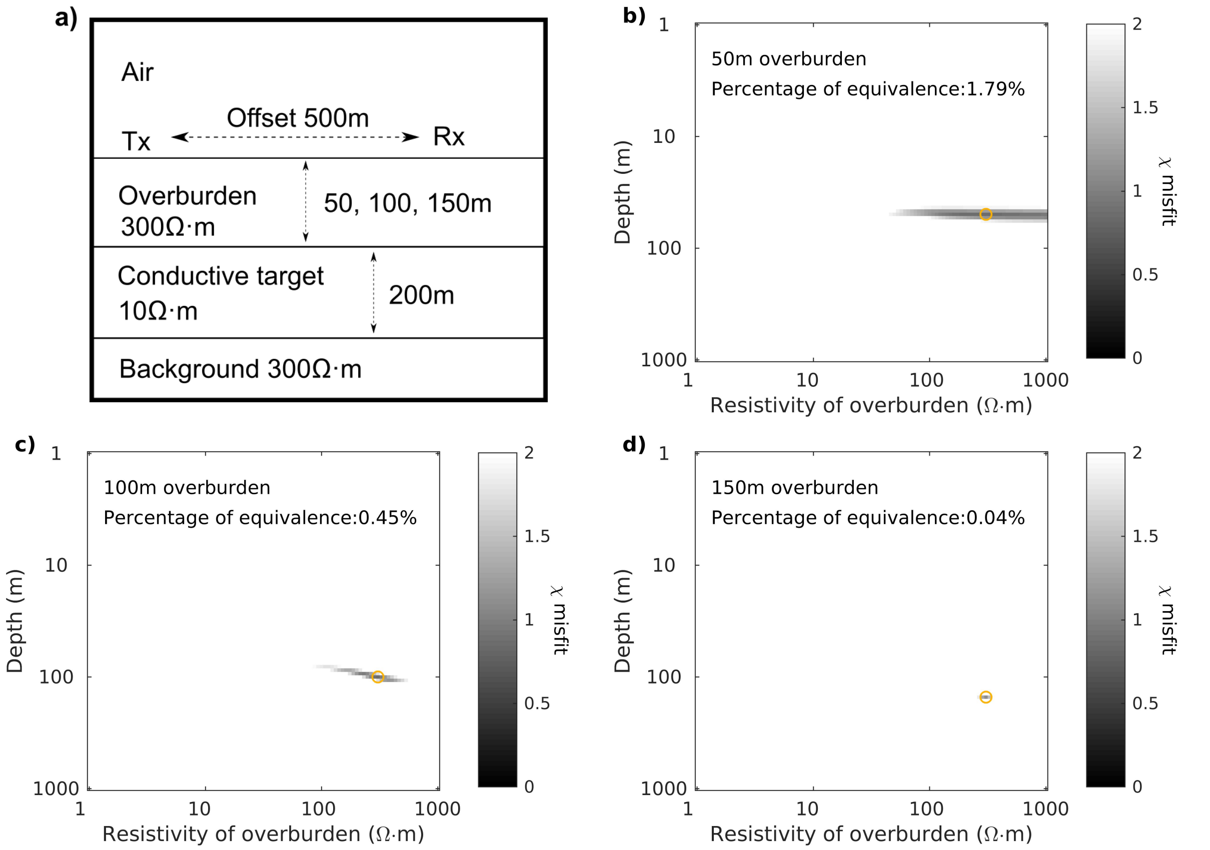

Figure A.5: Modelling studies investigating the resolution of LOTEM Ex to the resistivity and thickness of the overburden. (a) the sketch of the investigated model, the offset is 500m.

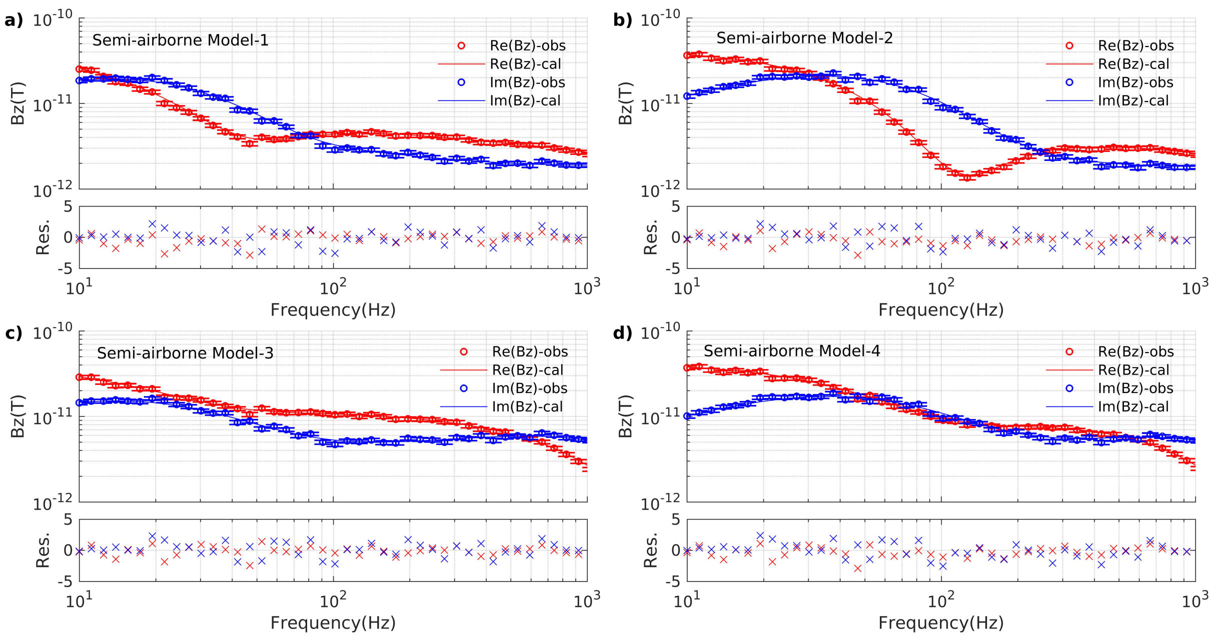

Figure A.6: resolution,semi-airborne, MarqDAT.

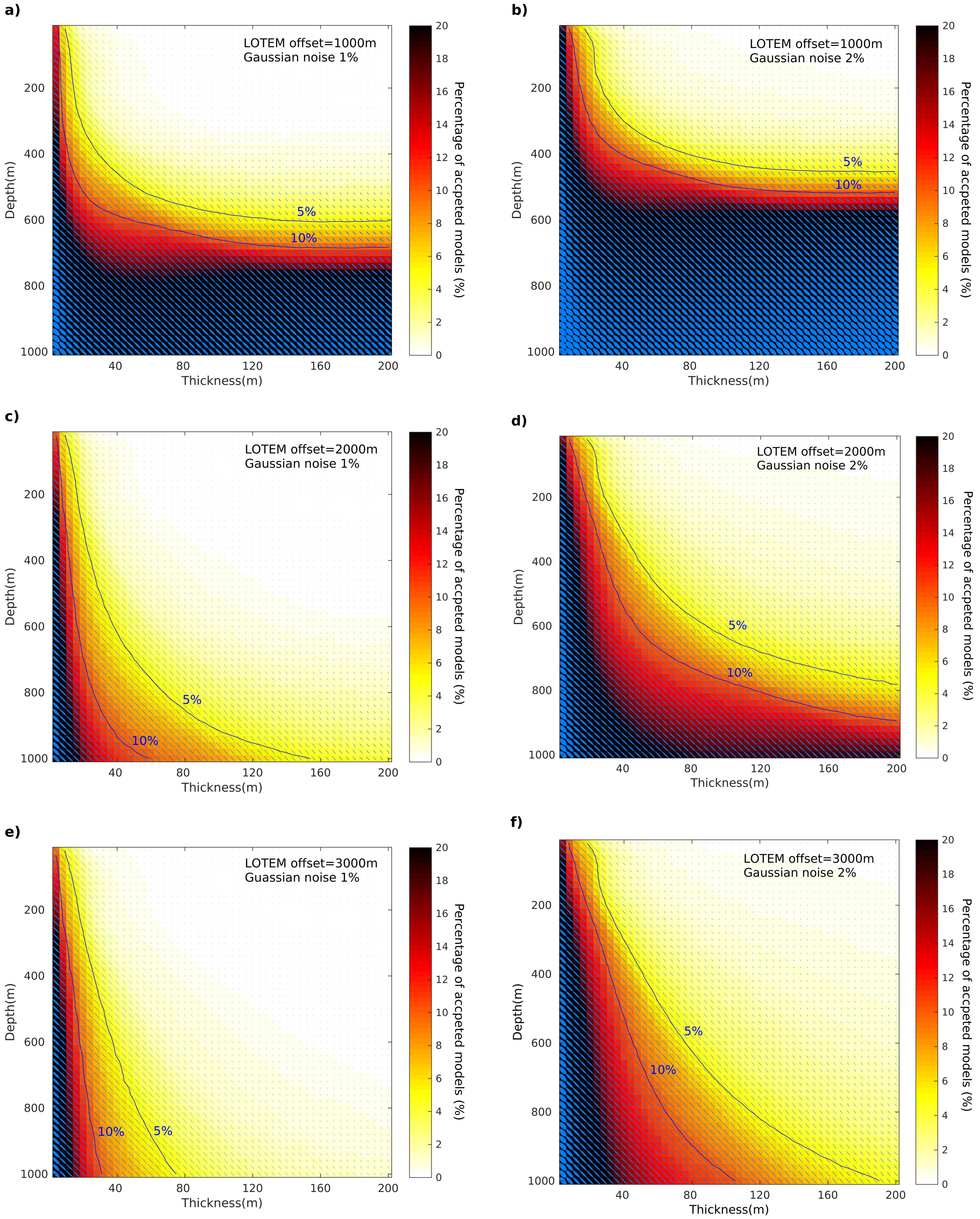

Figure A.7: Summary of resolution studies for step-on responses of LOTEM electric field. In the resolution study for each considered 1D model, the conductor resistivity varies from 1 to 25 $\Omega \cdot m$ and the thickness varies from 1/10 to 3 times of the true value. The summary of resolution studies are displayed respectively for different offsets (1000, 2000, and 3000m) and Gaussian noises (1% and 2%).

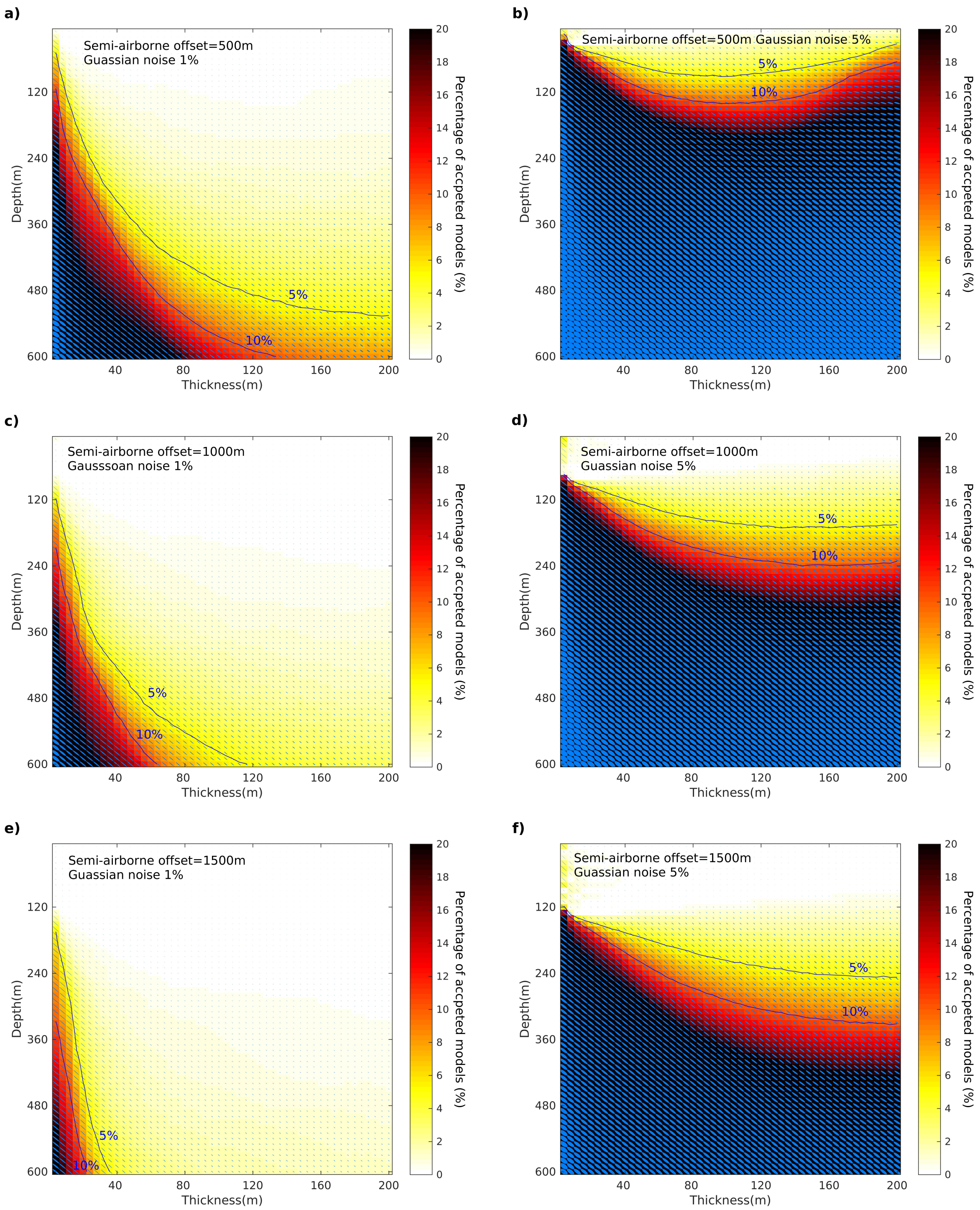

Figure A.8: Summary of resolution studies for semi-airborne magnetic field.In the resolution study for each considered 1D model, the conductor resistivity varies from 1 to 25 $\Omega \cdot m$ and the thickness varies from 1/10 to 3 times of the true value. The summary of resolution studies are displayed respectively for different offsets (500, 1000, and 1500m) and Gaussian noises (1% and 5%).

A.3 Supplementary for 1D joint inversions

A.3.1 Joint inversion of HEM and LOTEM data

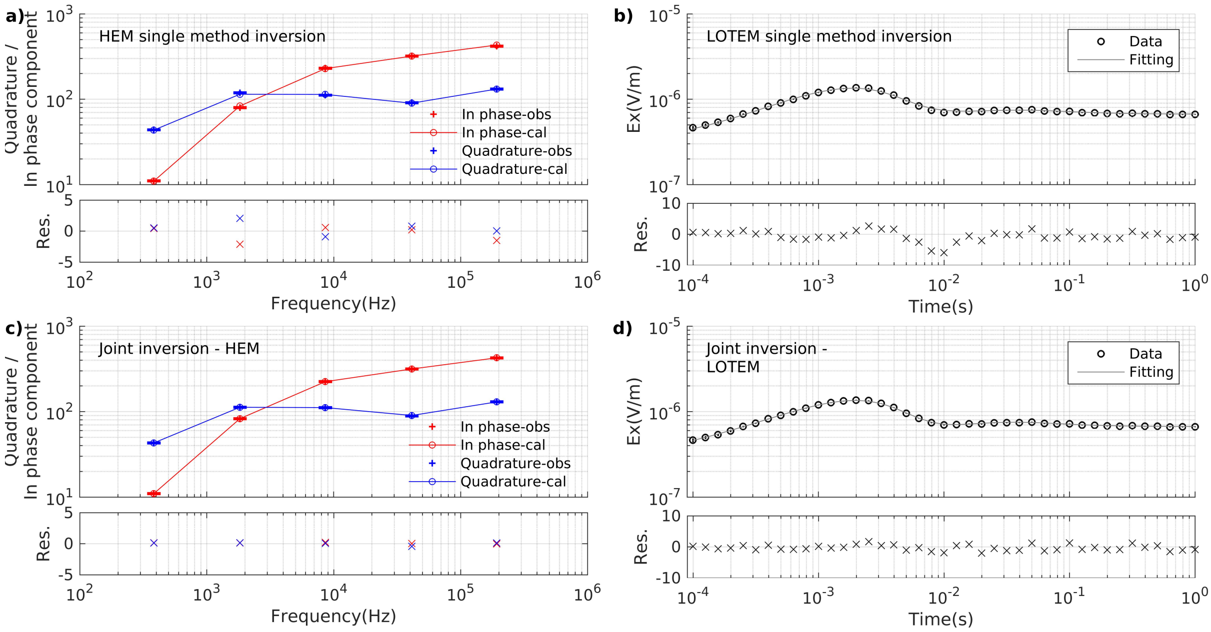

Figure A.9: Data fitting for HEM and LOTEM 1D joint inversion in Figure 4.20 and 4.21.

A.3.2 Joint inversion of HEM and semi-airborne data

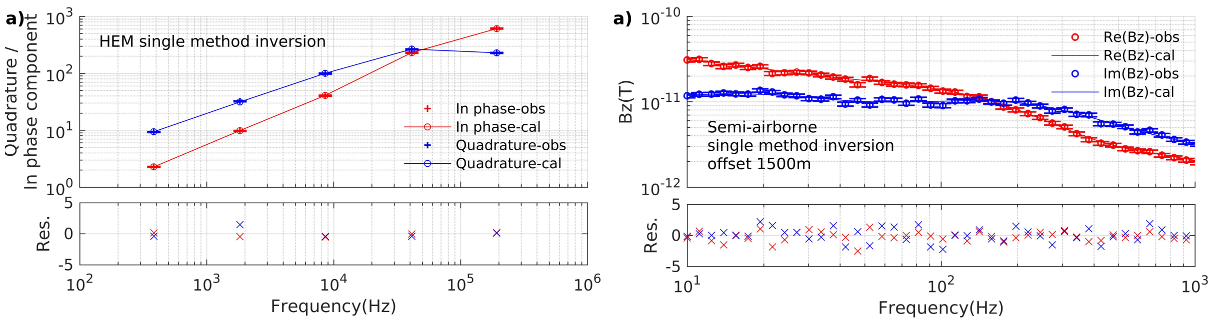

Figure A.10: Data fitting for (a) HEM and (b) semi-airborne EM (offset 500m) single method inversion in Figure A.11.

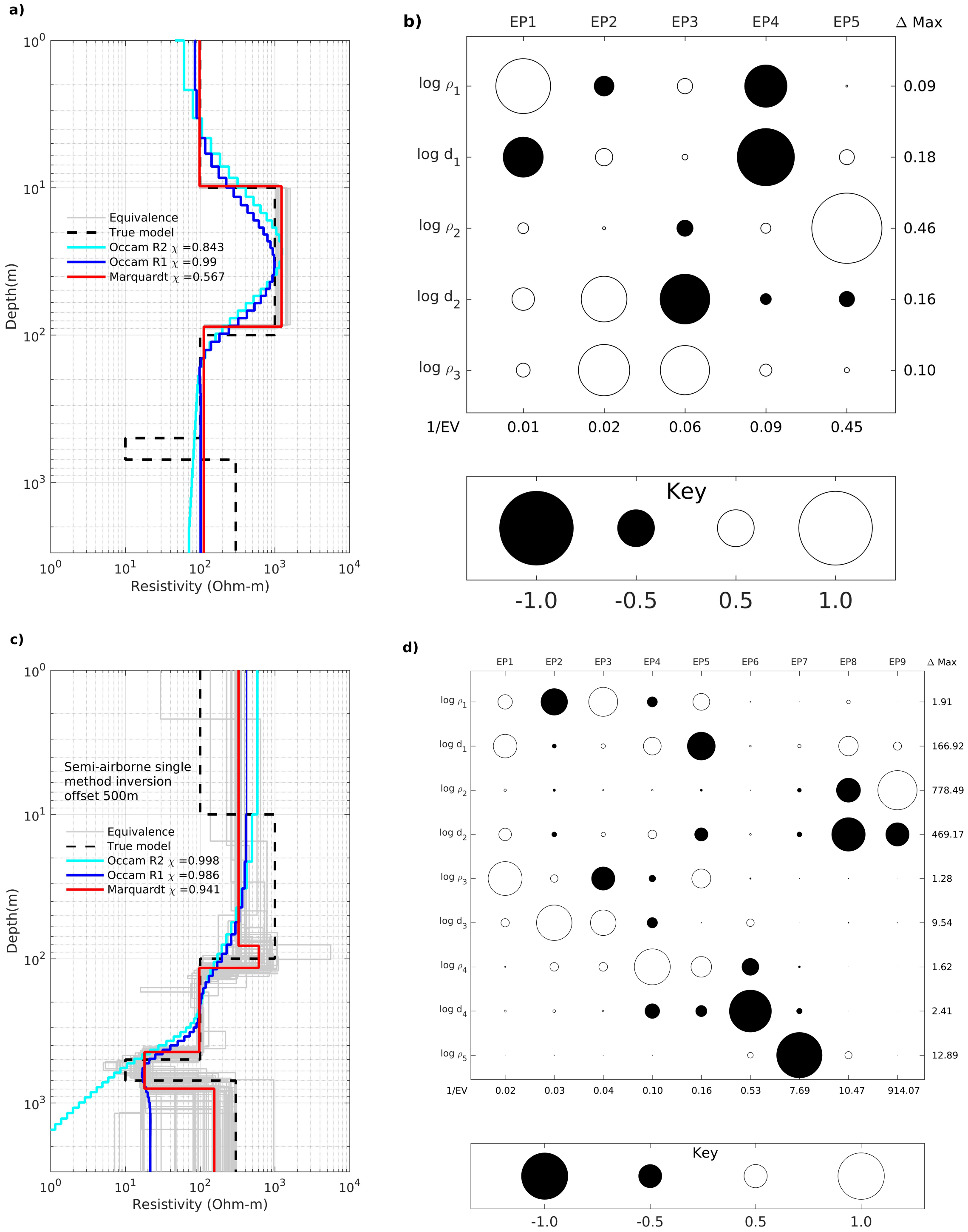

Figure A.11: Inversion result of (a) HEM single method inversion and (c) semi-airborne EM single method inversion with offset 500m. (b) and (d) display the corresponding SVD analysis for (a) and (c), respectively.

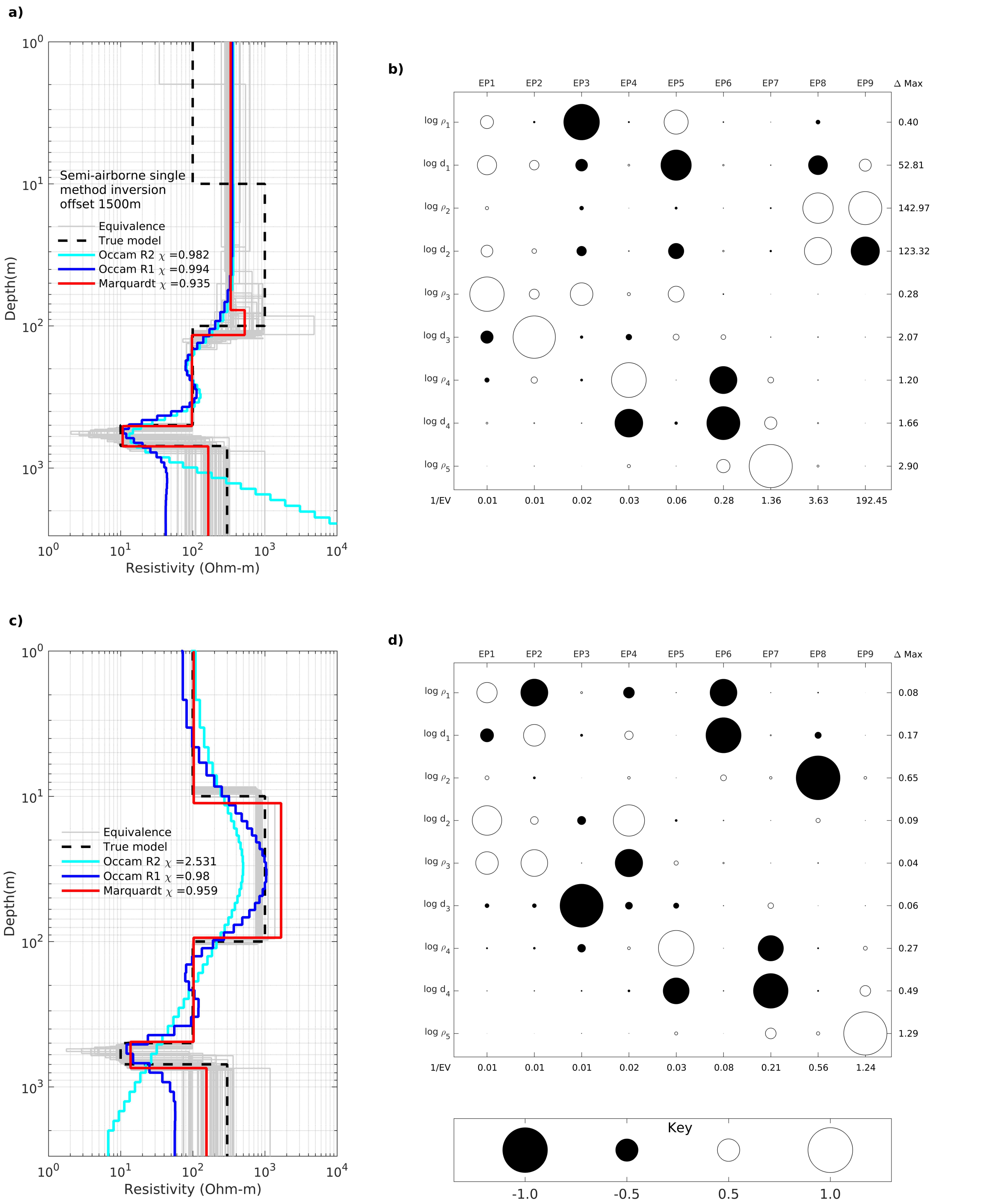

Figure A.12: Inversion result of (a) Semi-airborne EM single method inversion with offset 1500m and (c) semi-airborne EM (offset 1500m) and HEM joint inversion. (b) and (d) display the corresponding SVD analysis for (a) and (c), respectively.

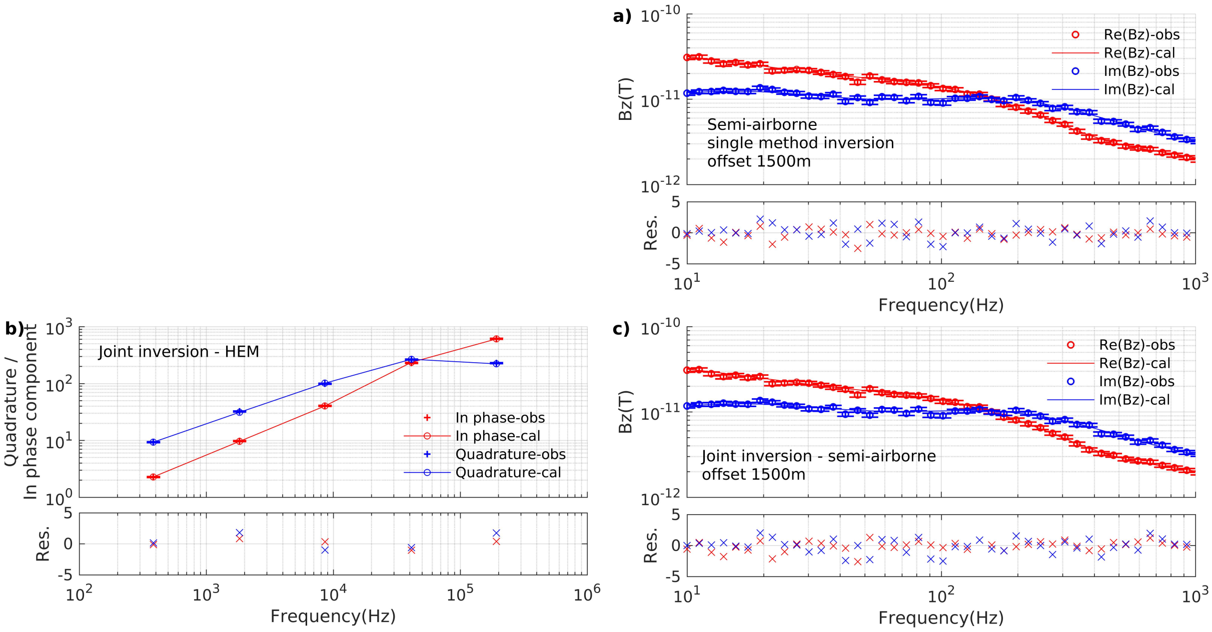

Figure A.13: Data fitting for semi-airborne EM single method inversion with offset 1500m in Figure A.12a, as well as HEM and semi-airborne EM (offset 1500m) 1D joint inversion in Figure A.12c.

A.3.3 1D Joint inversion of semi-airborne and LOTEM data

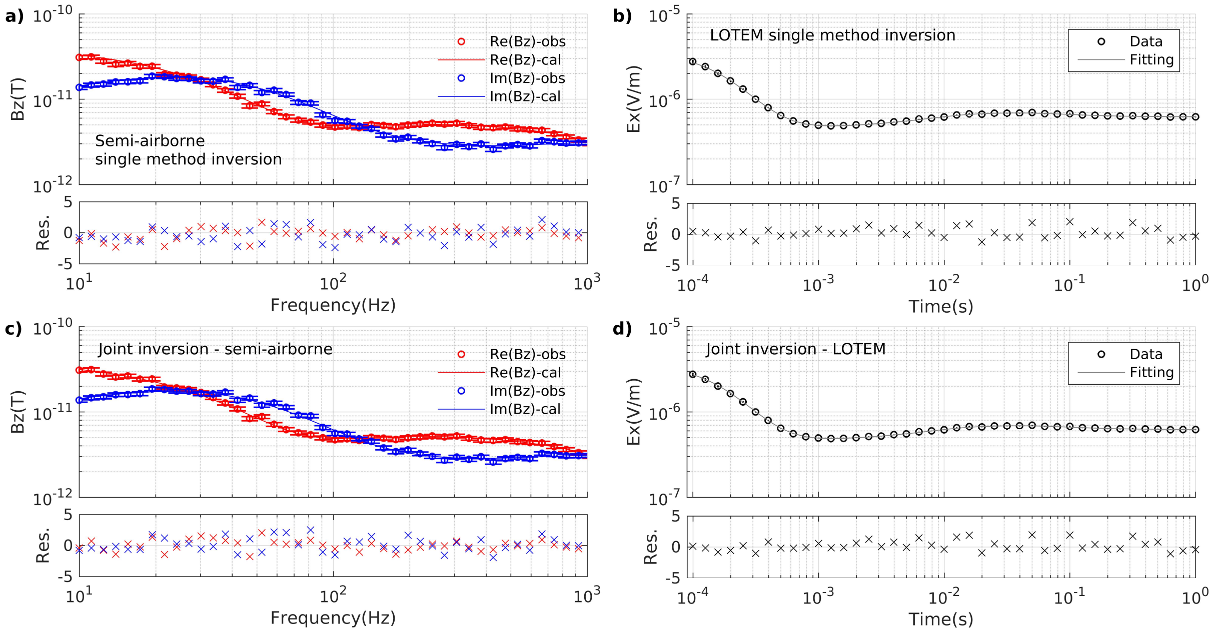

Figure A.14: Data fitting for semi-airborne and LOTEM 1D joint inversion in Figure 4.22 and 4.23.

A.3.4 1D Joint inversion of three EM methods

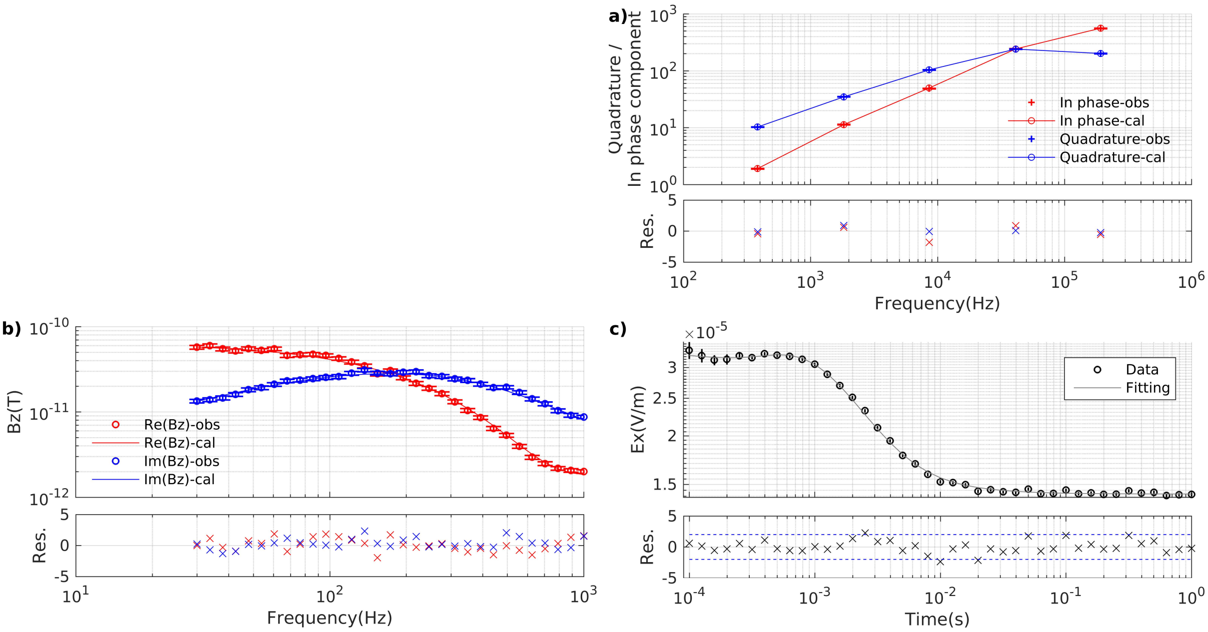

Figure A.15: Data fitting for joint inversion of HEM, semi-airborne and LOTEM in Figure 4.24. (a) HEM data fitting; (b) semi-airborne data fitting; (c) LOTEM data fitting.

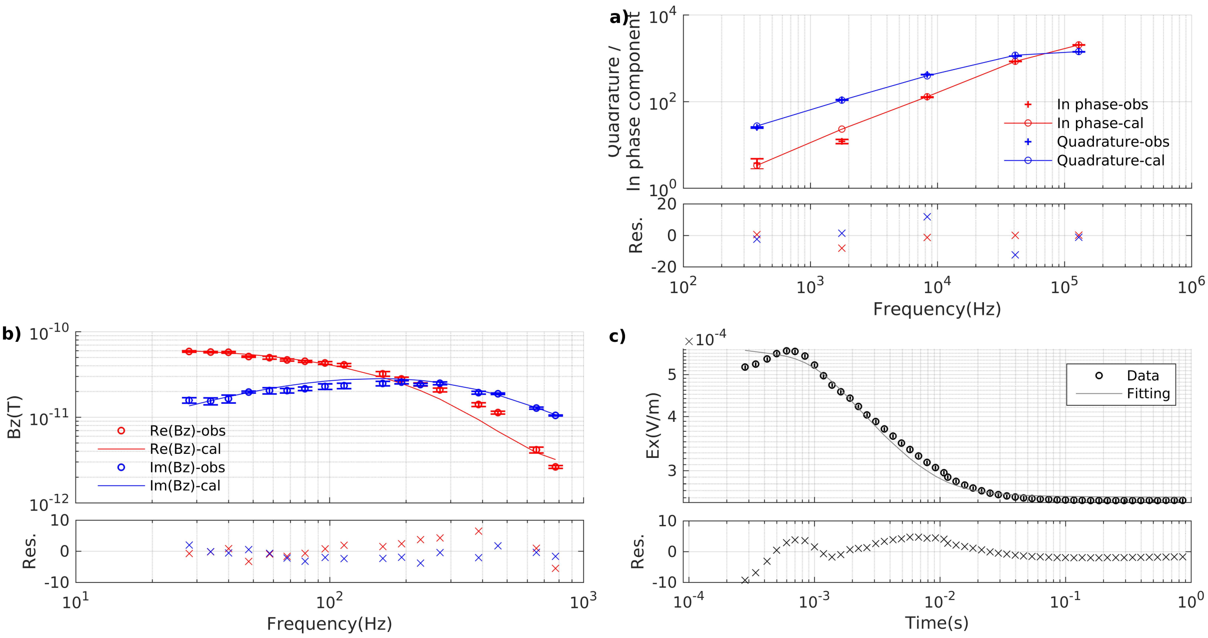

Figure A.16: Data fitting for joint inversion of HEM, semi-airborne and LOTEM field data in Figure 4.31. (a) HEM data fitting; (b) semi-airborne data fitting; (c) LOTEM data fitting.

A.3.5 Supplementary for weighting scheme studies

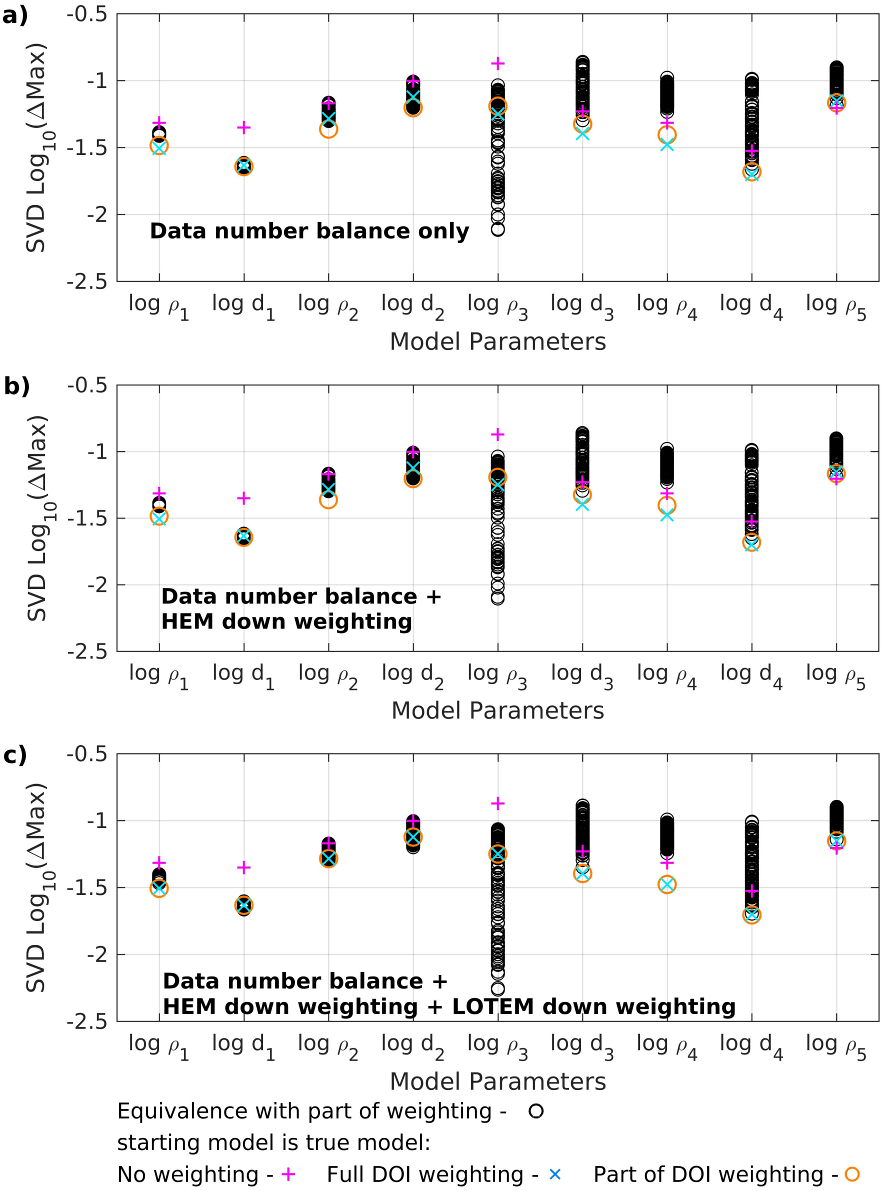

Figure A.17: The SVD ΔMax calculated by partly applying DOI weighted joint inversion on HEM and LOTEM synthetic data. (a) only data number balance is applied, (b) data number balance and HEM down-weighting are applied, (c) full DOI weighting is applied.

Appendix B Supplementary for 2D modeling studies

B.1 2D joint inversion on synthetic data in frequency-domain

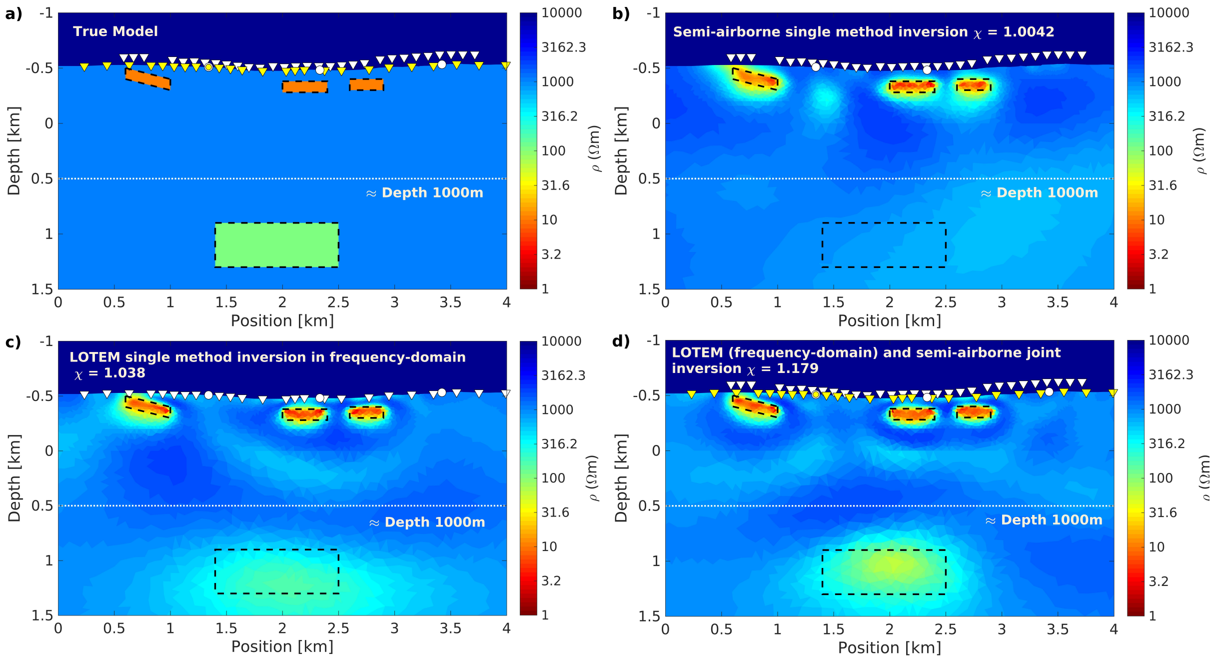

Figure B.1: Synthetic example for the 2D (joint) inversions on semi-airborne and LOTEM data in frequency-domain.(a) true model; (b) inversion result for semi-airborne data; (b) inversion result for LOTEM data (Ex component); (d) 2D joint inversion result.

B.2 Semi-airborne single method 2D inversion for field data

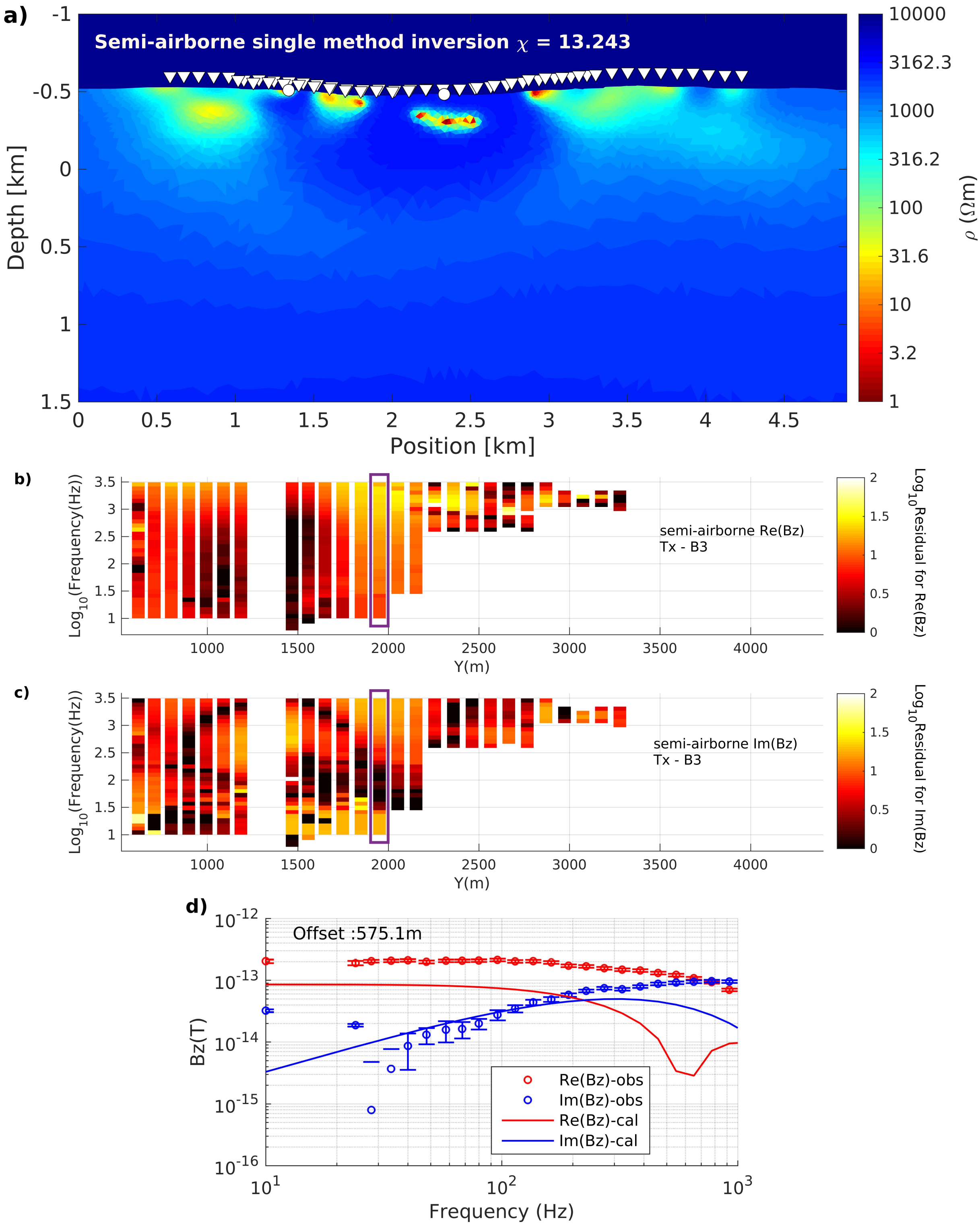

Figure B.2: Semi-airborne single method inversion result with all the data along the LOTEM profile (Line 16). Examples of the data fitting are also displayed.(a) 2D inversion result; (b) residuals for real part of data of Tx B3; (c) residuals for imaginary part of data of Tx B3; (d) an example of the data fitting which is also highlighted in (b) and (c) with purple rectangle.

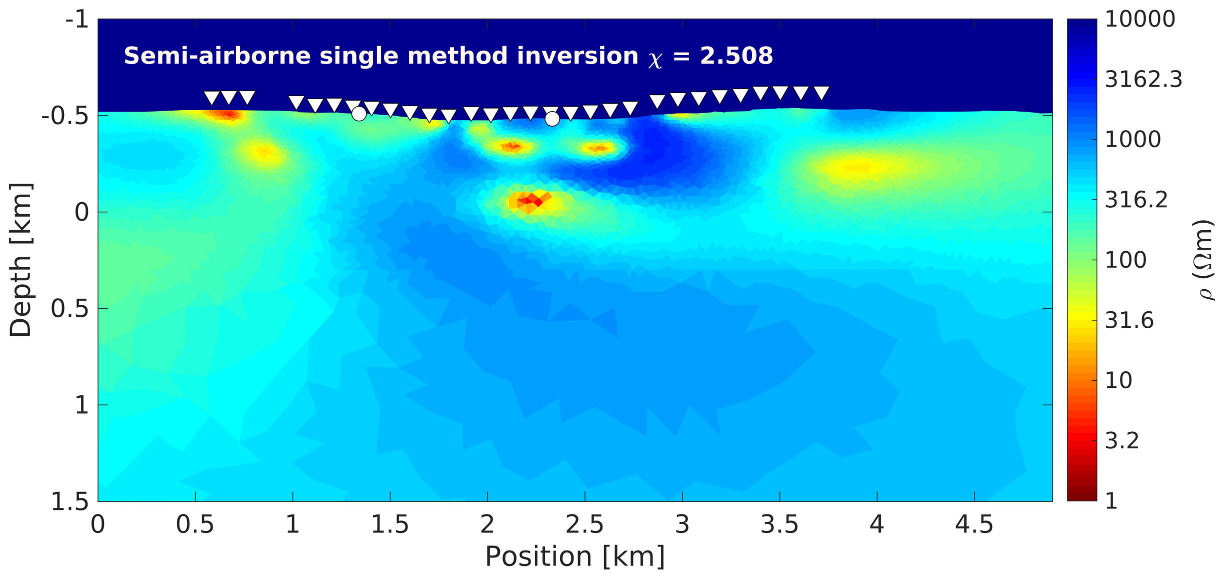

Figure B.3: 2D inversion result of semi-airborne data along the LOTEM profile. The Lagrange Value starts from 10 and the horizontal-vertical weight is 10.

B.3 Supplementary for 2D joint inversion of semi-airborne and frequency-domain LOTEM field data

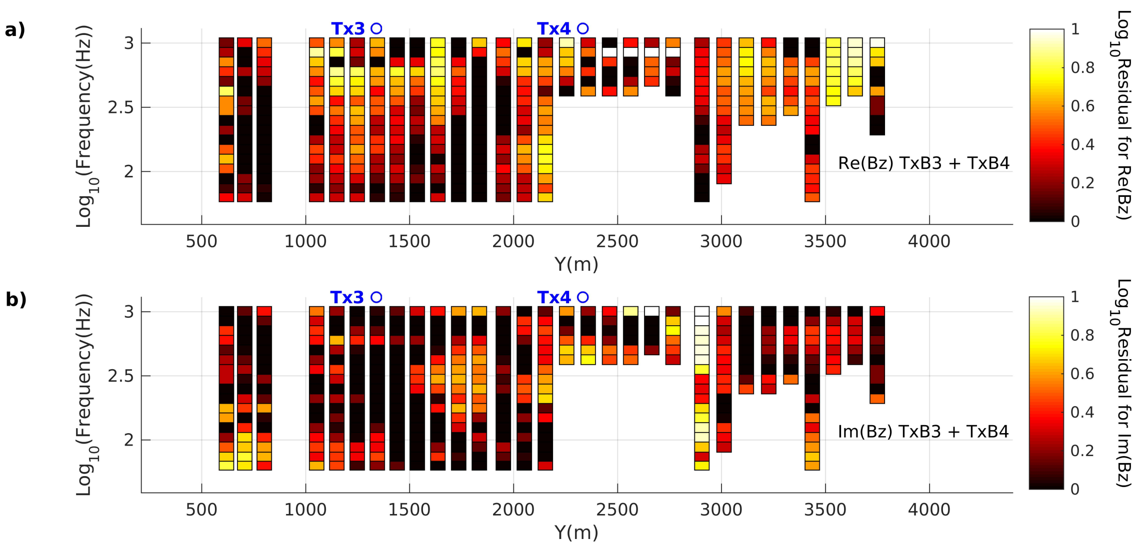

Figure B.4: Residuals of semi-airborne data for 2D joint inversion result displayed in Figure 5.17. (a) Residuals for real part of Bz; (b) Residuals for imaginary part of Bz.

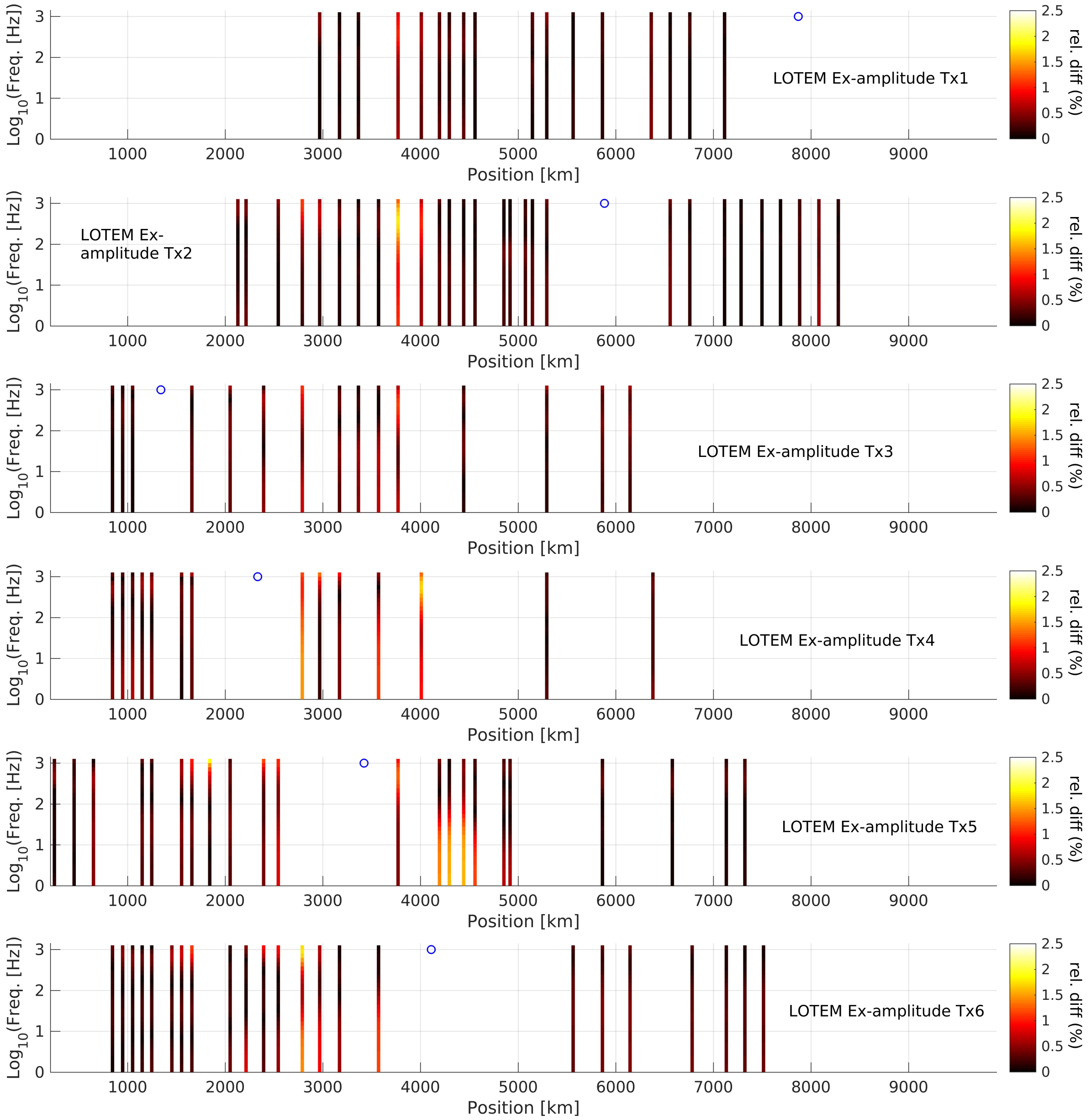

Figure B.5: Relative differences of LOTEM amplitude between the predicted data of 2D LOTEM single method inversion and 2D joint inversion.

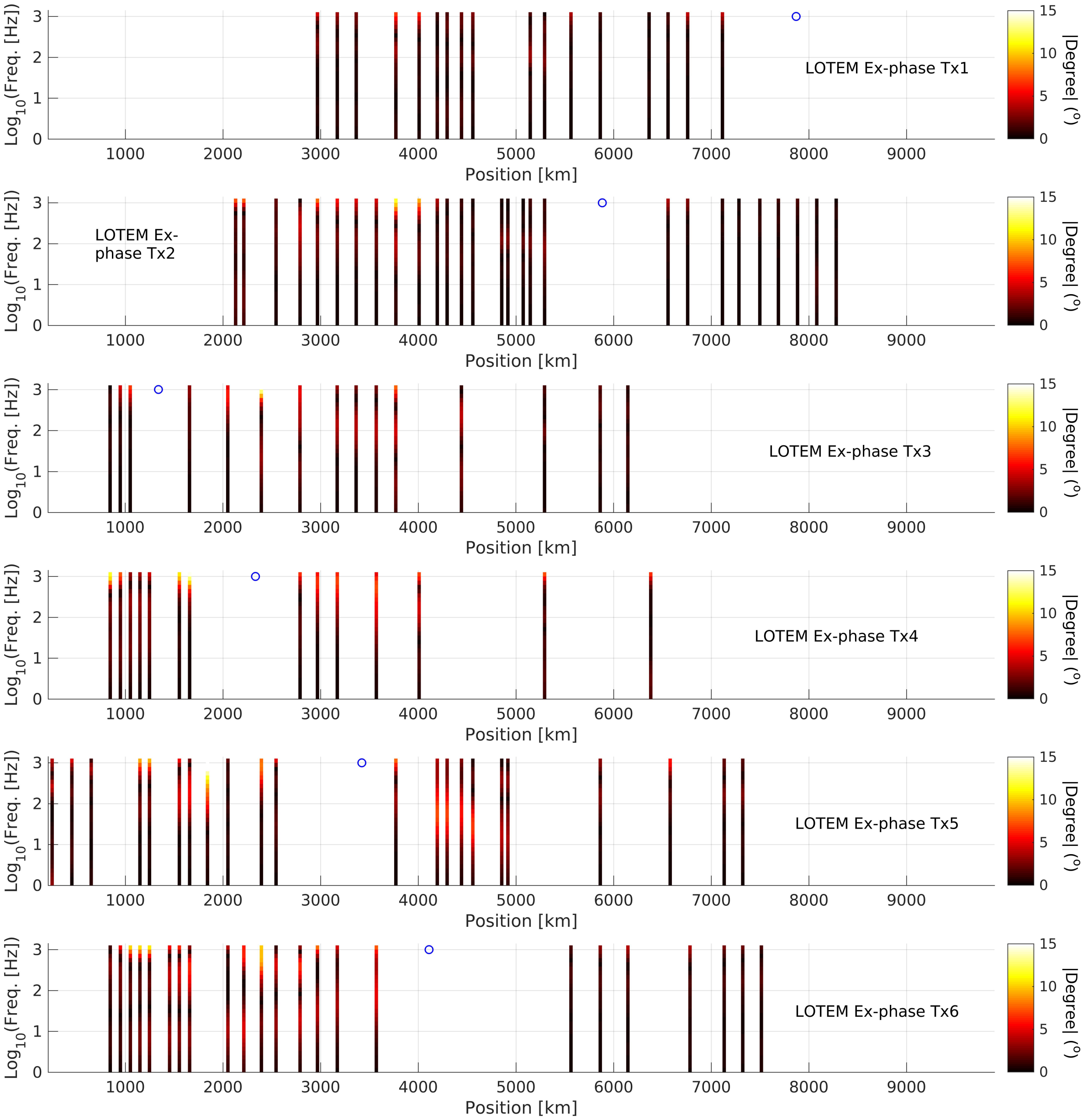

Figure B.6: Differences of LOTEM phase between the predicted data of 2D LOTEM single method inversion and 2D joint inversion.

B.4 Supplementary for 2D joint inversion of semi-airborne and time-domain LOTEM synthetic data

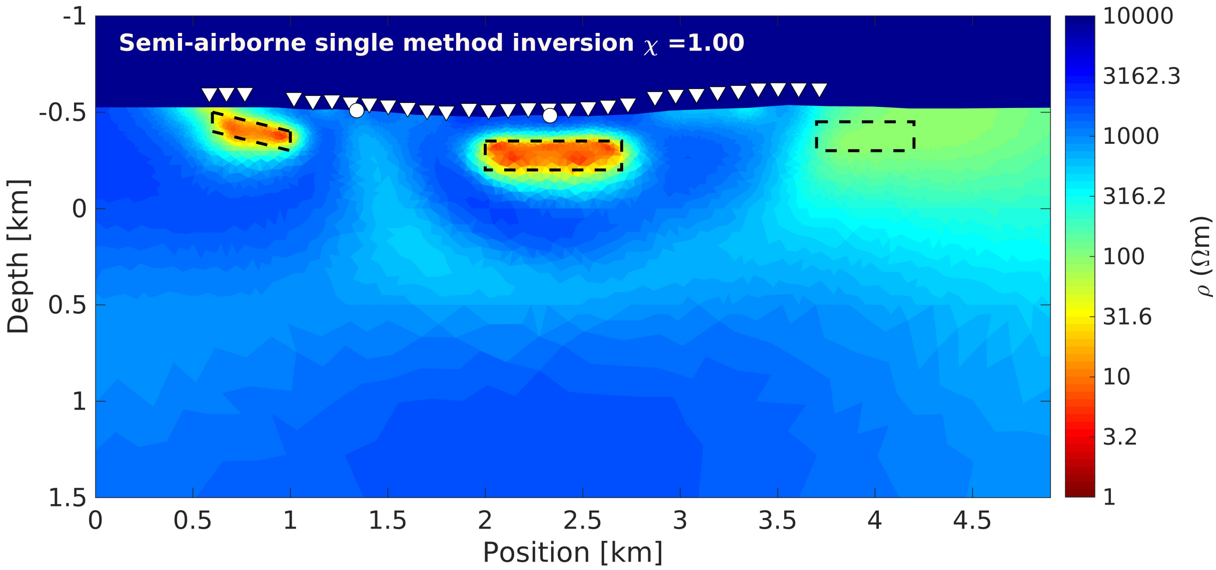

Figure B.7: 2D inversion results for the synthetic semi-airborne data if the C5 in Figure 5.22 doesn't exist.

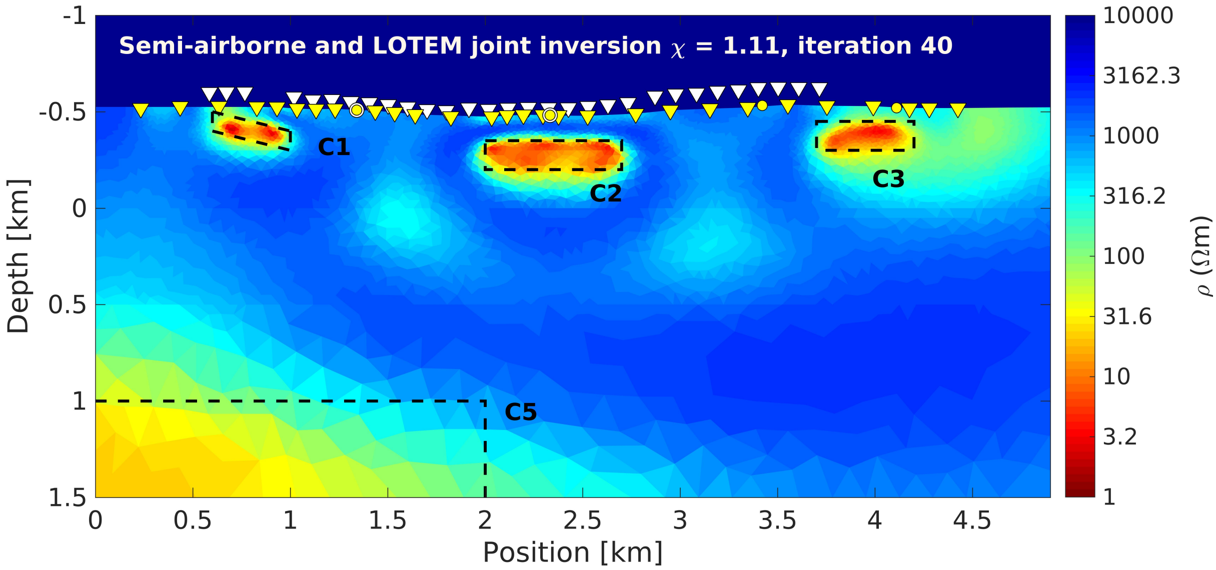

Figure B.8: 2D joint inversion results for the synthetic data of model shown in Figure 5.22 — iteration 40.

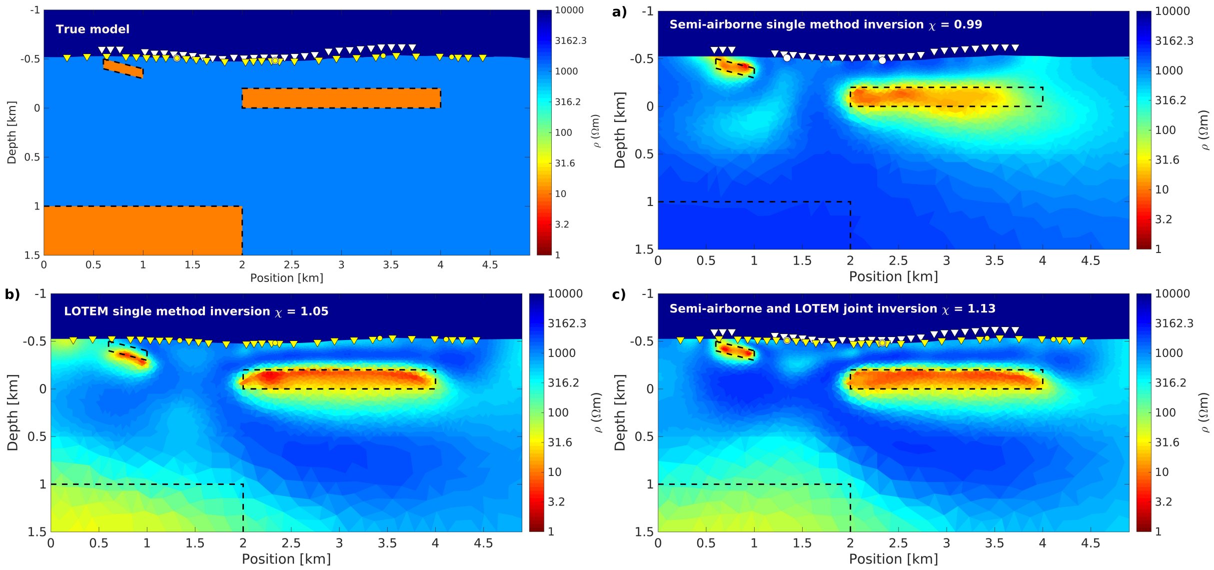

Figure B.9: Synthetic example for the 2D (joint) inversions on semi-airborne and time-domain LOTEM data. (a) true model; (b) inversion result for semi-airborne data; (b) inversion result for LOTEM data (Ex component); (d) 2D joint inversion result.

Acknowledgements

I would like to thank

- Prof. Dr. B. Tezkan for the supervision of this thesis and for giving me the opportunity to study in the Applied and Space Geophysics group. His encourage and positive attitude support me to finish this research.

- Prof. Dr. M. Becken for appraising this thesis, for sharing semi-airborne field data, and for the instructions about this research.

- Dr. P. Yogeshwar and Dr. M. Smirnova for their detailed advises and instructions. They answered tons of stupid questions from me, and helped me to address many technical problems about this research.

- Dr. W. Morbe and S. Schlegel for their helps especially in the aspect of life. Without their helps, many problems associated with language would be trick for me.

- Dr. A. Haroon and Dr. K. Lippert for their kindness and knowledgeable discussions in my first days in Germany. They are my respectable elder bothers.

- Dr. M. Smirnova, Dr. P. Yogeshwar, Dr. W. Morbe and Dr. A. Haroon for the proof-reading of this thesis.

- All the rest Applied and Space Geophysics group members.

- Chinese Scholarship Council for supporting my PhD study in Germany (File No.201506330059).

- My family, for everything.

Erklärung zur Dissertation

Ich versichere, dass ich die von mir vorgelegte Dissertation selbständig angefertigt, die benutzten Quellen und Hilfsmittel vollständig angegeben und die Stellen der Arbeit — einschließlich Tabellen, Karten und Abbildungen —, die anderen Werken im Wortlaut oder dem Sinn nach entnommen sind, in jedem Einzelfall als Entlehnung kenntlich gemacht habe; dass diese Dissertation noch keiner anderen Fakultät oder Universität zur Prüfung vorgelegen hat; dass sie — abgesehen von unten angegebenen Teilpublikationen — noch nicht veröffentlicht worden ist, sowie, dass ich eine solche Veröffentlichung vor Abschluss des Promotionsverfahrens nicht vornehmen werde. Die Bestimmungen der Promotionsordnung sind mir bekannt. Die von mir vorgelegte Dissertation ist von Prof. Dr. Bülent Tezkan betreut worden.

Köln Januar 2020: ....

(Unterschrift)